Author:
Shchepanovska, Darya

Title:
Ab initio methods for atmospheric photochemistry

Ab initio methods for atmospheric photochemistry

By

DARYA SHCHEPANOVSKA

Department of Chemistry
UNIVERSITY OF BRISTOL

A dissertation submitted to the University of Bristol in accordance with the requirements of the degree of DOCTOR OF PHILOSOPHY in the Faculty of Chemistry.

JUNE 2021

Word count: thirty six thousand nine hundred and three

Abstract

The interaction of molecules with sunlight has always played a crucial role in determining the chemical composition of the atmosphere. In this thesis, I intend to explore how describing photochemical reactions *in silico* can bridge the gap between performing a single-point electronic structure calculation, and being able to predict the rates of photochemical reactions.

Photolysis rates in models of atmospheric chemistry are frequently calculated from the measured absorption cross section. There are a number of methods for reproducing the broadening of excitation bands when this spectrum is unavailable, which I will test on a selection of atmospheric molecules so as to design a set of guidelines for selecting an appropriate strategy in each case.

One of these molecules, a hydroperoxy aldehyde, is of particular interest due to the role that nonadiabatic effects play in its photolysis. Using this model system I test an extension of the energy-grained master equation which factors in nonadiabatic transitions between different electronic states by comparing it to fully atomistic nonadiabatic dynamics. Looking at nonadiabatic processes in the excited state through a kinetic lens allows us to model the rate of population transfer between diabatic states when it is in the ergodic regime, with highly accurate transition probabilities obtained through Zhu-Nakamura theory.

In later chapters, I also explore and implement a novel nonadiabatic dynamics protocol, and apply explicit and implicit solvation methods in two case studies of photochemical reactivity.

Dedication and acknowledgements

As the old adage goes, it takes a department to raise a PhD student. All of the people mentioned here have – to a lesser or greater extent – had a hand in shaping this thesis, so it's appropriate to give them this dubious credit here.

First of all I must thank my supervisor Dave for giving me the freedom to explore my own interests, and for teaching me many things beyond chemistry – not least in the art of politics and foraging up Welsh mountains. Basile's patience, rigour, and scientific integrity make him, to me, a benchmark for what every good scientist should be. I would like to thank him for graciously giving me so much of his time, and working so hard to help publish the central paper of this thesis. Thank you also to Andrew for helping me see the relevance of my work in an experimental context, and for being so incredibly helpful in the last stretch.

Natalie, Adrian, Fred, and Tom Oliver I thank for always being willing to share valuable advice, support, and departmental gossip. Robin, my fellow revolutionary and maestro of the master equation – thank you for always being there when I reached out to you for help, whether it be a MESMER problem or generic PhD stress. Simon, thank you making me feel so welcome when I first arrived here, introducing me to great people (shout out to the Pathfinder crew), and your boundless enthusiasm for electronic structure.

Our lockdown Sunday walk crew: Helen, the reigning tea tzar; Becca, who unilaterally makes Prosexy happen; and Luke, the last bridge standing between the CCC and the laser group. Thank you for keeping me sane over these cold, strange winter months. To Alex, thank you for being such good company on our wanders out of Bristol, teaching me how to use the en-dash, and making the months I spent writing up so much happier (and probably longer). Callum, it's rare and valuable to find someone who's on the same wavelength as you about so many things. You're a good egg, I value your judgement, and I couldn't have done this PhD without you.

In no particular order I also want to thank: Rhos for giving me a run for my money in squash; Rob for getting me involved with style transfer; Stephanie for giving me almost her entire wardrobe; Zack for letting me stay in his room; Lars for introducing me to badminton (the squash game is still on the table); Harry, for the joy (and whiskey) he brings to any occasion; Jillisa for teaching me most of what I know about solvent models; Jonesy for putting me on to Prefab Sprout and periodically reminding me how unhealthy this academia business is; Jonathan for bringing huge boxes of Haribo to DnD and letting me speak at you in bad French; and the 2016 TMCS crew for the year that we spent together (especially Viivi for sharing a flat with me for two more). An honourable mention goes out to Mark's surrealistic Twitter account, Joe's chaotic anecdotes, and all the denizens of the tea room. Chalmers, Tess, Jennifer, Fay, and Rex – you may never read this, but I appreciate you all nonetheless. I'm grateful to my family, especially my mum, for being unconditionally supportive throughout, and rarely asking "When will you be done?".

Lastly, this thesis is dedicated to the memory of my friend, Jonathan Milward, whom I miss dearly.

AUTHOR'S DECLARATION

I declare that the work in this dissertation was carried out in accordance with the requirements of the University's Regulations and Code of Practice for Research Degree Programmes and that it has not been submitted for any other academic award. Except where indicated by specific reference in the text, the work is the candidate's own work. Work done in collaboration with, or with the assistance of, others, is indicated as such. Any views expressed in the dissertation are those of the author.

SIGNED: ..... DATE: .....

TABLE OF CONTENTS

Page

List of Tables **xi**

List of Figures **xiii**

1 Introduction **1**

1.1 A brief overview of the field 2

1.1.1 Experiment 4

1.1.2 Theory 5

1.2 Electronic structure for excited states 6

1.3 Thesis outline 9

2 Ab initio prediction of photoabsorbtion cross sections **11**

2.1 Absorption cross section 13

2.2 Methods 14

2.2.1 Franck-Condon Herzberg-Teller 14

2.2.2 Wigner sampling 16

2.2.3 Sampling from molecular dynamics 19

2.2.4 Including temperature 23

2.3 Results and Discussion 26

2.4 Conclusion 28

3 Comparison of energy grained master equation and atomistic dynamics for predicting nonadiabatic kinetics **31**

3.1 Introduction 31

3.2 Nonadiabatic molecular dynamics 34

3.3 Nonadiabatic energy grained master equation 36

3.3.1 Ground state EGME kinetics 38

3.3.2 Nonadiabatic EGME 39

3.3.3 Zhu-Nakamura theory of nonadiabatic transitions 39

3.3.4 Zhu-Nakamura equations for a nonadiabatic tunnelling type crossing . . . 40

3.4 Computational Details . . . 43
3.4.1 Characterising the PES . . . 43
3.4.2 Photoabsorption cross section . . . 44
3.4.3 Nonadiabatic dynamics . . . 45
3.4.4 Constructing a NA-EGME model . . . 46
3.5 Results . . . 47
3.5.1 Ground and excited state PES . . . 47
3.6 Single conformer model . . . 51
3.6.1 Dynamics . . . 51
3.6.2 Importance of time step size for an (3N-7) dimensional seam crossing . . . 53
3.6.3 NA-EGME . . . 56
3.7 Full conformational analysis of C_6-HPALD . . . 57
3.7.1 Dynamics . . . 57
3.7.2 An all-conformer NA-EGME model of OH loss . . . 58
3.7.3 Improving NA-EGME with CASPT2 energies . . . 60
3.8 Discussion . . . 61
3.9 Conclusion . . . 64

4 Photochemistry of HPALDs **67**
4.1 Atmospheric photolysis in isoprene chemistry . . . 67
4.1.1 HPALD formation in the atmosphere . . . 69
4.1.2 Evidence for HPALD photolysis . . . 70
4.2 UV-Vis spectra of HPALDs . . . 72
4.2.1 Computational Details . . . 72
4.2.2 Spectra of HPALD I and HPALD II . . . 74
4.3 The mechanism of OH loss . . . 76
4.4 Simulating sunlight-induced dynamics . . . 77
4.5 Conclusion . . . 78

5 Quantum Trajectory Surface Hopping **81**
5.1 Introduction . . . 81
5.2 Fewest switches surface hopping . . . 82
5.2.1 The problem of decoherence . . . 84
5.3 Consensus Surface Hopping . . . 85
5.3.1 Quantum Trajectory Surface Hopping . . . 88
5.4 Implementing the algorithm . . . 90
5.4.1 The integrator . . . 91
5.5 Testing the QTSH implementation . . . 92
5.5.1 Tully's model systems . . . 93

5.5.2 Spin-boson Hamiltonian . . . 96
5.6 Conclusions . . . 97

6 Solvent effects in photochemistry **99**
6.1 Introduction . . . 99
6.2 Continuum solvation models . . . 100
6.2.1 Excited states . . . 102
6.3 NPP Photochemistry . . . 103
6.3.1 Computational Details . . . 103
6.3.2 Results . . . 104
6.4 Projector based embedding for excited states . . . 107
6.4.1 Benzophenone photochemistry . . . 108
6.4.2 Computational details . . . 109
6.4.3 Results and Discussion . . . 109
6.5 Conclusion . . . 112

7 Conclusion **113**

A Appendix A **117**
A.1 Benchmarking excited state methods . . . 117
A.2 Fitting the survival probability . . . 117
A.3 Sensitivity testing the EGME model . . . 119
A.4 Influence of hindered rotor corrections on the EGME results . . . 119
A.5 TS diabat fitting parameters . . . 120
A.6 Critical Points . . . 120

B Appendix B **123**

C Appendix C **125**

Bibliography **129**

List of Tables

Table **Page**

2.1 Properties of spectrum simulation methods 30

4.1 DFT benchmarks for ensemble sampling 73
4.2 Excitation energy and oscillator strengths benchmark 74

A.1 Benchmarks for excitation energies at the S_0 optimised geometry of conformer B. . . 118
A.2 Parameters for LR-TDDFT/PBE0/6-31G diabats 121
A.3 Parameters for MS(4)-CASPT2(10,8)/6-31G* diabats 121
A.4 Energies, rotational constants, and frequencies at the critical points used in the EGME calculations. 122

C.1 Frequencies at S_0, S_1 and T_1 geometries of NPP 125
C.2 Excitation energies of NPP at S_0 geometry, singlets 126
C.3 Excitation energies of NPP at S_1 geometry, singlets 126
C.4 Excitation energies of NPP at T_1 geometry, triplets 127
C.5 Energy gaps for transitions from the S_1 state 127
C.6 Energy gaps for transitions from the T_1 state 128

List of Figures

Figure **Page**

1.1 Jablonski diagram 2

2.1 FC-HT spectrum schematic 15
2.2 Wigner ensemble sampling schematic 18
2.3 Classical MD sampling schematic 20
2.4 GLE sampling schematic 21
2.5 Rotamers of acetoin 24
2.6 Temperature effect in Wigner sampling 25
2.7 Formaldehyde spectra comparison 27
2.8 Acrolein spectra compaison 28
2.9 Hydroxypropanone spectra comparison 29

3.1 C_6-HPALD photodissociation 33
3.2 EGME schematics 37
3.3 Zhu-Nakamura nonadiabatic type crossing 41
3.4 Conformers of C_6-HPALD 48
3.5 Absorption cross section of C_6-HPALD 48
3.6 Benchmarks scan of the peroxide coordinate 49
3.7 3-D scan of the S_1/S_2 nonadiabatic crossing seam 50
3.8 IRC scan 51
3.9 C_6-HPALD trajectories: conformer C 53
3.10 C_6-HPALD EGME decay: conformer C 54
3.11 Time step size benchmark A 55
3.12 Time step size benchmark B 56
3.13 Interconversion between conformers from MD 58
3.14 C_6-HPALD trajectories: All conformers 59
3.15 C_6-HPALD EGME decay: All conformers 60
3.16 Fitted MS-CASPT2 diabatic potentials across S_1-TS 61
3.17 EGME results based on MS-CASPT2 energies 62
3.18 Comparison of MD and EGME models 63

3.19 Clasification of nonadiabatic PES crossings 65

4.1 LIM1 mechanism of Isoprene oxidation 71
4.2 HPALD I spectra 75
4.3 HPALD II spectra 76

5.1 Tully's model systems 84
5.2 Density matrix convergence with time step for various integrator algorithms 94
5.3 Comparison of integration algorithms: energy conservation 95
5.4 Comparison of integration algorithms: NAC vector 95
5.5 Tully's avoided crossing model, QTSH results 96
5.6 SBH model, QTSH result 98

6.1 UV-Vis spectrum of NPP 105
6.2 Density difference plot for S_0 to S_1, S_2, and S_3 excitations 106
6.3 NPP photodynamic mechanism 107
6.4 CC2 singlets: gas-phase Bzp 110
6.5 CIS singlets: Bzp-MeOH 110
6.6 CC2 singlets and triplets: Bzp-MeOH 111

A.1 Testing EGME robustness to initial energy and sensitivity to frequencies. 120
A.2 EGME results with hindered rotor correction 121

CHAPTER 1

INTRODUCTION

Light passing through matter is exponentially attenuated according to the Beer-Lambert law. Attenuation of light intensity occurs due to electromagnetic energy being absorbed by a material and converted to chemical energy, that is electronic, translational, vibrational, or rotational energy of the constituent molecules. This energy transfer can be the driving force of chemical change, with many naturally occurring examples including photosynthesis, vision, and bioluminescence. Light-driven reactions have also been used for industrial applications: photo-initiated free-radical polymerisation is used in the production of polystyrene,[1] photovoltaic cells are used to convert light energy to electricity,[2] sunscreens work by absorbing UV light.[3] In this work, I am interested in how light drives chemical reactivity in atmospheric molecules, and describing the dynamics of these processes from a theoretical perspective. This entails understanding and improving the methods that we as computational chemists use to bridge the gap between a single point electronic structure calculation, and tangible experimental observables.

A change in electronic state is typically accompanied by the absorption of a photon whose wavelength is in the 200-800 nm range. Electronic transitions are commonly understood in the terms presented by a Jablonski diagram – see Fig. 1.1 – which contains a set of electronic and vibrational (and implicitly, rotational) states which are connected through radiative and non-radiative transitions. We must however consider the information missing from these diagrams. Firstly, the energetic ordering of these states is only true at a particular nuclear geometry (configuration), so any dynamics or even rearrangement of the solvent cage around the new state can change how favourable a given process is. Timescales of electronic transitions differ significantly, with photon absorption being almost instantaneous (10^{-15} s), vibrational relaxation only a little slower (10^{-12} s), fluorescence occurring in 10^{-10}–10^{-7} s, and phosphorescence often

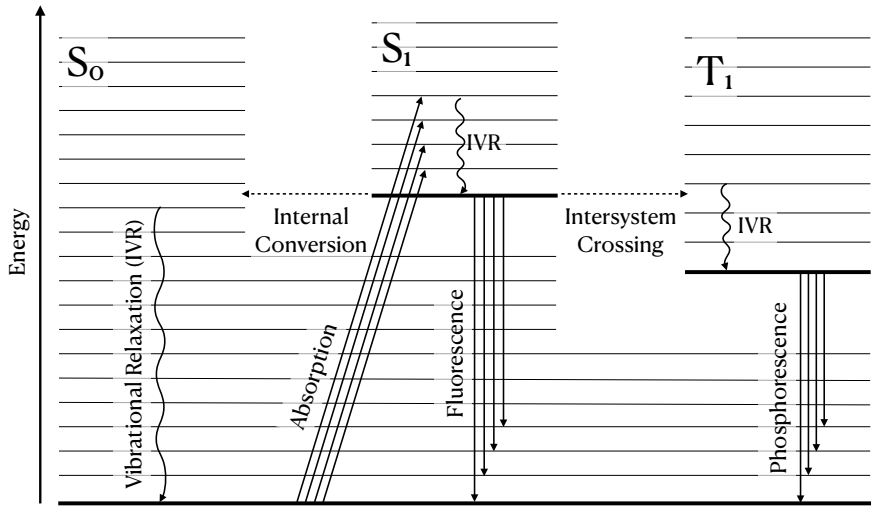

Figure 1.1: An example of a Jablonski diagram illustrating some common photochemical processes. Radiative processes, where a photon is absorbed or emitted include absorption, fluorescence, and phosphorescence. Non-radiative processes include (intramolecular) vibrational relaxation, intersystem crossing, and internal conversion.

taking longer that 10^{-6} s. These timescales are in part governed by photochemical processes such as internal conversion (IC), intersytem crossing (ISC), and vibrational relaxation (IVR) shown in Fig. 1.1. The work described in this thesis will mainly concern IC processes as they tend to occur faster than ISC. However, ISC can become important when the spin-orbit coupling is substantial, which is more common in molecules containing heavy atoms such as iodine or bromine. This leaves us with the question of why a particular photochemical mechanism is any more likely than another. This is the question that I would like to address in this work.

1.1 A brief overview of the field

The title of this thesis draws a connection between two vast research fields: atmospheric photochemistry and the computational study of excited states. Therefore, it is deeply necessary to narrow the scope of the discussion to a few specific questions that will be addressed here, while keeping in mind why, in practical terms, a particular question is important.

Building reliable models of atmospheric chemistry is crucial to understanding ground level pollution, making climate and weather predictions, and tracking the recovery of the ozone layer. Only recently, chemical transport models have been used to trace an increase in chlorofluorocarbon (CFC-11) emissions to a specific geographic region.[4] The implication of this, is that such models can be a tool of accountability in international agreements on emission targets, making their accuracy all the more crucial. Examples of atmospheric chemistry models include: the United Kingdom Chemistry and Aerosols (UKCA) model, which is used by the MET Office to forecast

air quality and for scientific research; the Master Chemical Mechanism (MCM), which contains a reaction network describing the gas-phase reactions of volatile organic compounds (VOCs);[5] and the GEOS-CHEM model, an open-access 3-D model which builds on historical meteorological data.[6] These are all numerical models, in which the production and loss of chemical species is governed by coupled ordinary differential equations. They all contain a reaction network, with the rates of those reactions; a photolysis scheme that incorporates the effects of cloud occlusion and aerosols; deposition/emission rates; and surface chemistry (e.g. on polar stratospheric clouds). In the following paragraph, I will give a very brief overview of some of the most important reactions occurring in the atmosphere.

The Chapman cycle is arguably the most important photochemical process, which describes the inter-conversion of ozone and oxygen in the stratosphere through the absorption of UV light (<310 nm).[7] While this reaction dominates the stratosphere, at ground level and in the troposphere the chemical reaction network has become significantly more complex due to an abundance of emissions. Those emissions can be anthropogenic, i.e. originating from human activity such as the burning of fossil fuels; biogenic, originating from natural functions of biological organisms; or non-biogenic, covering non-biological natural processes e.g. volcano eruptions. It was originally thought that pollutants must slowly diffuse into the stratosphere for them to be destroyed by oxidation, leading to predictions of long diffusion-limited atmospheric lifetimes.[8] In the 1970s it was discovered that those gases were in fact removed from the troposphere by reacting with hydroxyl (OH) radicals, which are present in the troposphere at concentrations of 10^6 molecule cm^{-3}. Hydroxyl rapidly oxidises most non-radical molecules, being especially reactive with hydrogen containing compounds, which is why OH is colloquially known as an atmospheric "detergent". The main source of OH is through the photolysis of ozone which produces $O(^1D)$ atoms that react with water vapour, however it is also produced in the oxidative cycle of isoprene which will be discussed in chapters 3 and 4 of this thesis. The OH radical then reacts mainly with CO, CH_4, and other VOCs, initiating chains of radical reactions that can produce more O_3 depending on ambient concentrations of NO_x.[9] These reactions mean that gross O_3 production in the troposphere is greater than the downwards flux from the stratosphere. Another important reaction is the ozonolysis of alkenes, which results in the formation of Criegee intermediates. These intermediates have been studied extensively, and are known to play an important role in the tropospheric oxidative cycle.[10]

The background gas-phase HO_x-O_3-CO-CH_4-NO_x-VOC tropospheric cycle is further complicated by interactions between different phases e.g. aerosols and particulate surfaces. Formation of sulphate aerosols is initiated by dimethyl sulphide (DMS) and sulphur dioxide (SO_2) reacting in the troposphere to form sulphuric acid. Aerosols can significantly impact the optical properties of air due to their ability to scatter and absorb sunlight, and affect cloud formation by acting as cloud condensation nuclei leading to changes in droplet size distribution. Observing the increase in cloud albedo as a result of sulphate emissions from the eruption of Mt. Pinatubo has led some

to suggest radical geoengineering solutions to climate change through artificial cloud seeding.[11] The knock-on effects of such interventions are extremely uncertain since artificial alterations in solar flux will impact the rates of all photochemical reactions at ground level. At current ozone concentrations, only solar radiation with wavelengths higher than 290 nm can penetrate the stratosphere to initiate ground-level photochemistry. Photolysis will occur if the photodissociation energy of an atmospheric species is below that threshold. The rates of these processes depend on the wavelength dependent quantum yield, solar flux, and on the absorption cross-section, which is therefore needed to obtain the photodissociation rates included in models of atmospheric kinetics.

Ultimately, I argue that computational tools will become indispensable if we seek to understand the full complexity of the chemical reaction networks present in the troposphere. In the following sections I describe how the quantities needed to construct chemical models can be obtained experimentally. Then, I give an overview of the main theoretical concepts used when describing excited state processes, leading into a discussion of electronic structure theory for excited states.

1.1.1 Experiment

In the Master Chemical Mechanism (MCM v3.1) the photolysis rates are calculated as a function of solar zenith angle, the absorption cross section, and literature quantum yields.[5] For stable molecules with a reasonable vapour pressure, collecting the UV-Vis spectrum is a routine procedure in analytical chemistry – although it may be more difficult for radicals and transient intermediates.[12] The Beer-Lambert law is applied to determine the wavelength-dependent absorbance and thus, the cross section. Experiments to determine quantum yields are less straightforward – often, a collapsible Teflon film reaction chamber (or a cloud chamber for the study of aerosols) is used, with a valve which takes out a sample of the gas mixtures in the chamber at regular time intervals. The product concentrations in these samples can be measured through mass spectrometry,[13] chromatography,[14] or FTIR spectroscopy[15] to calculate the rate. However, chamber reaction data can be unreliable due to wall reactions, and the product ratio may have a temperature and pressure dependence that is difficult to measure. Direct spectroscopic measurement of the quantum yield in the reaction chamber is also possible, as demonstrated by Pope *et al.* in their measurement of formaldehyde photolysis products.[16] Still, for many reactions in the MCM model, quantum yields are assumed to be unity.

Reaction chamber experiments are valuable for determining rates and yields but can't be used to understand the mechanisms of ultrafast photochemical processes. It is possible to observe the time-resolved mechanism of a reaction in detail through time-resolved transient absorption (TA) spectroscopy. This widespread pump-probe experimental technique is used to study the dynamics of a system and can be used to observe ultrafast processes such as electron or charge transfer, solvent relaxation, or photoisomerization. The initial laser pump pulse excites the system out of

equilibrium, while the subsequent probe pulse measures the response in its wavelength-resolved difference spectrum at discrete time intervals. The timescale of a TA experiment can range from 10s of femtoseconds to a few nanoseconds, determining the aspects of a mechanism that can be observed. While TA is especially difficult in the gas phase because of the low concentration of molecules, in atmospheric chemistry it has been used to study a wide range of reactions such as the wavelength dependence in chlorine dioxide photochemistry,[17] pressure dependence of hydroxyl radical recombination,[18] and photolysis of nitrophenol derivatives as potential sources of OH.[19]

1.1.2 Theory

In recent years, our understanding of atmospheric reaction networks has become more reliant on theoretical as well as experimental studies. Since many gas-phase atmospheric molecules are small (fewer than 6 non-hydrogen atoms), multireference electronic structure calculations allow us to calculate thermodynamic barriers to within the bounds of chemical accuracy (1 kcal mol^{-1}).[20, 21] It is now routine to use these values to determine *ab initio* rate constants through well-established rate theories originating in transition state theory (TST), such as variational TST,[22] and multi-conformer TST.[23] Exploring these reaction networks *in silico* lets us examine short-lived radical species, or molecules that are produced at a very low concentration, making the experimental determination of these values significantly more difficult. Some atmospheric mechanisms have been proposed based purely on a computational argument, including the isoprene oxidation mechanism LIM0[24] and the reactions of aliphatic amines with OH.[25] While this strategy is extremely useful for the ground electronic state, it cannot be applied straightforwardly to reactions that proceed via one or more excited states.

These computational protocols are confined to the ground state potential energy surface (PES) and are therefore implicitly reliant on the Born-Oppenheimer (BO) approximation. Stated simply, this is the assumption that atomic nuclei move on a significantly slower timescale than electrons and so their motion can be decoupled from each other. By expressing the total wavefunction as a separable product of electronic and nuclear parts $\Psi(\mathbf{r},\mathbf{R}) \approx \phi_e(\mathbf{r};\mathbf{R})\chi_n(\mathbf{R})$, finding a solution to the Schrödinger equation becomes much simpler, as the nuclear kinetic energy part of the Hamiltonian can be neglected. This leaves us with the electronic Hamiltonian $\hat{H}_e$ where the nuclear coordinate vector $\mathbf{R}$ is a fixed parameter, yielding an eigenvalue equation that can be solved approximately as

$$\hat{H}_e\phi_e(\mathbf{r};\mathbf{R}) = E_i\phi_e(\mathbf{r};\mathbf{R}).$$

This means that for every fixed nuclear configuration $\mathbf{R}$ and state i, there is a corresponding energy E_i defining the PES for that state.

Despite its utility, the BO approximation famously breaks down in many photochemically important scenarios. Motion of the nuclei can trigger an electronic transition when the states are close in energy.[26] These types of phenomena are described as *nonadiabatic* and play a crucial

role in most photodynamic processes,[27] charge-transfer reactions,[28] conductivity,[29] molecular electronics,[30] and a multitude of other scenarios. Simulations of molecular dynamics in these cases need to somehow incorporate nonadiabatic effects, and a multitude of methods have been developed to achieve this, which will be discussed in greater detail in chapter 3. Nonadiabatic dynamics simulations have been applied to explore the mechanisms of many atmospherically significant reactions, not least to investigate the photochemistry of Criegee intermediates,[31] the photodissociation of atmospheric mercury species,[32] and the passage through a conical intersection between two singlet states in sulphur dioxide.[33]

The idea of a PES informs much of our intuitive understanding of photochemical mechanisms, since transitions between electronic states are linked to topological features such as conical intersections, avoided crossings, saddle points, and potential energy barriers. Visualising molecular motion is simply easier in 3N-6 dimensional spaces described by nuclear coordinates, rather than abstract Hilbert spaces suggested by the Schrödinger equation. Perhaps this is why many modern nonadiabatic dynamics methods rely on the idea of a PES as a landscape guiding the evolution of a nuclear wavepacket. Even in Ehrenfest dynamics[34] where trajectories are not constrained to any particular PES, the dynamics occur on an average of multiple potentials and so are guided by them. We can therefore conclude that accurate excited state PES are crucial for making reliable predictions with nonadiabatic dynamics methods such as multiconfigurational time-dependent Hartree (MCTDH) or *ab initio* multiple spawning (AIMS).[35] How we can calculate accurate excited state PES is discussed in the following section. However, it should be mentioned that new theories are being developed that can bypass this decoupled view of nuclear and electron motion.[36]

Lastly, the Franck-Condon principle is the assumption that electronic transitions mediated by the absorption or emission of a photon are essentially instantaneous on the timescale of nuclear motion. This assumption allows us to calculate the probability of excitation between two vibronic states based on the overlap of their vibrational wavefunctions, i.e. the Franck-Condon factor. The Franck-Condon principle will be discussed further in the following chapter.

1.2 Electronic structure for excited states

The accuracy of any computational prediction made about the photochemical reactivity of a molecular system is limited by the quality of the electronic structure method used to compute its excited states. Choosing a suitable protocol depends on a number of factors, including system size, the type of excited state being investigated, and availability of computational resources. In this section I will outline some of the most popular approaches to predicting excitation energies, and contemporary developments in this field. Excited state methods are often used to calculate excitation energies, oscillator strengths for transitions (from transition dipole moments), or nonadiabatic coupling vectors between states. Like ground state methods, they can be split into

two broad categories: single reference and multi reference.

One way to performing an excited state calculation is by solving the electronic time-independent Schrödinger equation (TISE). Although it is the ground state whose energy is variationally minimised, it is possible to solve the TISE for multiple roots which correspond to higher states – this is the approach taken in post Hartree-Fock methods like configuration interaction (CI). Alternatively, we can use response theory by finding the frequency-dependent polarisability of the molecule and seeing how it interacts with a time-dependent electric field. The poles of this function then correspond to the excitation energies.

The full CI wavefunction is written as

$$|\Psi\rangle = c_0 |\Phi_0\rangle + \sum_{i,a} c_i^a \left|\Phi_i^a\right\rangle + \sum_{i<j,a<b} c_{ij}^{ab} \left|\Phi_{ij}^{ab}\right\rangle + \cdots$$

where $\left|\Phi_i^a\right\rangle$ and $\left|\Phi_{ij}^{ab}\right\rangle$ are Slater determinants that correspond to single and double excitations from the Hartree-Fock reference determinant $|\Phi_0\rangle$. Substituting $|\Psi\rangle$ into the TISE and solving the resulting eigenvalue equation returns a set of eigenvalues (excitation energies) and their corresponding eigenvectors (sets of expansion coefficients, c_i^j etc.). If all possible excitations are included, in the limit of a complete basis a full CI calculation will yield the exact energies of the ground and excited states. However, because the number of terms in the expansion grows factorially with the electron number, it is only possible to solve for extremely small systems.

Truncating $|\Psi\rangle$ at the first two terms such that the wavefunction contains only the HF determinant and all possible singlet excitations, gives us the simplest excited state method which is the single excitation configuration interaction (CIS). The formal scaling of this method with basis set size is $O(n^4)$, although tricks like using an auxilliary basis expansion can be used to reduce this.[37] By omitting higher order excitations this method suffers from lack of electron correlation, leading to overestimation of excited state energies by roughly 1 eV. Using CIS(D) adds a perturbative correction that approximately includes double excitations. This method reclaims some electron correlation missing in CIS but still has errors of approximately 0.5 eV.

Another approach to truncating $|\Psi\rangle$ is by manually choosing to use only the most important Slater determinants to be included in a CI-type procedure. The complete active space self-consistent field (CASSCF) method requires a degree of chemical intuition since the active space must be manually chosen to contain all the relevant molecular orbitals. This means it can work even at highly distorted geometries if the active space is chosen correctly, so is valuable for studying bond-breaking reactions. The number of Slater determinants can be reduced further by subdividing the active space into subspaces, and restricting the number of electrons or holes in each set of orbitals – this is the restricted active space self-consistent field method (RASSCF). The CASSCF wavefunction with a sufficiently large active space describes static correlation well, but lacks dynamic correlation which can be corrected by using perturbation theory (CASPT2) yielding highly accurate excitation energies. Methods covered in this paragraph are types of multiconfiguration self-consistent field (MCSCF) methods which follow a variational

optimisation procedure based on the wavefunction expansion $|\Psi\rangle$. Unlike CI they minimise the energy of the MCSCF wavefunction by rotating the molecular orbitals as well as optimising the linear expansion coefficients.[38] Some variants of MCSCF such as state-averaged CASSCF (SA-CASSCF) or multi-state CASPT2 (MS-CASPT2) will optimise the weighted average energy of multiple states.

For larger molecules a cheaper, and therefore more popular, method for excited state calculations is time-dependent density-functional theory (TDDFT). This is an extension to density-functional theory (DFT), which was initially proposed by Runge and Gross in 1984.[39] Later on Cassida suggested a linear-response formalism which took the approach of calculating the linear response of a ground state electron density matrix to an external electric field.[40] Solving the Cassida equations (Eqn. 1.1) should theoretically return the exact density response function, whose poles correspond to the excitation energies. Here, **A** and **B** are orbital rotation Hessians and $\mathbf{X} = -\mathbf{Y}$ is the normal mode eigenvector corresponding to frequency ω.[41] However, like with DFT, an approximate exchange-correlation functional must be used limiting the accuracy of the method.

$$\begin{pmatrix} \mathbf{A} & \mathbf{B} \\ \mathbf{B}^* & \mathbf{A}^* \end{pmatrix} \begin{pmatrix} \mathbf{X} \\ \mathbf{Y} \end{pmatrix} = \omega \begin{pmatrix} 1 & 0 \\ 0 & -1 \end{pmatrix} \begin{pmatrix} \mathbf{X} \\ \mathbf{Y} \end{pmatrix} \tag{1.1}$$

Often the Tamm-Dancoff approximation (TDA) is invoked by neglecting the **B** and **Y** matrices leading to a simpler Hermitian eigenvalue problem $\mathbf{AX} = \omega\mathbf{X}$. Applying the TDA returns results of comparable accuracy to LR-TDDFT in most cases, and it has been shown that poor agreement between the two is a symptom of a badly defined ground state.[42]

The popularity of LR-TDDFT spurred on such a large number of benchmark review papers that a review of them had to be conducted in order to make sense of this quickly expanding field.[43] It has an advantage over methods with comparable scaling like CIS, as it includes some dynamic correlation via the exchange-correlation functional. Like CIS, it has been applied to systems of over 1000 atoms.[44] Calculations can be accelerated by as much as 80× by using GPU-based integral routines, meaning that SCF (self-consistent field) iterations which take less than 60 seconds are possible even for systems containing hundreds of atoms.[45] Calculations for systems of this size are still impossible for methods like CASPT2. Depending on the state character, the accuracy of LR-TDDFT calculations can be reasonable: it works best for valence states, where the error is typically ≈ 0.3 eV. However, it underestimates excitation energies of diffuse charge-transfer (CT) and Rydberg states because of the incorrect description of the 1/R Coulombic attraction between the electron and hole. To improve the result for CT states we can use "asymptotically corrected" range-separated hybrid functionals with built-in long range correlation such as CAM-B3LYP or ωB97X. LR-TDDFT is also a poor choice for predicting double excitations and fails at the geometries where ground and excited states become degenerate.

Coupled cluster methods can be generalised to the calculation of excited states through either the equation-of-motion or the linear response formalism. Equation-of-motion coupled-cluster

singles and doubles (EOM-CCSD) is the excited state extension of the ground state coupled-cluster formalism which yields excellent accuracy for singly excited states, with errors relative to experiment as low as 0.2 eV. It works by solving the ground state CCSD equations, then performing a similarity transform on the Hamiltonian, and then using it to perform CIS(D). New electronic structure theories for excited states which can be applied to larger systems are constantly being developed. Delta-self-consistent field (ΔSCF) theory suggests re-optimising the molecular orbitals for an excited state electron configuration through an iterative SCF procedure. In spite of its simplicity, excitation energies and transition dipole moments are predicted with accuracy comparable to TDDFT.[46] Medium sized molecules can be tractable with the algebraic-diagrammatic construction propagator approach (ADC), which is closely related to the coupled-cluster method (CC2). Errors for ADC(2)/CC2 are on the order of 0.2 eV (higher for Rydberg states), while the scaling can be as low as $O(n^4)$ when coupled with the resolution-of-identity approximation.[47]

All of the above methods can be modified to calculate triplet as well as singlet excitations, however this discussion is beyond the scope of this work. The above selection is by no means exhaustive, but these approaches are some of the most popular methods implemented in widely available electronic structure packages such as Molpro, Molcas, Turbomole, and Q-Chem.

1.3 Thesis outline

In this introduction I have attempted to lay out the necessary groundwork for exploring computational methods which can be used for the prediction of tangible experimental observables. In the first results chapter, I will simulate inhomogeneous broadening in absorption cross sections in a number of ways and test them on a selection of atmospheric molecules. Predicting the outcome of photoexcitation through atomistic on-the-fly dynamics methods can become intractable when reactions occur on a slower timescale. In chapter 3, I propose an energy-grained master equation approach which has been modified to include nonadiabatic effects, and test it by using a product of isoprene oxidation as a bi-chromophoric model system for partially oxidized atmospheric VOCs. In chapter 4 I will consider the same reaction from the perspective of tropospheric chemistry and discuss the implications of including this photodissociative reaction in atmospheric models. Then, in chapter 5, I will discuss my work in the implementation of a novel nonadiabatic dynamics method and test the algorithm on a selection of familiar model systems. Lastly, I consider solvent effects in photochemical processes and suggest ways in which explicit solvent can be included in an efficient way.

CHAPTER 2

AB INITIO PREDICTION OF PHOTOABSORBTION CROSS SECTIONS

The photoabsorption cross section $\sigma(\lambda)$ measures the capacity of a chemical species to absorb light at wavelength λ. In other words, $\sigma(\lambda)$ is the net power absorbed by the molecule, divided by the incident power per unit of area (it's often reported in units of cm^2). The UV-Vis spectrum is an experimental observable measured in the 100-1000 nm range, which has a direct correspondence to $\sigma(\lambda)$. Bands in the spectrum correspond to transitions from the ground electronic state of the molecule to any energetically accessible electronic excited state. Using accurate $\sigma(\lambda)$ is important in the calculation of photolytic rates and therefore for the construction of atmospheric chemistry models described in the previous chapter, such as the Master Chemical Mechanism.[5] Tropospheric reactions are initiated by solar radiation reaching the Earth's surface whose wavelengths are in the UV-Vis range.[48] For transient molecules and radicals where experimental UV-Vis data often isn't available it is useful to have a set of guiding principles used to calculate the spectral shape *ab initio*.

An electronic structure calculation can give us the energy gap and oscillator strength for a transition from the ground to an excited state, for a given geometry. There is a vast toolbox of available methods for calculating electronic excitations, ranging in accuracy and expense.[43, 49, 50] Calculating vertical excitation energies at the geometry optimised minimum of the potential energy surface (PES) produces a stick spectrum with a line corresponding to each electronic transition. Although such a calculation is useful for assigning excitations to spectral bands it does not produce a realistic spectrum with the correct band shape. Broadening of spectral peaks in experimental spectra is caused by a number of factors which are outlined explicitly in Segarra-Martí *et al.*[51] Firstly, intra-molecular vibrations give rise to a progression of peaks in the absorption spectrum since the excitation can occur into a particular vibrational state. Because any excited state has a limited lifetime before it decays to the ground state or other products, spectral peaks are subject to lifetime broadening. This phenomenon which arises due to

the energy-time uncertainty principle broadens the peaks to a Lorentzian shape, however this significantly impacts the spectrum only on ultrashort timescales. Homogeneous broadening of a spectral band is caused by an excited state interacting with its environment, such as solvents, causing the energy gap between states to fluctuate. Lastly, inhomogeneous broadening is caused by there being numerous instantaneous geometries of a molecule absorbing light in a sample. The variations in the excitation energy cause the band to broaden, obfuscating the fine structure of a spectrum.

Spectral shape can also be used to tell us about the molecule's dynamics in the excited state. Presence of vibrational fine structure in the spectrum indicates that the gradient of the excited state potential is likely to be flat in the Franck-Condon region (PES near the S_0 geometry) indicative of a longer excited state lifetime.[52] A structure-less spectrum on the other hand hints at a steep potential slope, and potentially ballistic wavepacket dynamics leading to a direct photodissociation mechanism. In this work I will focus on a few atmospherically relevant volatile organic compounds (VOCs), which have readily available spectra that could be compared against our predictions. With this information it is possible to derive a set of guidelines on the best method for predicting an absorption cross section based on the properties of the molecule in question. This chapter does not cover the question of which is the best electronic structure method for predicting a given spectrum, but aims to examine a few nuclear ensemble sampling methods that have been suggested to capture inhomogeneous broadening effects.

I begin with a description of how Franck-Condon spectra can be computed to model vibrational broadening, and how the Herzberg-Teller approximation can be used to include weakly allowed transitions. Next, I discuss nuclear ensemble (NE) methods which are a means to capture the inhomogeneous broadening of the spectral band. An NE method is one that produces a spectrum by convolving stick spectra calculated for a given set of nuclear conformations (geometries). The main distinctions between NE methods are in how to assemble this ensemble such that it is representative of the molecule's ground state distribution. Such methods include sampling geometries from an uncorrelated Wigner distribution,[53] a ground-state harmonic oscillator distribution,[54] a classical MD trajectory, or path integral dynamics with a quantum thermostat (PI+GLE). Applying these methods to the selected example molecules will illustrate the factors that need to be considered when choosing how to simulate a UV-Vis spectrum for any given system. Here I should add that all these methods are time-independent, and I will not be discussing the variety of available time-dependent methods for cross-section simulation, notably those suggested by Eric Heller.[55] He pioneered an approach which used the semi-classical propagation of nuclear wavepackets in which the time evolving correlations between the ground and excited states were Fourier transformed from the time to the frequency domain to get the absorption spectrum.

2.1 Absorption cross section

The absorption cross section $\sigma(\lambda)$ has units of cm^2 as it is defined by the net power absorbed by the molecule at wavelength λ, divided by the incident power per unit of area. When an oscillating electric field interacts with a charged particle in the molecule it causes a transition whose signature can be seen in the UV-Vis range. The energy of this interaction at a given wavelength corresponds to $\sigma(\lambda)$, and is a product of the field and the dipole moment vectors. The classical dipole moment is a sum over all particle charges and their position vectors, $\mu = \sum -q_i r_i$, while the electric field is assumed to be constant for cases where the molecule length is much smaller than λ.

The $\sigma(\lambda)$ can then be expressed as

$$\sigma(\lambda) = \frac{4c\pi^2}{3\lambda} \sum_f |\langle \Psi_{i,\alpha} | \hat{\mu} | \Psi_{f,\beta} \rangle|^2 \delta(E_f - E_i - \hbar c/\lambda) \tag{2.1}$$

where $\hat{\mu}$ is the dipole moment operator and the transition dipole moment (TDM) integral $\langle \Psi_{i,\alpha} | \hat{\mu} | \Psi_{f,\beta} \rangle$ gives the intensity of the transition from the initial electronic state i and vibronic state α to the final electronic state f and vibronic state β. The strength of the electric field is contained in the prefactor, c is the speed of light, and energies of initial and final states are E_i and E_f respectively. Calculation of the TDM is simplified by using the Born Oppenheimer approximation which separates the total wavefunction into its nuclear ($\chi_{\gamma,j}(R)$) and electronic ($\psi_j(r;R)$) parts. Similarly, the TDM operator can be split into a sum of its electronic and nuclear parts.[56] Using these assumptions the TDM is expanded as

$$\langle \Psi_i | \hat{\mu} | \Psi_f \rangle = \langle \chi_{\alpha,i} | \langle \psi_i | \hat{\mu}_{elec} | \psi_f \rangle | \chi_{\beta,f} \rangle + \langle \chi_{\alpha,i} | \langle \psi_i | \hat{\mu}_{nuc} | \psi_f \rangle | \chi_{\beta,f} \rangle, \tag{2.2}$$

however the second term vanishes because the orthogonality of the electronic wavefunctions in two distinct electronic states means that

$$\langle \psi_i(r;R) | \hat{\mu}_{nuc}(R) | \psi_f(r;R) \rangle = \hat{\mu}_{nuc}(R) \langle \psi_i(r;R) | \psi_f(r;R) \rangle = 0.$$

The electronic TDM, $\bar{\mu}_{if} = \langle \psi_i | \hat{\mu}_{elec} | \psi_f \rangle$ does not have an exact analytical form, however it can be approximated by Taylor expanding $\bar{\mu}_{if}$ about the equilibrium ground state geometry R_0. This expansion is the starting point to defining the Franck-Condon and Hertzberg-Teller approximations which will be discussed further in the following section.

Some experimental observables can be directly related to the absorption cross section. The molar attenuation coefficient $\varepsilon(\lambda)$ of a material is related to $\sigma(\lambda)$ by the following factor, where N_A is Avogadro's number.

$$\sigma(\lambda) = 10^3 \ln(10) \frac{\varepsilon(\lambda)}{N_A}$$

According to the Beer-Lambert law there is a linear relationship between wavelength-resolved absorption and $\varepsilon(\lambda)$. Furthermore, the rate constant of photolysis J can be calculated from the

convolution of the cross section $\sigma(\lambda)$, the actinic flux F_{ac}, and the quantum yield for a particular reaction channel ϕ:

$$J = \int \phi(\lambda)\sigma(\lambda)F_{ac}(\lambda)\mathrm{d}\lambda \tag{2.3}$$

Experimentally obtained $\sigma(\lambda)$ includes broadened bands that correspond to excitations into any number of energetically accessible excited states. A single point excited state calculation gives us insufficient information to model the shape of a band when the molecule is exposed to the full spectrum of solar radiation rather than a monochromatic laser pulse.

2.2 Methods

2.2.1 Franck-Condon Herzberg-Teller

To describe the Franck-Condon (FC) spectrum we must return to the expansion of the transition dipole moment within the Born-Oppenheimer approximation given in equation 2.2 .

$$\langle \Psi_i | \hat{\mu} | \Psi_f \rangle = \langle \psi_i | \hat{\mu}_{elec} | \psi_f \rangle \langle \chi_{\alpha,i} | \chi_{\beta,f} \rangle = \bar{\mu}_{if} \langle \chi_{\alpha,i} | \chi_{\beta,f} \rangle \tag{2.4}$$

The first term on the LHS of Eqn. 2.4 is the electronic TDM $\bar{\mu}_{if}$, which is dependent on nuclear positions through the parametrical dependence of the electronic wave functions on atomic positions. Therefore we can approximate it by Taylor expanding about the ground state equilibrium geometry R_0.

$$\bar{\mu}_{if}(R) \approx \bar{\mu}_{if}(R_0) + \left|\frac{\partial \bar{\mu}_{if}(R)}{\partial R}\right|_{R_0} (R - R_0) + \left|\frac{\partial^2 \bar{\mu}_{if}(R)}{\partial R^2}\right|_{R_0} (R - R_0)^2 + \cdots \tag{2.5}$$

The electronic TDM can be evaluated straightforwardly by truncating Eqn. 2.5 at the zeroth-order term in the expansion. This assumes that the geometry of the molecule and its dipole moment doesn't change during the transition, which is the Franck-Condon approximation.[57–59] The first-order nuclear coordinate dependence of $\bar{\mu}_{if}(R)$ takes into account a limited change in the TDM during the photoexcitation and means that a weakly allowed or dipole-forbidden electronic transition can still produce a peak in the calculated spectrum. When the first order term in the expansion is included, the Franck-Condon Herzberg-Teller (FCHT) spectrum is returned.[60]

The second part of Eqn. 2.4 is the overlap between the ground and excited state nuclear wavefunctions, $\langle \chi_{\alpha,i} | \chi_{\beta,f} \rangle$, which is referred to as the Franck-Condon factor. This is an integral which gives the probability of a vibronic transition. Practically, to calculate this integral the ground and excited states must share a coordinate set. This is typically done through a linear transformation between the normal modes of the initial and final states, i.e. by using a Duschinsky matrix.[61] The vibrational states $|\chi_{\beta,f}\rangle$ can be determined from the Hessian by assuming that the PES of the ground and excited electronic states are harmonic in that region. The total absorption

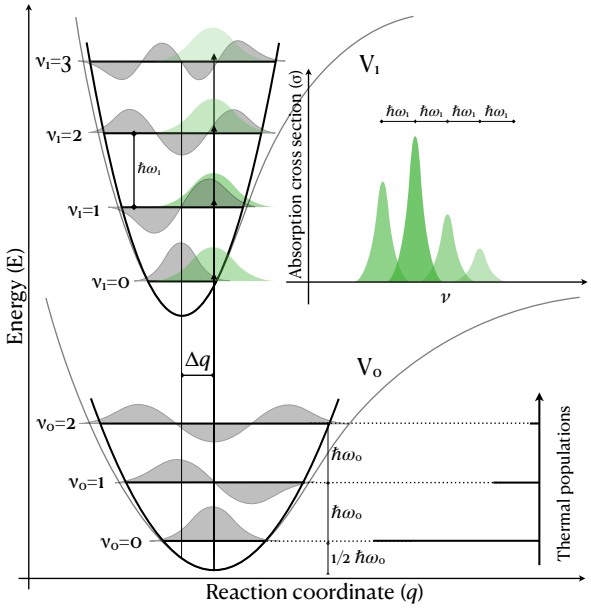

Figure 2.1: Schematic for a FC/FCHT spectrum simulation within the harmonic oscillator approximation. The overlap between the ground state $\nu_0 = 0$ and excited state vibrational wavefunctions correspond to the FC integrals. At finite temperature the thermal population of ground state vibrational levels are determined by the Boltzmann distribution. In experimental spectra transitions from ν_0=1 and higher correspond to hot bands.

cross section can then be given as a sum over a series of distinct vibronic peaks corresponding to vertical excitations between vibrational states.

In order to calculate $\sigma(\lambda)$ we need to know the optimised geometries and normal mode vibrational frequencies of the ground and excited states, the electronic TDM, and the energy gap $E_f - E_i$ at the S_0 minimum geometry. There are many advantages of applying FC and FC-HT simulation protocols in specific cases. The most obvious is that it's the only approach presented in this chapter that explicitly calculates vibrational fine structure. This can work well for small, rigid molecules being excited into long lived states. However, this strategy does not work for the general case.

Firstly, we have to rely on the uncoupled harmonic oscillator approximation in both the ground and excites states to calculate the Franck-Condon integral for the vibrational progression which can fail for cases where there is significant anharmonicity at the stationary points (e.g. normal modes with a significant internal rotational contribution). The optimised excited state geometry needs to be similar enough to the ground state that the FC integrals are not negligible, which limits the cases for which this method can be applied. Unlike the ensemble methods listed here only one excitation band at a time can be calculated, so typically only $S_0 \rightarrow S_1$ excitation bands are computed.

Lastly, I would like to highlight that there are a number of similar methods for simulating vibronic spectra. For example, the independent mode, displaced harmonic oscillator (IMDHO) model (implemented in ORCA)[62] requires only the ground state Hessian, but assumes that the excited state PES is equivalent to the GS PES shifted to a new equilibrium geometry.[63]

2.2.1.1 Computational details

All calculations used to produce FC and FC-HT spectra were performed in Gaussian 16.[64] Molecular geometries were optimised using DFT in the ground state and LR-TDDFT in the excited state, and analytical normal mode frequencies were then calculated at these geometries, with tight convergence conditions, to confirm they were stationary point minima on the PES. The PBE0 exchange correlation functional with the TZVP basis set was used for the optimisations.

2.2.2 Wigner sampling

Ensemble sampling methods aim to represent the vibrational wavefunction of an electronic state by a set of classical geometries and momenta. These methods do not rely on knowledge of the excited state PES, and because of this they cannot be used to predict vibrational fine structure. However, by applying the reflection principle a broadened spectrum may be constructed from individual excitations and their oscillator strengths. All nuclear ensemble methods rely on the semiclassical reflection principle which states that the absorption cross section is the reflection of the ground state coordinate distribution on the energy axis. The principle was justified by Schinke (1993) from the time-dependent expression for the absorption cross section (at short time intervals) for an arbitrary number of dimensions.[52] Its implication is that that spectral shape may be predicted from an accurate representation of ground state nuclear density.

An excited state calculation in most quantum chemistry software returns the oscillator strength $f_{0,n}(R_l)$ and excitation energy $\Delta E_{0,n}(R_l)$ for an excitation from the ground state 0 to excited state n at the geometry R_l. By assembling an ensemble of geometries that are representative of the ground state nuclear distribution it is possible generate spectra which replicate the experimentally observed inhomogenious broadening. Crespo-Otero *et al.* show the explicit derivation of the nuclear ensemble approach and the absorption cross section expression for any nuclear configuration ensemble of size N_p given in Eqn. 2.6.[53]

$$\sigma(E) = \frac{\pi e^2 \hbar}{2 m_e c \epsilon_0 n_r E} \sum_{n}^{N_{fs}} \frac{1}{N_p} \sum_{l}^{N_p} \Delta E_{0,n}(R_l) f_{0,n}(R_l) g(E - \Delta E(R_l), \delta) \tag{2.6}$$

In the above expression N_{fs} is the number of included excited states; electron charge and mass are e and m_e; refractive index of the medium is n_r; vacuum permittivity is ϵ_0; $g(E - \Delta E(R_l), \delta)$ is the line shape function peaked at the transition energy with phenomenological broadening δ. Line shape could be a Gaussian or a Lorentzian function; the choice is determined by whether thermal broadening (bath gas collisions – Gaussian process) or lifetime broadening (Lorentzian) are more important for that particular system.

The Wigner quasiprobability distribution P_W is sometimes referred to as the Wigner function. It is the integral part of the Wigner formulation (or phase-space formulation) of quantum mechanics, first presented in 1932 in Eugene Wigner's paper on quantum corrections to the Boltzmann equation.[65] It shows a direct correspondence between the quantum density matrix $\hat{\rho}$

in Hilbert space and the quasiclassical distribution in the classical phase space via the Wigner-Weyl transform.[66] Whilst the Wigner distribution is a real valued function, it can become negative which is why P_W must be referred to as a quasiprobability distribution. In its original formulation, the quantum mechanical density matrix $\hat{\rho}$ of a system in a pure state ψ is replaced by a function $\rho(k',k'') = \psi(k')\psi^*(k'')$. In this anzats, the Wigner distribution is given as

$$P_W(q,p) = (\pi\hbar)^{-1} \int \psi^*(q+y)\psi(q-y)e^{2iyp/\hbar}dy \tag{2.7}$$

for a 1-dimensional harmonic oscillator, where p is the momentum associated with the normal mode coordinate q. Solving the above integral in the case of ψ as a quantum harmonic oscillator wavefunction in its vibrational ground state produces the following distribution generalised for $3N-6$ vibrational modes.

$$P_W(\mathbf{q},\mathbf{p}) = \prod_{i=1}^{3N-6} (\pi\hbar)^{-1} \exp\left\{ -\frac{1}{\hbar\omega_i} \left(\mu_i\omega_i^2 q_i^2 + \frac{p_i^2}{\mu_i} \right) \right\} \tag{2.8}$$

This is a multidimensional Gaussian distribution in (**q**,**p**) space which can be sampled using a stochastic procedure.

The Wigner sampling method will be the first ensemble sampling method described in this chapter. As well as spectrum prediction, Wigner sampling is routinely applied to generate initial coordinates and momenta for classical and semiclassical trajectory calculations.[67, 68]

One notable advantage of this approach over FC/FC-HT is that the calculation may be straightforwardly extended to multiple excited states. However, spectra generated using the reflection principle cannot describe the vibronic features of the spectrum, or show the vibrational broadening of long lived states. The spectral shape must be converged with the number of sampled conformations.[53] This type of sampling also relies on the local harmonic approximation of the potential, which may fail for strongly anharmonic systems.

Spectral bands that show excitation into a dissociative state should be broad and structureless – in such cases the nuclear ensemble can be adequate. Artifact spikes in Wigner spectra can appear due to spuriously large hydrogen displacements in the ensemble sampling because it uses linear normal modes for some non-linear degrees of freedom, such as torsions. Using MD is preferable in these cases, although another option is to freeze such torsional modes when constructing the Wigner distribution.

2.2.2.1 Including multiple conformers

When predicting $\sigma(\lambda)$ for molecules with rotatable bonds, there may be a number of conformational minima that need to be considered. There is a wide selection of algorithms that can determine a set of conformers from molecular structure, including systematic rotor search, random rotor search, weighted rotor search, and genetic algorithm methods – all of these are implemented in OpenBabel.[69] However these strategies can become cumbersome for molecules with large

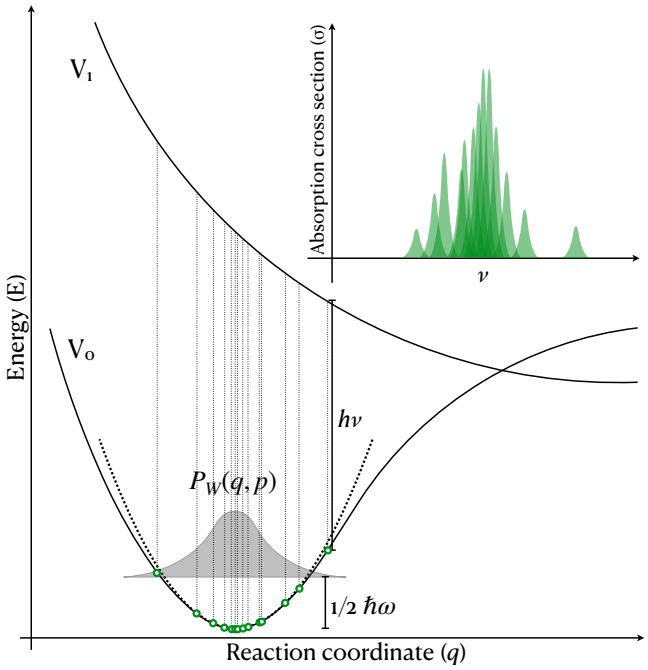

Figure 2.2: Schematic illustrating the Wigner ensemble method used to represent the ground state density. Normal modes (frequency ω) at the equilibrium geometry are assumed to be uncoupled harmonic oscillators in the construction of the Wigner quasiprobability distribution $P_W(q,p)$. Resulting spectrum is generated by applying the reflection principle where peaks are overlaid with a narrow Lorenzian or Gaussian function.

numbers of torsions, and the efficient exploration of conformations in proteins remains an active field of research.[70]

For spectrum modelling in molecules with multiple conformers, Barbatti *et al.* suggests a modified variant of the Wigner sampling approach whereby the conformers are weighted by their corresponding Boltzmann factor calculated from their energy.[68] This can become difficult for a large number of geometries since each must be sampled sufficiently, in which case only conformers with largest Boltzmann weights need be included.

Conformational space may also be explored with MD, since in the limit of an infinitely long trajectory all thermally accessible conformers of a molecule will be sampled. The challenge of this approach is the existence of high rotational barriers which may mean that a prohibitively large number of MD steps would be necessary to obtain a representative ensemble.

2.2.2.2 Computational details

A set of N_{conf} nuclear geometries is generated in the Newton-X package,[71] from the distribution shown in equation (2.8) generalised for an n-dimensional system.

For each geometry, q_N of N_{conf}, in the ensemble, a TDDFT calculation is performed to determine the energy gap $\Delta E_{0,n}$ and oscillator strength f_{0n} between the ground state and an arbitrary number of excited states N_{final}. The spectrum $\sigma(E)$ is constructed by overlaying the peak at each conformation with a Lorenzian (or Gaussian) centered at ΔE with width δ as seen

in equation 2.9

$$\sigma(E) = \frac{\pi e^2 \hbar}{2mc\varepsilon_0 E} \sum_{n=1}^{N_{final}} \frac{1}{N_{conf}} \sum_{i=1}^{N_{conf}} \Delta E_{0,n}(\mathbf{q}) f_{0n}(\mathbf{q}) \times g\left(E - \Delta E_{0,n}(\mathbf{q}), \delta\right) \tag{2.9}$$

For molecules with multiple conformers, I adopt the strategy suggested by Barbatti[68], and draw their relative populations from the Maxwell Boltzmann distribution, with total energies (electronic + vibrational ZPE) calculated at the PBE0/TZVP level. Rotamers are found with the conformer search tool in OpenBabel, that uses a genetic algorithm to scan over the rotatable bonds and returns geometries optimised for minimum energy.

Ensembles are generated from an uncorrelated Wigner distribution for each conformer, in the same manner as described earlier. Spectra are assembled by combining numbers of geometries from the ensemble corresponding to their Boltzmann weights.

2.2.3 Sampling from molecular dynamics

An alternative method of generating an ensemble of phase space points for spectrum simulation is by taking snapshots of uncorrelated geometries along a molecular dynamics trajectory. Unlike Wigner, dynamics naturally account for anharmonicity effects since no assumptions are made about the underlying shape of the PES.

2.2.3.1 Classical molecular dynamics

Classical molecular dynamics (CMD) simulations treat atoms as point particles i which evolve in time according to Hamilton's equations of motion

$$\dot{q_i} = \frac{\partial H}{\partial p_i} \text{ and } \dot{p_i} = -\frac{\partial H}{\partial q_i}$$

in a phase space defined by their position and momentum coordinates, q_i and p_i.

Classical trajectories are applied extensively in the modelling of chemical reactions,[72] collisions,[73] and intramolecular energy redistribution.[74, 75] Ensembles of geometries generated from CMD have been used for generation of broadened UV-Vis spectra of liquid water, [76–78] and photoionization spectra of sodium-water clusters.[79] Whilst it can be useful for simulation of fast, classically allowed chemical dynamics, CMD does not account for tunnelling effects, vibrational ZPEs, or nonadiabatic coupling which I will collectively describe as nuclear quantum effects (NQEs). Such effects become especially important for predicting the dynamics of lighter atoms and at colder temperatures. For example, in a study of proton transfer in water, CMD results were shown to be significantly different from quantum simulations even at room temperature.[80] It has been suggested that ZPE can be included in the simulation of spectra by sampling the initial conditions of classical trajectories from a semiclassical (Wigner) distribution,[81] or by setting the initial internal energy of the system at an energy corresponding to its quantum state – the quasiclassical trajectory method.[82] However, these approaches still incorrectly model the energy redistribution between modes and are inefficient for strongly anharmonic potentials.[83]

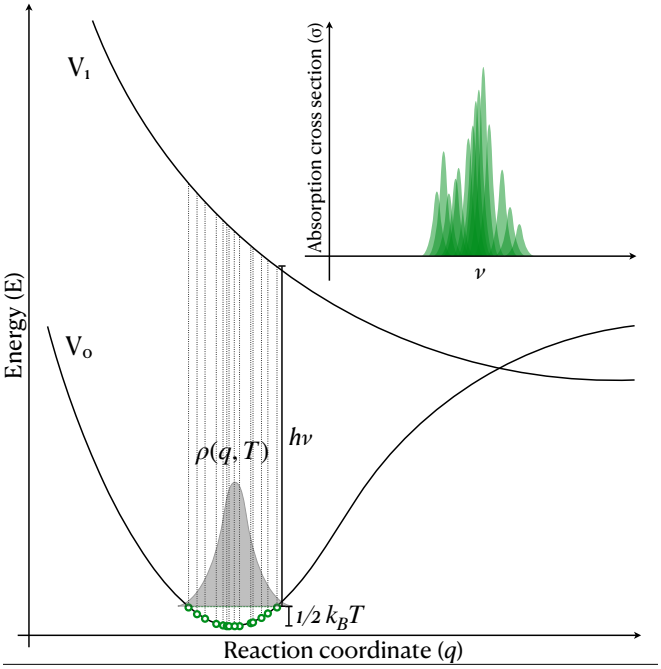

Figure 2.3: CMD ensemble sampling. Kinetic energy of the one reaction coordinate q shown on the diagram is $1/2k_BT$, according to equipartition theorem. The canonical NVT ensemble is sampled by taking uncorrelated snapshots of a trajectory. The boundaries of the phase space it can explore are limited by its total energy, resulting in narrower spectral bands than PIMD spectra because zero-point energy is not included.

2.2.3.2 CMD with a quantum thermostat

The generalised Langevin equation (GLE) thermostat can be used to improve the dynamical properties of classical simulations at approximately the same cost. The equations of motion (EOM) of a non-Markovian GLE for a unit mass particle moving under the influence of potential $V(q)$ is

$$\dot{q} = p$$
$$\dot{p} = -\frac{\partial V}{\partial q} - \int_{-\infty}^{t} K(t-s)p(s)ds + \zeta(t)$$

where $\zeta(t)$ is the Gaussian random noise and $K(t)$ is the friction memory kernel. These equations are non-Markovian precisely because the memory kernel $K(t)$ is finite, and related to the autocorrelation function of the random noise $\zeta(t)$. Integrating this form of the EOM isn't practical as it relies on storing and integrating over the complete particle trajectory to compute $K(t)$. To avoid this, the classical phase space $(\mathbf{p},\mathbf{q})$ is extended by a set of auxiliary momenta $\mathbf{s}$, which can be interpreted as the system memory, coupled to the momentum variable. This gives us the Markovian form of the GLE, which contains parameters (a_{pp}, $\hat{\mathbf{b}}_p$, $\mathbf{B}$, etc.) that need to be iteratively optimised to obtain the desired sampling properties.[84]

$$\dot{q} = p$$
$$\begin{pmatrix} \dot{p} \\ \dot{\mathbf{s}} \end{pmatrix} = -\begin{pmatrix} \frac{\partial V}{\partial q} \\ 0 \end{pmatrix} - \begin{pmatrix} a_{pp} & \mathbf{a}_p^T \\ \bar{\mathbf{a}}_p & \mathbf{A} \end{pmatrix} \begin{pmatrix} p \\ \mathbf{s} \end{pmatrix} + \begin{pmatrix} b_{pp} & \mathbf{b}_p^T \\ \bar{\mathbf{b}}_p & \mathbf{B} \end{pmatrix} \begin{pmatrix} \xi \end{pmatrix}$$

Here, $\boldsymbol{\xi}$ is a vector of $n+1$ uncorrelated Gaussian random numbers – the power spectrum obtained by a Fourier transform of its correlation function $\langle\xi(t)|\xi(0)\rangle$ is white noise. This noise term must be balanced against the friction term in the equation such that the damping of the oscillators in the system is optimal. Tuning the parameters contained in the GLE thermostat (i.e. the drift and diffusion matrices [85]) should converge to the correct friction kernel $K(t)$. The advantage of using a GLE thermostat over a global one is that each normal mode of the system will be thermalised to a different effective temperature T^* corresponding to its ZPE, whilst avoiding the need to explicitly calculate its frequencies.

A known artefact of this semi-classical method is that anharmonic coupling between modes causes the energy to "leak" from high frequency modes to low frequency modes in an non-physical way. The CMD+GLE scheme is therefore better suited to sampling static properties, rather than dynamic properties such as diffusion coefficients since at longer timescales ZPE leakage causes significant deviations from true quantum behaviour. The thermostat may be tuned to increase the coupling, counterbalancing the effect of ZPE leekage.

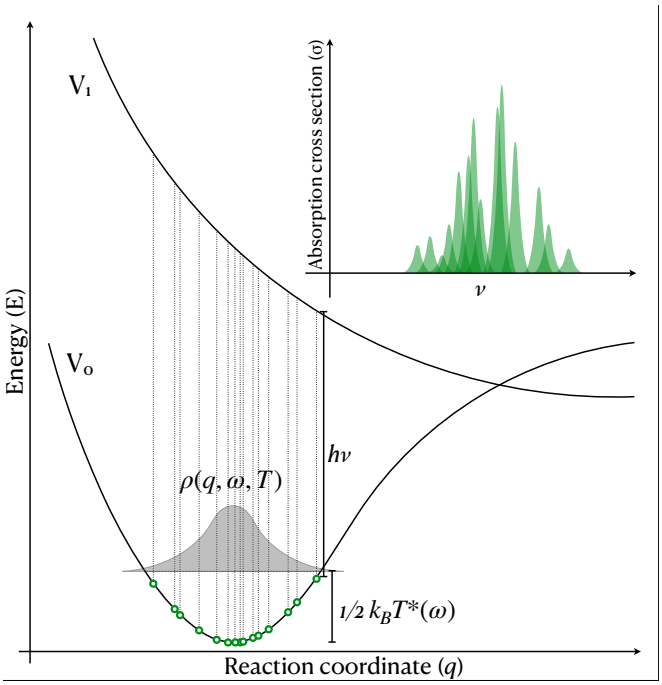

Figure 2.4: Generalised Langevin equation thermostat applied to PI+GLE or CMD+GLE sampling for spectrum simulation. NQEs are included by thermalising each mode of the system to a frequency-dependent effective temperature T^*. In the case of an uncoupled harmonic oscillator mode with frequency ω, T^* is given by $\frac{\hbar\omega}{2k_B}\coth\frac{\hbar\omega}{2k_BT}$. Because ZPE is included, more phase space is sampled leading to a broader band in the resulting spectrum.

2.2.3.3 PI+GLE dynamics

Path integral molecular dynamics (PIMD) is a method that uses the isomorphism between the quantum mechanical partition function of the physical system and the classical partition function of a ring polymer consisting of replicas (beads) of the system that are connected by harmonic springs.[86] It accounts for NQEs and, if the sampling is optimal, it will generate an ensemble that reflects the exact ground state nuclear density.[85] Whilst the quantum thermostat enforces the exact quantum configurational distribution in the uncoupled harmonic limit, PIMD is a

systematically improvable method that gives the exact quantum result for all temperatures, and captures ZPE and tunnelling effects. When Della Sala *et al.* applied PIMD to study the absorption cross sections of Lithium clusters at very low temperatures, they observed qualitative differences in temperature dependence and band shape in comparison with the CMD ensemble method.[87] However, PIMD often requires a large number of replicas to converge to the correct result, especially at lower temperatures, leading to a 10× to 100× computational cost overhead over CMD.

PI+GLE is a method that uses a colored-noise GLE thermostat to accelerate the convergence of imaginary-time PIMD.[86] Ceriotti *et al.* showed that thermodynamic properties of liquid water can be calculated as accurately from a 16-bead PI+GLE simulation as a 128-bead PIMD run. A white noise GLE thermostat is optimally efficient at a particular frequency, and a high sampling efficiency is only obtained for a small frequency range. In contrast, a colored noise thermostat has an optimal sampling frequency range that spans 4 orders of magnitude which includes both the slow modes of the system, and the high-frequency internal modes of the ring polymer.[88]

2.2.3.4 Computational details

All ground state MD simulations for ensemble generation used in this chapter were performed using the multipurpose *ab initio* MD package, ABIN, developed by Dr. Daniel Hollas.[89] This code was interfaced with Gaussain 09[90] and the electronic structure method used for the MD simulations were identical to those used to generate the Wigner ensemble – PBE0 in TZVP basis for all molecules.

Each trajectory was executed for 50000 steps, with a time step of 20 a.u. (or 0.484 fs), and an equilibration period of 2000 time steps (0.968 ps), such that the overall length of the trajectory is 24.2 ps.

In the CMD simulations, a Nosé-Hoover chain thermostat (4 chains, relaxation time 0.001 a.u.) was applied to maintain the temperature at 300 K. Parameters for the GLE thermostat used in the PI+GLE and CMD+GLE simulations were obtained from an online generator,[91] with target temperature T = 300K and spanning a frequency range up to ω_{max} = 10392 cm^{-1}. In the PI+GLE calculation 4 replicas were used, running concurrently over 4 cores.

For each of the CMD, CMD+GLE, and PI+GLE trajectories, 500 uncorrelated conformations were chosen at random uncorrelated points along the trajectory. A LR-TDDFT calculation was performed for each geometry in ORCA,[92, 93] using the PBE0 functional in TZVP basis to calculate the first 5 singlet states. Absorption spectra were then assembled by overlying each S_0 to S_1 excitation with a Lorenzian with a broadening parameter of 0.05 eV.

Shell scripts for spectrum generation from ABIN trajectory output were supplied by Daniel Hollas, with methods described in Hollas *et. al.* [94]

2.2.4 Including temperature

Finite temperature effects can influence the shape of the UV-Vis spectral band in a number of ways. Higher kinetic energy in the molecule's vibrational modes will increase the scope of its dynamics, and populate higher vibrationally excited states. In this section I will outline the ways in which the aforementioned methods of spectrum simulation are able to include (or not) finite temperature effects in predicting the cross section.

In FC/FCHT spectra, the main way to include temperature is by altering the Boltzmann populations of the vibrational levels in the ground electronic state, and computing the FC integrals for $v = 1$ vibrational levels and higher. As the size of the molecule increases, so does the number of normal modes for which these integrals must be calculated, so the computation of vibrationally resolved spectra at finite temperature can become computationally intractable for all but the smallest systems. Santoro *et al.* suggested a filtering strategy which selected only the most relevant FC integrals.[95]

For sampling the NVT canonical ensemble with classical molecular dynamics, a constant finite temperature is enforced through use of thermostats. Examples include Nosé-Hoover,[96, 97] Andersen,[98] Langevin,[99] and a multitude of others which are more fully described in this review by Hünenberger.[100] These thermostats work by altering the velocity of the atoms to fit with a Maxwell-Boltzmann distribution of particle kinetic energies.

In path integral molecular dynamics where nuclei are treated as quantum entities by extending the phase space of the dynamics, the same classical MD thermostats can be applied to each of the beads in the ring polymer. The coloured-noise GLE thermostat can enforce a quantum distribution at the cost of classical MD by setting the effective temperature of each mode, thus modifying the sampling. However, when Sršeň *et al.* used the PI+GLE method to simulate the temperature dependence of the (E)-Azobenzene spectrum they showed that the convergence with the number of ensemble points is very slow.[101] Even with 40,000 geometries, the difference between experimental spectra at 380 K and 300 K could not be captured with the PI+GLE method for ensemble generation.

Typically Wigner sampling is performed at 0K because of the assumption that $k_B T \ll \hbar\omega$ for most frequencies. There are two main approaches to introduce finite temperaure effects into the Wigner sampling protocol. Firstly, the population of higher vibrational states can be described by summing temperature-independent Wigner functions for each vibrational state, weighted by their population at temperature T.[102] Alternatively, the Wigner distribution from which the ensemble points are sampled can be broadened by a factor of $B = \tanh(\hbar\omega/2k_B T)$.

$$P_W(q,p,T) = \frac{B}{\pi\hbar}\exp\left\{\frac{-B}{\hbar\omega}\left(\mu\omega^2 q^2 + \frac{p^2}{\mu}\right)\right\}$$

This analytical expression is true for a canonical ensemble of harmonic oscillators, and corresponds exactly to the quantum density distribution at a finite temperature.[103] Therefore, it works well at lower temperature regimes where anharmonicity of the potential does not have a

strong effect. Anharmonic effects are also more likely to impact the results for larger systems containing many low-frequency modes. At higher temperatures where $k_B T \gg \hbar\omega$ trajectory sampling methods would be preferred since the molecule is likely to move outside of the region where its potential can be described by the harmonic approximation.[102]

To look at the effects of temperature on the spectral band shape, I have selected the example of 3-hydroxy-2-butanone (acetoin) whose experimental spectrum was measured by Messaadia *et al.* at 298K and 353K.[104] This molecule is an energy store in bacteria, and gives butter its distinctive taste – although admittedly it isn't of much atmospheric interest. However, it is one of the few molecules for which spectral data was available at two distinct temperatures, which I suspect is because it is liquid at R.T.P., making it easier to record its UV-Vis spectrum. As can be seen in the top panel of figure 2.6, the experimental absorption cross sections show only subtle temperature effects which will be captured through the Wigner ensemble method, as described above.

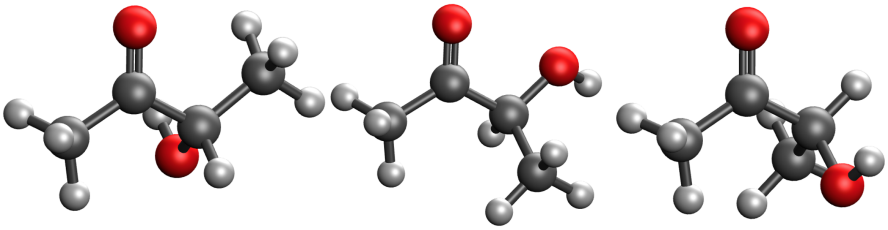

Figure 2.5: Rotational isomers of 3-hydroxy-2-butanone (acetoin)

2.2.4.1 Computational Details

The structure of acetoin contains a chiral centre and 3 rotational isomers corresponding to a twist about the chiral carbon, which are shown in figure 2.5. We optimised each of the rotamers with DFT/PBE0/cc-pVDZ and calculate their normal mode frequencies at these ground state stationary points, verifying that all normal mode frequencies are positive. Boltzmann weights of each rotamer were calculated from their free energies (electronic + zero-point correction from vibrations) at 298K and 353K. Their relative energies in kJ mol^{-1} are 0, 13.8, and 16.3. The lowest energy conformer is stabilised by the hydrogen bond between the carbonyl and the OH group. This stabilisation means that it has a significantly higher Boltzmann weight than the other two, and in an ensemble of 500 geometries, 497 correspond to that conformer at 298K (497:2:1) and 494 at 353K (494:4:2). Initially, 500 nuclear configurations were sampled, then 1500 in the same ratios to improve convergence of the results and reduce statistical error in the predicted spectra. These ensembles were used to simulate the spectra according to the protocols described earlier. The uncorrelated Wigner distribution was constructed based on the normal modes calculated with DFT/PBE0/cc-pVDZ, applying the temperature broadening parameter at 298K and 353K for each rotamer. Excitation energies and oscillator strengths were calculated for the first 10 singlet states

with LR-TDDFT/PBE0/aug-cc-pVDZ in Gaussian 09. Spectra were then assembled by overlaying the peak at each conformation with a Lorenzian curve (phenomenological broadening parameter $\delta = 0.05$ eV). Results can be seen in the bottom panel of figure 2.6. Ensemble generation and spectrum simulation was performed in Newton-X,[71] and all electronic structure calculations were performed in Gaussian 16.[64]

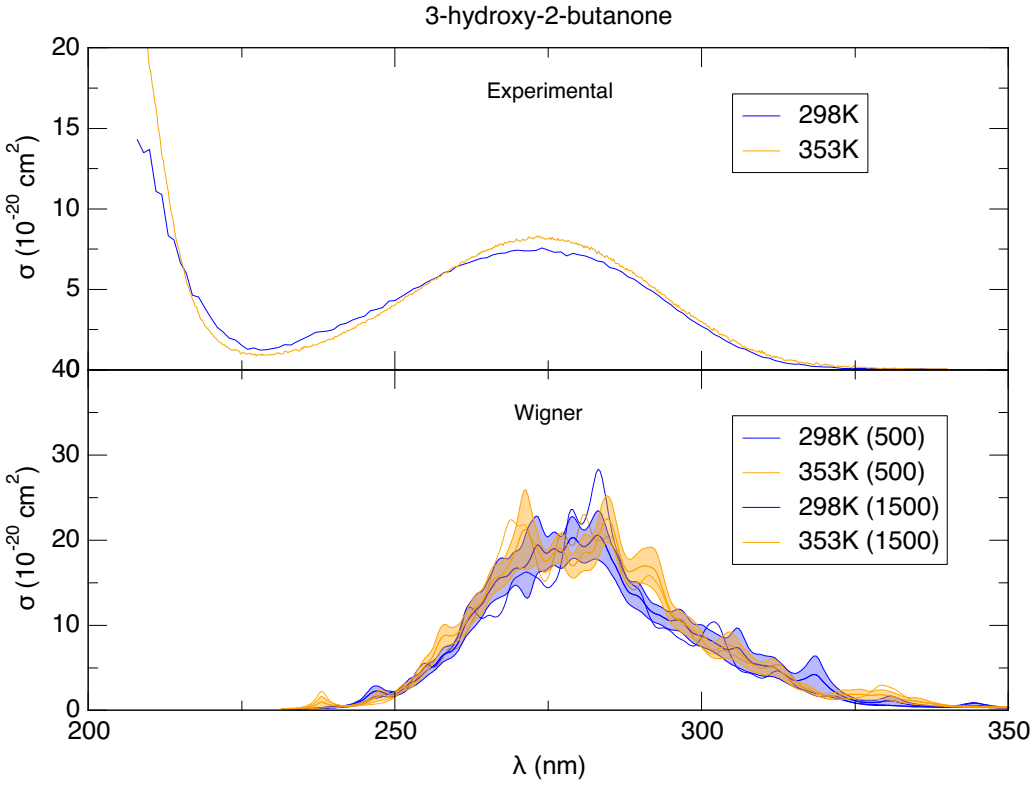

Figure 2.6: Influence of finite temperature effects on the absorption cross section of acetoin. Top panel contains the experimental spectra taken by Messadia *et al.*[104], which demonstrate subtle changes in band shape. Wigner spectra shown in the bottom panel are calculated for 500 and 1500 sample points, with 95% confidence interval error bars shown for the latter set.

Computed spectra shown in the bottom panel of figure 2.6 are indistinguishable between the two temperatures when 500 conformations are used. Increasing the ensemble size to 1500 reduces the statistical error in the predicted spectra, but it is evident from the error bars on the figure that resolving the subtle differences seen in the experimental bands would require a much larger ensemble size. These results show the limits of the Wigner approach for capturing finite temperature effects when the changes in band shape are subtle. They show that convergence with ensemble size can be improved using importance sampling techniques, albeit only when the

ensembes are computed for a range of temperatures.[105]

2.3 Results and Discussion

This section will report the spectra simulated by using the methods described in section 2.2 and compare them against experimental data. All experimental cross sections shown here were found in the MPI-Mainz UV/VIS Spectral Atlas of Gaseous Molecules.[106]

Formaldehyde is the smallest, simplest molecule examined using all the available protocols. Fig. 2.7 illustrates that FC and FCHT can successfully reproduce the vibrational fine structure of the experimental spectrum, including the gaps between consecutive peaks (this is more apparent towards at the shorter wavelengths tail of the progression. FC and FCHT peaks overlap, with intensity of the transition being the main difference between the two spectra. Because formaldehyde is a small and relatively stiff molecule (primary vibrational mode is stretching of a double bond C=O) the uncoupled harmonic oscillator model works well. The nuclear ensemble methods also capture the broadness of the peak well, except CMD which underestimates it significantly due to its neglect of ZPE. The quantum MD methods return functionally identical results although the bands, like the Wigner band, are red-shifted in relation to the FC/FCHT results. This can be attributed to the harmonic approximation which predicts larger ΔE between the ground and excited states, whilst nuclear ensemble methods use the computed S_0 and S_1 energies. The intensity of the transitions is significantly higher in the FC/FCHT spectra than for the nuclear ensemble methods (max at c.a. 20 cm^2 $molecule^{-1}$ vs 9 cm^2 $molecule^{-1}$). This could also be attributed to the overestimation of FC factors in the harmonic approximation.

FCHT and FC also perform impressively for acrolein, with the FCHT prediction almost exactly overlapping the experimental result (taken from Magneron *et al.*,[108]). The optimised excited state geometry of acrolein is very similar to that of its ground state. In such cases we might expect the largest FC integrals to be between the $v = 0$ ground state nuclear wavefunction, and low v_k excited state nuclear wavefunctions, where the shape of the potential is most similar to its harmonic approximations. The vibrational progression isn't as apparent in the experimental spectrum, although some peaks are visible on the longer wavelength side of the band. Wigner sampling also captures the band shape and amplitude extremely well, although it is slightly blue-shifted which could be attributed to TDDFT overestimating the excitation energies. Since Wigner also invokes the harmonic approximation, albeit only in the ground state, the assumption that normal modes are mostly harmonic and uncoupled is probably valid in this case. MD ensemble sampling methods in the bottom panel of figure 2.8 show the peaks were also blue shifted relative to the FCHT and the experimental result. As with formaldehyde, the CMD spectrum was significantly less broad than QT and PI+GLE spectra due to lack of quantum nuclear effects.

Hydroxypropanone was supposed to be a test case for the multiple-conformer sampling strategy as it has two major conformers – A, with the dangling OH group hydrogen bonded to the

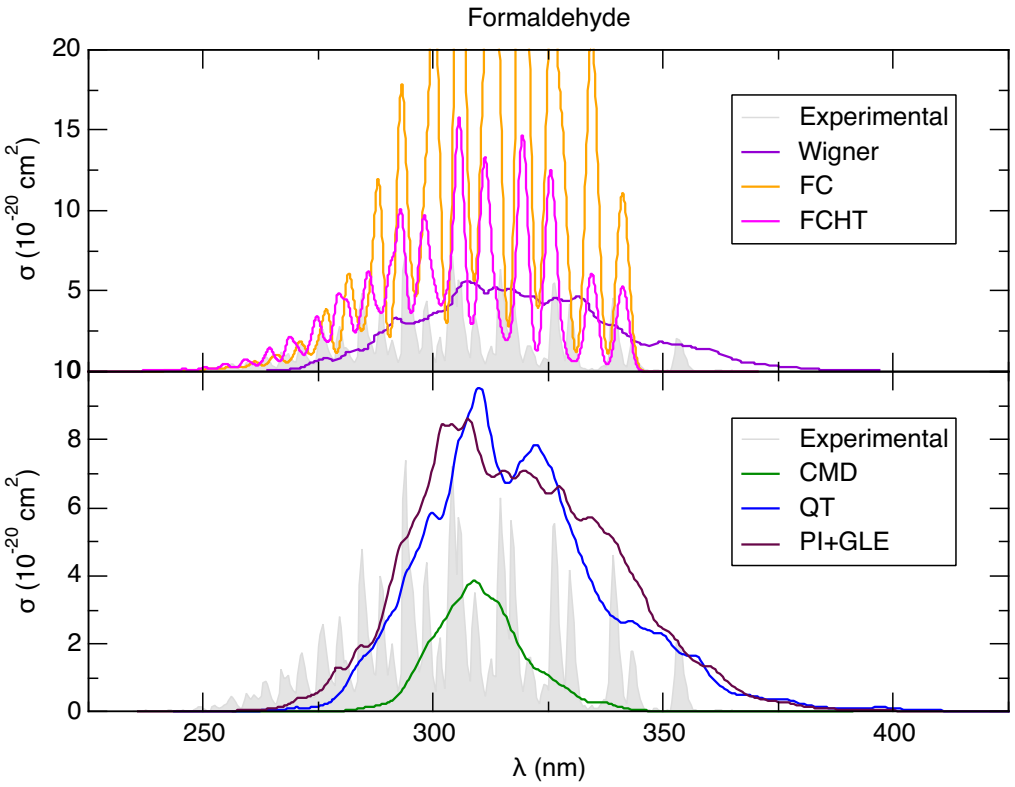

Figure 2.7: Photoabsorption spectra of formaldehyde, comparison of experimental results from Rogers *et al.*,[107] FC-HT, and nuclear ensemble approaches. All calculated spectra include only S_0 to S_1 excitations.

carbonyl, and B, with the carbonyl and OH in an antiparallel conformation. At 298K, there is 99.7% A and 0.3% B, as calculated from the Maxwell-Boltzmann distribution. Because of this, the spectrum in figure 2.9 doesn't look much different from the spectrum that just includes conformer A. Nevertheless, this figure once again shows that Wigner can capture the inhomogenous peak broadening well, and demonstrates one of the key advantages of the Wigner method over FCHT. It was impossible to calculate an FC or FCHT spectrum in this case because the optimised S_1 state of hydroxypropanone was significantly distorted from S_0 and so the FC integral is negligible, which means that the resulting spectrum would be highly unreliable. This severely limits the calculation of FCHT spectra to cases in which the excited state is bound, and the minimum is near enough to the Franck-Condon region.

What is also notable in Fig. 2.9 is that the spectra are not smooth, and show many spurious peaks not seen in the very smooth experimental spectrum. This could be because 500 ensemble points are insufficient to converge the spectral shape. In the Wigner spectrum, this could also be

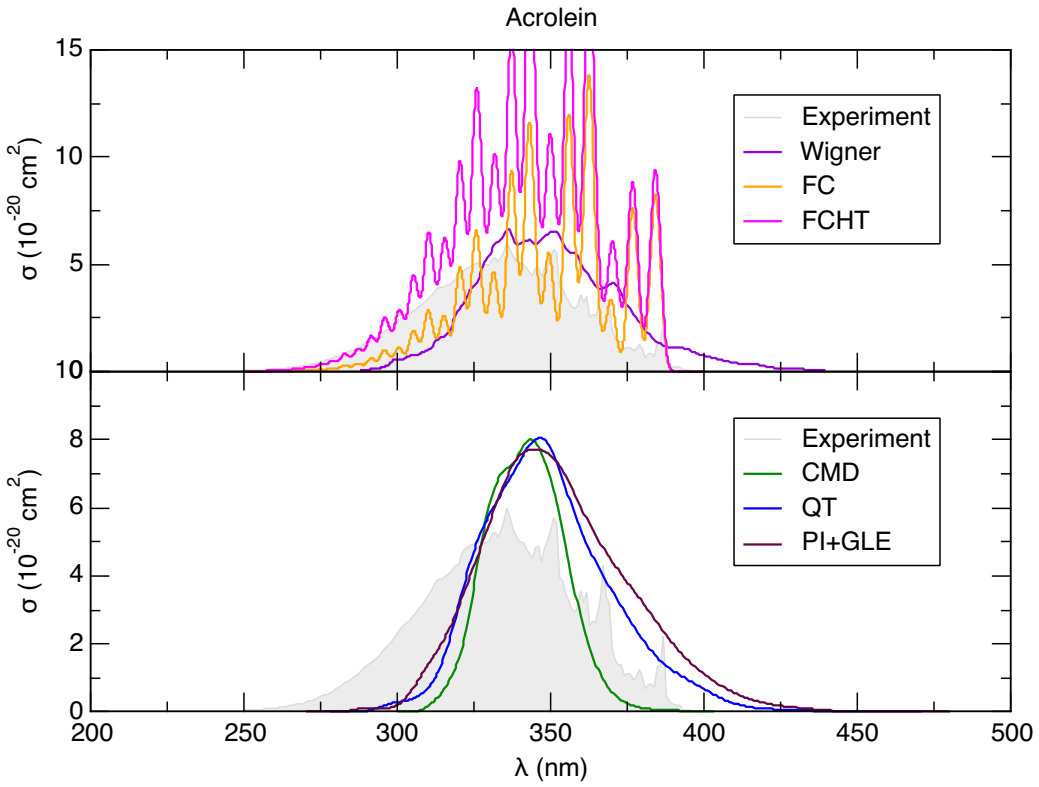

Figure 2.8: Photoabsorption spectra of acrolein, comparison of experimental results from Magneron *et al.*,[108] FC/FCHT, and nuclear ensemble approaches. All calculated spectra include only S_0 to S_1 excitations.

due to the spurious hydrogen displacements discussed earlier.

2.4 Conclusion

In this chapter I compared a selection of available strategies for predicting band broadening in UV-Vis spectra. The capabilities of the methods are summarised in table 2.1. FCHT is the only method which can reproduce the vibrational fine structure of a spectrum. It is best used for small-to-medium sized molecules with high symmetry, which are excited into a bound state which is geometrically similar to its ground state. Sampling from a Wigner distribution gives a universally good description of peak broadening, although a large number of ensemble points may be necessary for convergence. It is good for mid-sized molecules with few torsional modes, and can include temperature in the sampling procedure. Of all the MD ensemble sampling approaches CMD should not be applied to spectrum prediction as it always underestimated the broadening

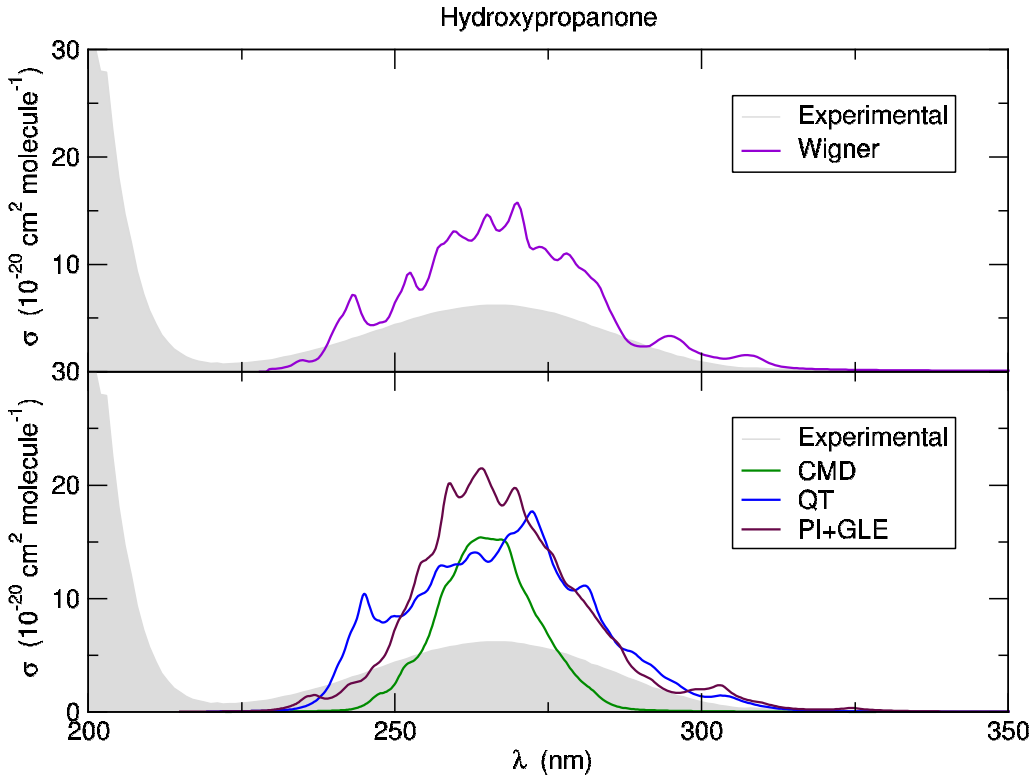

Figure 2.9: Photoabsorption spectra of hydroxypropanone, comparison of experimental results from Messaadia *et al.*[104] and nuclear ensemble approaches. All calculated spectra include only S_0 to S_1 excitations.

of the spectrum relative to the experimental peak. The MD methods which included quantum effects gave good results, but require a degree of understanding of GLE thermostats to set up the sampling. For non-experts Wigner sampling is much more straightforward to apply, and is computationally less expensive since the number of steps in an MD trajectory must be at least 10× higher than the number of ensemble points to ensure that they are uncorrelated.

Lastly, the result is sensitive to the selected electronic structure method – if the ground state being sampled is inaccurate, it will return an inaccurate spectrum. To make quantitative statements about the methods outlined here, I would have used a benchmark set of molecules to generate spectra so as to make a direct statistical comparison with experimental $\sigma(\lambda)$. However, it would be necessary to use extremely accurate oscillator strengths and energy gaps to distinguish between the error of the sampling method, and error of electronic structure. Since normal mode frequencies, or ensemble sizes of over 500 points are needed for spectrum generation such an endeavour would be extremely expensive, and therefore beyond the scope of this work.

	FCHT	Wigner	CMD	CMD+GLE	PI+GLE
Vibrational structure	y	n	n	n	n
Anharmonic	n	n	y	y*	y*
ZPE	y	y	n	y†	y
Temperature	y	y	y	y	y
Conformers	n	y**	y	y	y

Table 2.1: Breakdown of the methods discussed in this chapter. * In MD the ground state potential isn't assumed to be harmonic, but the GLE thermostat is tuned to a set of harmonic frequencies (although performance of GLE for anharmonic potentials can be improved by tuning the coupling).[84, 85] † ZPE is included with the GLE thermostat, but is susceptible to "leaking" from fast to slow normal modes. ** Although it is possible to include multiple conformers by performing a conformer search prior to the sampling, in comparison with MD methods the conformer search isn't built-in to the sampling method.

CHAPTER 3

COMPARISON OF ENERGY GRAINED MASTER EQUATION AND ATOMISTIC DYNAMICS FOR PREDICTING NONADIABATIC KINETICS

In accordance with the University of Bristol guidance on the integration of publications as chapters within a dissertation, I declare that this chapter was previously published in the Journal of Physical Chemistry A.[109] My contribution as first author was to design, execute, and analyse the calculations, and to write the manuscript. David R. Glowacki and Basile F. E. Curchod began working on this project in 2015 and both contributed their expertise towards this publication. Robin J. Shannon contributed his expertise in Master Equation kinetics and his knowledge of MESMER software. Several additions have been made to the manuscript to give the reader a more comprehensive introduction to the methods described in this chapter. These are the section on Nonadiabatic dynamics methods, the discussion of the Zhu-Nakamura equations, and the discussion of the impact of time step size (which has been moved from the supporting information in the paper).

3.1 Introduction

Accuracy of molecular photodynamic simulations in the excited state is inherently constrained by the dimensionality of the system. Exact non-relativistic quantum mechanical dynamics of a nuclear wavepacket can be described by solving the time-dependent Schrödinger equation, but exponential scaling limits this approach to small molecular systems. At the opposing end of the scale, there is a growing interest in describing the nonadiabatic dynamics of very large systems characterised by exciton transfer between chromophores.[110–114] In fact, an analytical description of nonadiabatic transitions for a simple one-dimensional two-state system in the weak coupling limit has been available since 1932, developed simultaneously, and separately, by Landau, Zener,

and Stueckelberg.[115–117] In many cases Landau-Zener (LZ) theory works reasonably well even for larger, multidimensional systems. Later, Zhu and Nakamura built on this framework to produce a set of exact nonadiabatic transition probabilities for different types of nonadiabatic curve crossings.[118–124] Zhu-Nakamura (ZN) theory is valid over the entire coupling regime, is fully analytical, and incorporates tunnelling contributions. Like LZ theory, it is formulated in a single dimension.

On-the-fly trajectory-based semiclassical dynamics accounts for the full dimensionality of a molecular system. For example, Tully's fewest switches surface hopping (FSSH) is a well-known and efficient way of simulating femtosecond timescale processes in the excited state,[125] where the time evolution of a nuclear wavepacket is approximated by a swarm of independent trajectories that classically propagate the nuclear degrees of freedom on a PES calculated on-the-fly. Each trajectory can stochastically switch between electronic states in regions of strong nonadiabatic coupling. While FSSH has known shortcomings (including overcoherence and neglect of tunnelling and interference effects)[126] it often provides an accurate and scalable method that is now widely used to explore photochemical and photophysical phenomena, also for atmospheric chemistry.[32, 127–129] Given that FSSH typically has a sub-femtosecond integration time step, pushing the simulation into the nanosecond regime necessitates compromises with respect to the electronic structure method and number of trajectories. It has been suggested that this bottleneck might be overcome through machine learned energies and couplings.[130]

For longer timescale simulations in the statistical regime, alternatives to conventional nonadiabatic dynamics strategies are needed. The energy grained master equation (EGME) is the numerical implementation of the exact master equation which discretises the density of states ρ, recasting it in matrix form. The EGME has recently been applied to the study of non-RRKM reaction kinetics in the gas phase,[131] in solution,[132, 133] and in surface chemistry.[134] Unlike FSSH, where an electronic structure calculation is performed at each step of a trajectory, an EGME calculation needs only the energies, frequencies and rotational constants of the relevant stationary points. This allows for the use of more computationally demanding electronic structure calculations and detailed sensitivity analyses on the results. The EGME also enables treatment of collisional activation and energy dissipation from the system. Furthermore, unlike molecular dynamics simulations where zero-point energy can leak, vibrational zero-point energy at the stationary points can be included explicitly in an ME calculation. Approaches to zero-point energy conservation in quantum-classical trajectories exist,[135] but they are not adopted in the standard FSSH algorithm used in this work. Tunnelling corrections may also be included in the framework of the EGME approach using an asymmetric Eckart barrier[136] or semiclassical WKB theory.[137] Solving the ME returns temperature and pressure dependent species profiles, making it a useful tool for modelling atmospheric or interstellar reactions.

Nonadiabatic analogues of standard statistical rate theories generalise classical transition state theory (TST) to reactions involving multiple PESs.[138–140] For example, intersystem cross-

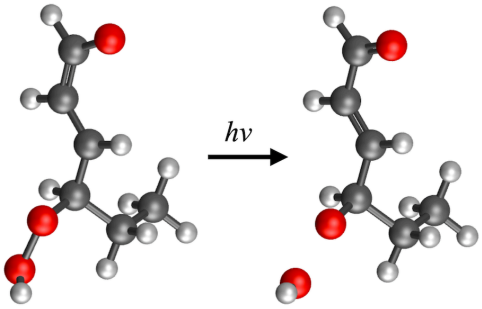

Figure 3.1: Main reaction channel for C_6-HPALD photodissociatio in the 300-400 nm range.

ings have been successfully modelled by using both the LZ and ZN expression for the inter-state surface hopping probability at the minimum energy crossing point (MECP).[141–144] Until recently, simulation of intersystem crossings in the surface hopping framework has been limited by the need for the global calculation of the spin-orbit coupling matrix elements[145] or spin-orbit coupling gradients.[146] It is now possible to run FSSH simulations that include coupling between states of arbitrary spin multiplicity.[147, 148] Using the LZ approach to describe coupling between states with differing multiplicity works well in the weak coupling regime, but fails for strong coupling.[115] A nonadiabatic EGME model (NA-EGME) of internal conversion should instead use the ZN expression, which is able to accurately treat the analytical nonadiabatic transition probabilities for the full range of energies and couplings,[122] giving the LZ result in the weak coupling limit, and the transition state theory result in the strong coupling limit. The ZN description of the coupling region can also be formulated to include contributions from tunnelling through the crossing barrier. In contrast to the full-DOF description of quantum-classical dynamics, the ZN equations are only formulated for 1-D crossings. Here, we provide evidence that – for seam-like crossings – the ZN approach offers a good approximation to describing nonadiabatic transitions between adiabatic states.

In this work, we apply the NA-EGME to predict the dissociation rate of a photoexcited bi-chromophoric hydroperoxy aldehyde, C_6-HPALD, whose primary photodissociation channel is shown in Fig. 3.1. In order to evaluate the validity of this approach, we show that the NA-EGME results are similar to the outcomes of nonadiabatic molecular dynamics (NA-MD, in this case FSSH). HPALDs are a class of molecules important in atmospheric chemistry, and it has been suggested that they participate in OH radical recycling in low NO_x regions of the troposphere.[24, 149–153] As a product of isoprene oxidation, they contain an α,β-enone chromophore that absorbs sunlight in the UV range, which is close to a labile peroxide bond. Previous experiments investigating the photodissociation kinetics of C_6-HPALD reported OH radical production under UV light.[154] In this chapter, we are less concerned with the atmospheric details of HPALD photodissociation, which will be addressed in the following chapter, but rather with C_6-HPALD as a prototypical example of a multi-chromophore system with an interesting

seam-like nonadiabatic coupling topology between two low-lying excited states. We show that the dissociation rate obtained using a NA-EGME model shows qualitative agreement with the results of NA-MD, at a significantly reduced computational cost.

This chapter will be structured as follows. First, we describe how nonadiabatic effects can be included in an EGME model using ZN transition probabilities. Second, we describe the electronic structure calculations used to characterise the relevant excited states of C_6-HPALD in the Franck-Condon region, and along the dissociative coordinate. Third, we describe the NA-MD and NA-EGME calculations and their adiabatic counterparts. Fourth, we compare the results of these contrasting methods for a single isolated reaction coordinate which corresponds to the molecule moving over a transition state on the S_1 surface leading to photodissociation. Lastly, we extend both models to include all rotational conformers of C_6-HPALD.

3.2 Nonadiabatic molecular dynamics

In Newtonian classical dynamics the motion of a system is driven by the sum of the applied forces. For an N-atom molecular system the force at a given point in phase space is defined by the potential energy surface (PES) which is a 3N dimensional function of the nuclear geometry. The PES is a core concept in molecular dynamics, that arises as a consequence of the Born-Oppenheimer (BO) approximation. The total BO wavefunction is defined as

$$\Psi(r,R) = \Phi(r;R)\Omega(R)$$

where the electronic wavefunction $\Phi(r;R)$ is a function of electron position r parametrically dependent on the nuclear position R. The expectation value of the electronic Hamiltonian determines the potential on which the nuclear wavepacket can evolve, i.e. the PES. By applying the BO approximation we assume that the motion of nuclei and electrons in a molecule can be treated as independent due to their large disparity in mass. This is useful for dealing with ground state dynamics on a single potential when the coupling to other electronic states is negligible. However, this approximation breaks down for many photochemical processes where electronic states may intersect, and electron and nuclear motion becomes coupled. Over the years a multitude of ways have been developed that can treat such problems of nonadiabatic dynamics and track the motion of a wavepacket across multiple PES in an approximate way.[26, 35] This section will discuss the taxonomy of the most widely used methods, starting with the most exact.

The time dependent Schrödinger equation (TDSE) gives a complete description of a wavefunction evolving on a potential.

$$i\hbar\frac{\partial}{\partial t}\Psi(r,R,t) = \hat{H}\Psi(r,R,t)$$

This wavefunction contains the full description of a molecular system and its formally exact form is given by the Born-Huang expansion, where α denotes the electronic state.

$$\Psi(r,R,t) = \sum_{\alpha}^{\infty}\Phi_{\alpha}(r;R)\Omega_{\alpha}(R,t)$$

The Born-Huang expansion is the starting point in the derivation of many of the following methods. Electronic and nuclear degrees of freedom (DoF) are treated on equal footing, but the exponentially scaling cost to finding the solution to the TDSE numerically is prohibitive. As such, this method is restricted to systems containing no more than three atoms, or model systems.

As early as the 1930s suggestions were made to improve the scalability of the problem by solving the TDSE variationally.[155] This mean-field method is known as time-dependent Hartee (TDH or TDSCF), and it works by approximating the wavefunction as a Hartree product of one-dimensional single particle functions. Solving this problem using the Dirac-Frenkel variational principle returns a set of coupled one-dimensional equations of motion (EOM) for each DoF of the wavepacket.[156] However, due to the mean-field description of each DoF this method often fails to correctly describe the correlation between them.

A more sophisticated approach uses a multiconfigurational wavefunction anzats in combination with the variational approach to capture some of this correlation. This is the multiconfigurational time dependent Hartree (MCTDH) method, and it is a numerically exact in the limit of a basis that includes all possible configurations.[157] One of the requirements to solving the MCTDH EOM is fitting of multiple PES in a multidimensional phase space, which numerically is performed on a fixed grid. Because of this, full MCTDH is still exponentially scaling, albeit with a small prefactor. It is most suitable for molecules with 4-12 DoF, although variants of the method have previously been used to describe systems as large as pyrazine (24 DoF).[158]

A subset of direct dynamics methods are the Gaussian based approaches which expand the wavepacket in a basis of coupled fixed-width Gaussians moving on the PES. The variational multi-configuration Gaussian wavepacket method[159] (vMCG) is derived from a variant of MCTDH,[160] (G-MCTDH) that uses Gaussian expansion functions. In vMCG parameters of the time dependent Gaussian wave packets (GWPs) evolve according to equations of motion obtained from the Schrödinger equation via the Dirac-Frenkel variational principle. This set of EOMs couple the GWPs to each other, and wavepacket propagation is nonclassical allowing them to tunnel through barriers. This quantum dynamics method can be used "on-the-fly" (DD-vMCG) by calculating Hamiltonian matrix elements using a local harmonic approximation – necessitating the calculation of a Hessian at each time step.[161] Running dynamics "on-the-fly" is generally preferred for larger systems as the need for electronic structure calculations is limited to the regions of phase space explored by the wavepacket.

In full multiple spawning (FMS) the nuclear wavepacket is represented by an adaptive basis of frozen Gaussian trajectory basis functions that, unlike in vMCG, follow classical trajectories.[162] Nonadiabatic transitions are included via a spawning algorithm that expands the basis set over the course of a trajectory by creating new Gaussian basis functions when the parent trajectory enters an area of strong nonadiabatic coupling. In an infinite basis, FMS converges to the exact TDSE solution.[26, 162]

Ab initio multiple spawning (AIMS) is an approximate "on-the-fly" version of FMS which is

robust enough to be employed to simulate the excited state dynamics of molecules.[26, 35] There are two key elements which distinguish these methods. Firstly, the "saddle-point" approximation for the Hamiltonian matrix elements in FMS – which in AIMS are calculated by an overlap of proximal Gaussians. Secondly, treating the trajectories as independent at $t = 0$, until the point when a new Gaussian is spawned. The approximations necessary to take AIMS to its FMS limit are explicit, allowing the user to tune the method to suit the complexity of the system.[163]

Mixed quantum-classical (MQC) dynamics methods allow the nuclear degrees of freedom to evolve on a quasi-classical potential, and incorporate nonadiabatic effects. Examples of MQC methods include multiconfigurational Ehrenfest and Tully's surface hopping dynamics.[34, 125]

The Ehrenfest wavefunction ansatz is similar to that used in FMS, in that it is also expanded on a set trajectory basis functions composed of electronic and nuclear parts. However, Ehrenfest trajectories evolve on a potential which is a time dependent linear combination of adiabatic potentials weighted by their electronic coefficients.[34] Because the trajectories move on this average potential, Ehrenfest dynamics have been described as a mean-field solution to the TDSE. Because of the non-physical nature of a wavepacket moving on an average potential this approach has been predominantly used to model solid state systems.[26]

The surface hopping method was first introduced by Tully and Preston in the 1970s,[164] who later developed the fewest switches algorithm in 1990.[125] The wavepacket is represented by a swarm of independent trajectories which evolve classically on a potential that is calculated on-the-fly. Nonadiabatic effects are included by allowing the trajectories to "hop" to another state with a probability that depends on the coupling strength. This method is highly efficient and parallelizable and has been applied to larger systems including the LH2 complex,[111] and recently, the pentacene/buckminsterfullerene heterojunction.[165] However, there are cases where this approach fails – particularly in its treatment of decoherence. Another important caveat is that the accuracy of the dynamics is limited by the electronic structure method used.

Novel machine learning approaches have been proposed to reduce the cost of accurate PES for running "on-the-fly" dynamics calculations without the requirement to perform electronic structure calculations at each time step.[166, 167] Approximate kernel ridge regression potentials have been integrated with trajectory based dynamics, although ML methods still struggle to capture the shape of rapidly varying nonadiabatic coupling.

3.3 Nonadiabatic energy grained master equation

We propose an alternative approach to dynamics methods covered in the previous section: a kinetic model that includes nonadiabatic transitions to a different electronic state. The energy grained master equation (EGME) is a Markov-state model that has found widespread application to non-equilibrium problems in chemical kinetics.[20, 132, 133, 168, 169] EGME is especially useful for modelling atmospheric reactions as it has the option of including energy transfer by bath

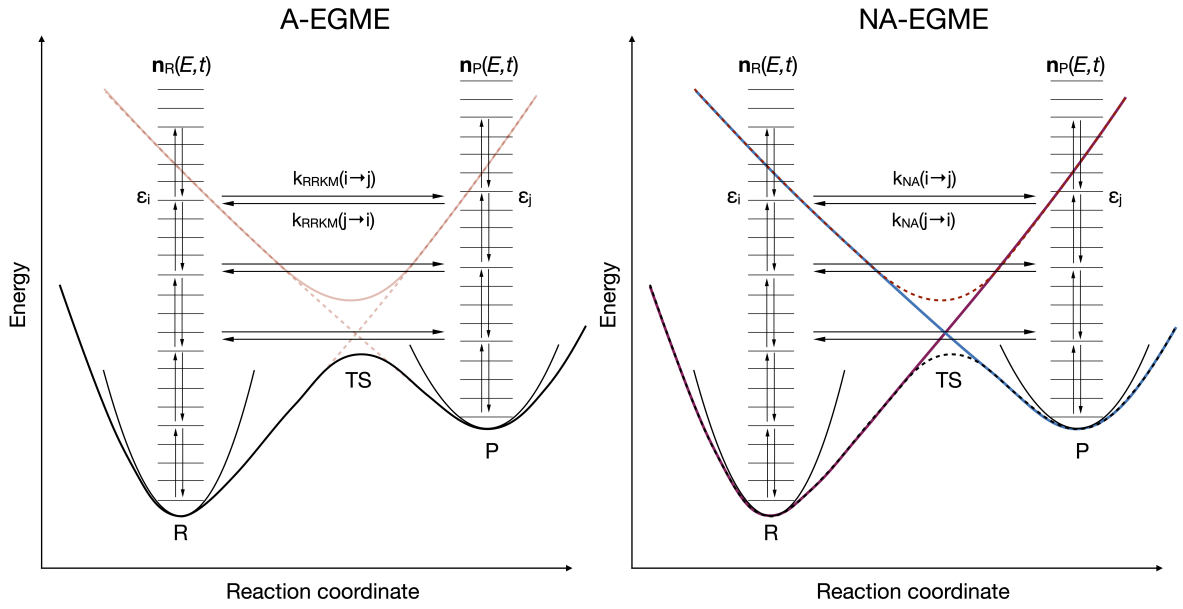

Figure 3.2: Left: A-EGME schematic; density of rovibrational states is discretised into grains with energy ε_i, microcanonical rates between reactant R and product P connect the two isomers. Right: NA-EGME schematic with included Zhu Nakamura crossing probabilities $p_{ZN}(E)$.

gas collisions. It can also be used to determine the pressure and temperature dependence of rate constants. The vast majority of applications of EGME models focus on reactive processes on a single electronic state and do not incorporate nonadiabatic coupling. While strategies for calculating microcanonical rate coefficients for nonadiabatic processes do exist, to our knowledge there has only been one attempt to incorporate such transitions into an EGME framework. Plane *et al.* modelled temperature and pressure dependent intersystem crossing kinetics by treating the extended seam between the singlet and triplet state as a dividing surface.[169] The MECP between these states was treated as a pseudo-transition state, and the probability of spin-forbidden hopping transitions between these states was calculated by convoluting the density of states at the MECP with the LZ expressions to obtain microcanonical rate coefficients.

Building on the work of Plane *et al.*, we have extended the NA-EGME to calculate the rate of HPALD photodissociation, where the nonadiabatic transition of interest involves coupling between two states of the same multiplicity – i.e., significantly stronger coupling than the intersystem crossing investigated by Plane *et al.* The LZ model is ill-suited to internal conversion as it assumes the inter-state coupling is both localised and weak. For these reasons, we used ZN theory to describe nonadiabatic transition probabilities in the coupling region. The ZN equations produce the correct analytical hopping probability coefficients over the full range of coupling regimes for a 1-D nonadiabatic tunnelling type crossing,[123, 170] returning the LZ result in the limit of weak coupling, and the classical transition state theory result in the limit of strong coupling.

3.3.1 Ground state EGME kinetics

An adiabatic master equation model (A-EGME, illustrated in Fig. 3.2) is constructed from any number of connected potential energy wells (isomers) and the transition states between them. In order to make the problem computationally tractable, the energy of each species is discretised into bins or grains of a set size. The population density across each energy grain of every isomer in the system is then defined by a vector $n(E,t)$, and it is possible to formulate a set of coupled differential equations in terms of $n(E,t)$ that describe the time-evolution of the grain populations. Recasting these differential equations in matrix form defines the chemical master equation.

$$\frac{d}{dt}\mathbf{n}(E,t) = \mathbf{M}\mathbf{n}(E,t)$$

The matrix $\mathbf{M}$ is given as $[\omega(\mathbf{P}-\mathbf{I})-k]$, where ω is the Lennard Jones collision frequency, $\mathbf{P}$ is a matrix of transition probabilities between grains, $\mathbf{I}$ is the identity, and k is a diagonal matrix of energy-resolved microcanonical rate constants, $k(E)$, for the reactive process. In the EGME population transfer between grains can arise due to interactions with a bath gas or through reactive loss/gain to a connected isomer. Energy transfer as a result of bath interactions is typically modelled using an exponential down model. For reactions between different isomers, population transfer can only occur between corresponding grains of the same energy.

Such reactions are included in the model through unimolecular microcanonical rate coefficients calculated from RRKM theory. Rice-Ramsperger-Kassel-Marcus theory (RRKM), is a microcanonical transition state theory for unimolecular reactions. In the MESMER EGME implementation, $k(E)$s calculated from RRKM theory are used to model the transfer of population from an energy grain in one species to the corresponding energy grain in another, across a transition state.

$$k(E) = \frac{W_{TS}(E-E_0)}{h\rho(E)} \tag{3.1}$$

In equation 3.1 $W_{TS}(E-E_0)$ is the sum of rovibrational states at the optimized transition state geometry between E and reaction threshold energy E_0 (excepting the degree of freedom associated with passage through the TS), $\rho(E)$ is the density of rovibrational states of the reactant isomer, and h is Planck's constant.

It is appropriate to apply RRKM theory to a system when the following conditions are satisfied. Firstly, there should be a free exchange of energy between rovibrational modes causing rapid intramolecular energy transfer. If this is true, the total phase space of the molecule should be populated statistically – this is sometimes referred to as the ergodicity assumption.[171] The flow of energy between active modes implies that every activated molecule will eventually be converted to products, unless deactivated by a collision. Non-RRKM behaviour can be seen in cases of weak coupling between vibrational modes, but most molecular systems are anharmonic enough that this assumption is satisfied. The second assumption is that of strong collisions between molecules and the bath gas. Energisation and de-energisation are considered single step

processes where energies $>> kT$ are transfered between molecules. Like in classical TST it is assumed that the forward flux across the dividing surface is the same as backwards flux such that the system is at equilibrium and no net reaction is occurring. RRKM theory views energy as a continuous and not a quantised variable. The number of quantum states in energy range $E^* \rightarrow E^* + dE^*$ is written as a density of states which is generally true for dE^* on the order of 4×10^{-4} J mol^{-1}.

Because the EGME can be used to model out-of-equilibrium phenomena,[172] it can be applied to reactions in atmospheric and combustion chemistry which cannot be modelled with equilibrium TST techniques due to the non-Boltzmann distribution of energy in the isomers. This feature allows us to replicate the non-equilibrium energy distribution of a wavepacket directly following photoexcitation.

3.3.2 Nonadiabatic EGME

Having established how a kinetic EGME model works in the ground state, we now consider how nonadiabatic transitions could be included.

The NA-EGME model, illustrated in Fig. 3.2, is constructed analogously to the conventional ground state A-EGME, except that the microcanonical rate coefficients are not calculated through RRKM theory. Nonadiabatic coupling between states is included through an energy resolved ZN expression for the transition probabilities P_{ZN} between two diabatic states in the vicinity of a crossing point. We can then compute a set of nonadiabatic microcanonical rate coefficients $k_{NA}(E)$ which transfer population between the different diabatic states. The expression for $k_{NA}(E)$ is similar to the RRKM expression in Eqn. 3.1.

$$k(E) = \frac{N_{TS}(E)}{h\rho_{S_1}(E)} \tag{3.2}$$

where the density of states at the optimised S_1 minimum is ρ_{S_1} and N_{TS} is the convolution of the ZN transition probabilities, P_{ZN}, and the density of states at the transition state, ρ_{TS}.

$$N_{TS}(E) = \int_0^{E'} \rho_{TS}(E - E')P_{ZN}(E)dE' \tag{3.3}$$

Therefore, to find the master equation solution it is necessary to have a set of energy resolved ZN transition probabilities. These can be calculated from the 1-D adiabatic profile across the crossing point using the equations described in the following section.

3.3.3 Zhu-Nakamura theory of nonadiabatic transitions

Nonadiabatic transitions are a fundamental phenomenon, inherent in describing fundamental chemical processes. First notable attempts to find an analytic solution for the probability of

a nonadiabatic transition were made in 1932 by Landau,[115] Zener,[116] and Stueckelberg[117] independently. Landau-Zener, or Landau-Zener-Stueckelberg theory, has had a foundational influence on new theories that account for nonadiabatic effects. The LZ formula returns the probability of a diabatic transition between energy states for a two-state system, and is straight forward to derive by contour integration.[173]

$$P_{LZ} = \exp\left(-\frac{2\pi A^2}{\hbar v|\Delta F|}\right)$$

Here A is the diabatic coupling, v is the velocity of the wavepacket, and ΔF is the difference in the gradients of the two diabatic surfaces.

However, the LZ formula was only correct at higher energies so it could not evaluate the nonadiabatic transition probability at energies near to, or below, the crossing point. The LZ formula also could not describe strong coupling regimes or account for tunnelling below the barrier.

Zhu-Nakamura theory addressed all of these concerns. Originally derived for linear diabatic potentials,[119–122, 174] it provides us with the exact solutions to the general two state curve crossing problem. This theory works for the full range of energies and coupling strengths. [175] ZN theory distinguished between two types of nonadiabatic crossing. In the "Landau Zener" case, the two diabatic potential cross with the same signs of slopes whereas in the nonadiabatic tunnelling case the diabatic curves have opposite slopes, creating a potential barrier at the crossing. Both expressions contain the parameters a^2 and b^2, where a^2 can be seen as the effective coupling strength and b^2 is the energy ($b^2 = 0$ at the crossing point). The derivation will only cover the nonadiabatic crossing case as it is comparable of the shape of the S_1 PES in HPALD photodissociation.

3.3.4 Zhu-Nakamura equations for a nonadiabatic tunnelling type crossing

This section contains the full set of Zhu-Nakamura equations, as they are implemented in MESMER. Figure 3.3 is an illustration of a prototypical 1-dimensional nonadiabatic type crossing, where all the parameters that will be significant in the equation are highlighted. We will use the conventions of the original paper[123] to label all the variables. Dummy variables will be labelled generally as g_n. In the diabatic representation we define parameters a and b as

$$a^2 = \frac{\hbar^2 F(F_1 - F_2)}{16\mu V_X^3} \tag{3.4}$$

$$b^2 = \frac{(E - E_X)(F_1 - F_2)}{2FV_X} \tag{3.5}$$

where F_n are the slopes of the nth diabatic potential, $F = \sqrt{|F_1 F_2|}$, μ is the reduced mass of the system, and V_X is the diabatic coupling between the electronic states. In the adiabatic

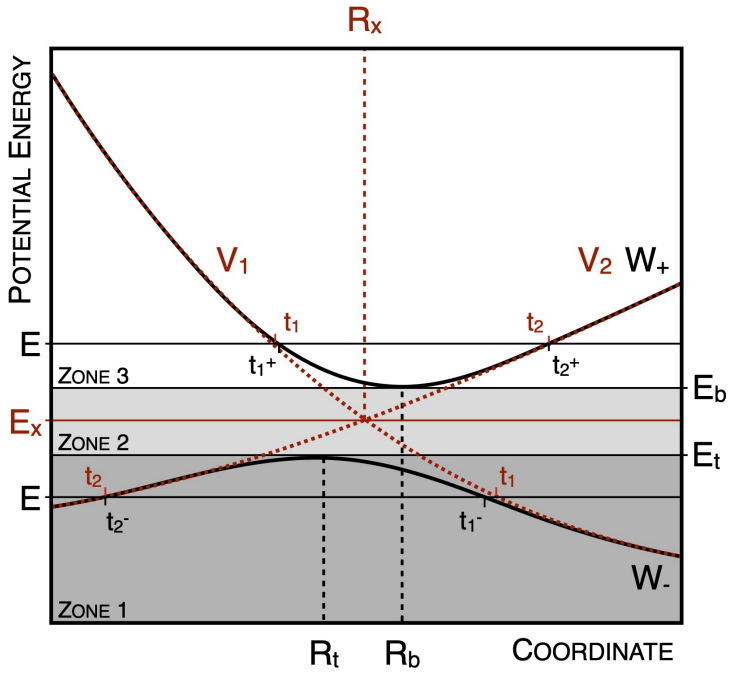

Figure 3.3: Nonadiabatic-type crossing illustrating the parameters used in the Zhu-Nakamura equations. Features in red highlight the variables used in the diabatic representation (V_1 and V_2), and black show those in the adiabatic representation (W_+ and W_-).

representation these parameters are re-defined here

$$a^2 = \frac{(1-\gamma^2)\hbar^2}{\mu(R_b - R_t)^2(E_b - E_t)} \tag{3.6}$$

$$b^2 = \frac{E - (E_b + E_t)/2}{(E_b - E_t)/2} \tag{3.7}$$

where γ is a parameter expressed in terms of adiabatic state energies (W_+, W_-) and can be interpreted as the separation of the adiabatic potentials in the crossing vicinity.

$$\gamma = \frac{E_b - E_t}{W_+\left(\frac{R_b + R_t}{2}\right) - W_-\left(\frac{R_b + R_t}{2}\right)} \tag{3.8}$$

Each of the energy range "zones" have a different expression for the transition probability, which will be given here.

Zone 1 transmission probabilities ($E \leq E_t$)

To define the transition probability below E_t we introduce an adiabatic parameter δ, the integrand

of the classical action over the nuclear coordinate on the lower adiabatic curve, W_-.

$$\delta = \int_{t_2^-}^{t_1^-} |K_-(R)| dR \tag{3.9}$$

$$K_-(R) = \frac{1}{\hbar}\sqrt{2\mu(E - W_-(R))} \tag{3.10}$$

This integrand can be used to calculate the Gamow factor for tunnelling $e^{-2\delta}$ while the impact of nonadiabatic coupling is given by the function $B(\sigma_c/\pi)$ of another adiabatic parameter σ as well as δ, and where $\Gamma(X)$ is simply the standard Gamma function.

$$B(X) = \frac{2\pi X^{2X} e^{-2X}}{X\Gamma^2(X)} \tag{3.11}$$

$$\sigma = \frac{\pi}{16a|b|} \frac{\left(6 + 10\sqrt{1 - 1/b^4}\right)^{1/2}}{1 + \sqrt{1 - 1/b^4}} \tag{3.12}$$

$$\sigma_c = \sigma(1 - 0.32 \times 10^{-2.0/a^2} e^{-\delta}) \tag{3.13}$$

Which finally gives us the transition probability P_{12} in energy range $E \leq E_t$.

$$P_{12} = \frac{B(\sigma_c/\pi)e^{-2\delta}}{\left(\left(1 + \frac{a}{2(1+a)} B(\sigma_c/\pi)e^{-2\delta}\right)^2 + B(\sigma_c/\pi)e^{-2\delta}\right)} \tag{3.14}$$

Zone 2 transmission probabilities ($E_t \leq E \leq E_b$)

In scattering theory, which is the starting point for the derivation of Zhu-Nakamura theory, the nonadiabatic transition probability can be directly evaluated from the Stokes constant. The analytical expression for the Stokes constant in this energy range given by Zhu-Nakamura theory contains the quantity W. The expression for W has been improved from the original paper by introducing empirical corrections g_1 and g_2.[175]

$$g_1 = \frac{a - 3b^2}{a + 3}\sqrt{1.23 + b^2} \tag{3.15}$$

$$g_2 = 0.38 \frac{(1 + b^2)^{1.2 - 0.4b^2}}{a^2} \tag{3.16}$$

$$W = \int_0^\infty \frac{1 + g_2}{a^{2/3}} \cos\left(\frac{t^3}{3} - \frac{b^2 t}{a^{2/3}} - \frac{\frac{g_1}{a^{2/3}} t}{0.61\sqrt{2.0 + b^2} + a^{1/3} t}\right) dt \tag{3.17}$$

And so the final expression for the ZN transition probability in the energy span $E_t \leq E \leq E_b$ is

$$P_{12} = \frac{W^2}{1 + W^2}. \tag{3.18}$$

Zone 3 transmission probabilities ($E_b \leq E$)

Similarly to Zone 1, here we evaluate the classical action integral over the span of the crossing.

$$K_+(R) = \frac{1}{\hbar}\sqrt{2\mu(E - W_+(R))} \tag{3.19}$$

This can then be used to evaluate the adiabatic parameters σ and δ

$$\sigma = \int_{t_1^+}^{t_2^+} |K_+(R)| dR \tag{3.20}$$

$$\delta = \frac{\pi}{16ab} \frac{\left(6 + 10\sqrt{1 - 1/b^4}\right)^{1/2}}{1 + \sqrt{1 - 1/b^4}} \tag{3.21}$$

These parameters can then used to find the quantity present in the Zhu-Nakamura expression for the Stokes constant, ϕ

$$\phi = \sigma + \frac{\delta}{\pi} - \frac{\delta}{\pi}\ln\left(\frac{\delta}{\pi}\right) + \frac{\pi}{4} + \mathrm{Arg}\Gamma\left(i\frac{\delta}{\pi}\right) - g_3 \tag{3.22}$$

with an empirical correction

$$g_3 = \frac{0.23a^{1/2}}{a^{1/2} + 0.75} 40^{-\sigma}. \tag{3.23}$$

The Stokes constant in this energy range also contains the Landau-Zener transition probability p defined as

$$p = \exp\left(\frac{-\pi}{4a}\sqrt{\frac{2}{b^2 + (b^4 + g_4)^{1/2}}}\right) \tag{3.24}$$

where

$$g_4 = -0.72 + 0.62a^{1.43}. \tag{3.25}$$

After defining these extra variables the probability of transition for energies above E_b is expressed as

$$P_{12} = \frac{4cos^2(\phi)}{4cos^2(\phi) + p^2/(1-p)}. \tag{3.26}$$

3.4 Computational Details

3.4.1 Characterising the PES

C_6-HPALD is a conformationally flexible molecule. A systematic rotor search performed in Avogadro V1.2.0 finds 7 conformational isomers which we label A-G. Ground state geometries of these conformers were then optimised with DFT/PBE0/TZVP and their analytical frequencies confirm that these geometries are local minima on the ground state PES.

Excited state properties, including energies, nuclear gradients, and nonadiabatic couplings, can be calculated accurately and efficiently with linear response time dependent density functional theory (LR-TDDFT). LR-TDDFT, like DFT, is formally exact on the condition that the true frequency-dependent exchange-correlation functional is used. Its shortfalls are well documented, including its tendency to underestimate energies of states with high charge transfer character or regions of the PES with strong coupling between ground and excited states.[176, 177] Nevertheless, LR-TDDFT is widely used for nonadiabatic dynamics simulations of larger systems due to its favourable scaling with basis set size.[178, 179] Employing LR-TDDFT for excited state dynamics always requires a careful validation of its accuracy in comparison to high-level wavefunction methods.

To determine a method for running NA-MD in the relevant region of the PESs, we performed a number of excited state benchmarks at the S_0 geometry of the lowest energy conformer (B) of C_6-HPALD. A scan along the PES cross section of the -O-OH internal coordinate was initiated at the S_0 geometry of conformer B to validate the use of LR-TDDFT/PBE0/6-31G (calculated for 5 singlets) against MS(4)-CASPT2(10,8)/6-31G* and a number of other methods. The active space of the MS-CASPT2 calculation was selected to include the bonding and anti-bonding orbitals of the peroxide and α,β-enone chromophores, as well as the lone pairs on the oxygen atoms. All DFT/LR-TDDFT calculations were performed in Gaussian 16.[64] Ground state energies at the optimised geometries were refined with density fitted CCSD(T)-f12//cc-pVDZ-f12//def2-QZVPP in Molpro 2019.[180] MS-CASPT2 calculations were performed in OpenMolcas v18.09.[181]

The transition state (S_1-TS) on the S_1 surface was optimised using an eigenvector following Berny algorithm in Gaussian 16[64] with LR-TDDFT/PBE0/6-31G. Finding this first order saddle point on the S_1 surface was not a trivial task: because the seam is quite sharp, optimisation steps that were too large would cause the optimisation to proceed down the steep slopes of the ridge. The S_1-TS geometry was verified through a vibrational frequency analysis that yielded a single imaginary frequency. An intrinsic reaction coordinate (IRC) scan was performed, initiated at this S_1-TS geometry. Geometries of each conformer were optimised in the S_1 state with the optimisation starting at their respective S_0 geometry. The minimum energy conical intersection (MECI) between the S_1 and S_2 states was optimised by using the search algorithm described by Harvey *et al.*[182]

3.4.2 Photoabsorption cross section

The photoabsorption cross section of C_6-HPALD is yet to be measured experimentally. We can predict it *ab initio* by using the nuclear ensemble approach based on a harmonic Wigner distribution in the ground state[183] which captures the inhomogeneous broadening of the spectral bands, which has been described in chapter 2. Ground state frequencies used to generate the Wigner distribution were calculated for each conformer with DFT/PBE0/TZVP. For each of the 7 conformers, 100 nuclear configurations are sampled from their respective distribution. We

calculate the absorption in the 300-400 nm range into the S_1 and S_2 electronic states separately, as well as the combined spectrum. For each sample point the vertical transitions and oscillator strengths are calculated with LR-TDDFT/PBE0/TZVP. Each peak is overlaid with a Lorentzian curve whose phenomenological broadening is set to 0.05 eV to return a continuous spectrum. The final photoabsorption cross section is a linear combination of the spectra for each conformer where the Boltzmann weights of the conformers are calculated from their CCSD(T) electronic energies. We approximated the Gibbs free energy by the electronic energy because free energy corrections (from PBE0/TZVP frequencies) did not change the ordering of states.

3.4.3 Nonadiabatic dynamics

All trajectory dynamics simulations were performed using the following protocol, unless stated otherwise. Fewest switches surface hopping simulations were performed in Newton-X.[139, 184] Energies and gradients of the first four singlet states (S_0-S_3) were calculated at each step with LR-TDDFT/PBE0/6-31G using Gaussian 09.[64] Energy based decoherence corrections were applied, as described by Granucci and Persico,[185] with the decoherence parameter α set to 0.1 a.u. Nonadiabatic coupling terms between electronic states were calculated using a time-derivative coupling scheme.[186]

The importance of the nonadiabatic effects was quantified by comparing against adiabatic molecular dynamics (A-MD) in which the nonadiabatic coupling between states was set to 0, effectively restricting the trajectories to the S_1 state. A-MD calculations were also performed in Newton-X with identical initial conditions to the NA-MD run.

Starting geometries and velocities for the trajectories were generated by randomly sampling points from a ground state Wigner distribution (for a harmonic oscillator). For each conformer this distribution was constructed using DFT/PBE0/TZVP level normal mode frequencies at the optimised S_0 geometries, where a larger basis set is selected to improve the quality of the distribution. In total, we ran 250 NA-MD and 50 A-MD trajectories, whose initial conditions corresponded to the Wigner distribution of conformer C. A further 109 trajectories were performed with both NA-MD and A-MD, corresponding to the realistic conformer distribution where the number of trajectories corresponds to the Boltzmann weight of the conformer in the ground state. All trajectories were initiated on the S_1 electronic state as it corresponded to the strongest peak in the actinic region, $\lambda > 320$ nm, of the photoabsorption cross section (available in the SI, S5).

All trajectories were propagated up to 4 ps or until photodissociation was observed. Total energy was conserved in all trajectories up to the end point of the trajectory. Because LR-TDDFT fails to describe homolytic bond dissociation, trajectories were stopped soon after the dissociation was initiated. Classical nuclei were propagated with a 0.5 fs time step. The rationale behind this choice is discussed further in section 3.6.2.

3.4.4 Constructing a NA-EGME model

Each electronic structure calculation used to construct an EGME model was performed at the same level of theory (LR-TDDFT/PBE0/6-31G) as that used for NA-MD so that we might directly compare the results. Energies of all stationary points were specified with respect to the energy of the geometry optimised S_1 minimum which was treated as the reactant well in the model. Zero-point energy corrections were not used when defining the relative energies so as to make a direct comparison with results of dynamics calculations, in which ZPE was not rigorously constrained.

The electronic structure theory codes which we utilized provided states energies in the adiabatic (S_0, S_1, S_2, etc.) representation. However, as illustrated in Fig. 3.2, the NA-EGME treats the different states in the diabatic representation (in this case an $n\pi^*$ and $n'\sigma^*$ state), and requires as input an analytical form of the diabatic states in the vicinity of the crossing point to determine P_{ZN} at the seam. To derive an analytical form of the diabats from the adiabatic energies, we considered only the coordinate along the imaginary eigenvector of the S_1-TS Hessian, investigating 1-D motion along the 3N-7 dimensional coupling seam. The eigenvector describing this motion takes the system across the $n\pi^*/n'\sigma^*$ seam, which corresponds to extension of the peroxide bond and loss of OH, denoted by reaction coordinate R. Energies of the S_1 and S_2 adiabatic states across this coordinate are used to fit the diabatic states near the TS. We do this by constructing a simple Hamiltonian, $\mathbf{H}(R)$, which includes the two diabatic states and a coupling between them (H_{12}), assumed to be constant in that region.

$$H(R) = \begin{pmatrix} H_{11}(R) & H_{12} \\ H_{12} & H_{22}(R) \end{pmatrix}$$

Analytical expressions for its two eigenvalues, λ_1 and λ_2 are determined by diagonalizing $H(R)$. These eigenvalues correspond to the S_1 and S_2 adiabatic states respectively. Calculated adiabatic states which are shown in figure 3.8 are fitted to the analytical form of the diabats given in equation 3.28. We assumed the dissociative state, $H_{22}(R)$, to have the form of an exponential decay, and the bound state, $H_{11}(R)$, to have the form of a harmonic well.

$$H_{11}(R) = A_{\pi^*}\left(R - \beta_{\pi^*}\right)^2 + \epsilon_{\pi^*} \tag{3.27}$$

$$H_{22}(R) = A_{\sigma^*}\exp\left(-R\beta_{\sigma^*}\right) + \epsilon_{\sigma^*} \tag{3.28}$$

The fitted parameters (available in Appendix A) were used in the NA-EGME calculation to determine P_{ZN} and calculate a set of microcanonical rate constants for each energy grain.

The initial population vector $n(E,t_0)$ is set up with N energy grains. To replicate the energy distribution of the wavepacket at the start of the dynamics, $n(E,t_0)$ must mirror the initial conditions used in the NA-MD calculations. Each initial condition sampled from the Wigner ensemble corresponds to an initial energy, a sum of its kinetic energy and its potential energy

referenced to S_1. The distribution of total energies resembles a normal distribution, with the average initial energy above the S_1 minimum. This average energy corresponds to the ${n_i}^{\text{th}}$ energy grain in the population vector $n(E,t)$ so the EGME calculations are initiated with 100% of the initial population in this grain.

We used a grain size of 50 cm^{-1} in all EGME calculations and standard temperature and pressure (300K and 760 Torr) to replicate atmospheric conditions. Collision parameters used for the bath gas, He, were ϵ = 10.2 K and σ = 2.55 Åand the collisional energy transfer was treated using an exponential down model.[187] The collisional energy transfer parameter is set to 250 cm^{-1}, a value which is typical for standard atmospheric conditions.[20] Photodissociation was assumed to be irreversible and the dissociation products were treated as a sink. To quantify the impact of nonadiabatic effects at the $n\pi^*/n'\sigma^*$ seam in these EGME calculations, the same model was re-run without allowing nonadiabatic transitions, using a standard non-equilibrium ground state EGME model. Microcanonical $k(E)$ were calculated using the RRKM formulation given in 3.1.

The NA-EGME model was then modified by substituting MS(4)-CASPT2/6-31G* energies at the same LR-TDDFT optimised stationary points to refine the EGME result. These calculations use the same frequencies, and rotational constants calculated with LR-TDDFT/PBE0/6-31G. Single point energy calculations were performed for the following geometries: the S_1 minimum of the B conformer; geometries found by taking steps along the imaginary eigenvector of S_1-TS. For the latter case, a crossing point between the diabatic surfaces is found at a small displacement from the S_1-TS geometry. New diabats were fitted to the results of the scan, leading to slightly different ZN parameters.

All of the energy grained master equation calculations reported in this study were performed using the open source master equation solver, MESMER (master equation solver for multi-well energy reactions).[168, 188]

3.5 Results

3.5.1 Ground and excited state PES

Ground state geometries and relative CCSD(T) energies of all 7 conformers are shown in Fig. 3.4. Optimising these rotamer structures on the S_1 PES with LR-TDDFT converged on 7 distinct structures that maintain the orientation of the peroxide and (-CH_2CH_3) branches such that there are multiple S_1 minima. Conformer B remained the lowest energy conformer on the S_1 PES.

Our predicted photoabsorption cross section shown in Fig. 3.5 indicates the majority of the photoexcitation in the UV-Vis region is into the S_1 state. Integrating over $\sigma(\lambda)$, actinic flux, and quantum yield in the actinic region we can make an *ab initio* estimate of the photolysis rate. Assuming a unity quantum yield we predict this rate to be 1.4×10^{-4} s^{-1}, which is within one

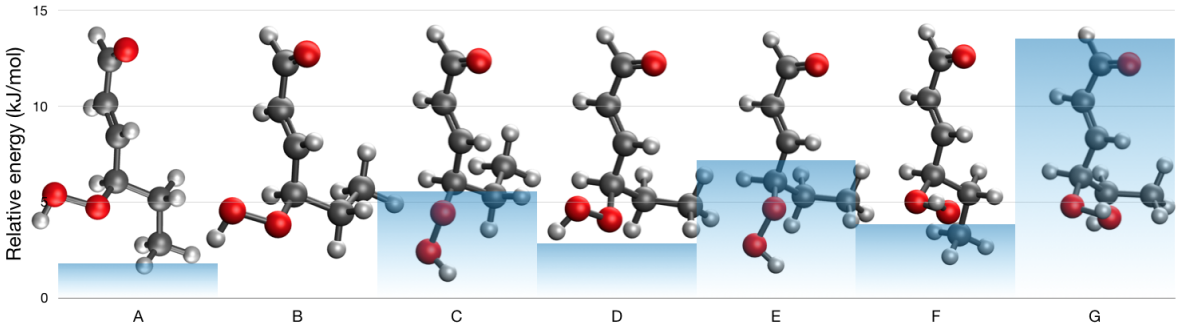

Figure 3.4: 7 conformers of C_6-HPALD found via a systematic rotor search, optimised with PBE0/TZVP. Relative energies were refined using density fited CCSD(T).

order of magnitude of the observed experimental rate of $6.3 \pm 0.1 \times 10^{-5}$ s^{-1}.[154] The cross-section indicates that in the actinic region the strongest peak corresponds to absorption into the S_1 state.

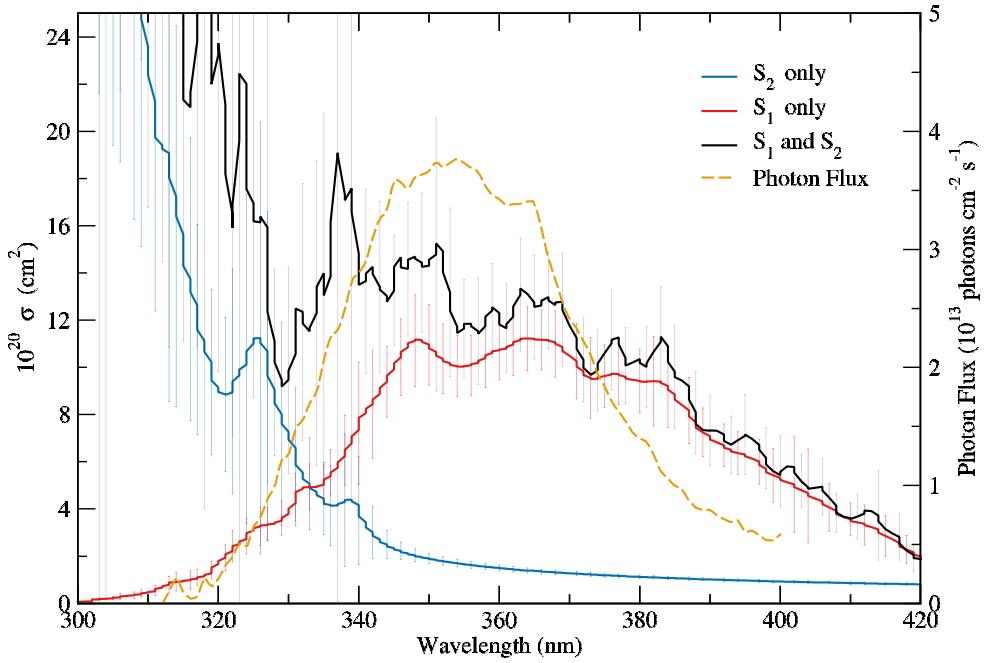

Figure 3.5: Absorption cross section of C_6-HPALD calculated using Wigner ensemble sampling. Absorption into the S_1 state dominates in the actinic region, above 320 nm.

Shapes of the excited state PESs along the peroxide bond coordinate calculated with LR-

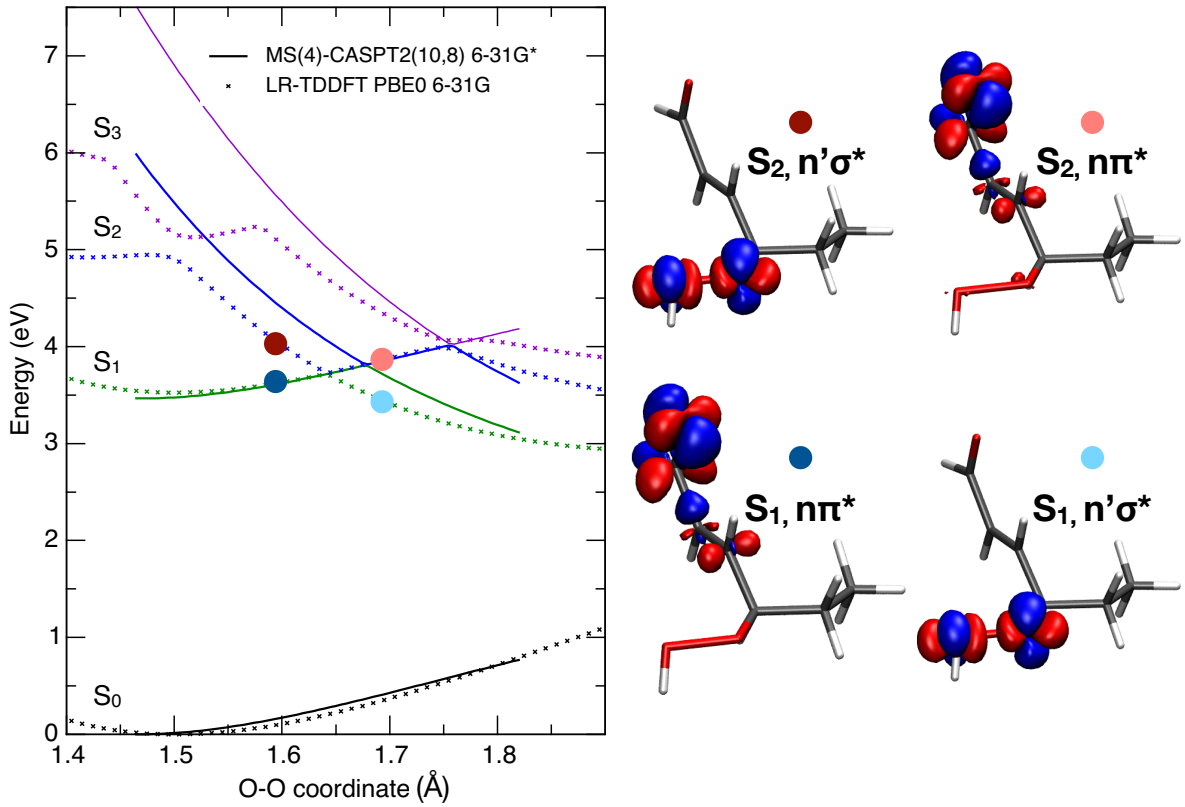

Figure 3.6: Energies of the first 4 excited states of conformer B calculated with LR-TDDFT/PBE0/6-31G and MS(4)-CASPT2(10,8)/6-31G*, alongside electron density difference plots between S_0 and specified state at 2 points along the peroxide bond coordinate illustrating the change in diabatic character.

TDDFT/PBE0/6-31G and MS-CASPT2(10,8)/6-31G* show good qualitative agreement. On this basis, we decided to use LR-TDDFT/PBE0/6-31G as the electronic structure method for all NA-MD and A-MD calculations in this work. Rigid scans along the peroxide bond dissociation coordinate in Fig. 3.6 show a near degenerate region between the S_1 and S_2 states at 1.65 Å, and between S_2 and S_3 states at 1.76 Å. Benchmarks using larger basis sets show that as the bond extends beyond 1.75 Å, LR-TDDFT provides a poor description of homolytic dissociation. This, however, will not be a significant problem for the dynamics because the S_1 potential is dissociative beyond this point, at which point trajectories were terminated.

The density difference plots shown in Fig. 3.6 shows that the nπ^* transition which characterises the S_1 state in the bound region of the PES (O-O extended to 1.6 Å) is located mostly on the α,β-enone chromophore. At the same geometry, the n$'\sigma^*$ transition to the S_2 state is located mostly along the -O-OH bond. When the peroxide bond is extended to 1.7 Å, the electronic character of the two states swaps, such that the S_1 state is now characterised by the n$'\sigma^*$ transition. The region of strong nonadiabatic coupling observed between the S_1 and S_2 at 1.65 Åin Fig. 3.6

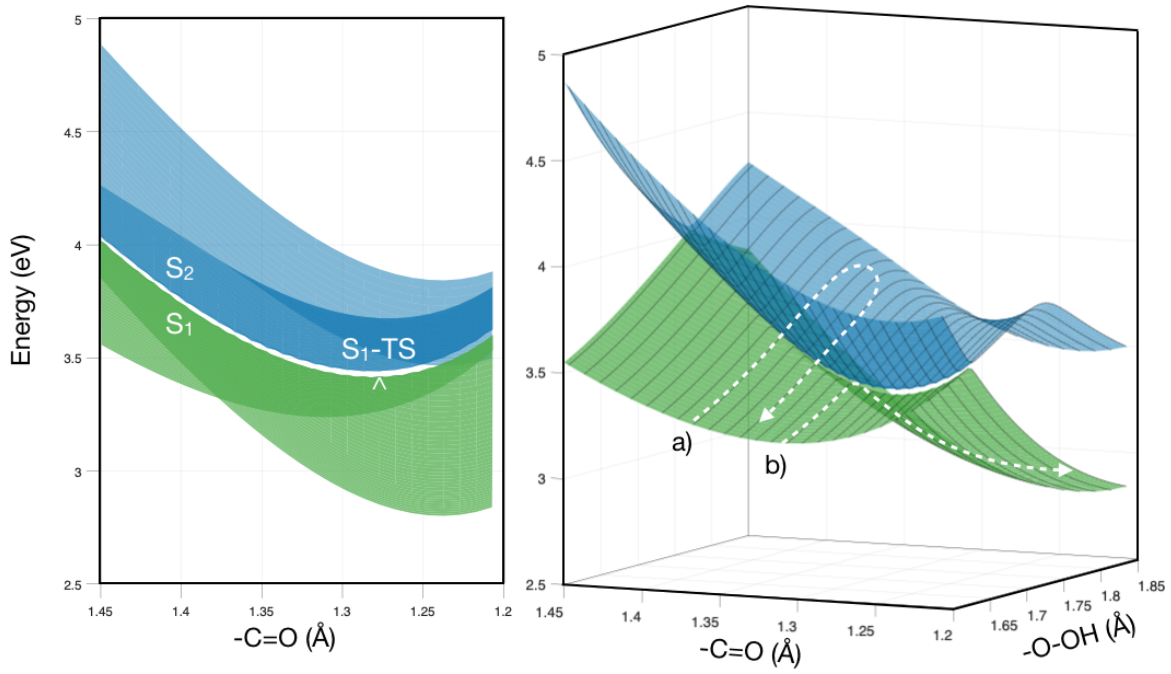

Figure 3.7: Scan of the S_1/S_2 nonadiabatic seam initiated at S_1-TS, excitation energies calculated with LR-TDDFT/PBE0/6-31G. Left panel highlights the extended near-degenerate (3N-7) seam. a) Diabatic trapping mechanism; b) Adiabatic passage across seam leading to loss of OH.

is a single point on an extended (3N-7) seam where the $n\pi^*$ and $n'\sigma^*$ diabatic states cross. We located critical points along this seam which included an S_1/S_2 MECI as well as a saddle point on the S_1 surface (S_1-TS) which is the minimum energy geometry in the space of this seam. The energy of the MECI is 31.3 kJ mol^{-1} above the S_1 minimum of the lowest energy conformer, B. The energy of the S_1-TS is at 16.1 kJ mol^{-1} relative to conformer B. Visualising the normal mode corresponding to the only imaginary frequency at the S_1-TS showed synchronization between stretching in the -O-OH coordinate and compression in the C=O coordinate. This highlights that this mode couples the α,β-enone and peroxide chromophores and therefore will be important for describing the reaction coordinate. Furthermore, the remarkably high value of the imaginary frequency (ν_{im} = -3534.1 cm^{-1}) illustrates the sharpness of the (3N-7) seam in the vicinity of the S_1-TS. To visualise this seam, we performed a rigid 2D scan along the -C=O and -O-OH stretching coordinates of C_6-HPALD that correspond to the two coupling chromophores. Results of this scan are shown in Fig. 3.7.

An intrinsic reaction coordinate (IRC) scan initiated at the S_1-TS geometry converges on the dissociated structure and the S_1 minimum of conformer C, as can be seen in Fig. 3.8. Energies, frequencies, and rotational constants at these critical points are tabulated in Appendix A.

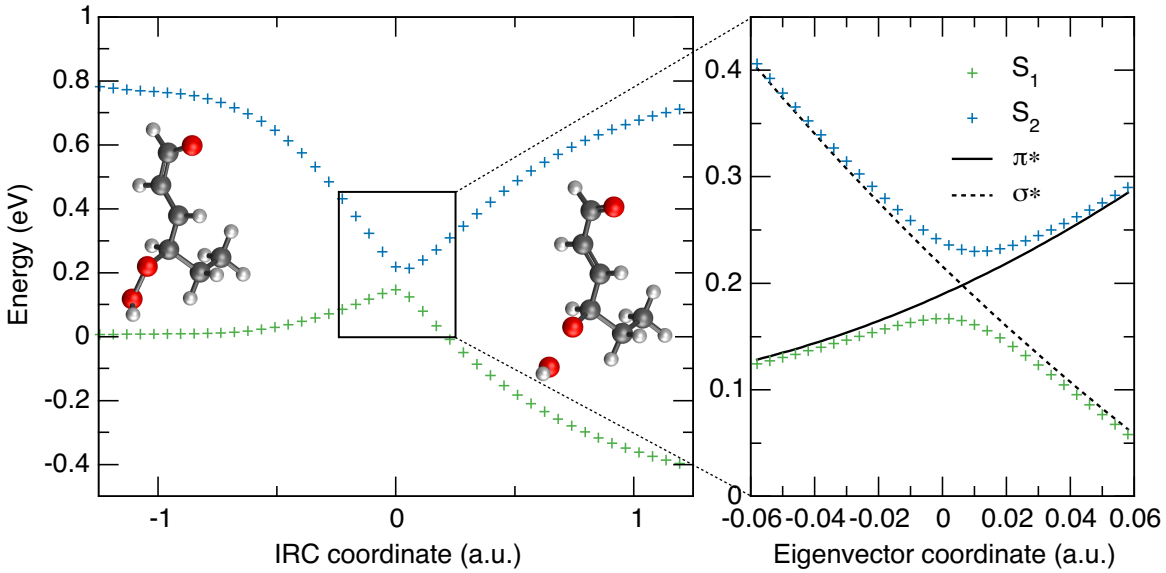

Figure 3.8: Intrinsic reaction coordinate scan started at the S_1-TS. Energy is shown relative to the S_1 minimum of conformer C. Geometries are shown at the terminal step of the IRC scan. Right panel shows a scan across the TS geometry along the eigenvector of the imaginary normal mode. Fitted diabatic states used in the NA-EGME calculation are shown in black.

3.6 Single conformer model

Our exploration of the excited state PES located a direct reaction coordinate between the S_1 minimum of conformer C and the S_1-TS, shown by the IRC in Fig. 3.8. In the following section, we consider a simple photodissociation model based on a potential well (S_1-C) and a single barrier (S_1-TS) linked by this reaction coordinate, that ignores all other C_6-HPALD conformations. We should highlight that the dissociation rate calculated here is distinct from the photolysis rate calculated in section 4.1; it is difficult to obtain a direct experimental measurement of the dissociation rate, given that experimental studies involve a photoexcitation step (and corresponding photoexcitation rate) which prepares the molecule in S_1.

3.6.1 Dynamics

We began the investigation by running 50 A-MD and NA-MD trajectories, whose initial conditions on the S_1 state were sampled from the ground state Wigner distribution of conformer C. The two sets of trajectories shown in Fig. 3.9 are projected on to the -C=O and -O-OH coordinates, illustrating the passage of trajectories across the seam. By observing HPALD dynamics prior to dissociation we see that the molecule remains in the S_1 potential well for a number of vibrational periods and explores the available phase space within its initial conformation.

For all 50 NA-MD trajectories the net adiabatic population remained largely on the S_1 state,

with 90% hopping to the S_2 state at some point during the run. Only a single trajectory hopped to the S_3 state, and no population on S_0 was ever observed. On this timescale we expect that the dynamics are limited to the S_1 and S_2 adiabatic states. In the Franck-Condon region of the PES the S_1 state exhibits $n\pi^*$ character and is near an S_1 PES minimum. A-MD trajectories in Fig. 3.9 indicate that for loss of OH to occur, the -O-OH coordinate must extend in concert with the compression of the -C=O bond, causing the S_1 state to change character from predominantly $n\pi^*$ to the dissociative $n'\sigma^*$ character. The nuclear wavepacket must necessarily proceed across the seam adiabatically, however hopping to the non-dissociative S_2 state can occur.

In Fig. 3.9 we also observe that while many NA-MD trajectories that travel across the barrier rebound back towards the S_1 well, almost all A-MD trajectories which cross the barrier dissociate. In the nonadiabatic case such motion visibly corresponds with a switch to the S_2 state. This mechanism is referred to as diabatic trapping (originally described by Martínez *et al.* as up-funnelling) whereby a trajectory remains on the same diabatic state as it crosses the coupling region thereby preserving its electronic character.[27, 189] Because of this, OH loss is faster for A-MD trajectories since crossing this (3N-7) seam will necessarily lead to a dissociative outcome, whereas in NA-MD the trajectory might become trapped in S_2 and rebound instead. A similar upwards hopping process is observed in the work of Blancafort *et al.* in the bis-adamantyl radical cation that contains two weakly coupled chromophores.[190] We note some similarities between their system and ours, such as the extended near-degenerate seam between two adiabatic states. Qualitatively, we note that diabatic trapping is likely in systems where the conical intersection (CI) branching space vectors are of significantly different magnitude, as is the case here (Available in the SI of the paper).

Next, we consider the rate of dissociation as determined by the dynamics. Three possible outcomes have been observed in the NA-MD results: loss of OH (38 trajectories), loss of HO_2 (9 trajectories), and no dissociative reaction (3 trajectories). The corresponding A-MD results are as follows: loss of OH (45 trajectories), loss of HO_2 (3 trajectories), and no dissociative reaction (2 trajectories). A dissociative outcome is defined as the extension of either the C-OOH or O-OH bond coordinate beyond 1.75 Åand 1.9 Årespectively. Benchmark scans of the PES along these coordinates have shown a potential barrier at 1.65 Å, beyond which the molecule is unlikely to recombine. Dissociating trajectories terminated soon after this nonadiabatic barrier is crossed due to the unreliability of LR-TDDFT in its description of homolytic dissociation. These trajectories are included in the analysis up to the point of dissociation since we can assume that once the bond has extended beyond the threshold, the rate coefficient for reassociation is very small. Loss of HO_2 is a minor dissociative channel which has been suggested experimentally for other peroxides.[191] Its mechanism in C_6-HPALD appears to be linked with diabatic trapping because all NA-MD trajectories terminating in this way show an S_2 to S_1 hop 20 fs prior to dissociation. Given its low probability, and because it cannot be treated with a kinetic model, the HO_2 loss channel is excluded in the following analyses.

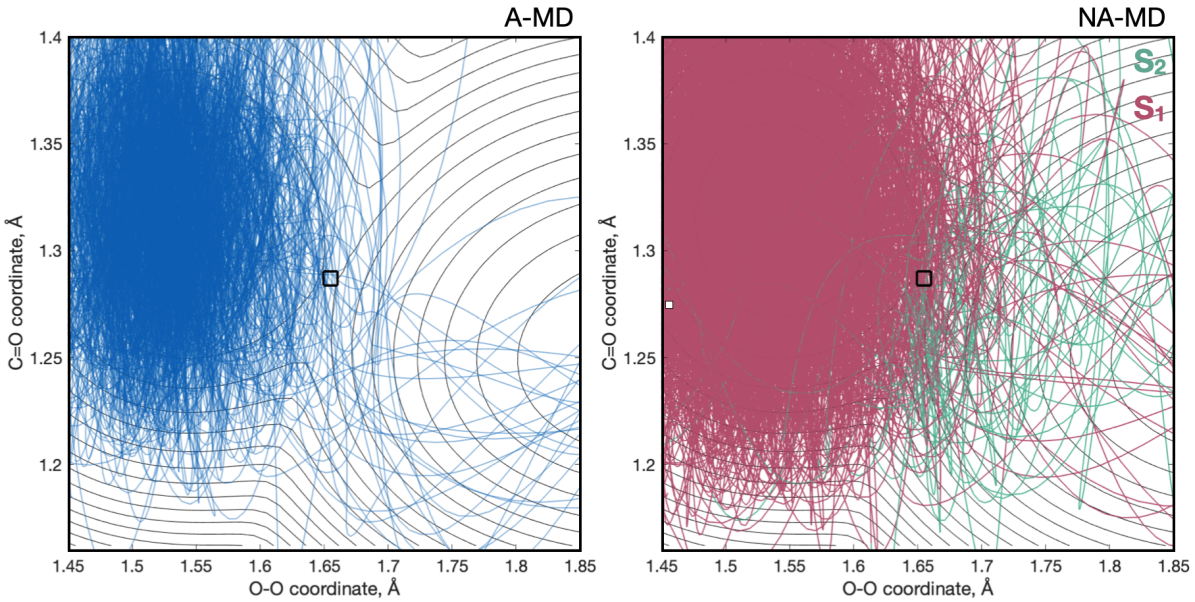

Figure 3.9: Projection of 50 A-MD and NA-MD trajectories of conformer C into the -C=O and -O-OH coordinates. NA-MD panel (right) illustrates the switch from S_1 to S_2 with a colour change. Background contour plot shows the shape of the S_1 PES from a rigid scan initiated at the S_1-TS (indicated by the black square) then scanned across these two coordinates, illustrating the S_1 potential energy well where the trajectories are initialised, and the dissociative potential on the other side of the barrier.

To ensure that the NA-MD result is fully converged we ran another 200 trajectories by using the same 50 initial conditions but inserting a new random seed for the surface hopping algorithm 4 times.[192] In Fig. 3.10 we see that the results are well converged with as few as 50 trajectories. Biexponential fits of HPALD population decay are available in Appendix A. A biexponential least-squares fit indicates that there are two separate decay timescales.[193] The fast decay corresponds to trajectories that dissociated ballistically (OH loss takes less than 200 fs), while others remained in the pre-dissociative S_1 well until the trajectory was able to cross the seam allowing more time for intra-vibrational relaxation to occur. Decay constants for the slow fraction of the decay are 1.87 ps for NA-MD and 1.29 ps for A-MD.

3.6.2 Importance of time step size for an (3N-7) dimensional seam crossing

Running FSSH requires a judicious choice of many parameters, one of which is the time step (dt) with which the classical degrees of freedom evolve on the PES. In most cases, this decision is made by selecting the smallest dt for a given computational cost, to maximise the accuracy of the dynamics. However, what exactly is compromised when dt is too large? For example, the accuracy of the classical integration of nuclear coordinates may be diminished. The more subtle point is that the transition probabilities between states also depend on time discretization.[194]

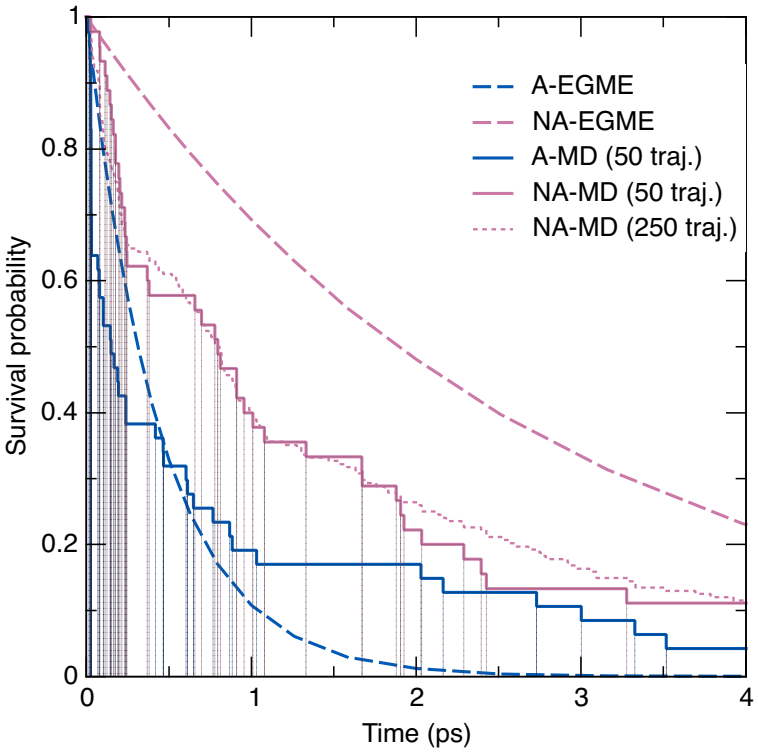

Figure 3.10: Comparison of C_6-HPALD decay rate between EGME and trajectory-based methods for conformer C. Convergence of NA-MD at 50 trajectories indicated by the similarity to the 250 trajectory result.

At each time step the time derivative coupling (TDC) is calculated to determine if a hop to another adiabatic state occurs and when TDC is very localised it can be poorly resolved, or missed altogether.

Meek *et al.* highlighted this problem for trivially unavoided crossings (TUC)[195] which are (3N-7) dimensional intersections between two weakly coupled states, where N is the number of nuclear degrees of freedom. If the coupling between the states is infinitesimal, a crossing trajectory must necessarily remain on the same diabatic state. As it passes through the seam there would be a sudden narrow spike in the TDC which might not be resolved with a larger dt, and so the trajectory will, incorrectly, move to a different diabatic state. For (3N-8) dimensional conical intersections this problem is less significant, as the nonadiabatic coupling is highly localised in position space.

In this case, the topology of the C_6-HPALD seam can be described as a TUC as there is an effective (3N-7) crossing at the intersection of the $n\pi^*$ and $n'\sigma^*$ diabatic states with a weak nonadiabatic coupling between them. Slowness of the dissociation process limits us in how small the time step can be, but it becomes necessary to verify the extent to which this might affect the outcomes of the FSSH dynamics.

Although the loss of OH typically takes picoseconds, many trajectories encounter the (3N-7)

seam in the first 50 fs of the simulation. It is then possible to explore how the shape of the TDC is affected by the time step and to see if the spike in TDC is too sharp to detect with dt=0.5 fs. Three example trajectories were taken from the set initiated at conformer C, and repeated for 50 fs using identical initial conditions for dt = 0.25; dt = 0.1 fs; dt = 0.05 fs; dt = 0.025 fs. Results are shown in Fig. 3.11. In this figure we see the results converging with progressively smaller values of dt. Ideally, the trajectories should be ran with at least a 0.1 fs time step to properly capture the shape of the TDC, however the computational cost of doing this is prohibitive. Luckily, the peak is still present for 0.5 fs time step trajectories, even though they are visibly more coarse.

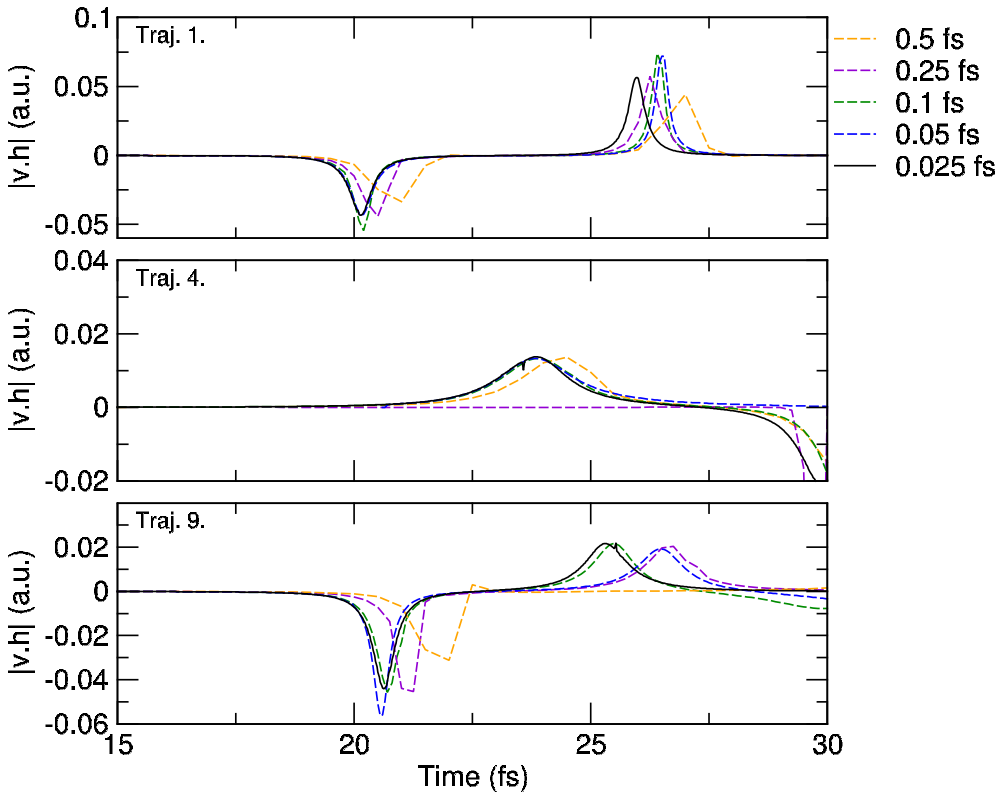

Figure 3.11: Convergence of time derivative coupling with time step size for three example trajectories in the first 30 fs of the simulation.

Most trajectories encounter this seam multiple times, so it is still possible that the error in the shape of the TDC peak for 0.5 fs time step may affect the long term dynamics of OH loss in HPALD. Full length trajectories were ran to look for trends in dissociation behaviour between dt = 0.25 fs and dt = 0.5 fs. For each of a set of 3 IC, we ran 20 replicas which were seeded with a different random number. Results can be seen in Fig. 3.12. These results appear to indicate that the time step size makes no systematic difference to the rate of OH loss and so on this basis we conclude that it is safe to use a 0.5 fs time step for FSSH dynamics.

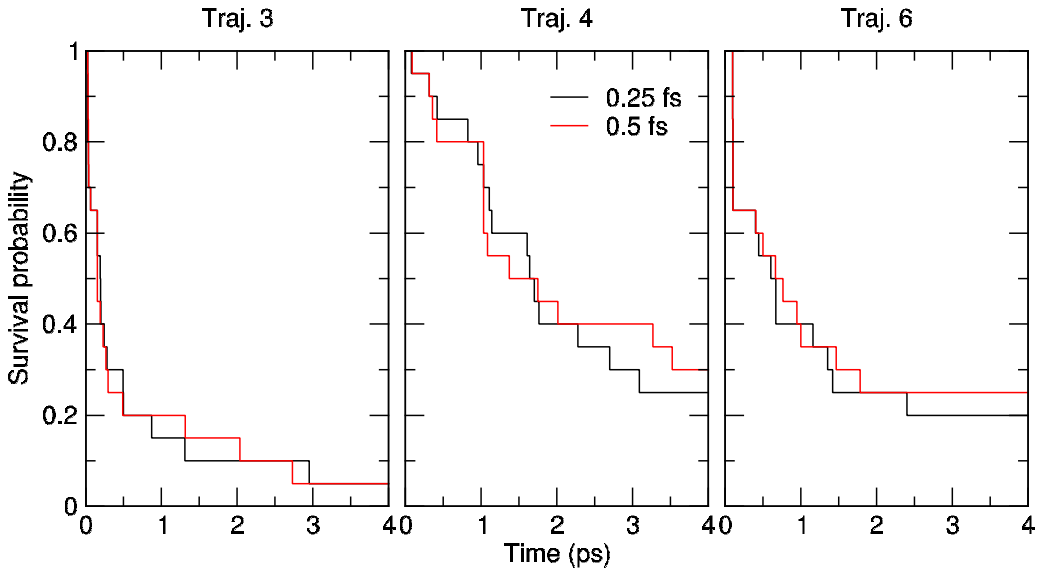

Figure 3.12: Impact of time step size on the rate of OH loss in HPALD.

3.6.3 NA-EGME

Our NA-EGME model assumes that to describe the primary photodissociation channel leading to the loss of OH we need only to consider the $n\pi^*/n'\sigma^*$ state coupling along a 1-D coordinate over the top of the TS. This necessitated only a normal mode analysis at the S_1 minimum of conformer C (S_1-C) and the S_1-TS barrier which is energetically 14.13 kJ mol^{-1} higher. The optimised MECI is 15.2 kJ mol^{-1} above the S_1-TS. The 3N-7 dimensional geometry of the nonadiabatic seam means the MECI is unlikely to be an important critical point since the molecule does not need to pass through it to reach the S_2 state. For this reason, the MECI's influence on the dissociation rate can be neglected and we choose not to include it in the model. Total energies of the 50 initial conditions are normally distributed with the average initial energy at 453.4 kJ mol^{-1} above the S_1-C minimum. This energy corresponds to the 758th grain in the population vector $n(E,t)$ and so, the EGME calculations were initiated with 100% of the population in this energy grain.

The HPALD decay rates calculated using A-EGME and NA-EGME are presented in Fig. 3.10, illustrating that the photodissociation rates obtained with the trajectory-based approaches are qualitatively similar to those obtained from EGME models, and more importantly that both strategies capture the effect of diabatic trapping. Including nonadiabatic effects slows down the decay rate approximately 6-fold ($\tau_{NA-EGME}$ = 2.72 ps) in comparison to the rate calculated when nonadiabaticity is neglected (τ_{A-EGME} = 0.45 ps). The decay rate is shown to be robust to the initial energy grain distribution and small variations in frequencies by the sensitivity analyses provided in Appendix A.

3.7 Full conformational analysis of C_6-HPALD

Now that we have shown for the conformer C that both NA-EGME and NA-MD results capture the effect of diabatic trapping during the OH photodissociation process, we will extend this simple model to include all conformers of C_6-HPALD highlighted in Fig. 3.4. For the dynamics calculations we simply projected the ground state conformer distribution into the excited state such that the set of trajectory initial conditions was representative of the rotamer distribution. Boltzmann weights of the A-G conformers determine the number of trajectories to be run for each. For TST-type methods like EGME, molecular torsions can be challenging because the rigid rotor approximation breaks down due to the highly anharmonic hindered rotor modes. Ideally, each conformation and its corresponding TS should be treated separately.[196] However, for 7 rotational conformers this approach would necessitate a cumbersome search for 30 separate TSs in a 3N dimensional phase space. Instead, we propose a pared down model that uses the global conformer minimum (S_1-B) and the S_1-TS to calculate the OH loss rate.

3.7.1 Dynamics

The relative numbers of trajectories sampled from each conformer corresponds to their Boltzmann weight in the ground state calculated using CCSD energies: A: 24; B: 50; C: 5; D: 16; E: 3; and F: 11.

Dihedral angles ϕ_1 and ϕ_2 can be used as a shorthand to distinguish the conformers over the course of a trajectory. This can be seen in figure 3.13 which shows all of the dissociating trajectories exploring the rotational phase space, and highlighting the fact that internal rotations are not fast on this timescale. Trajectories corresponding to conformers C and F especially tend to remain conformationally locked, which supports our previous assumption that conformer C could be treated independently. There is a flux of trajectories from conformer B to C suggesting that the rotational barrier towards C is small.

Of the 109 FSSH trajectories initiated on the S_1 state we observed the following outcomes: loss of OH (50 trajectories), loss of HO_2 (15); no dissociation (43). Corresponding result of the AIMD simulations are as follows: loss of OH (82), loss of HO_2 (10), no dissociation (17). The 95% margin of error is shown by the error bars in Fig. 3.14 c) illustrates that the difference between dissociative outcomes is significant.

Analysis of the mean adiabatic population shows that on average it remained on the S_1 surface, rarely falling below 95%, with a fraction of population moving in to the S_2 state. Very few trajectories hopped into the S_3 state and no population of the S_0 state was observed on the timescale of the simulation. Survival probability is fitted to an exponential decay, with a first order lifetime, τ_{NA-MD}, of 4.6 ps. A-MD dynamics of OH loss are better fitted to a double exponential, shown in Fig. 3.14 d). Approximately a quarter of A-MD trajectories are dissociated on a fast timescale with a lifetime, τ_{fast}, of 58 fs. The rest of the trajectories dissociate on a

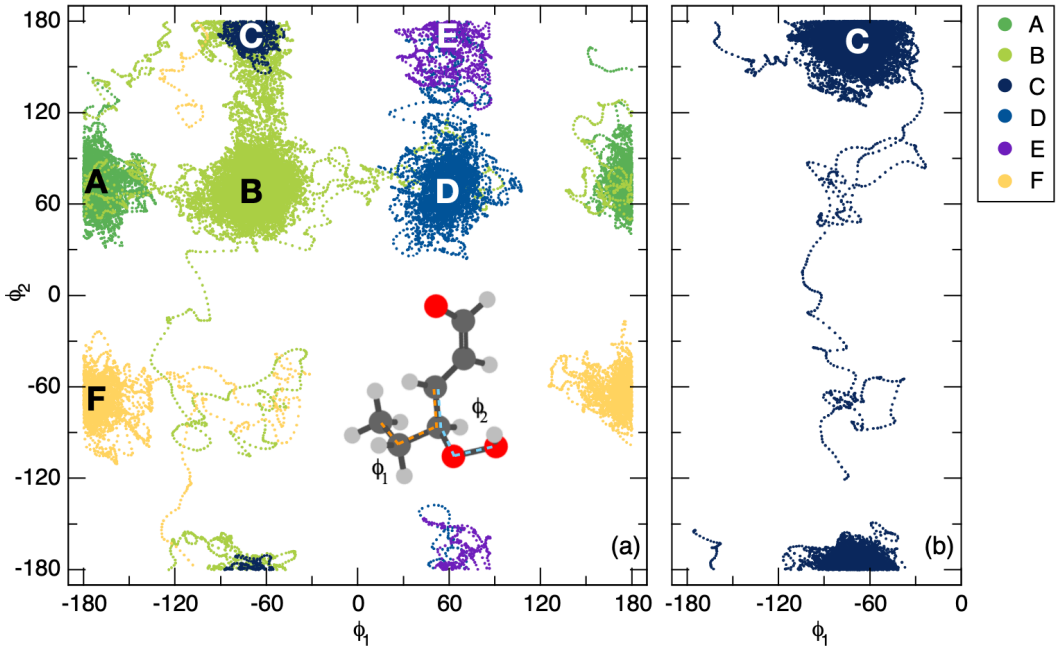

Figure 3.13: HPALD conformer interconversion over a 4 ps timescale. Left panel shows the evolution of the two dihedral angle coordinates ϕ_1 and ϕ_2 that define the conformation of the HPALD molecule at a given time step for all 109 FSSH trajectories. Right panel shows 50 trajectories of conformer C only.

similar timescale to the NA-MD simulations with lifetime, τ_{slow}, of 2.4 ps.

3.7.2 An all-conformer NA-EGME model of OH loss

Now that we have the results of trajectory dynamics initiated from a realistic ground state conformer distribution, we can construct a new, more realistic, NA-EGME model. Since a large fraction (50 out of 109) of the trajectories were initiated from the conformer B initial condition we use its S_1 minimum as the reactant well (S_1-B) and the S_1-TS. The average initial energy of these trajectories was at 487.0 kJ mol^{-1} above the S_1-B minimum corresponding to the 814th energy grain in the population vector $n(E,t)$. Results of the NA-EGME calculations based on this model are shown in Fig. 3.15. We see that including nonadiabaticity once again has a strong effect on the microcanonical rate coefficients shown in the inset. The nonadiabatic lifetime $\tau_{NA-EGME}$ is 1.7 ps, once again approximately 6 times greater than the adiabatic lifetime, τ_{A-EGME} = 0.3 ps.

We have tested the importance of torsional anharmonicity using the hindered rotor approach, as implemented in MESMER. This sensitivity analysis ensures that the presence of anharmonic rotational modes does not significantly alter the ratio of densities of states, and the corresponding decay constants. Normal mode frequencies corresponding to torsional motion were projected out of the Hessian.[197] Results of rigid torsional scans performed over 4 torsional bonds at the S_1-B

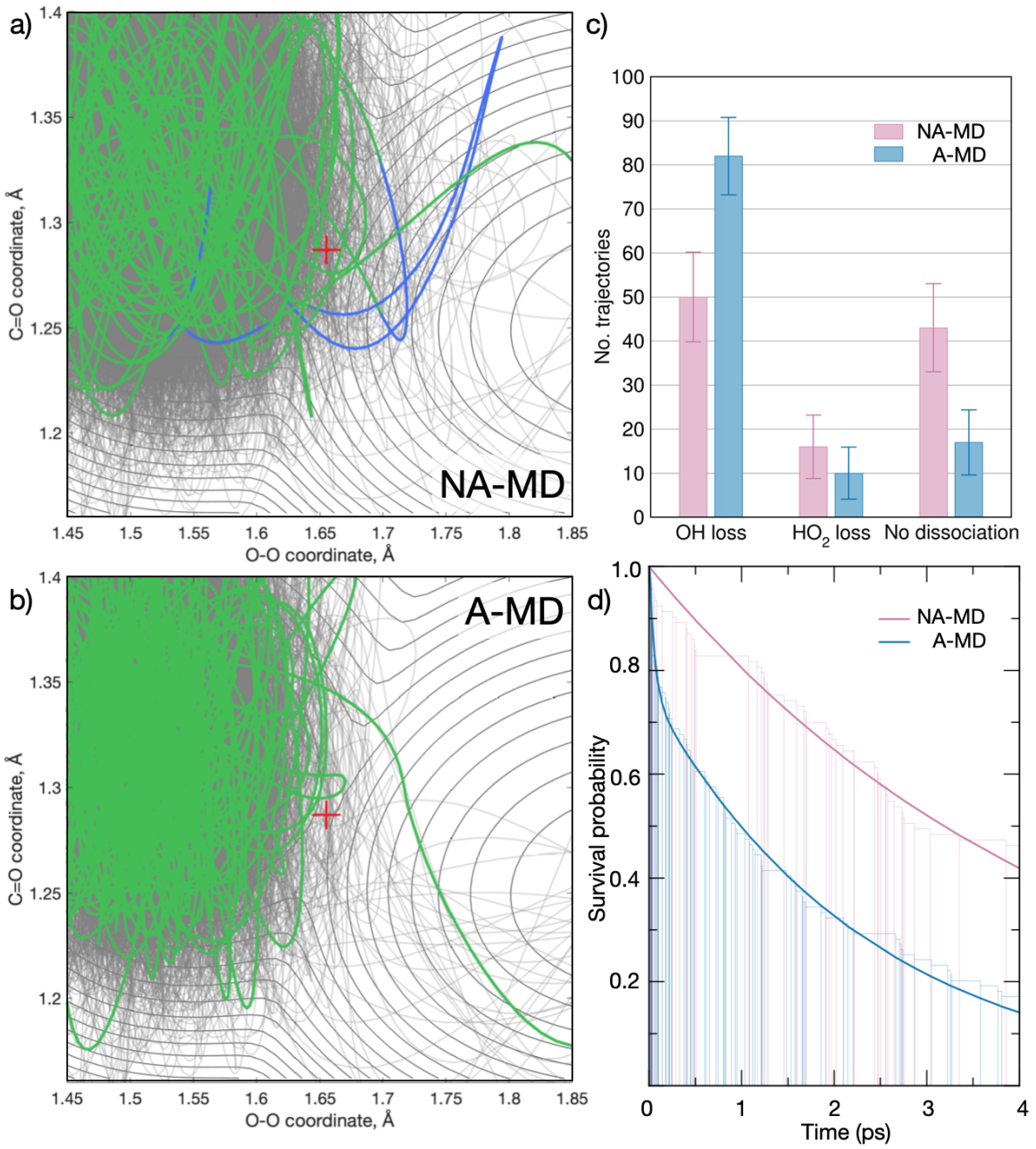

Figure 3.14: Dynamics results for all conformers of C_6-HPALD. a) An example of a diabatically trapped trajectory where the switch to S_2 is illustrated by a colour change. b) Example A-MD trajectory that moves in the S_1 well for a number of vibrational periods before crossing the barrier and dissociating immediately. c) Outcomes of the 109 trajectories with 95% confidence intervals showing that differences between NA-MD and A-MD are significant. We calculate the error for a sample proportion as $Z\sqrt{(p(1-p)/n)}$ where p is the proportion of trajectories with given outcome, n is the number of trajectories, and Z the multiplier giving the 95% confidence interval. d) Survival probabilities with respect to OH loss, fitted to exponential decay functions.

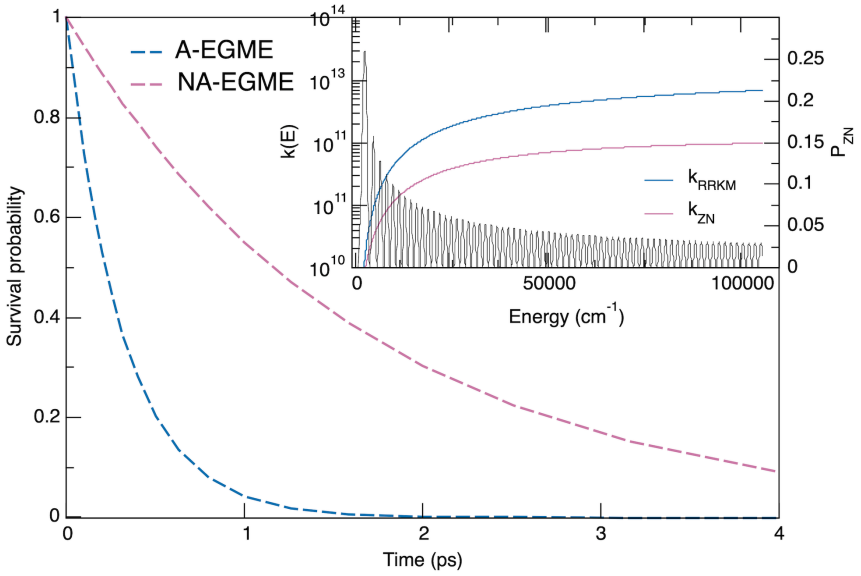

Figure 3.15: Results of EGME calculations, with microcanonical rates calculated using an adiabatic (A-EGME) and a nonadiabatic (NA-EGME) expression. Inset shows the energy resolved microcanonical rate constants (k_{RRKM} and k_{ZN}) and the ZN transition probability (black line).

minimum and S_1-TS geometries were input into the MESMER calculation. Results available in Appendix A show that incorporating these torsional effects does not significantly impact the reaction profiles. We suggest this could be due to the similarity between torsional profiles at the S_1 minimum and TS geometries that result in a cancellation of errors.

An implicit assumption in this treatment of hindered rotations is that rotamer interconversion is fast on the reaction timescale. However, conformational analysis of the trajectories in Fig. 3.13 shows that while internal rotations are present, they are not fast. For this simplified model we make an approximation to consider only the global S_1 minimum (S_1-B) and a single lowest point on the (3N-7) seam (S_1-TS). Similarity between the frequencies and rotational constants of the conformers suggest that this is an acceptable compromise in this case.

3.7.3 Improving NA-EGME with CASPT2 energies

Our NA-EGME model could be improved by the addition of all inter-conformer transition states. However, the need to search for each critical point on a 3N dimensional PES can undermine the simplicity of the approach proposed here. Instead, we can exploit the comparatively low computational cost of the EGME calculations by using energies calculated with a more sophisticated, multireference, electronic structure method at the stationary points. By assuming that the locations of the stationary points optimised with LR-TDDFT give a broadly accurate representation of the PES, the model can be adjusted by using MS(4)-CASPT2(10,8)/6-31G* energies (with LR-TDDFT frequencies and rotational constants) to calculate the population profile of

HPALD over time. Results of this scan are shown in Fig. 3.16. New parameters are used in the ZN equations, based on the fitting of diabats to new MS-CASPT2 energies calculated across the same eigenvector coordinate as in the earlier calculation.

Results of NA-EGME calculations based on MS-CASPT2 energies show that the difference between the nonadiabatic and adiabatic rates is more significant than that produced using TDDFT/PBE0 energies. The adiabatic lifetime of HPALD is τ_{A-EGME} = 0.44 ps whereas the nonadiabatic lifetime, $\tau_{NA-EGME}$ = 30 ps, is 70 times slower. Nonadiabatic coupling between the states is weaker increasing the likelihood of transition to the S_2 state illustrating the sensitivity of the coupling strength to the selected electronic structure method. To improve the quality of the model, accurate multireference methods – often too expensive for on-the-fly excited state dynamics – must be used. In this section we showed how they can be built in to the EGME approach.

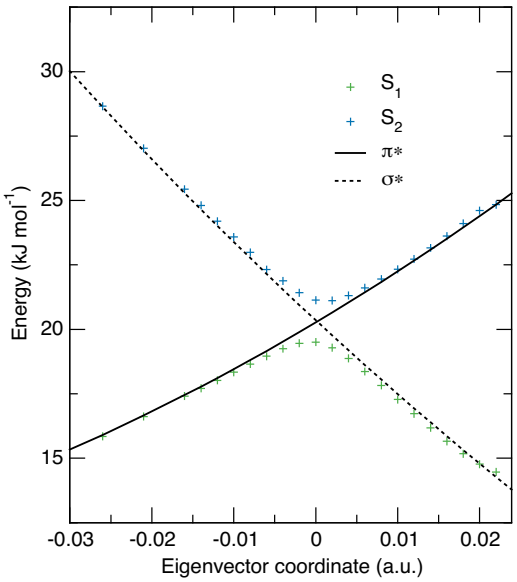

Figure 3.16: Diabatic potentials fitted to PES scan across eigenvector calculated with MS(4)-CASPT2/6-31G*

3.8 Discussion

The most direct comparison between the two approaches can be seen in the models that isolate conformer C. Fig. 3.10 demonstrates the remarkable similarity between the results of trajectory-based methods and EGME: the NA-MD photodissociation lifetime τ_{NA-MD} = 1.9 ps is comparable to the NA-EGME lifetime $\tau_{NA-EGME}$ = 2.7 ps. The impact of nonadiabatic effects on the photodissociation rate is stronger in the EGME results: the calculated adiabatic lifetimes are τ_{A-EGME} = 0.5 ps and τ_{A-MD} = 1.29 ps. A direct comparison between the decay rates in the extended

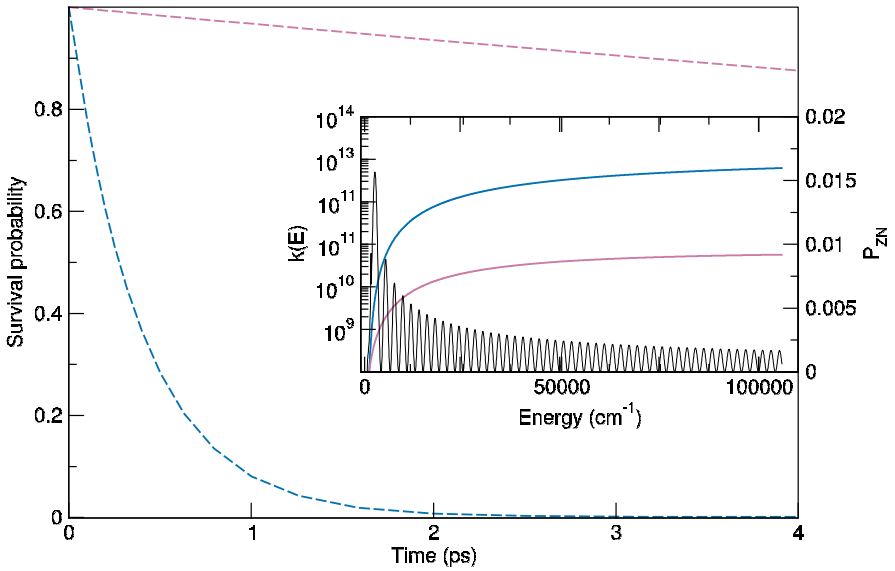

Figure 3.17: Result of EGME calculation using MS(5)-CASPT2(10,8) energies at the critical points. Inset shows the microcanonical rate coefficients across the state vector in the nonadiabatic and RRKM cases, with the ZN transition probabilities.

models that include all conformers can be seen in Fig. 3.18. Nonadiabatic EGME and NA-MD methods returned lifetimes differing by less than factor of 3: $\tau_{NA-EGME}$ = 1.7 ps and τ_{NA-MD} = 4.6 ps. That these results match to within an order of magnitude is remarkable given the stark differences between the two approaches. For the adiabatic simulations the comparison is made with the slow component of the fitted decay, with τ_{A-EGME} = 0.31 ps and τ_{A-MD} = 2.4 ps, out by less than a factor of 8. Trajectory surface hopping simulations indicate that a diabatic trapping mechanism is responsible for this deceleration as it causes the nuclear wavepacket to be trapped in a bound diabatic state, preventing direct dissociation. To quantify the impact of nonadiabatic effects at the seam, we compare the ratios of the nonadiabatic/adiabatic lifetimes for both the dynamical and the master equation approaches. We note that Plasser *et al.*[28] showed, in the context of surface hopping and Landau-Zener probabilities, that the difference between the adiabatic and nonadiabatic rates in diabatic trapping processes can be related to the electronic transmission coefficient. This value is 1.9 for the trajectory methods, and 5.5 for the kinetic model. The difference may arise in part from the assumption within the EGME model that allows for only a single seam crossing. Formulations of LZ transition probability that allow for multiple recrossing of the seam have been developed, notably by Delos and Nikitin[198, 199] and could be applied to this method in future work. Another fundamental difference is that EGME is a statistical method which assumes that the system is ergodic – i.e. energy has no preference for residing in a specific mode and can be instantaneously exchanged with all of the available modes in a particular molecule. The accuracy of the ergodicity assumption typically

applies to timescales longer than 4 ps. For any dynamical approach at short timescales (including excited-state dynamics), the energy is likely to be distributed in a non-Boltzmann way due to the out-of-equilibrium nature of the dynamics following photoexcitation, and the fact that the timescale for energy redistribution amongst intramolecular modes is finite. Unlike a dynamical approach in which excited-state trajectories can explore different regions of the intersection space, the EGME is ignorant of the broader PES topology, given that the crossing can only occur at the TS along the defined one-dimensional coordinate. We finally note that nonadiabatic tunnelling effects are built-in to the Zhu-Nakamura formulas.

It is also important to highlight that the excited-state dynamics performed here assume the formation of a nuclear wavepacket upon light absorption. Such initial conditions corresponds to a scenario where the molecule is photoexcited by an ultrashort laser pulse, rather than continuous irradiation with sunlight as it would happen under atmospheric conditions. The question of selecting proper initial conditions for the excited-state dynamics of atmospheric molecules is discussed further in Suchan *et al.*.[200] A protocol aiming at simulating sunlight absorption processes was also recently proposed.[201] In the context of this work, this assumption does not affect the comparison between the EGME models and the dynamics, but does limit the claims we can make about the atmospheric implications of our results.

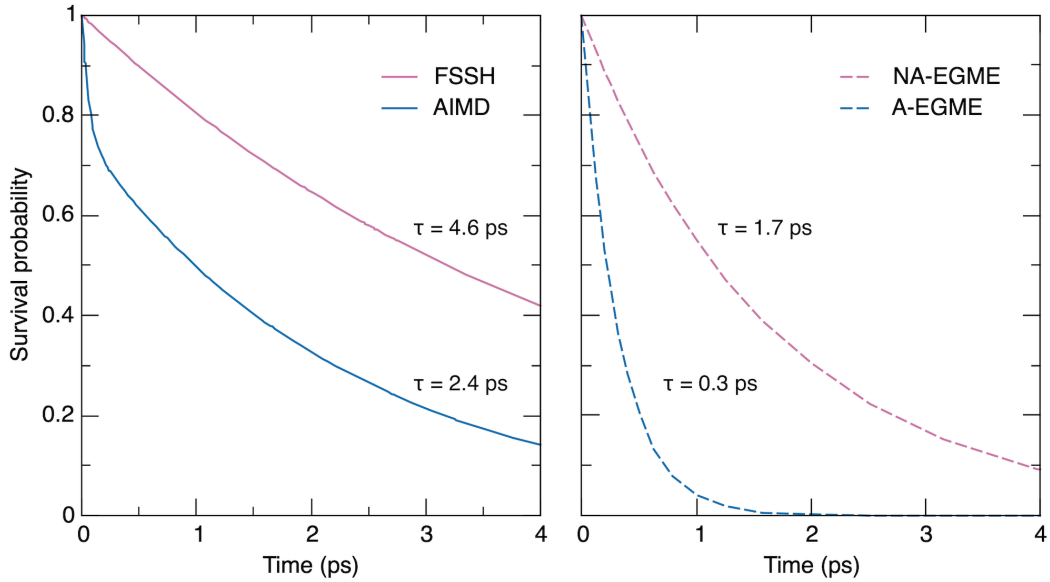

Figure 3.18: Side-by-side comparison of the two models used to calculate the dissociation rate for C_6-HPALD. The fit to the population decay is presented for both NA-MD and AIMS.

In this chapter we aimed to validate a nonadiabatic EGME model against NA-MD by calculating the rate of OH loss in C_6-HPALD, which has been experimentally investigated by Wolfe *et al.*[154] We highlight the approximations made in the construction of the master equation model and outline how this model can be improved. Many features of the C_6-HPALD dissociation process

seem to justify these approximations. This includes the picosecond timescale of photodissociation; ease of energy exchange between the many modes of HPALD; the (3N-7) geometry of the seam which makes the 1-D seam crossing model appropriate. Of course, the exploratory value of running dynamics simulations cannot be superseded by a model that requires existing knowledge of important stationary points. Without performing the NA-MD calculations the diabatic trapping mechanism would not have been identified. Nonadiabatic transitions are ultimately caused by nuclear motion and so atomistic simulations are necessary for an accurate description of wavepacket dynamics. However, when nonadiabatic transitions between excited states occur on a slow timescale we are limited by the computational cost of running long trajectories and using the NA-EGME model allows us to refine the energies of the critical points whilst reproducing the overall impact of diabatic trapping on the photodissociation rate. The NA-MD calculations are without any doubts more computationally expensive than the NA-EGME approach and would scale less favourably with the number of nuclear degrees of freedom. In instances of slow photodynamic reactions with known mechanisms, alternative models might be explored before choosing to run trajectory dynamics.

The workflow to perform a nonadiabatic EGME analysis on this type of crossing can then be summarised as follows. 1. Locate and characterise the critical points on the excited state PES. These include the bound minima near the Franck-Condon region, the conical intersections, and the adjacent transition states. 2. Identify the normal mode at the crossing point that corresponds to the exciton moving from one chromophore to the other. 3. Perform a scan across this normal mode and fit the shape of the crossing point to a 1-dimensional analytical model. 4. Construct an EGME model of the seam crossing, using the fitting parameters obtained in step 3 for ZN transition probabilities. This utility is currently implemented in MESMER.

These findings describe a type of crossing between adiabatic surfaces that is intermediate to the traditional representation of a two-cone type conical intersection (Fig. 3.19, left panel) and a fully degenerate seam one might see in the context of intersystem crossing (Fig. 3.19, right panel). The protocol described here is applicable when calculating rates for this type of trivially unavoided crossing i.e. when collapsing the reaction coordinate to a single dimension is appropriate. These coordinates could be identified through principal component analysis of trajectory dynamics.

3.9 Conclusion

We directly compared the performance of NA-MD to that of a nonadiabatic EGME model by conducting two side-by-side studies of C_6-HPALD photodissociation. Both methods establish that the nonadiabatic coupling at the extended seam is significant and reduces the rate of OH loss. The lifetimes of C_6-HPALD based on these fundamentally different models indicate that a reduced dimensionality NA-EGME treatment for avoided crossings can reproduce results of dynamics to

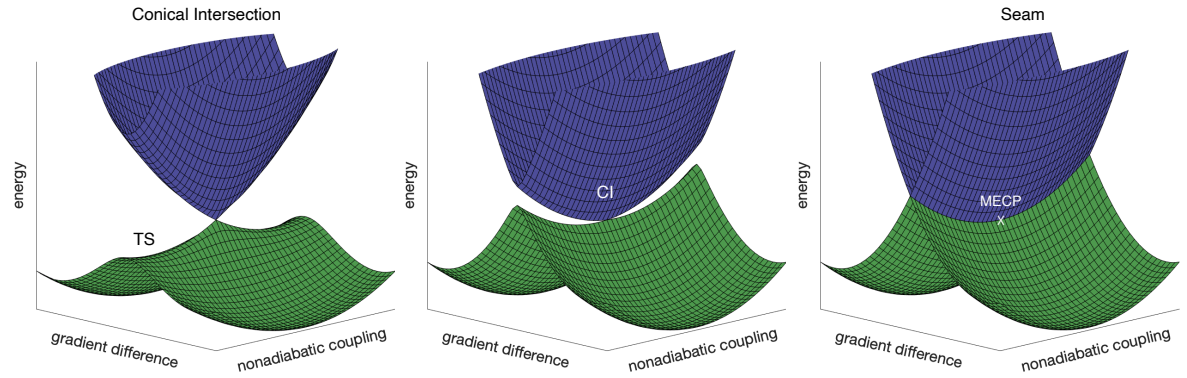

Figure 3.19: Types of crossings between electronic states

within an order of magnitude. Further work is needed to investigate the rate of intra-vibrational relaxation between all modes, so as to determine the exact limits of the regime where this kind of protocol can be applied. Similarity between the dynamic and EGME results also raises the question of timescale, since intra-vibrational relaxation must be fast to satisfy the key assumption of RRKM theory. It is unclear whether this is satisfied in this case, and so merits further work to investigate the energy redistribution between modes prior to the dissociation. Some purely dynamical features such as loss of HO_2 could not be included in an EGME treatment, and merit further exploration to determine the significance of HO_2 loss to the atmospheric mechanism. Alongside the significant improvement in computational cost we highlight that approaching this photodissociation mechanism from both the kinetic and the dynamic perspective offers insights into different aspects of the dissociative process.

CHAPTER 4

PHOTOCHEMISTRY OF HPALDS

The purpose of this chapter is to explore the atmospheric importance of hydroperoxy aldehydes (HPALDs) using the computational tools developed in previous chapters. They will be used to answer questions about its atmospheric properties and the strength and weaknesses of these conclusions will be considered. Firstly, I will review the literature in atmospheric chemistry to discuss the role HPALD plays in the complex mechanism of isoprene oxidation first proposed by Peeters *et al.* in 2009.[24] This will help to highlight the uncertainties that remain regarding the mechanism of HPALD production and loss. I will then use the best possible methods to calculate a reliable UV-Vis spectrum for two isomers of HPALD following the protocol described in chapter 2, and use these spectra to predict their photolysis rates. Then the mechanism of HPALD photodissociation is described, which was determined based on mixed quantum-classical dynamics simulations described in the previous chapter. Lastly, I address the difficult question of initial conditions in excited state dynamics initiated by sunlight and consider the existing literature which addresses this issue.[201]

4.1 Atmospheric photolysis in isoprene chemistry

Terrestrial vegetation releases substantial quantities of volatile organic compounds (VOCs) into the atmosphere. Subsequent oxidative reactions of these VOCs have a significant knock-on effect on the atmospheric oxidation capacity, air quality, and the carbon cycle. In quantitative terms, one of the most important VOCs is isoprene, 500 teragrams of which is released yearly, mainly over tropical rainforests. The foremost oxidant in the atmosphere is the hydroxyl (OH) radical which is formed primarily through ozone photolysis. Hydroxyl radicals are known to be important in the removal of gaseous pollutants from the daytime atmosphere and are colloquially referred to as the "detergent" of the atmosphere.

It had been previously assumed that biogenic VOCs such as isoprene would deplete hydroxyl radicals and hence the oxidative capacity of the atmosphere.[202–204] However, unexpectedly high concentrations of the OH radical have been detected in field studies over the Amazon rainforest where biogenic isoprene is released in large quantities. An example of this would be the aircraft measurements performed by the GABRIEL campaign which measured HO_x concentrations of 5.6×10^6 cm^{-3}, which were 5-10 times higher than those predicted by the original Mainz Isoprene Mechanism (MIM).[150, 205]

To reconcile these differences Taraborrelli *et al.* suggested that atmospheric hydroxyl concentrations are buffered via an oxidative mechanism involving a product of isoprene oxidation.[151] Such a mechanism must have a total HO_x recycling efficiency of 40-80% through the breakdown of isoprene-derived peroxy radicals.

In 2009, Peeters *et al.* [24] proposed a mechanism of isoprene oxidation that aimed to rationalise higher hydroxyl concentrations in low nitric oxide (NO_x) regions. The first Leuven Isoprene Mechanism (LIM0) was proposed based on a purely computational argument, using DFT and MP2 energies combined with multi-conformer transition state theory to determine reaction rates. A theoretical re-evaluation of the mechanism by Peeters *et al.* in 2014[153] extended the reaction network and recomputed energy barriers and partition functions with higher level electronic structure methods. This newer mechanism was labelled as LIM1. Calculated rate coefficients for these reactions are published as part of the LIM1 mechanism. These findings have already been integrated into the Master Chemical Mechanism (MCM v3.3.1), however it altered some rate constants to account for results obtained by Crounse *et al.* in 2014. A more recent study by Wennberg *et al.* in 2018 re-parametrised the mechanism once more[206] to fit with emerging experimental evidence.[207]

As part of this mechanism, Peeters *et al.* postulated one of the OH recycling processes happens via the photon absorption by the α,β-enone chromophore of an unsaturated hydroperoxy aldehyde (HPALD). Absorbing sunlight in the 290-370 nm range would prompt an ($n\pi^*$) excitation of the enone chromophore to its singlet S_1 state. Peeters *et al.* initially suggested that this excitation would result in a fast internal conversion to a vibrationally excited S_0 state, leading to the homolysis of the peroxide bond faster than the rate of vibrational relaxation.[24] However, in their 2010 paper Peeters *et al.* suggest a faster and more efficient photolysis mechanism which proceeds via an avoided crossing between the bound S_1 state on the enone chromophore and the repulsive S_2 state on the peroxide group.[149] They postulated that there is a low-lying transition state for RO–OH dissociation on the S_1 surface which acts as an energetic barrier to homolysis. A crossing would lead to lysis of the weak peroxide bond and produce a hydroxyl radical with an alkoxy radical co-product. This photodissociation would, at least in part, reconcile the discrepancy in the measured hydroxyl radical concentration and that predicted by atmospheric models.

4.1.1 HPALD formation in the atmosphere

The importance of the HPALD channel in the process of isoprene oxidation has been contested in the literature.[24, 207, 208] To better understand it's role, the oxidative process by which HPALD is generated in the troposphere will be briefly described here. The full reaction scheme is presented in Fig. 4.1. The reaction is initiated by the addition of an OH radical at the terminal carbon of an isoprene molecule, and an O_2 molecule, forming six OH-Iso-O_2 adduct species that can interconvert rapidly. The concentrations of these six species are in an equilibrium, and each is depleted by unimolecular decomposition or further reaction with HO_x, NO_x, and RO_x radicals. Some of these radical species can directly reform hydroxyl radicals via a 1,5 hydroxy-hydrogen shift which forms oxygenated organic side products including methacrolein (MACR), methyl vinyl ketone (MVK), and formaldehyde (HCHO). Two of the six radical intermediates referred to as Z-δ-OH-peroxy I and II in the LIM1 paper can perform a 1,6-H shift followed by O_2 addition at two possible positions. Early papers on this mechanism assumed a 100% yield of HPALD following this 1,6-shift[24, 208] but when Peeters *et al.* updated their mechanism in 2014 they suggested an alternative reaction pathway to dihydroperoxy-carbonyl peroxy (di-HPCARP) radicals. After di-HPCARP radicals were predicted in theoretical calculations by Peeters in 2014[153] they were observed experimentally by Teng *et al.* in 2017.[207] Hydroxyl radicals and other products may then be recovered from di-HPCARP via a fast aldehydic hydrogen shift.[209] The other product is an unsaturated hydroperoxy aldehyde suggested to regenerate OH radicals via a photolytic dissociation. HPALDs are a set of compounds which contain both an α,β-enone chromophore and a labile peroxide bond. Formation of HPALDs has been observed in numerous experiments [207, 208, 210, 211] and they have been shown to produce OH radicals under UV light.[154]

The product yield of HPALD relative to di-HPCARP has also been contested. The LIM1 mechanism and MCM v3.3.1 use a 50:50 ratio for these two products, whereas Wennberg *et al.* put it at 60:40 in favour of di-HPCARP.[206] Teng *et al.* suggested an HPALD yield around 0.4, split 0.15:0.25 between β- and δ-HPALDs.[207] However, new experimental work by Berndt *et al.*[211] suggests an HPALD yield as high as 0.75, and Möller *et al.*[212] speculate that the low yield observed by Teng *et al.* can be explained by its loss on the walls of the sample tube. In summary, the main uncertainties in this mechanism include: the temperature dependent rate constant of the 1,6 H-shift of the Z-δ-OH-peroxy radical; product ratios following the 1,6-H shift; reactivity following on from HPALD or di-HPCARP formation.

Recently, Novelli *et al.*[209] performed high level calculations (CCSD(T)/aug-cc-pVTZ) that explored the reactions of di-HPCARP and its role in OH formation. They find that its main reaction channel is the migration of the aldehyde H followed by fast CO loss, leading to an unstable alkyl radical that will eliminate an OH radical to form di-hydroperoxy methyl vinyl ketone (DHP-MVK). This reaction channel was included in the model, however a notable result in this study was that varying the yield of HPALD from 0.4 to 0.75 in model calculations made no meaningful difference to the results. This could be because both HPALD and di-HPCARP produce

hydroxyl radicals and CO quickly (on a 1 hour timescale) and in a similar ratio, even though they proceed by quite different mechanisms. If this is the case, the main question that remains is the mechanism and rate of HPALD photodissociation.

4.1.2 Evidence for HPALD photolysis

The LIM1 mechanism assumes that HPALD cleanly dissociates to produce an OH radical, with an overall yield of 1.65 OH per HPALD molecule.[206] In the original LIM0 mechanism the rate of HPALD photodissociation was estimated at 3.5×10^{-4} s^{-1} which would mean an atmospheric lifetime of 30 – 180 minutes.[149] Breaking of the -O-OH bond was suggested to occur following internal conversion to a vibrationally excited S_0 state as described in section 4.1. Later work amended this mechanism of hydroxyl regeneration, supposing it to occur via an avoided crossing on the S_1 state, with the exciton transferring to a repulsive state whose character is localised on the peroxide chromophore.[153] By using a comparison to a $MeCO_2H$ potential along the RO-OH stretching coordinate, the height of this energy barrier was estimated to be around 8 kcal/mol. The photolysis rate was estimated to be on the order of 5×10^{-4} s^{-1}, based on the average absorption cross sections of MVK and MACR which have a similar α,β-enone chromophore to HPALD, and which would absorb sunlight in the 270-380 nm range.

These estimates were corroborated by controlled reaction chamber photolysis studies performed by Wolfe *et al.*[154] on a six-carbon HPALD proxy, C_6-HPALD, whose photolysis mechanism was described in the previous chapter. Because of its low vapour pressure, gas phase UV-Vis spectra of C_6-HPALD could not be measured directly. Instead, an averaged UV-Vis spectrum of three analogous molecules containing an α,β-enone chromophore was used to calculate rate constants. The uncertainty in the averaged $\sigma(\lambda)$ was quoted as 30%. The averaged spectrum may not be representative of the true C_6-HPALD spectrum, in part because it ignores the possibility of UV-Vis absorption directly by the peroxide bond. In this work the experimental rate constant for photolysis was quoted as $(6.3\pm0.2)\times10^{-5}$ s^{-1}. Combined with the estimated spectrum, this was used to estimate the bulk photolysis quantum yield of 1 ± 0.4 over the 300-400 nm range (range of UV lamp used in the experiment).

Other reactions of HPALD can compete with photolysis, including reactions with the OH radical and ozone both of which are present in significant quantities in the troposphere. Although Wolfe *et al.* concluded that reaction with OH was not a major sink for C_6-HPALD, they indirectly measured its rate at $(5.1\pm1.8)\times10^{-11}$ cm^3 $molecule^{-1}$ s^{-1} which is remarkably close to an earlier estimate based on analogous reactions of OH with unsaturated carbonyls.[149] Various reaction channels for HPALDs and OH have been suggested,[149, 206] but crucially most of them are expected to regenerate OH. This reaction is expected to becomes more competitive with photolysis at higher OH concentrations and a higher solar zenith angle (when it is darker).[154]

Similarly, rate of C_6-HPALD reaction with O_3 was measured at 1.1×10^{-18} cm^3 which would mean an atmospheric lifetime of 10 days. This is significantly slower than the rates for direct

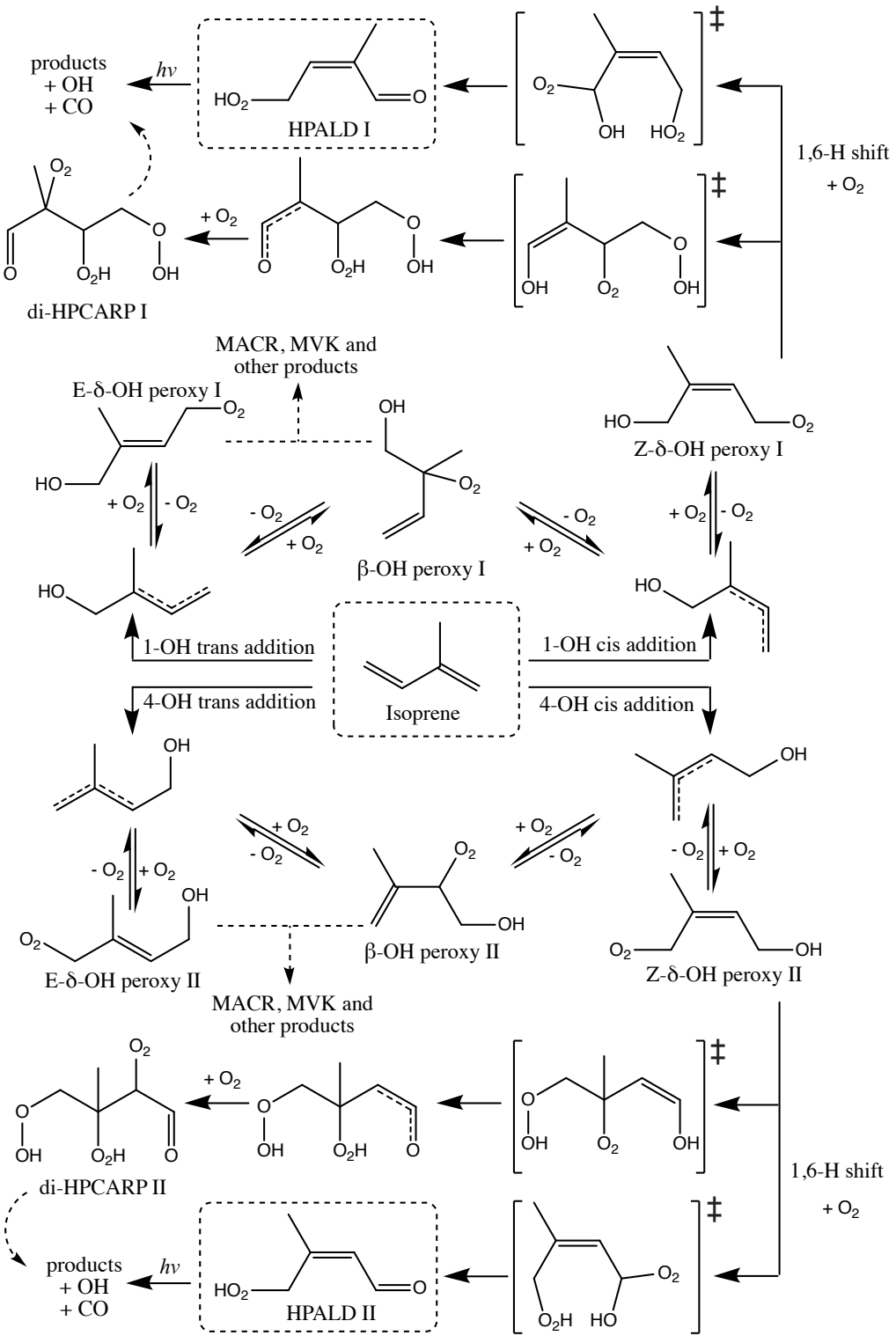

Figure 4.1: LIM1 isoprene oxidation mechanism, with naming conventions taken from Peeters *et al.* [153]

photolysis and OH reaction and so can safely be ignored in a model of HPALD chemistry.

4.2 UV-Vis spectra of HPALDs

In order to make a reliable prediction of the photolysis rate of both HPALD I and HPALD II, in this section I will use the best available methods within the limitations of electronic structure theory to predict the absorption cross section of these molecules. The Wigner sampling approach described in chapter 2 is a simple strategy best suited to medium sized molecules such as C_5-HPALD and so will be the method used here.

4.2.1 Computational Details

Rotational conformers of HPALD I and HPALD II are found through a systematic rotor search, and pre-optimised with the UFF forcefield in Avogadro v1.2.0. This search finds 3 conformers for HPALD I (labelled A-C) and 2 conformers for HPALD II (labelled A,B), all emerging due to the rotation of the C-O bond adjacent to the peroxide chromophore. Geometries were then optimised with a range of methods, including DFT, MP2 and spin component scaled MP2 (SCS-MP2), with tight convergence criteria. We used the following DFT functionals to optimise the structures: PBE0, wB97XD, and B3LYP. These optimisations used the def2-TZVP basis set and were calculated using Gaussian 16.[64] Post-HF methods such as MP2 and SCS-MP2 are known to return accurate geometries[213] so it was used as a benchmark to select a suitable DFT method. MP2 and SCS-MP2 calculations were performed in Orca v4.2.0[92] with the cc-pVTZ basis, and with the use of the resolution-of-identity (RI) approximation. The important -O-OH and -C=O bond lengths and RMSD of the geometry compared to the benchmark SCS-MP2/cc-pVQZ are shown in table 4.1. By comparing the RMSD between the different structures, shown in table 4.1, we have chosen the B3LYP functional with the def2-TZVP basis owing to it's similarity to the benchmark SCS-MP2 result.

The spectra are simulated by sampling from a multi-dimensional Wigner distribution based on normal mode frequencies. These frequencies are calculated at the optimised geometry in the S_0 state. It is known that harmonic frequencies calculated with MP2 and SCS-MP2 are competitive with, but not significantly better than those calculated with DFT.[214] Furthermore, MP2 and other post-HF methods tend to converge more slowly with respect to basis set size. Increased accuracy of SCS-MP2 frequencies would not account for increased computational cost, so DFT frequencies at the B3LYP/def2-TZVP level will be used to construct the distribution. An anharmonicity correction of 1.0044 is applied to the normal mode frequencies, as recommended in Kesharwani *et al.*[214] for this combination of functional and basis.

Accurately modelling the ground state distribution is only one half of the problem. We also need a reliable method to calculate the excitation energies and oscillator strengths for each geometry in the ensemble. To this end, we benchmarked a number of excited state methods

HPALD I			
Conformer A	-C=O (Å)	-O-OH (Å)	RMSD
PBE0/def2-TZVP	1.203	1.423	0.960
B3LYP/def2-TZVP	1.207	1.451	0.746
wB97X-D/def2-TZVP	1.202	1.421	1.073
MP2/cc-pVTZ	1.215	1.454	0.292
SCS-MP2/cc-pVTZ	1.211	1.455	0.059
SCS-MP2/cc-pVQZ	**1.211**	**1.456**	-
Conformer B			
PBE0/def2-TZVP	1.203	1.425	0.959
B3LYP/def2-TZVP	1.207	1.452	0.687
wB97X-D/def2-TZVP	1.202	1.425	3.766
MP2/cc-pVTZ	1.216	1.453	0.256
SCS-MP2/cc-pVTZ	1.211	1.454	0.061
SCS-MP2/cc-pVQZ	**1.212**	**1.455**	-
Conformer C			
PBE0/def2-TZVP	1.204	1.424	1.386
B3LYP/def2-TZVP	1.207	1.451	1.354
wB97X-D/def2-TZVP	1.202	1.422	0.606
MP2/cc-pVTZ	1.216	1.449	0.270
SCS-MP2/cc-pVTZ	1.211	1.450	0.159
SCS-MP2/cc-pVQZ	**1.212**	**1.451**	-
HPALD II			
Conformer A	-C=O (Å)	-O-OH (Å)	RMSD
PBE0/def2-TZVP	1.208	1.423	1.406
B3LYP/def2-TZVP	1.212	1.450	1.330
wB97X-D/def2-TZVP	1.206	1.422	1.143
MP2/cc-pVTZ	1.221	1.454	0.097
SCS-MP2/cc-pVTZ	1.216	1.454	0.062
SCS-MP2/cc-pVQZ	**1.216**	**1.455**	-
Conformer B			
PBE0/def2-TZVP	1.209	1.427	1.470
B3LYP/def2-TZVP	1.212	1.455	2.172
wB97X-D/def2-TZVP	1.207	1.425	1.307
MP2/cc-pVTZ	1.221	1.455	0.128
SCS-MP2/cc-pVTZ	1.216	1.457	0.054
SCS-MP2/cc-pVQZ	**1.216**	**1.457**	-

Table 4.1: Benchmarking the DFT methods that will be used for ensemble sampling against SCS-MP2/cc-pVQZ using the RI approximation

including TD-DFT, ADC(2), CC2, their spin coupled variants (SCS), and EOM-CCSD at the B3LYP S_0 geometry to select the most suitable approach for the simulation of the spectrum. TD-DFT and EOM-CCSD calculations were carried out in Gaussian 16, and (SCS-)CC2 and (SCS-)ADC(2) calculations were carried out in Turbomole v7.1,[215] always applying the RI approximation.

Excitation S_0 to	S_1	S_2	S_3
B3LYP/def2TZVP	3.55 (0.0003)	4.61 (0.0167)	5.18 (0.2514)
PBE0/def2TZVP	3.59 (0.0003)	4.83 (0.0301)	5.30 (0.2472)
SCS-ADC(2)/aug-cc-pVDZ	3.73 (0.0003)	5.82 (0.0842)	5.94 (0.2539)
SCS-ADC(2)/aug-cc-pVTZ	3.75 (0.0003)	5.84 (0.2004)	5.95 (0.1418)
ADC(2)/aug-cc-pVDZ	3.54 (0.0003)	5.49 (0.0348)	5.74 (0.2617)
CC2/aug-cc-pVTZ	3.73 (0.0003)	5.55 (0.0492)	5.78 (0.2583)
SCS-CC2/aug-cc-pVTZ	3.91 (0.0003)	5.87 (0.1264)	5.98 (0.1916)
EOM-CCSD/aug-cc-pVDZ	3.83 (0.0003)	5.77 (0.0170)	5.97 (0.2900)

Table 4.2: This table contains benchmark calculations performed to determine the most suitable method for the prediction of $\sigma(\lambda)$. Excitation energies to the first 3 states are given in eV, with oscillator strengths shown in parentheses (Calculated for first 5 singlets).

The results of these calculations are given in table 4.2, where the EOM-CCSD/aug-cc-pVDZ result is the benchmark for comparison. The closest result which is computationally tractable is SCS-ADC(2) with the aug-cc-pVDZ basis, so this method will be used to calculate the excitation energies for the ensemble.

HPALD photoabsorption cross sections were calculated for each conformer by using the Wigner ensemble method implemented in Newton-X v2.2.[71] Points were sampled from an uncorrelated quantum harmonic oscillator Wigner distribution based on the anharmonicity corrected frequencies calculated at the S_0 minimum. The temperature was set at 0 K and so it is assumed that all the normal modes are in their ground vibrational state. This is an acceptable approximation since at room temperature only low frequency modes (< 200 cm^{-1}) are likely to be excited, and such modes tend not to significantly affect absorption cross sections. For each conformer, 100 nuclear geometries were sampled from the distribution, and the electronic transitions (excitation energies and oscillator strengths) were computed for 5 singlet states with SCS-ADC(2) and the aug-cc-pVDZ basis set, applying the RI approximation. The number of ensemble points for each conformer used in the spectrum generation corresponded to their respective Boltzmann weights. The Boltzmann weights of each conformer were calculated from their B3LYP/def2-TZVP free energies (sum of electronic and vibrational ZPE) at T = 298K. In order to generate a continuous spectrum each spectral transition is broadened by being overlaid with a Lorentzian curve with a phenomenological broadening coefficient Δ of 0.05 eV.

4.2.2 Spectra of HPALD I and HPALD II

The generated spectra for each conformer can be seen in figures 4.2 and 4.3 in the relevant range of solar radiation. To generate $\sigma(\lambda)$ of HPALD I, an ensemble size of 164 was used (38 conformer A, 26 conformer B, 100 conformer C). For $\sigma(\lambda)$ of HPALD II, the ensemble size was 119 (19 conformer A, 100 conformer B). There are few noticeable differences between the conformers, with a smaller S_1 peak at longer wavelengths partly obscured by the significantly larger overlapping S_2 and S_3

peaks. At wavelengths in the visible range (380 nm and above) the absorption is mainly into the S_1 state. This indicates that in the troposphere most HPALD molecules would be promoted into this state.

In figures 4.2 and 4.3 the calculated bands corresponding to excitations into S_2 and S_3 states do not extend above 300 nm. By extrapolating the S_2 band into the longer wavelength part of the spectrum we may expect some excitation into that state above 300 nm. However, there are too few ensemble points to make a reliable estimate of the band shape in that region.

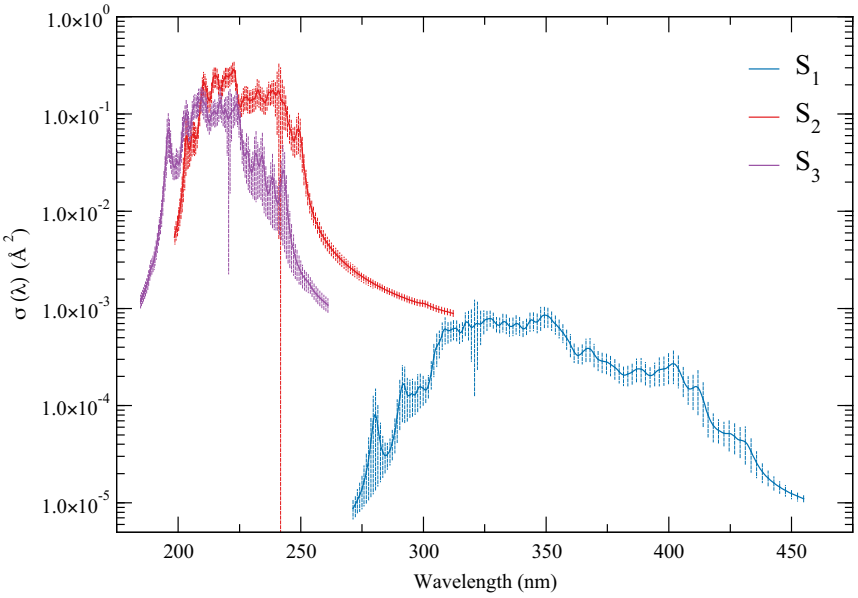

Figure 4.2: Absorption cross sections generated from the Wigner ensemble of HPALD I, using a weighted combination of its 3 conformers. Excitations calculated at SCS-ADC(2)/aug-cc-pVDZ level.

The photolysis rate J, which is a first order rate constant, can be determined by integrating the absorption cross section, actinic flux, and quantum yield over the full range of wavelengths, as shown in equation 4.2.2.

$$J = \int_{\lambda_{min}}^{\lambda_{max}} \sigma(\lambda) F(\lambda) \phi(\lambda) d\lambda$$

The actinic flux $F(\lambda)$ is the rate of incident photons per unit area, which will be used at solar zenith angle of 30°. Photolysis rate, J, is distinct from a photochemical lifetime which is the time taken for a photoexcited molecule to decay back to its ground state. On the other hand, if photoexcitation leads to a number of reaction channels each with its own corresponding quantum yield $\phi(\lambda)$ then the rate for that channel can be calculated with equation 4.2.2. To calculate this rate we will be using actinic flux data generously provided by John Crounse and Glenn Wolfe,

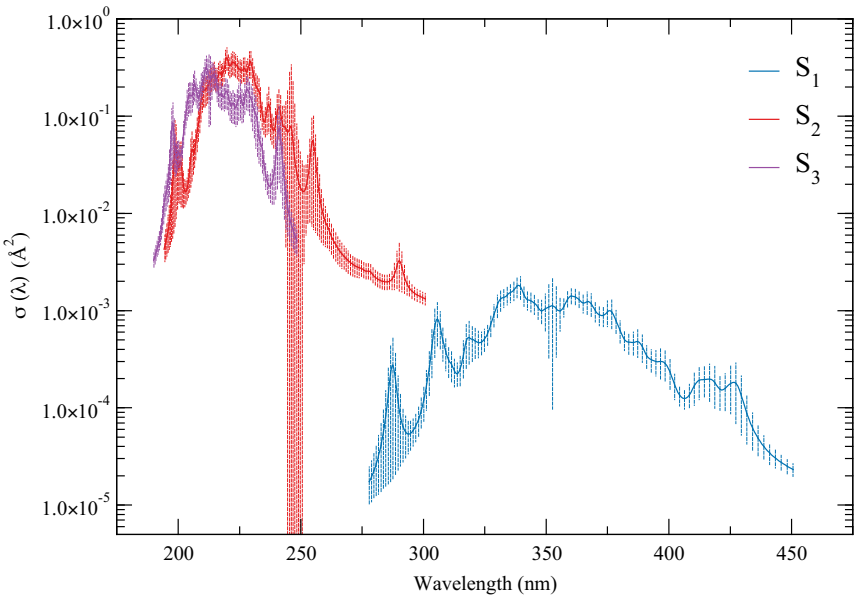

Figure 4.3: Absorption cross sections generated from the Wigner ensemble of 2 conformers, A and B, of HPALD II. Absorption bands for the first 3 singlet states calculated at SCS-ADC(2)/aug-cc-pVDZ level. Excitation band for each state is shown separately. Error bars indicate the uncertainty in the cross section due to statistical sampling.

measured for the UV-Vis lamp used in their experiments in the 300-400 nm range. Rates are calculated using two approaches: integrating over $\sigma(\lambda)$ for excitations into the S_1 state only, or $\sigma(\lambda)$ that include all states S_1 to S_3. It is recommended to consider primarily the S_1 rates, since the result that includes all excitations is very sensitive to the Lorenzian broadening parameter. Since the oscillator strength of the $S_0 - S_2$ absorption is significantly higher, the tail of the curve overlaps with the S_1 peak causing the rate to appear artificially high. For example, if the broadening coefficient Δ were set to 0.01 eV, the σ_{S_1} only photolysis rate for HPALD I would barely increase to 1.05 $\times 10^{-4}$ s^{-1} whilst the σ_{All} rate would almost halve to 1.37 $\times 10^{-4}$ s^{-1}. Using only the S_1 excitations, the photodissociation rate for HPALD I is then 9.15 $\times 10^{-5}$ s^{-1} and that for HPALD II is 1.93 $\times 10^{-4}$ s^{-1}.

4.3 The mechanism of OH loss

Dynamics simulations performed in the previous chapter give us an insight into the mechanism of HPALD photolysis after photoexcitation into S_1. Although the aforementioned calculations used C_6-HPALD as a proxy molecule for the two isomers of C_5-HPALD, these molecules are

similar enough to infer the photochemistry of the former from the latter.

As we have established from the absorption cross sections, the HPALD molecule is primarily photoexcited into the S_1 state in the 300-400 nm range. An EOM-CCSD benchmark indicates that the peak of the $S_0 \rightarrow S_2$ transition occurs at a significantly lower wavelength (202 nm) than $S_0 \rightarrow S_1$ (330 nm), such that it's out of the UV-Vis range. However, some geometries sampled from the tail of the Wigner distribution show a lower energy $S_0 \rightarrow S_2$ transition so some all-atom nonadiabatic dynamics were performed to explore this pathway. Ab initio multiple spawning (AIMS) calculations initiated in S_2 (10 trajectories, LR-TDDFT/lc-ωPBE/6-31G) show that the wavepacket slides down the dissociative S_2 potential, leading to ultrafast ballistic loss of OH within 20 fs.[1] The $S_2 \rightarrow S_1$ crossing is purely diabatic such that the wavepacket follows the $n'\sigma^*$ character of the S_2 state in the actinic region.

Next, I will discuss the dominant photodissociation channel, following excitation into S_1. In the Franck-Condon region this electronic state exhibits $n\pi^*$ character. Surface hopping calculations described in the previous chapter indicate that the nuclear wavepacket moves on the PES near the S_1 minimum for a number of vibrational periods, eventually losing OH or HO_2 on a picosecond timescale. As the peroxide bond is extended (and enone bond is relaxed), the S_1 and S_2 states become strongly coupled and it is possible for the wavepacket to proceed through the coupling region adiabatically as the character of the S_1 state changes from $n\pi^*$ to $n'\sigma^*$. We can then say that the dynamics calculations support the hypothesis proposed by Peeters *et al.* in 2010.[149] We can however add that the dissociative process is slowed by the wavepacket becoming diabatically trapped on the $n\pi^*$ potential as it moves through the coupling region.

The lifetime of C_6-HPALD following photoexcitation into S_1 is approximated to be on the order of 5 ps when nonadiabatic dynamics are performed at LR-TDDFT/PBE0/6-31G level of theory.

4.4 Simulating sunlight-induced dynamics

Many reactions whose photochemistry we wish to understand are caused by the molecules' interaction with sunlight, including photosynthesis, energy conversion by photovoltaics, or eyesight. In this section I will outline the applicability of conventions in trajectory based methods for reactions caused by such continuum-wave (CW) or black-body radiation, and consider possible strategies to make these simulations more realistic.

Standard practice when simulating an ultrashort excitation is to generate initial conditions by invoking the Franck-Condon approximation and vertically projecting the ground state nuclear density given by a Wigner distribution onto the excited state potential. In the limit of an infinitesimally short light pulse (i.e. a delta function in time) it will generate a wavepacket which has the exact shape of the ground state nuclear wavefunction. The shortest pulse length that

[1] These AIMS calculations were ran by Dr. Basile Curchod at Stanford.

has been generated in a controlled experiment at this time is 43 attoseconds,[216] but any laser pulse shorter than a couple of picoseconds is considered ultrashort. This wavepacket is not an eigenstate of the system, but a coherent superposition of excited eigenstates, which will then dephase as the wavepacket moves on the new potential.

Longer laser pulses do not generate localised wavepackets, but rather excite the molecule into a particular eigenstate which must be resonant with the radiation frequency. This is fundamentally due to the energy-time uncertainty principle $\Delta E \Delta t \geq \hbar/2$ that means that a laser pulse of length Δt = 10 fs would have uncertainty in its energy spanning ΔE = 0.03 eV. For longer pulses and CW radiation, ΔE will be significantly smaller. An adjustment to the nonadiabatic dynamics protocol has been made by Suchan *et al.*[200], that generates initial conditions for trajectories in the long-pulse limit with a constraint that enforces the resonance condition. This is achieved by running ground state dynamics with the generalised Langevin equation thermostat which enforces a quantum distribution – as described in chapter 2 – but using importance sampling techniques such as umbrella sampling or Lagrange multipliers to ensure that only the configurations that fulfil the resonance condition are sampled. This type of initial condition sampling is computationally more demanding than ground state sampling, as it requires the knowledge of excited state energies at each point. While this work addresses the question of how to simulate excitation via long monochromatic pulses, it still isn't a realistic model of black-body radiation (sunlight).

A method for simulating thermal (black-body) light excitation based on the Chennu-Brummer approach was suggested by Barbatti .[201] Absorption of thermal, incoherent, CW radiation leads to a statistical mixture of stationary eigenstates, which evolve in time without the coherences present in ultrafast spectroscopy. In the Chennu-Brummer ansatz this type of radiation is treated as an ensemble of coherent pulses occurring at different times which is intuitive when thinking of a bulk ensemble of molecules interacting with thermal radiation. Furthermore, an advantage of this approach is that after the initial conditions are determined, the trajectories can evolve in exactly the same way as conventional nonadiabatic mixed quantum-classical dynamics.

This discussion is an important caveat when we make claims about the behaviour of atmospheric systems based on simulations of nonadiabatic dynamics. The question of how to approach mixed quantum-classical dynamics simulations for arbitrary irradiation merits further investigation.

4.5 Conclusion

This chapter intends to address questions pertaining to the LIM1 mechanism of HPALD photodissociation. We make a prediction of the HPALD absorbtion cross section which has not yet been determined experimentally and elucidate the mechanism of OH loss from dynamics simulations. The calculated absorption cross sections for C_5-HPALD show that rates of photolysis on the

order of 2×10^{-4} s^{-1} are a fair estimate of the real rate and are in agreement with predictions made in the LIM1 mechanism. However, we highlight that when making statements about the mechanism on the basis of nonadiabatic dynamics simulations, the question of how to replicate photoexcitation caused by sunlight remains a pertinent one.

CHAPTER 5

QUANTUM TRAJECTORY SURFACE HOPPING

5.1 Introduction

Tully's fewest switches surface hopping (FSSH) is one of the most popular algorithms for simulating quantum-classical dynamics following photoexcitation. I applied it in chapter 3, where it was used to model the photodissociation of C_6-HPALD. There are many reasons for the popularity of FSSH, amongst them its conceptual simplicity and relative efficiency in comparison to fully quantum wavepacket dynamics. Because trajectories can be ran independently, the cost scales with the selected electronic structure method rather than the dimensionality of the system. Therefore, when systems are well-benchmarked against cheaper methods such as LR-TDDFT and ΔSCF, FSSH can be applied to run dynamics on larger systems.[217, 218]

By assuming that the wavepacket can be approximated as a swarm of independent trajectories allows us to easily parallelise the calculation over multiple cores such that many trajectories can be run simultaneously. This independent trajectory approximation results in the most well known shortcoming the FSSH algorithm – its failure to correctly capture quantum coherence effects. More formally, over the course of the simulation the off-diagonal elements of the density matrix for each trajectory become larger than they would be in a fully quantum representation. Several authors have made modifications to the FSSH algorithm that include decoherence corrections, while still preserving the independent trajectory ansatz.[219–221]

Each trajectory is not meaningful on its own, but only as part of an ensemble representing the wavepacket. To ensure that energy is conserved at the ensemble level, the FSSH algorithm artificially rescales the momentum of a trajectory following a hop to compensate for the energy gap between adiabatic states. While ad hoc corrections such as this are reasonable and make the algorithm more robust, they do not have any physical meaning.

In this chapter I will explore and implement a novel nonadiabatic dynamics strategy introduced by Craig Martens, based on an exact formalism derived from the quantum Liouville equation. This approach preserves the independent trajectory property of the FSSH algorithm, but removes the energy rescaling step while still conserving energy at the ensemble level. I will begin by outlining the classic fewest switches surface hopping (FSSH) algorithm. Then I will introduce the formally exact Consensus Surface Hopping (CSH) formalism and summarize its derivation from the quantum mechanical Liouville equation.[222] Quantum Trajectory Surface Hopping (QTSH) is the independent trajectory limit of CSH, but is a more computationally tenable algorithm so I will describe the stepwise approximations necessary to link the two. I will then benchmark possible strategies for the implementation of the QTSH algorithm, comparing integration step algorithms and their convergence with time step size. My optimised implementation in a development version of Newton-X will then be compared against the results of FSSH when applied to a few model systems, including the problems outlined by Tully, and the spin-boson Hamiltonian model.

5.2 Fewest switches surface hopping

The seminal paper describing the fewest switches surface hopping (FSSH) method was first published by John C. Tully in 1990.[125] As the QTSH algorithm is formulated to resemble FSSH, it is useful to define the terms and give a brief overview of the original method.

We begin by defining the full Hamiltonian for a system

$$H = T_q + H_0(\mathbf{r},\mathbf{q}) \tag{5.1}$$

where T_q is the nuclear kinetic energy and $H_0(\mathbf{r},\mathbf{q})$ is the electronic Hamiltonian for a given nuclear configuration $\mathbf{q}$. Matrix elements of H_0 can be written in terms of an orthonormal basis $\phi_i(\mathbf{r};\mathbf{q})$.

$$V_{jk}(\mathbf{q}) = \langle \phi_j(\mathbf{r};\mathbf{q}) | H_0 \phi_k(\mathbf{r};\mathbf{q}) \rangle \tag{5.2}$$

The nonadiabatic coupling (NAC) vector $\mathbf{d}_{ij}(\mathbf{q})$ can also been written in terms of the electronic basis in the adiabatic representation where $\nabla_{\mathbf{q}}$ is the gradient with respect to the nuclear configuration $\mathbf{q}$.

$$\mathbf{d}_{jk}(\mathbf{q}) = \langle \phi_j(\mathbf{r};\mathbf{q}) | \nabla_{\mathbf{q}} \phi_k(\mathbf{r};\mathbf{q}) \rangle \tag{5.3}$$

The sequence of nuclear configurations and momenta as a function of time defines a classical trajectory ($\mathbf{q}(t)$,$\mathbf{p}(t)$). For a given trajectory path we can then expand the time-dependent electronic wavefunction as

$$\psi(\mathbf{r},t) = \sum_j c_j(t) \phi_j(\mathbf{r};\mathbf{q}(t)) \tag{5.4}$$

where c_j are complex expansion coefficients. This electronic wavefunction can then be substituted into the time dependent Schrödinger equation (TDSE). Using the chain rule, $\langle \phi_j | \dot{\phi}_k \rangle = \dot{\mathbf{q}} \cdot \mathbf{d}_{jk}$ we obtain a set of coupled first-order differential equations for the expansion coefficients.

$$i\hbar \dot{c}_j(t) = \sum_k c_k \left(V_{jk} - i\hbar \dot{\mathbf{q}} \cdot \mathbf{d}_{jk} \right) \tag{5.5}$$

This result implies that for any trajectory the expansion coefficients c_j can be integrated numerically. These time-dependent coefficients correspond to the amplitude of each electronic state at time t. It is then useful to define the electronic density matrix $\mathbf{a}$ as $a_{jk} = c_j c_k^*$ for a given trajectory. Diagonal elements of $\mathbf{a}$ are the populations of an electronic state and off-diagonal elements are the coherences between these states. State populations a_{jj} evolve according to this equation of motion

$$\dot{a}_{jj} = \sum_{k \neq j} b_{jk} \text{ where} \tag{5.6}$$

$$b_{jk} = \frac{2}{\hbar} \mathrm{Im}(a_{jk}^* V_{jk}) - 2\,\mathrm{Re}(a_{jk}^* \dot{\mathbf{q}} \cdot \mathbf{d}_{jk}) \tag{5.7}$$

In practice, implementations of the FSSH algorithm proceed according to the following steps.

1. Positions and momenta at $t = 0$ are assigned to replicate the shape of the wavepacket directly following photoexcitation. Typically this is done by vertically projecting a ground state distribution into an excited state (j) or splitting the wavepacket between a number of excited states.

2. Positions of the atomic nuclei evolve classically on potential energy surface j for a time interval Δt.

3. Probability of hopping to electronic state k, g_{jk}, is evaluated based on the off-diagonal matrix elements of $\mathbf{a}$. If g_{jk} is negative, it is set to 0. The expression for g_{jk} has been constrained to minimise the frequency of state switches for arbitrarily small time steps. A uniform random number ζ between 0 and 1 is generated, and a hop occurs if ζ is smaller than g_{jk}.

$$g_{jk} = \Delta t \frac{b_{jk}}{a_{jj}} \tag{5.8}$$

4. If hopping occurs, the trajectory is transferred to the new state. To conserve the total energy, a velocity adjustment is made to compensate for the ΔE between the two states. The velocity adjustment is made in the direction of the NAC vector. Cases where the magnitude of the velocity adjustment is greater than the magnitude of the original velocity are called "frustrated hops", and in Tully's original formulation they are forbidden. If there is no hop, the algorithm returns to step 2.

This procedure then repeats itself for a specified simulation time for all trajectories. The number of trajectories typically ranges from 100 to a few 1000s, which is sufficient to reach statistical convergence. A higher number of trajectories is needed for reactions with many possible outcomes in order to properly sample the rare reaction channels. Tully tested this scheme on three typical crossings illustrated in figure 5.1, which are now known as Tully's models and are widely used to benchmark novel nonadiabatic molecular dynamics methods. Molecular analogues of these 1-D models are useful to test the robustness of these methods when extended into multiple dimensions.[192]

I will use Tully's models to test my implementation of QTSH later on in this chapter.

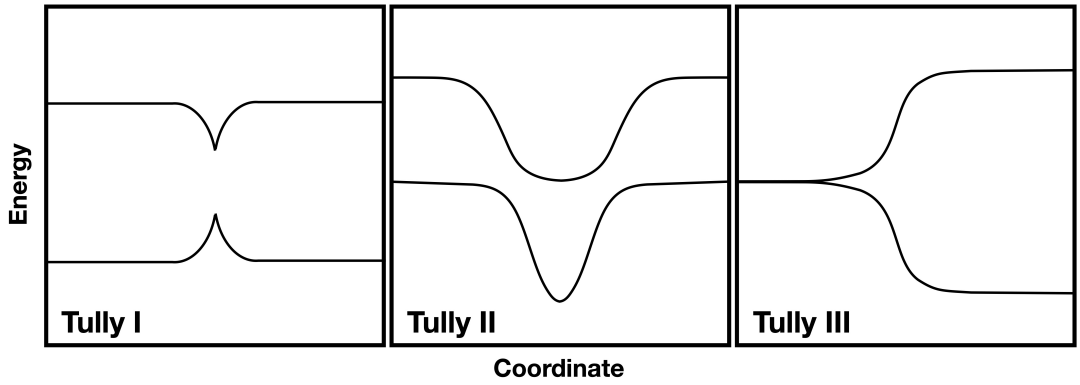

Figure 5.1: Three one-dimensional model systems Tully used to test the FSSH algorithm. Tully I is the single avoided crossing; Tully II is the dual avoided crossing where branching and recoherence of the wavepacket is observed; Tully III has a wavepacket which moves through an extended coupling region until state degeneracy is lifted and the wavepacket transfered to the upper state may reflect backwards depending on initial momentum.

5.2.1 The problem of decoherence

In FSSH the electronic density matrix **a** is integrated continuously, preserving the quantum phase coherence. However, this coherence is naturally damped in many-atom systems in a way that isn't replicated in the FSSH algorithm. Because of this, the FSSH algorithm suffers from over-coherence. Coherences are the off-diagonal elements of **a** corresponding to the overlap of wavepackets between surfaces. As diverging wavepackets move away from each other these elements should tend to 0. Multiple ways to artificially enforce decoherence have been suggested.[220] Simply damping the off-diagonal electronic amplitudes can be effective in many cases. Granucci and Persico suggested an ad hoc scheme that dampens the hopping probability by an exponential factor $e^{-\Delta t/\tau_{jk}}$, where the decoherence timescale τ_{jk} is inversely proportional to the energy gap between adiabatic states.[219] This is a popular decoherence scheme, and is implemented by default in Newton-X. Still, it isn't applicable in all cases – for example, it fails to reproduce the

branching ratios for Tully's second model system.[223] Another approach collapses the amplitudes to a single state when a trajectory leaves a region of strong coupling.[224] Schwartz *et al.* also suggested that the decoherence rate is proportional to the difference in the forces on the two PES.[225]

Ultimately, the slow loss of phase coherence is an unavoidable consequence of the independent trajectory ansatz. Most schemes that artificially enforce decoherence are useful, but reliant on parametrization for a given system and are not formally derived. In the method presented here, an empirical decoherence correction parameter has been suggested based on the ensemble average of trajectory phases.[222] This correction is not yet implemented in the results presented here, since the dependence of this parameter on the statistics of the trajectory ensemble creates a degree of interdependence between the trajectories.

5.3 Consensus Surface Hopping

In this section I describe the Consensus Surface Hopping (CSH) formalism which provides a rigorous theoretical framework for a trajectory-based nonadiabatic dynamics method that is fully exact. Starting from a basic outline of its derivation from the multi-state quantum Liouville equation, I will explain how trajectory ensembles can be used to exactly represent the time-evolution of phase space density. A more complete explanation is given in the papers of Craig Martens,[222, 226] however here the derivation is generalised for an arbitrary number of electronic states.

The quantum Liouville equation (QLE) for the density operator $\hat{\rho}(t)$ and system Hamiltonian $\hat{H}$ is displayed below, alongside its classical limit.

$$\begin{array}{ll} \text{Quantum LE} & \text{Classical LE} \\ i\hbar\frac{d\hat{\rho}}{dt} = \left[\hat{H},\hat{\rho}\right] & \frac{d\rho}{dt} = \{H,\rho\} \end{array}$$

Whilst in the QLE $\hat{\rho}$ is a quantum density operator, in the classical analogue ρ is a function of the phase-space position and momentum variable $\Gamma(\mathbf{q},\mathbf{p})$ and time t. Here $\{H,\rho\}$ are the Poisson brackets of classical phase space functions H and ρ, defined as

$$\{H,\rho\} = \frac{\partial H}{\partial q}\frac{\partial \rho}{\partial p} - \frac{\partial \rho}{\partial q}\frac{\partial H}{\partial p}.$$

We can rewrite the QLE in the basis of N electronic states, such that the operators $\hat{H}$ and $\hat{\rho}$ are written in terms of their matrix elements as $H_{mn} = \langle m|\hat{H}|n\rangle$ and $\rho_{mn} = \langle m|\hat{\rho}|n\rangle$ respectively.

$$i\hbar\frac{d\rho_{mn}}{dt} = \sum_{k=1}^{N} H_{mk}\rho_{kn} - \rho_{mk}H_{kn} \tag{5.9}$$

At this point it should be noted that the CSH formalism is independent of representation, i.e. that diabatic and adiabatic representations yield the same result. However, for a direct

comparison to FSSH it is simpler to proceed along the adiabatic route in this derivation. We can begin by defining the Hamiltonian and density matrix for N states in the adiabatic representation in the following way.

$$\hat{H} = \begin{pmatrix} H_{1,1} & \cdots & V_{1,N} \\ \vdots & \ddots & \vdots \\ V_{N,1} & \cdots & H_{N,N} \end{pmatrix} \quad \hat{\rho} = \begin{pmatrix} \rho_{1,1} & \cdots & \rho_{1,N} \\ \vdots & \ddots & \vdots \\ \rho_{N,1} & \cdots & \rho_{N,N} \end{pmatrix}$$

Note that these matrices are nuclear operators, and not functions. The crucial step that translates the operators to functions, and thus makes a semiclassical approximation to the QLE, is the use of the Wigner-Moyal expansion in the powers of $\hbar$. This replaces the commutators in the QLE with Poisson brackets, where $A(q,p)$ and $B(q,p)$ are functions defined in phase space (q,p). [227]

$$\left[\hat{A},\hat{B}\right] \rightarrow i\hbar\{A,B\} + O\left(\hbar^2\right)$$

Products of two quantum operators in the Wigner-Moyal representation can be expressed as a Moyal (star) product – this is fundamental for the phase space formulation of quantum mechanics, which is exactly equivalent to the Hilbert-space representation. By keeping only the first order non-classical term in the Moyal expansion, the quantum-classical Liouville equation (QCLE) is then be derived.

$$i\hbar\frac{\partial\rho_{mn}}{\partial t} = \sum_{k=1}^{N} H_{mk}\rho_{kn} - \rho_{mk}H_{kn} + \frac{i\hbar}{2}\sum_{k=1}^{N}\{H_{mk},\rho_{kn}\} - \{\rho_{mk},H_{kn}\} \tag{5.10}$$

The off-diagonal coherences between states ρ_{mn} are written in terms of their real and imaginary parts.

$$\rho_{mn} = \alpha_{mn} + i\beta_{mn}$$

The density matrix is Hermitian such that $\rho_{mn} = \rho_{nm}^*$ with the implication that $\alpha_{mn} = \alpha_{nm}$ and $\beta_{mn} = -\beta_{nm}$. Diagonal elements and the off-diagonal couplings of H in the adiabatic representation are given as

$$H_{nn} = \frac{\mathbf{p}^2}{2m} + U_n(\mathbf{q}) \quad \text{and} \quad V_{mn} = -V_{nm}^* = -i\hbar\mathbf{d}_{mn}\cdot\frac{\mathbf{p}}{\mu}$$

in the semiclassical limit, where U_n is the adiabatic potential and μ is the mass.

By substituting these quantities into equation 5.10 we can derive the equations of motion for the diagonal elements of the density matrix.

$$\frac{\partial\rho_{nn}}{\partial t} = \{H_{nn},\rho_{nn}\} + 2\sum_{k\neq n}^{N}\mathbf{d}_{kn}\cdot\frac{\mathbf{p}}{m}\alpha_{kn} - \hbar\sum_{k\neq n}^{N}\left\{\mathbf{d}_{kn}\cdot\frac{\mathbf{p}}{m},\beta_{kn}\right\} \tag{5.11}$$

Since the total density matrix ρ is written as

$$\rho = \sum_{n=1}^{N}\rho_{nn}$$

we can derive the EOM for ρ

$$\frac{\partial \rho}{\partial t} = \sum_{n=1}^{N} \{H_{nn}, \rho_{nn}\} - 2\hbar \sum_{n=1}^{N} \sum_{k<n}^{N} \left\{ d_{kn} \cdot \frac{p}{m}, \beta_{kn} \right\} \tag{5.12}$$

which is equivalent to the classical Langevin equation, with an additional term (multiplied by $\hbar$). This term contains the non-classical modifications to the nuclear dynamics and is dependent on the NAC vector and the off-diagonal coherences. By splitting the off-diagonal elements of the density matrix in the QCLE into real and imaginary parts it is also possible to derive the time evolution of the coherences following a similar procedure

$$\begin{aligned} \frac{\partial \alpha_{mn}}{\partial t} = & \sum_{k \neq m,n}^{N} \left[\alpha_{mk} \mathbf{d}_{kn} \cdot \frac{\mathbf{p}}{m} - \alpha_{kn} \mathbf{d}_{mk} \cdot \frac{\mathbf{p}}{m} \right] + \{H_0, \alpha_{mn}\} + \omega \beta_{mn} \\ & + \sum_{k \neq m,n}^{N} \left\{ \alpha_{mk}, \mathbf{d}_{kn} \cdot \frac{\mathbf{p}}{m} \right\} - \left\{ \mathbf{d}_{mk} \cdot \frac{\mathbf{p}}{m}, \alpha_{kn} \right\} + \mathbf{d}_{mn} \cdot \frac{\mathbf{p}}{m} \left(\rho_{nn} - \rho_{mm} \right) \end{aligned} \tag{5.13a}$$

$$\begin{aligned} \frac{\partial \beta_{mn}}{\partial t} = & \sum_{k \neq m,n}^{N} \left[\beta_{mk} \mathbf{d}_{kn} \cdot \frac{\mathbf{p}}{m} - \beta_{kn} \mathbf{d}_{mk} \cdot \frac{\mathbf{p}}{m} \right] + \{H_0, \beta_{mn}\} - \omega \alpha_{mn} \\ & + \sum_{k \neq m,n}^{N} \left\{ \beta_{mk}, \mathbf{d}_{kn} \cdot \frac{\mathbf{p}}{m} \right\} - \left\{ \mathbf{d}_{mk} \cdot \frac{\mathbf{p}}{m}, \beta_{kn} \right\} - \frac{\hbar}{2} \left\{ \mathbf{d}_{mn} \cdot \frac{\mathbf{p}}{m}, \rho_{nn} + \rho_{mm} \right\} \end{aligned} \tag{5.13b}$$

where $H_0 = (H_{mm} + H_{nn})/2$ and ω is the difference frequency between adiabatic states $\omega = (U_m - U_n)/\hbar$ (proof of this is available in the Appendix).

These equations of motion for the phase space densities can be written using the trajectory ensemble ansatz.

$$\rho(\Gamma, t) = \frac{1}{N_{\text{traj}}} \sum_j \delta\left(\Gamma - \Gamma_j(t)\right) \tag{5.14a}$$

$$\alpha_{mn}(\Gamma, t) = \frac{1}{N_{\text{traj}}} \sum_j \alpha_{mn,j}(t) \delta\left(\Gamma - \Gamma_j(t)\right) \tag{5.14b}$$

$$\beta_{mn}(\Gamma, t) = \frac{1}{N_{\text{traj}}} \sum_j \beta_{mn,j}(t) \delta\left(\Gamma - \Gamma_j(t)\right) \tag{5.14c}$$

An ensemble of N_{traj} trajectories $\Gamma_j(t) = (\mathbf{q}_j(t), \mathbf{p}_j(t))$ represents the phase space densities. Quantum population transfer between states is represented by stochastic hops at trajectory level – each $\Gamma_j(t)$ has an integer attribute $\sigma_j^k(t)$ which indicates the state that trajectory j occupies at time t (1 if it's on state k and 0 otherwise). The delta function $\delta\left(\Gamma - \Gamma_j(t)\right)$ at the location of the jth trajectory needs to be smoothed by a phase space Gaussian for a finite ensemble in the numerical implementation. By inserting this trajectory ansatz into the coupled differential equations 5.11-5.13b it is possible to derive the trajectory equations of motion for the classical

ensemble given in equations 5.15a-5.15b.

$$\dot{\mathbf{q}}_j = \frac{\mathbf{p}_j}{\mu} - \frac{2\hbar}{\mu} \sum_n \sum_{k<n} \mathbf{d}_{kn,j} \beta_{kn,j} \tag{5.15a}$$

$$\dot{\mathbf{p}}_j = -\nabla U_j(\mathbf{q}) + \frac{2\hbar}{\mu} \sum_n \sum_{k<n} \mathbf{p}_j \cdot (\nabla \mathbf{d})_{kn,j} \beta_{kn,j} \tag{5.15b}$$

These are Hamilton's equations describing the time evolution of the semi-classical trajectory $\Gamma_j(t)$ on state n which can be derived from the corresponding Hamiltonian (where terms of order $\hbar^2$ and higher are neglected).

$$H = \frac{\left(\mathbf{p} - 2\hbar \sum_n \sum_{k<n} \mathbf{d}_{kn} \beta_{kn}\right)^2}{2\mu} + U(\mathbf{q}) \tag{5.16}$$

By substituting equations 5.14b and 5.14c into 5.13a and 5.13b respectively, it's also possible to derive EOM for the coherences α_{mn} and β_{mn}. Finally, the probability of hopping to state n for the jth trajectory moving on state m is given by the following expression, which closely resembles the FSSH switching probability.

$$P_{mn}^{CSH} = \left| \frac{2}{\langle \rho_{mm} \rangle} \frac{\mathbf{d}(\mathbf{r}_j) \cdot \mathbf{p}_j}{\mu} \langle \alpha_{mn} \rangle_j \Delta t \right| \tag{5.17}$$

Here $\langle \rho_{mm} \rangle$ and $\langle \alpha_{mn} \rangle_j$ are the local values of density ρ_{mm} and coherence α_{mn} at the phase space point Γ_j, both of which depend on the knowledge of the complete ensemble.

5.3.1 Quantum Trajectory Surface Hopping

CSH is a useful framework for examining nonadiabatic dynamics in a statistical trajectory ensemble representation. Interdependence of the trajectories that arises through the use of local functions depending on the full ensemble in the equations of motion and hopping probabilities means that quantum decoherence is treated correctly. This is demonstrated by its application to 1- and 2- dimensional model systems.[222, 226] However, the need for "consensus" means that this method is more expensive than FSSH, although the exact scaling with dimensionality is not yet determined. Furthermore, CSH removes the known advantage of trajectory based dynamics, that of being easy to run in parallel on novel GPU architectures, which significantly improves their efficiency.[110] Independent trajectories are simple to parallelize, so this ansatz makes QTSH a more practical method. In this section I will describe the approximations needed to take CSH to its independent trajectory limit: QTSH.

Firstly, ensemble average quantities such as $\langle \rho_{mm} \rangle = \rho_{mm}(\Gamma_j)$ and $\langle \alpha_{mn} \rangle_j = \alpha_{mn}(\Gamma_j)$ are replaced by their single-trajectory proxies. As FSSH relies on the correspondence between the individual trajectory density matrix populations $\mathbf{a}_{nn}$, and the total trajectory populations on each state – so QTSH assumes that the CSH functions (Eqn. 5.14) are smoothly varying in local phase

space. For example, if phase space population density of state m, ρ_{mm}, is varying slowly in the vicinity of trajectory point Γ_j we can say that

$$\langle \rho_{mm} \rangle_j \approx \langle \sigma^m \rangle_j \langle \rho \rangle_j .$$

where the expectation value of the stochastic variable $\langle \sigma^m \rangle_j$ is just the trajectory density matrix element $a_{mm,j}$. Furthermore, if the system is fully coherent we can assume that the function α_j^m is also slowly varying near the phase space point Γ_j allowing the following replacement.

$$\langle \alpha_{mn} \rangle_j \approx \alpha_{mn,j} \langle \rho \rangle_j$$

This allows the CSH hopping probability to be rewritten in terms of parameters that aren't expressed in terms of the whole ensemble.

$$P_{mn}^{QTSH} = \left| \frac{2}{a_{mm,j}} \frac{\mathbf{d}(\mathbf{q}_j) \cdot \mathbf{p}_j}{\mu} \alpha_{mn,j} \Delta t \right| \tag{5.18}$$

Equation 5.18 is equivalent to the FSSH hopping probability g_{mn} in Eqn. 5.8. Like FSSH, the QTSH algorithm can be broken down into 4 basic steps:

1. Generate initial conditions for the trajectories in an identical way to FSSH.
2. Propagate the classical nuclei in phase space following the QTSH equations of motion that contain a non-classical component.
3. Integrate equation 5.5 to obtain $\mathbf{a}$ at this timestep. $\mathbf{a}$ contains the smoothly varying coherences ($\alpha + i\beta$) and state populations (a_{nn}) necessary to integrate the classical EOM.
4. Determine if the running state of the trajectory changes by comparing random number ζ taken from a uniform distribution between 0 and 1 against the hopping probability in equation 5.18. Return to step 2 until the end point of the trajectory.

This algorithm is extremely similar to FSSH and uses many of the same parameters (density matrix coherences, hopping probabilities, classical positions and momenta). The following section outlines the differences which are contained in steps 2 and 3, and the specifics of integrating QTSH into an existing FSSH codebase.

While CSH is formally exact, the accuracy of QTSH is more comparable to FSSH in the cases of the simple model systems explored by Martens. Advantages of using QTSH over FSSH are as follows: QTSH is equivalent in the diabatic and the adiabatic representations; some contrivances of FSSH such as forbidden hops are eliminated; QTSH is time-reversible at ensemble level, which is impossible for FSSH due to frustrated hops and momentum rescaling.[222] In comparison to the exact wavepacket calculations for the case of Tully's single crossing model, QTSH can reproduce the coherence with near-quantitative accuracy. However, FSSH shows better agreement to the benchmark final state population (Martens speculates that this is due to the stricter energy conservation procedure).[226]

5.4 Implementing the algorithm

In the papers where the method was originally published, QTSH was applied to a selection of 1-D and 2-D model systems. To extend the applicability of QTSH, possibly to molecular systems, I implemented the algorithm in the development version of the mixed quantum-classical dynamics software package Newton-X.[71, 184] Because many of the steps used in the FSSH algorithm are the same as those in QTSH (in the adiabatic representation), there were limited changes to be made to the architecture of the source code. Firstly, I needed to modify to the surface hopping algorithm such that it removed the velocity re-scaling that occurred after a hop. Secondly, I needed to implement the semiclassical equations of motion in Eqn. 5.19. The momentum derivative $\dot{\mathbf{p}}$ is expensive to calculate since it contains the spatial derivative of the NAC vector $\nabla \mathbf{d}_{mn}$. Furthermore, to my knowledge neither the analytical nor numerical gradient of $\mathbf{d}_{mn}$ is readily available as an output in any electronic structure packages. To bypass this, the momentum gradient can be rewritten as

$$\dot{\mathbf{p}} = -\nabla U(\mathbf{q}) + 2\hbar \sum_{n} \sum_{k<n} \dot{\mathbf{d}}_{kn}(\mathbf{q}) \beta_{kn} \tag{5.19}$$

since $\dot{\mathbf{d}}_{kn} = \dfrac{\mathbf{d}_{kn}}{\mu}(\mathbf{p} \cdot \nabla)$. It is significantly easier to evaluate the time derivative of $\mathbf{d}_{kn}$ at each step along a trajectory, by simply subtracting $\mathbf{d}_{mn}(t - \Delta t)$ from $\mathbf{d}_{mn}(t)$ and dividing through by the time step. However, this introduces numerical errors that scale with step size.

Another approach to simplifying the integration of the classical EOM is to transform the canonical momentum $\mathbf{p}$ to the kinematic momentum $\mathbf{p}_{kin}$ as described by Cotton *et al.*[228] This avoids both the costly requirement to evaluate the spatial derivative of the nonadiabatic coupling in equation 5.15b, and the numerical errors in the calculation of the time derivative of the coupling. For a two state system, the kinematic momentum is written as

$$\mathbf{p}_{kin} = \mathbf{p} - 2\hbar \mathbf{d}(\mathbf{q}) \beta \tag{5.20}$$

and its time derivative can be determined by applying the chain rule.

$$\dot{\mathbf{p}}_{kin} = \dot{\mathbf{p}} - 2\hbar \dot{\mathbf{d}}(\mathbf{q}) \beta - 2\hbar \mathbf{d}(\mathbf{q}) \dot{\beta} \tag{5.21}$$

Combining the fact that the time derivative of the coherence $\dot{\beta}$ is $-\omega(\mathbf{q})\alpha$ and that the time derivative of the canonical momentum is given in the original EOM (equation 5.19) transforms equation 5.21 to

$$\dot{\mathbf{p}}_{kin} = -\nabla U(\mathbf{q}) + 2\hbar \omega(\mathbf{q}) \mathbf{d}(\mathbf{q}) \alpha \tag{5.22}$$

which in combination with

$$\dot{\mathbf{q}} = \frac{\mathbf{p}_{kin}}{\mu} \tag{5.23}$$

makes this set of EOM far simpler to integrate numerically.

5.4.1 The integrator

To ensure the accuracy of the QTSH algorithm, a suitable integration method for solving the differential equations of motion (equations 5.14) must be selected. Desirable properties for an integrator include energy conservation, tolerance of larger time step size without significant errors, and symplecticity (conservation of phase space volume). It is especially important for an integrator to be symplectic at longer timescales.[229] Velocity Verlet is a popular choice for classical molecular dynamics due its accuracy and simplicity. As the classical Hamiltonian for molecular motion is fully separable, $H(q,p) = T(p) + V(q)$, the Verlet algorithm is symplectic. The difficulty that arises in this case, is that the Hamiltonian for the system (given in equation 5.16) is not separable. There is no general explicit method for integrating non-separable Hamiltonians – although there are existing methods for some sub-classes of such Hamiltonians.[230] Here an *explicit* integration method is one where it is possible to calculate the state of a system at time $t + \Delta t$ knowing only the state of the system at time t – familiar Euler and Verlet schemes fall into this category. Generally, non-separable Hamiltonians are integrated by *implicit* integration methods which work by solving an equation whose limits are the initial and final states of a given system. This approach is significantly more expensive, and difficult to implement for on-the-fly dynamics.

The Euler integrator is the most straightforward explicit method for the solution of ordinary differential equations (ODEs) with some initial value. The implementation of the Euler integrator at each time step with initial values $(\mathbf{q}(t_0), \mathbf{p}(t_0))$ is as follows,

$$\mathbf{q}(t_0 + \Delta t) = \mathbf{q}(t_0) + \dot{\mathbf{q}}(t_0)\Delta t$$
$$\mathbf{p}(t_0 + \Delta t) = \mathbf{p}(t_0) + \dot{\mathbf{p}}(t_0)\Delta t$$

where the time derivatives of position and momentum are given in equation 5.14. Because this is the most basic integrator, the error scales with the square of the time step Δt causing significant divergence from the analytical solution at longer timescales. This method is neither symplectic nor time-reversible, but is used here as a baseline for testing the implementation of QTSH.

The Euler method is the simplest of a larger set of Runge-Kutta methods. Of these, fourth order Runge-Kutta (RK4) is one of the most commonly used numerical integration methods. Its error scaling with time step size is much more favourable than the Euler integrator, scaling as $O(\Delta t^5)$. The standard RK4 propagation algorithm is complicated by applying it to multiple co-dependent variables evolving in time, which in this case are $\mathbf{p}_{kin}$, $\mathbf{p}$, $\mathbf{q}$, $\mathbf{d}(\mathbf{q})$, α, β, and the density matrix $\mathbf{a}$ for each trajectory. In the following algorithm, I use the general notation $F(\{v\})$ where F is a general function of a set of variables $\{v\}$ whose values at the start of the integration

step are $\{v_0\}$.

$$
\begin{aligned}
k_1^F &= \Delta t \dot{F}(\{v_0\}, t + \Delta t/2) \\
k_2^F &= \Delta t \dot{F}(\{v_0 + k_1^v/2\}, t + \Delta t/2) \\
k_3^F &= \Delta t \dot{F}(\{v_0 + k_2^v/2\}, t + \Delta t/2) \\
k_4^F &= \Delta t \dot{F}(\{v_0 + k_3^v\}, t + \Delta t) \\
F(t_0 + \Delta t) &= F(t_0) + \frac{k_1^F + 2k_2^F + 2k_3^F + k_4^F}{6}
\end{aligned}
$$

This numerical integration strategy is often favoured because of its accuracy. However, because this method requires the re-calculation of the forces, and therefore α, β, and $\mathbf{d}(\mathbf{q})$ at each time step it can become expensive, so typically RK4 uses a larger time step.

Second order Runge-Kutta (RK2), sometimes referred to as the midpoint method, is a cheaper alternative to RK4 as forces only need to be re-calculated twice per time step, while maintaining favourable scaling of $O(\Delta t^3)$. RK2 uses the gradient at the midpoint of the integration step to predict the subsequent position. This algorithm is written out explicitly below, this time in terms of the phase space variables $\mathbf{q}$ and $\mathbf{p}$.

$$
\begin{aligned}
k_1^q &= \Delta t \dot{\mathbf{q}}(t_0) \qquad k_2^q = \Delta t \dot{\mathbf{q}}(t_0 + \Delta t) \\
k_1^p &= \Delta t \dot{\mathbf{p}}(t_0) \qquad k_2^p = \Delta t \dot{\mathbf{p}}(t_0 + \Delta t) \\
\mathbf{q}(t_0 + \Delta t) &= \mathbf{q}(t_0) + \frac{(k_1^q + k_2^q)}{2} \\
\mathbf{p}(t_0 + \Delta t) &= \mathbf{p}(t_0) + \frac{k_1^p + k_2^p}{2}
\end{aligned}
$$

The last integration method that I will consider is leapfrog integration. This strategy is appealing in this case due to its time reversibility, meaning that if at the end point of each trajectory the sign of the time step was reversed, the trajectory will return to its exact original position. Time reversibility means that many important quantities such as energy and angular momentum are conserved. Furthermore, the error scales favourably as $O(\Delta t^3)$. The equations for propagating the phase space variables are

$$
\begin{aligned}
\mathbf{p}(t_0 + \Delta t/2) &= \mathbf{p}(t_0 - \Delta t/2) + \mathbf{a}(\mathbf{q}(t_0))\mu\Delta t \\
\mathbf{q}(t_0 + \Delta t) &= \mathbf{q}(t_0) + \mathbf{p}(t_0 + \Delta t/2)\Delta t
\end{aligned}
$$

where $\mathbf{a}$ is the acceleration at position $\mathbf{q}(t_0)$. Ultimately, I choose to implement the leapfrog integration method in Newton-X. It's simple, its error is comparable to RK2, and energy drift is limited on a longer timescale, making it an appealing choice in this case.

5.5 Testing the QTSH implementation

In this section the performance of the QTSH algorithm will be compared against FSSH for a number of model systems that are commonly used to benchmark novel nonadiabatic dynamics

methods. Strengths and weaknesses of the various algorithms described in the previous section will be explored, and the limitations of the QTSH method will be highlighted. The results will be compared to exact quantum wavepacket calculations in the diabatic representation which used Kosloff's propagation method.[231] Scripts that implement this method were generously provided by Prof. Martens.

5.5.1 Tully's model systems

The three 1-dimensional systems suggested by Tully in 1990 have become benchmarks for new nonadiabatic dynamics methods.[192] The integration algorithms for non-separable Hamiltonians described in the previous section will be tested on Tully's single avoided crossing model in order to determine the best integrator to implement in Newton-X.

These algorithms were implemented in a set of Fortran 90 scripts that executed the QTSH calculations for an ensemble of 10^4 trajectories that evolved for 2400 a.u. (an atomic time unit is $\hbar/E_h$) with $\Delta t = 0.1$ a.u. and with initial momentum $\hbar k = 10$. In the following calculations I used the kinematic momentum instead of the canonical momentum, as given in Cotton *et al.*,[228] as it avoids the need to calculate the time derivative of the NAC vector which would introduce additional errors to the calculation. In Fig. 5.2 the comparison is shown in how the state populations evolve over the course of the simulation for the set of integrators that were considered. Convergence with time step length is also illustrated, showing that all methods converge to the same answer even with the relatively large time step of 10 a.u..

Energy conservation over the course of the simulation is illustrated in Fig. 5.3. The total energy E_{tot} is the diagonal energy E_{diag} with an additional coherence energy term E_{coh}. The coherence energy is required to balance the energy budget and depends on the coupling between the states and off-diagonal coherences of the density matrix, and therefore it peaks as the wavepacket moves through the crossing region. Fig. 5.3 shows that there is a small upwards drift in E_{tot} of 2%, which becomes marginally less significant with the use of a smaller time step. Because the energy re-scaling after a hop is not applied in the QTSH algorithm, there is no artificial constraint that enforces the conservation of energy at the individual trajectory level. Formally, the energy is conserved at ensemble level so some variation may be expected due to finite ensemble size, or the cumulative error of numerical precision.

Another variable in the implementation is the question of how the NAC vector will be used in the EOM, discussed in section 5.4. There are three possible options: using explicit spatial derivatives of the NAC vector which is not available to compute in most electronic structure packages; using the time derivative of the NAC vector; or using the kinematic momentum. In Fig. 5.4 a comparison is shown between the latter two implementations, for the same model as used previously. Although the time derivative strategy returns noisier results, it can be seen that energy is conserved more effectively than when using $\mathbf{p}_{kin}$. For this reason, this strategy is used in the Newton-X implementation by storing the NAC coupling vector from the previous time step

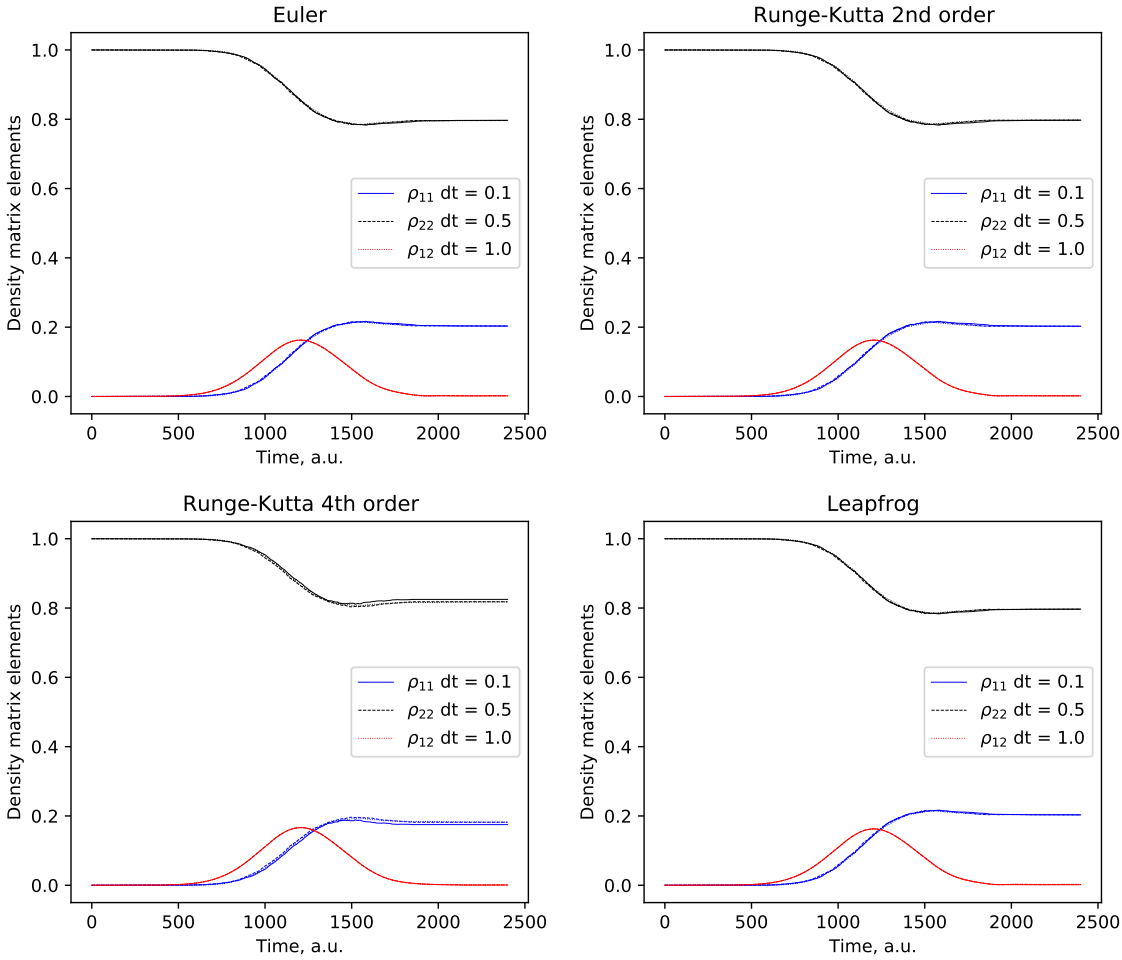

Figure 5.2: Density matrix element convergence with time step size. Comparison between integrator algorithms for 10000 trajectories moving through Tully's avoided crosssing model in the adiabatic representation.

in memory.

In order to implement these changes in the Newton-X code (also written in Fortran 90) I created a separate module containing the new integrator functions and a corrected surface hopping subroutine which removed the momentum rescaling following a hop. Results of the QTSH calculation in the adiabatic representation for Tully's single avoided crossing model are shown in Fig. 5.5 for two initial momenta $\hbar k = 10$ and $\hbar k = 15$. In these calculations I ran 500 trajectories each, with a time step of 0.2 a.u.. The initial positions are generated from a Gaussian distribution centered on $\mathbf{q} = -6.0$ with $\sigma = 1.0$. These results are consistent with those given in Martens' paper.[222]

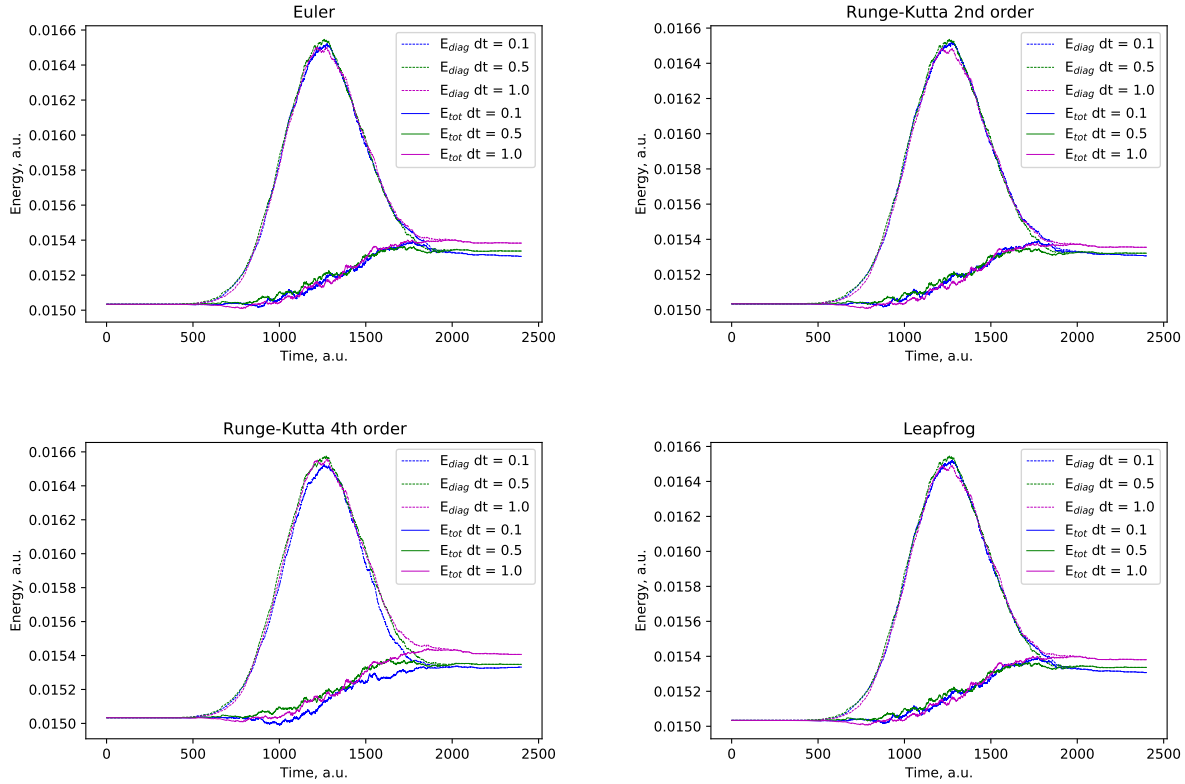

Figure 5.3: Conservation of total energy over time, compared for all considered integration algorithms and time step sizes. Plots show evolution of total energy E_{tot} and sum of kinetic and potential energy E_{diag} which excludes coherence energy discussed in Martens' paper.[222]

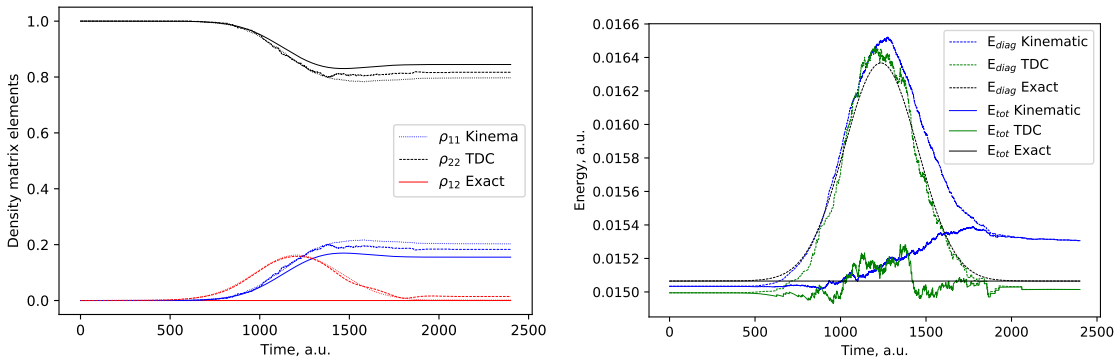

Figure 5.4: Comparison between strategies of trajectory propagation, using kinematic momentum given in Eqn. 5.21, or the time derivative coupling in Eqn. 5.19.

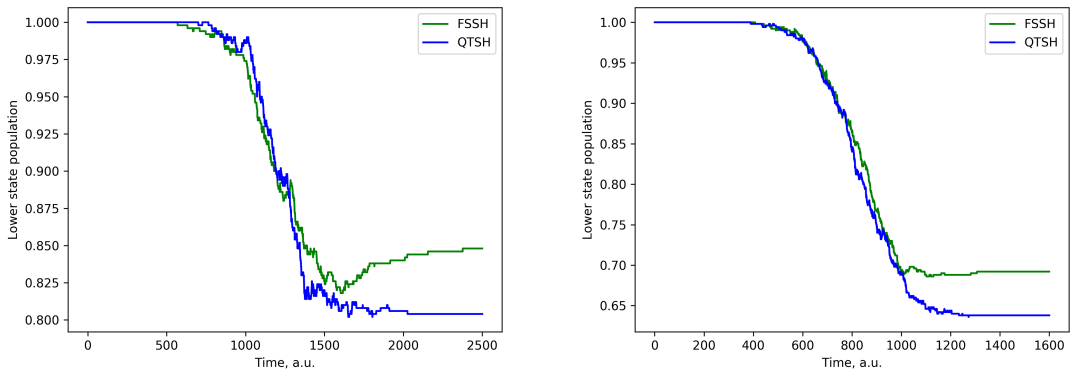

Figure 5.5: Time dependence of the adiabatic lower state population computed with FSSH and QTSH for Tully's avoided crossing model, with initial momenta $\hbar k = 10$ (left) and $\hbar k = 15$ (right). The RK2 integrator is used in the QTSH calculations and no decoherence corrections are applied.

5.5.2 Spin-boson Hamiltonian

A widely studied analytical model system for electron transfer processes is the spin-boson Hamiltonian (SBH).[232] The SBH is a two state system coupled to a dissipative environment, in this case a bath of harmonic oscillators. The SBH Hamiltonian contains three components – system, bath, and the linear system-bath coupling. When decoupled from the bath, the two electronic states of the system are separated by $2\epsilon_0$ and coupled by ν_0.

$$\hat{H} = H_{system} + H_{bath} + H_{coupling} \tag{5.24a}$$

$$H_{system} = \sigma_z \epsilon_0 + \sigma_x \nu_0 \tag{5.24b}$$

$$H_{bath} = \mathbf{I}\frac{1}{2}\sum_{k=1}^{N}\left(\frac{P_k^2}{M_k} + M_k\omega_k^2 R_k^2\right) \tag{5.24c}$$

$$H_{coupling} = \sigma_z \sum_{k=1}^{N} g_k R_k \tag{5.24d}$$

In the above equations, σ_x and σ_z are Pauli matrices N is the number of oscillators each with respective mass, momentum, position, and frequency M_k, P_k, R_k, and ω_k. The coupling constant for each oscillator to the system is g_k and $\mathbf{I}$ is the 2×2 identity matrix. Energies, gradients and nonadiabatic couplings are all available for this model in an analytical form.[167]

Example parameters for this model were taken from Dral *et al.*[167] which used an adiabatic SBH model intended to roughly reproduce the S_1/S_0 dynamics of cytosine. Oscillator frequencies are the 33 normal modes at the cytosine ground state optimised with B3LYP/6-31G(d). Of these modes, two couple strongly to the system (as in a CI branching space) with system-bath coupling $g_k = 0.012\ E_h/a_0$ and the rest coupling with $g_k = 0.001\ E_h/a_0$. Other parameters are set arbitrarily, $\epsilon_0 = 12000\ \text{cm}^{-1}$ and $\nu_0 = 800\ \text{cm}^{-1}$.

The initial conditions for the trajectories $[\mathbf{p}_0, \mathbf{q}_0]$ can be sampled in a number of ways, including sampling from a Wigner distribution, or using action angle variables. In this case we simply randomly sampled a set of 200 velocities and geometries from a 2 ps MD run. Each initial condition was ran with 5 replicas to aid convergence (same geometry and velocity, new random seed), so a total of 1000 SBH trajectories were executed. Each QTSH trajectory evolved for 2 ps with time step of 0.1 fs, whilst for the FSSH results a time step of 0.2 fs was used.

In Fig. 5.6 we see a comparison between the QTSH and FSSH result for the evolution of the upper state population in the adiabatic SBH model. The FSSH result was taken from Dral *et al.*[167] The QTSH decay from the upper S_1 state reproduces the final state fraction from FSSH to an acceptable accuracy, as well as the shape of the decay profile including the slight oscillations in the state populations seen at 250, 500, and 750 fs. The total energy is conserved over the course of the simulation, although there are fluctuations that could be due to the numerical instability of the integrator at larger time steps. This agreement indicates that it will be possible to apply the QTSH algorithm to more complex, atomistic molecular systems, although further work is needed to ensure that the algorithm is numerically stable.

5.6 Conclusions

In this chapter I have reported on the work I carried out in the implementation of a novel nonadiabatic dynamics algorithm in an existing complex code base. The challenges of implementation were mainly due to the non-separable nature of the Hamiltonian, which were resolved by selecting an appropriate numerical integration scheme for the EOM. Another limit in the applicability of this method in comparison to FSSH is that it requires the explicit calculation of the NAC vector. Most implementations of FSSH use time derivative couplings to compute surface hopping probabilities, which can be calculated from wavefunction overlaps for any electronic structure theory method.[233] The NAC vector isn't as readily available as the CI (wavefunction) overlap in electronic structure software. In fact, CI overlaps have been shown to be more numerically stable in cases of rapidly varying NAC vectors.[234]

Questions also remain about how to implement decoherence corrections which in Martens' work are based on trajectory "phases", but are applied at ensemble level. This is difficult to apply to each trajectory when they are being executed independently, so for now the Granucci-Persico scheme based on the energy gap between states is deemed sufficient. With further work, the QTSH strategy could prove to be a successful alternative to FSSH with an explicit stepwise derivation from the QLE, whilst maintaining the useful independent trajectory feature. In future work it will be valuable to apply this method to well benchmarked molecular systems such as the photodynamics of the methaniminium cation.

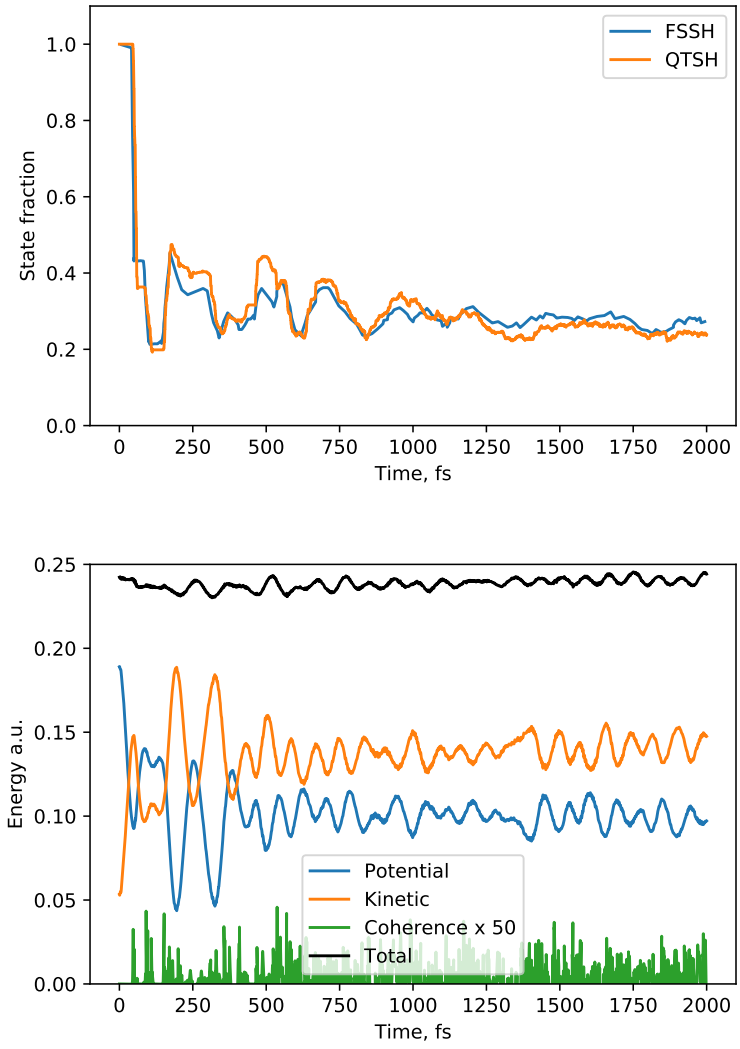

Figure 5.6: QTSH results for an adiabatic SBH model. Top panel shows the average fraction of trajectories (1000 total) on the upper S_1 adiabatic state over the course of the simulation. The bottom panel shows the energy budget of the QTSH simulation.

CHAPTER 6

SOLVENT EFFECTS IN PHOTOCHEMISTRY

In accordance with the University of Bristol guidance on the integration of publications as chapters within a dissertation, I declare that sections of this chapter were previously published in Zeitschrift für Physikalische Chemie.[235] My role in this work was to design the computational protocol, run the calculations, and write the parts of the manuscript that related to the computational parts of this study. Experiments were performed primarily by Dr Mahima Sneha with Luke Lewis-Borrell, Prof. Aditi Bhattacherjee and Jasper Tyler. The manuscript was written primarily by Prof. Andrew J. Orr-Ewing.

6.1 Introduction

Photosynthesis, bio-fluorescence, photon-induced charge transfer, and photoredox catalysis are all examples of photochemical processes that occur in solution.[236–239] Transient absorption spectroscopy experiments designed to study the photochemical dynamics of these and other processes are typically performed in a solvent phase due to the low concentration of molecules in the gas phase. However, in theoretical calculations the solute is often treated independently of its surroundings because of the complexity of selecting an appropriate model of the solvent environment. Theoretical descriptions of solvation can be split into two general categories: implicit solvation where the solvent is treated as a bulk polarising environment for the solute; or explicit solvation where atomistic solvent molecules surrounding the solute are included in the calculation.

Methods for calculating excited state properties also fall between these two limits. There are numerous studies that use the solvent shift calculated using implicit solvent, often in combination with LR-TDDFT, to interpret their experiments.[240–242] In hydrogen bonded complexes, or for ionic solutes, where the solute-solvent interaction is strong, we might see some charge transfer to

the solvent molecule in the excitation process.[243] For such cases an implicit solvent model is inadequate to describe the impact of solvation on the electronic character of the excited state.

Explicit solvent is preferred in cases where non-electrostatic and hydrogen bonding interactions play an important role. For example, it improves the prediction of solvatochomic shifts in Nile red,[244] and for solvents with a low dielectric constant where electrostatic polarisation is weak. To create a realistic description of an explicitly solvated system necessitates the sampling of many solute-solvent conformations, typically by taking snapshots of an MD trajectory. This process is time consuming, and far from black-box, requiring a judicious choice of many parameters. Moreover, including a large number of explicit solvent molecules in the simulation will incur a significant increase in computational expense. Implicit solvation is appealing because it removes the solvent degrees of freedom such that it is similar in cost to a gas phase calculation. Some popular implicit solvation models, including the polarizable continuum model (PCM)[245] and the conductor-like screening model (COSMO),[246] are classified as apparent surface charge (ASC) methods. ASC methods use the notion of a charge distribution on the solute cavity surface to calculate the electrostatic potential on the solute. They are a subset of a wider range of continuum models, which include the generalised Born, multi-pole expansion, and SMx methods.[247]

Embedding methods can cut down the cost of explicit solvation by separating the system into parts that can be treated with different levels of theory. Density embedding approaches, such as projector-based embedding, do this by partitioning the electronic density matrix into two subsystems, and will be discussed further in section 6.4.[248] They have also been successfully applied to the prediction of highly accurate excitation energies in solvated systems.[249, 250] Polarizable embedding is a different embedding scheme which can also be used to calculate excitations in anisotropic environments like protein matrices. In this case the permanent charge distribution of the environment is represented by a multicenter multipole expansion.[251] Polarizable embedding has also been applied to the calculation of solvent shifts using a number of electronic structure methods including the algebraic diagrammatic construction (ADC) scheme,[252] LR-TDDFT,[253] and coupled cluster methods.[254]

In the first part of this chapter I will discuss the most widely used implicit solvation methods implemented in popular electronic structure packages, and use the example of N-phenyl phenoxazine photochemistry to show how these strategies can be applied to aid in the interpretation of time relsolved experiments. In the second part I will apply the projector based embedding approach developed by Bennie *et al.*[249] to a hydrogen bonded benzophenone complex and discuss how it might be used to reduce the cost of explicit solvation.

6.2 Continuum solvation models

Dielectric continuum models of solvation describe the bulk solvent in terms of the dielectric permittivity constant ε_s. This value defines the ability of a bulk medium to hold electrical charge

so tends to be higher for polar solvents like water (ε_s = 80.1) and acetonitrile (ε_s = 37.5), than for apolar solvents like toluene (ε_s = 2.4) or hexane (ε_s = 1.9).[255] The notion of a "cavity surface" which acts as the interface between solvent and solute is a central idea to continuum solvation methods. The cavity is defined so as to exclude all solvent atoms, but be large enough to contain the full electron density of the solute. Algorithms for the construction of the solute cavity are numerous, including the GEPOL algorithm where this surface is defined as a series of interlocking atom-centered spheres, segmented into triangular faces.[256]

A solute surrounded by an infinite dielectric is polarized by its solvent environment, which in turn is polarized by the charge of the solute. This sets up a self-consistent reaction-field (SCRF) problem where the result is found iteratively. This electrostatics problem can be solved by using the Poisson equation,

$$-\nabla \cdot [\varepsilon_s(r)\nabla V(r)] = 4\pi\rho_M(r) \tag{6.1}$$

where ρ_M is the solute charge distribution and $V(r)$ is the electrostatic potential. Given a ρ_M obtained from an electronic structure calculation, the Poisson equation is solved, given some boundary condition, for $V(r)$ which contains both the electrostatic potential generated by the solute's charge density and the "reaction field" arising from the polarization of the continuum.[247]

Approaches to numerically solving Eqn. 6.1 fall into a number of categories – ACS, multipole expansion (MPE), generalised Born models (GB), and finite element/finite difference methods.[257] I will focus on ACS methods in this chapter, since they are commonly implemented in electronic structure software. ASC methods simplify a 3-D problem to a 2-D representation by discretizing the cavity surface instead of the whole volume to compute the reaction field potential. I should note that it is also possible to solve the Poisson equation analytically for spherical or ellipsoidal cavities if we use a multipole expansion to express the inside charge density.[258] However, this doesn't work for most real molecules which need arbitrary shaped cavities.

Finally, there are a number of assumptions which apply when the solvent is treated as a continuum. The following methods give explicit expressions only for the electrostatic part of the solute-solvent interactions, and when non-electrostatic components are included it is only through empirical parameters. Solvent molecules are all assumed to be in their ground electronic state, and are not reacting with the solute. Concentration is assumed to be low enough that interactions between solute molecules are negligible. Bulk solvent beyond the cavity is completely isotropic therefore no influence of ordering or field effects is possible.

Polarizable Continuum Model The polarizable continuum model (PCM) is an ASC method in which the bulk dielectric permitivity is the ε_s of a given solvent while inside the cavity $\varepsilon = 1$. The original polarizable continuum model (PCM) paper was published in 1981 by Miertuš *et al.*[245] In their model, the solute is described by a charge distribution $\rho(r)$ within a cavity, beyond which is a continuum dielectric with permittivity ε_s. Since then a whole family of methods based on PCM have sprung up, with the original method being referred to as D-PCM (dielectric PCM),

and newer methods including C-PCM (conductor-like PCM) and IEF-PCM (integral equation formalism PCM) which is the formalism most commonly implemented in electronic structure software. IEF-PCM has been used in the calculation of circular dichroism spectra.[259]

COSMO The conductor like screening model (COSMO) is very similar to C-PCM in its formulation. It simplifies the ASC formulation of the Poisson problem by treating the solvent as a conductor $\varepsilon_s = \infty$ such that the total electrostatic potential vanishes at the cavity surface. To account for ε_s actually being finite, the unscreened charge density vector is scaled by a function of ε_s.

$$f(\varepsilon_s) = \frac{\varepsilon_s - 1}{\varepsilon_s + x}$$

The original COSMO paper[246] suggests that the value of x should be 0.5 based on the Onsager model of a dipole in a spherical cavity, but is in part determined by the cavity shape and the solute charge distribution.[247] A major limitation of COSMO was its inability to distinguish between solvents with similar dielectric constants, although this has been corrected to some extent in COSMO-RS (COSMO for realistic solvation).[260]

SMD The Universal Solvation Model (SMD) requires significantly more parameters than either of the previous methods.[261] It is based on the generalised Born model (which comes from an approximation to the Poisson equation) but its main advantage is the inclusion of non-electrostatic effects through these extra parameters, which are available for over 170 different solvents. For example, cavitation and dispersion energies are a product of the solvent accessible surface area of the cavity and the solvent specific surface tension. There is a whole class of SMx methods that are parametrized for different properties, and they are recommended for calculating solvation energies.[247]

6.2.1 Excited states

Solvent can stabilise or destabilise excited states depending on the dipole moment of the solute charge distribution, and the ε_s of the solvent. For vertical excitation energies it has been shown that a continuum IEF-PCM model can reproduce the solvent shift with similar accuracy to including explicit solvent.[243] There are two strategies to calculating the solvent shift, depending on the purpose of the calculation. Equilibrium solvation implies that the density used in the SCRF procedure is that of a specific excited state. This approach is often implemented as default for the geometry optimisation of excited states, as it implies that the solvent has reoriented itself in response to the new electrostatic potential generated by the excited state density. Alternatively, non-equilibrium calculations use the ground state density in the SCRF so are preferred for calculating vertical excitation energies from the ground state geometry because the solvent molecules do not have time to respond on that timescale.

6.3 NPP Photochemistry

Ruthenium and Iridium complexes have been widely used for selective and tunable catalysis of single-electron transfer (SET) reactions. A dearth of rare earth metals has inspired a search for more sustainable alternatives amongst organic dyes with suitable excited state properties, such as long S_1 and T_1 lifetimes, to faciliate SET. N-phenyl phenoxazine (NPP) is a prototypical N-aryl phenoxazine type organic photoredox catalyst (OPC) which is used to control rates of atom-transfer radical polymerisation reactions.[262–267] Polymerization rates in this type of OPC can be deliberately tailored by altering the side groups on the aryl rings using known design principles.[268] Fine tuning NPP photochemistry also relies on choosing a suitable solvent which can selectively stabilise particular states, and destabilise others, thus altering the rates of internal conversion or intersystem crossing involved in the catalytic mechanism.

The following computational study is intended to accompany a set of transient vibrational absorption spectroscopy (TVAS) and transient electronic absorption spectroscopy (TEAS) experiments. These experiments were used to explore the ultrafast photodynamics of NPP prior to SET. Equivalent TVAS and TEAS experiments were performed in N,N-dimethyl formamide (DMF), dichloromethane (DCM) and toluene. There were two core aims to this study. Firstly, to determine how the system evolves following photoexcitation with a 318 nm laser pulse. Secondly, to explore how this mechanism is affected by changing the solvent. Using a set of LR-TDDFT calculations performed in a continuum solvent model I assign the peaks of TVAS and TEAS spectra to electronic states and attempt to explain some of the experimentally observed differences in rate between the solvents.

6.3.1 Computational Details

Geometry optimisation of NPP and ground state vibrational frequency calculations in toluene, DCM and DMF solvents were performed using the Gaussian 09 program.[90] The CAM-B3LYP density functional was used with a 6-31+G* basis and Grimme dispersion corrections with Becke-Johnson damping. Solute-solvent interaction effects were accounted for through the conductor polarizable continuum model (C-PCM). TDDFT optimisations of S_1 and T_1 geometries using the same functional and basis were also performed in toluene and DMF, with normal mode analysis confirming that these geometries were the minima on their respective potential energy surfaces. An anharmonicity scaling factor of 0.953 was applied to the calculated normal mode frequencies prior to comparisons with experimental spectra.[269] Vertical excitation energies and oscillator strengths were calculated using the ORCA program (v4.2.0)[62] at the TDDFT/CAM-B3LYP/6-31+G* level of theory. The solvent shift was computed via the SMD solvation model that includes both electrostatic and non-electrostatic contributions. Transition dipole moments and oscillator strengths between excited states for the S_1 and T_1 geometries were computed from the results of the TDDFT calculations using the Multiwfn program for electronic wavefunction analysis.[270]

6.3.2 Results

Absorption spectra of NPP in the 250–450 nm range show a strong band centered at 325 nm which does not shift significantly in different solvents. The UV-Vis spectrum of NPP in toluene is shown in Fig. 6.1. Here, the $S_0 \rightarrow S_1$ excitation is calculated to be at 307 nm, with predominantly local excitation (LE) character over the phenoxazine core as can be seen at the bottom of Fig. 6.1. The stronger $S_0 \rightarrow S_2$ $\pi \rightarrow \pi^*$ absorption band with f = 0.056 at λ = 303 nm has similarly LE character, but the $S_0 \rightarrow S_3$ transition (λ = 290 nm, f = 0.0877 in toluene) shows more charge transfer (CT) character. Similar calculations in DCM and DMF (Fig. 6.2) predict $S_0 \rightarrow S_1$, S_2 and S_3 transitions at λ = 307, 294 and 289 (DCM) or 287 nm (DMF) respectively, with oscillator strengths of f = 0.022, 0.029 and 0.128 in DMF and f = 0.028, 0.039 and 0.115 in DCM. The S_2 state now shows CT character implying that it has been stabilized relative to the LE states by the more polar DCM or DMF solvents. At the excitation wavelength of 318 nm used in these experiments it is likely that the molecule is excited into a mixture of states, primarily LE S_2 and CT S_3 state for NPP in toluene, and the LE S_3 state in DCM or DMF.

Transient electronic absorption (TEA) spectra are measured up to 1200 ps in the 350–700 nm wavelength range. The most prominent feature observed in the TEA spectra is a band with Gaussian profile centred near 460 nm in all three solvents. This feature is the last to emerge over the course of the reaction and is accordingly assigned to absorption from the T_1 state of NPP. This assignment is supported by calculations reported in Appendix C which predict a strong T_1 excited state absorption band (with oscillator strength f = 0.13) at 513 nm in DMF and 496 nm in toluene (with f = 0.08). Similar triplet state ES absorption bands were observed by Sartor et al. for modified versions of NPP with phenyl or biphenyl core substituents, albeit shifted to longer wavelength by the additional core conjugation.[271] Earlier on in the experiment we observe the loss of absorption at wavelengths above 550 nm and a growth then decay of an intermediate band peaking near 520 nm (with a secondary peak at wavelengths around 390 nm). The evolution of the spectral shape shows solvent-dependence, as this double-peaked feature at 520 nm is more prominent for spectra measured in DCM or DMF than in toluene where it is barely discernible as a broad feature above 500 nm. Plausible assignments of the rapidly decaying long-wavelength absorption and the 520 nm intermediate band are to excited state absorption from the initially photoexcited S_n (n = 2 or 3) state and the S_1 state into which it relaxes by internal conversion (IC). TDDFT calculations summarized in Appendix C predict a strong S_1 absorption band at 560 nm in DMF (f = 0.44) and 565 nm in toluene (f = 0.14). The lower oscillator strength in toluene may explain why this feature is less distinct for TEA spectra measured in this solvent. Decay of the S_1 state population proceeds either via a) intersystem crossing (ISC), resulting in growth of T_1 population, or b) relaxation by IC or fluorescence to S_0, or c) reaction with the solvent which occurs in the case of DCM.

In the transient vibrational absorption (TVA) spectra obtained following the 318-nm photoexcitation of NPP we observe peaks emerging and disappearing on a slower 1000 ns timescale. We

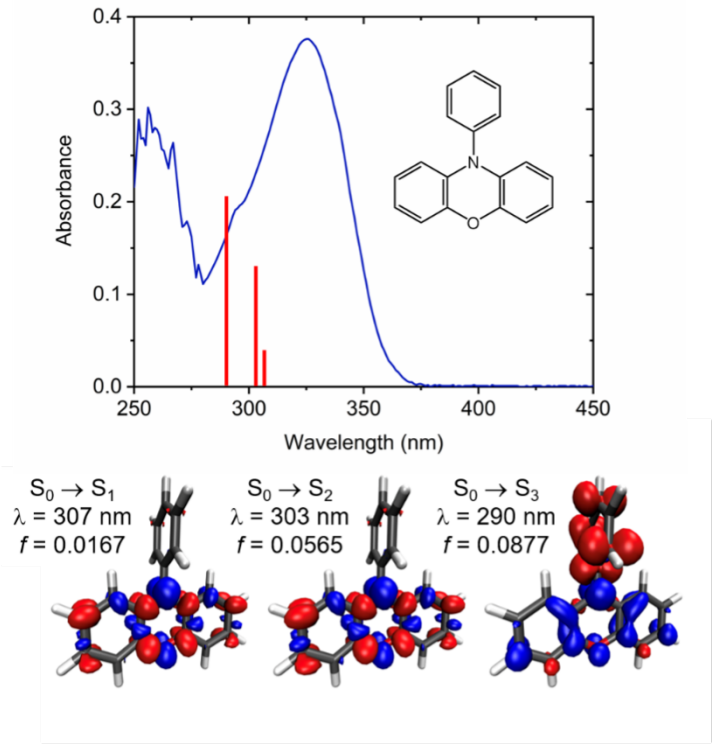

Figure 6.1: UV absorption spectrum of a 3.2 mM solution of NPP in toluene. The structure of NPP is shown as an inset. Bottom: Electron density difference plots between the S_0 and S_n states for n = 1, 2 and 3 at the S_0 geometry, showing the local excitation character for $S_0 \rightarrow S_1$ and $S_0 \rightarrow S_2$ transitions, and greater charger transfer character for the S_3 state. The calculations were performed in toluene, the densities are visualised with isovalues set to 0.002, and an increase in electron density is shown in red, with a decrease in blue. Calculated excitation wavelengths (λ) and oscillator strengths (f) are given for the first three ES. These computed properties are also shown as red vertical bars superimposed on the absorption spectrum, with the bar heights proportional to f values.

can assign these peaks by comparing them against the computed IR band wavenumbers at S_1 and T_1 geometries, available in Appendix C. A broad transient absorption feature spanning 1500 – 1590 cm^{-1} is assigned to absorption from the S_1 state because of its observed wavenumber range and time-dependence corresponding to the peak at ~ 560 nm in TEA spectra. The reason for the breadth of this band is not apparent from the calculations which predict a single strong feature and other much weaker bands in this wavenumber region. We see no bands that can be assigned to NPP excitation from the T_1 state because the calculated T_1 band positions are masked by strong solvent absorptions in DMF, and the bands intensities are computed to be weak in all three solvents.

A schematic that illustrates the suggested mechanism for the excited state dynamics of NPP can be seen in Fig. 6.3. Lifetimes of each state are calculated from the time-dependent integrated

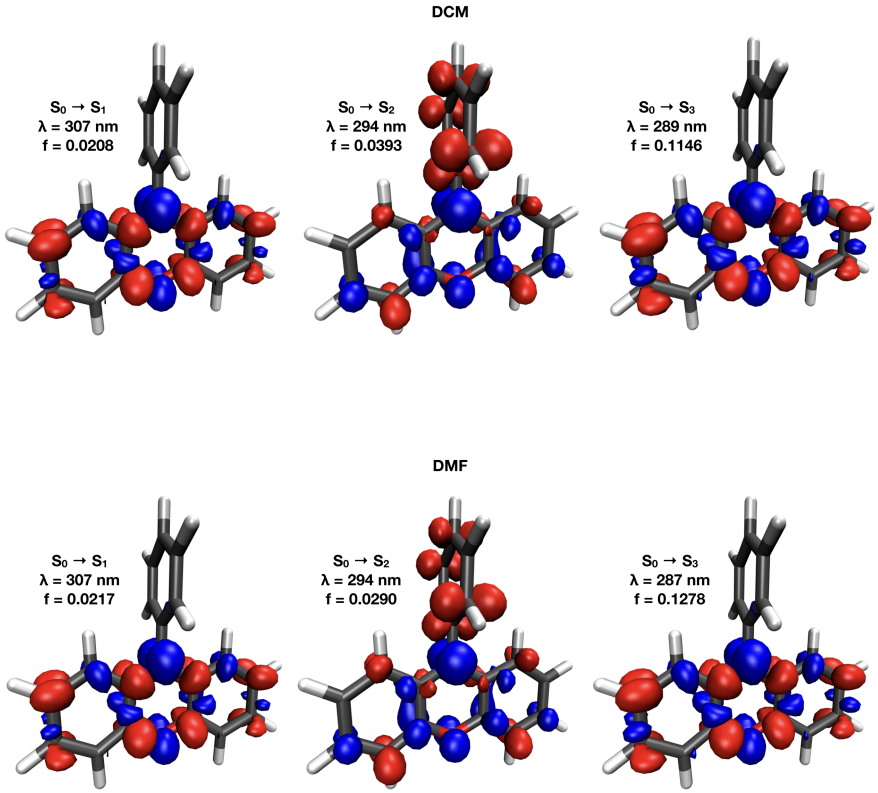

Figure 6.2: Electronic density difference plot for S_0 to S_1, S_2, and S_3 excitations in dichloromethane (Top) and dimethyl formamide (Bottom).

band intensities which were extracted using the KOALA program.[272] Photoexcitation to the S_n state (n = 2 or 3) at 318 nm is followed by competitive IC to S_1 and S_0 (the latter perhaps instead from vibrationally hot S_1 molecules) and vibrational energy transfer to solvent on timescales of over 20 ps. IC from S_n or S_1 to S_0 requires conical intersections which are not shown. The S_1 lifetime is 2 ns, with decay by competing fluorescence to S_0 (blue arrow) and ISC to the triplet manifold (represented here only by the T_1 state). The T_1 state decays to S_0 on timescales greater than 25 ns which appear to be influenced by quenching by dissolved O_2. Computational normal mode analysis confirms the assignment of these states to peaks in TEA and TVA spectra. Excited state calculations in implicit solvent show a change in the ordering of CT and LE character states (S_2 and S_3) between DMF and Toluene. In future work, we could identify the CI between S_n and S_1 states in Toluene and DMF so as to better understand the greater prominence of the TEA spectral peak at 520 nm in a more polar solvent.

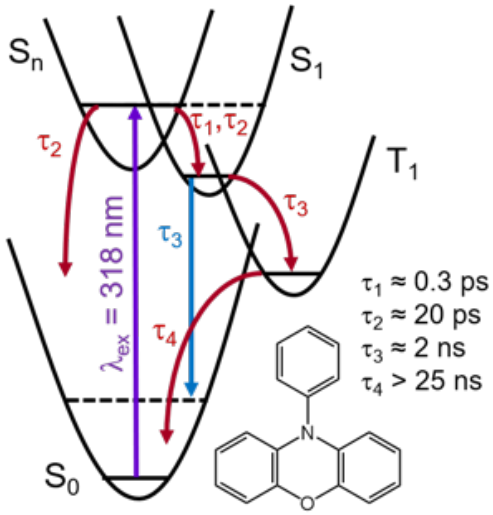

Figure 6.3: Schematic potential energy curves and relaxation pathways for the photochemistry of NPP in solution. Horizontal solid and dashed black lines indicate the lowest and an excited vibrational level of an electronic state, respectively.

6.4 Projector based embedding for excited states

Continuum solvent models cannot be used to compute excitations for systems in which non-bonded interactions between solute and solvent play a significant role in stabilising/destabilising the excited state.[273] Including explicit solvent molecules in the system can quickly become expensive, and such calculations would be limited to LR-TDDFT which introduces a functional dependence and can fail for Rydberg, CT states, and double excitations. It is however possible to calculate excited state energies using state-of-the-art wave function methods at a reasonable cost by using projector-based embedding (PBE). This systematically improvable method was first proposed for ground state systems by Manby *et al.* in 2012.[248] PBE treats a subsection of the system with a higher level wave function (or DFT) method polarized by a potential constructed using a cheaper DFT (or HF) method, thereby allowing WF-in-DFT, DFT-in-DFT, or WF-in-HF embedding. As well as the improvement in computational cost, PBE can be used to pinpoint the importance of specific MOs in determining the excitation energy.

Following a Kohn-Sham (KS) DFT calculation, the total density matrix is split into a sum of active (A) and background (B) parts.

$$\rho = \rho_A + \rho_B$$

Whether an orbital is part of ρ_A or ρ_B can be determined by where it is localised, its Mulliken population, or by any other sensible criterion. These sets of KS orbitals are used to construct the reduced one particle density matrices of the two subsystems, γ_A and γ_B. The Fock matrix for the active region A is given in Eqn. 6.2

$$\mathbf{F}^A = \mathbf{H} + \mathbf{J}\left[\gamma^A + \gamma^B\right] + \mathbf{v}_{xc}\left[\gamma^A + \gamma^B\right] + \mu\mathbf{P}^B \tag{6.2}$$

where $\mathbf{H}$ is the core Hamiltonian, $\mathbf{J}$ is the Coulomb potential, $\mathbf{v}_{xc}$ is the exchange-correlation potential, and $\mu\mathbf{P}^B$ is the level shift operator. Projection operator $\mathbf{P}^B$, and level shift parameter μ, in the limit of $\mu \to \infty$, enforce orthogonality between the active and background orbital sets by elevating the orbitals that construct γ_B to an inaccessibly high energy, thus enforcing the Pauli principle. Practically, the level shift parameter μ is typically set to 10^6–10^{10}. Because subsystem A is treated independently of B, PBE gives us flexibility in the choice of electronic structure method for A which is specified by modifying the core Hamiltonian $\mathbf{H}$ in the Fock matrix.

Recent applications of this method to excited states include formaldehyde solvated in water (EOM-CCSD),[249] and an NO-Ruthenium Nitrosyl model complex (SA-CASSCF).[274] A similar, absolutely localised, embedding approach based on the Huzinaga operator was suggested by Wen *et al.*.[250] By drastically truncating the basis to only include orbitals localised on the atoms involved in the excitation, they were able to significantly reduce the cost of the calculation while maintaining a reasonable level of accuracy.

6.4.1 Benzophenone photochemistry

Benzophenone (Bzp) is a molecule with interesting photophysical properties. Its S_1 ($n\pi^*$) and T_2 ($\pi\pi^*$) state minima are almost isoenergetic, leading to highly efficient inter-system crossing (ISC). This property has led to its widespread use in sunscreen, as an industrial photocatalyst, and as a DNA photosensitizer.[3, 275, 276] However, the mechanism of this ISC remains open to investigation and has been a subject of many experimental and computational studies.[277–281]

There are two main pathways that follow the photoexcitation of Bzp into its S_1 state. The lowest triplet state T_1 ($n\pi^*$) could be populated directly, or via a T_2 ($\pi\pi^*$) intermediate, with subsequent internal conversion to T_1. The latter pathway is favoured by El-Sayed's rule which forbids direct ($n\pi^* \to n\pi^*$) transitions. Recently, Venkataraman *et al.* highlighted the crucial role that solvation, specifically hydrogen bonding, plays in determining the relative importance of the direct and indirect pathways.[278] They showed that a solution of Bzp in methanol can be selectively photoexcited by using a shorter 340 nm pulse to excite the hydrogen-bonded (HB) Bzp and a 380 nm pulse to excite the free, "dangling carbonyl" (DC) Bzp. The time constant for ISC is significantly slower with the shorter 340 nm pulse : 1.7 ps compared to <0.2 ps with a 380 nm pulse, which is ascribed to HB altering the energies of these states.

Previously, the nonadiabatic dynamics of this reaction were explored with Floating Occupation Molecular Orbitals Configurations Interaction (FOMO-CI),[280] and CASSCF(12,11),[282] however solvent was not included in either of these studies. Accurate calculations of the HB and DC Bzp structures are necessary to understand this mechanism, and in this study I apply PBE to explore the excited states of Bzp in MeOH solution.

6.4.2 Computational details

Geometry optimisations of gas-phase Bzp and a hydrogen bonded Bzp-MeOH complex were performed with B3LYP/cc-pVDZ in Gaussian 16.[64] Firstly, I ran PBE calculations on the gas-phase Bzp, iteratively increasing the active region from 5 MOs, until it included the whole molecule. In these calculations, I used the Laplace-transformed local CC2 response method described in Freundorfer *et al.* in the active region,[283] and density fitted DFT with the B3LYP exchange-correlation functional for the background region. I selected LT-CC2 for the calculation of the first 10 singlet states as this method shows good accuracy against a CASPT2 benchmark for singlet states, even when they contain double excitation character (0.4 eV average error).[284, 285] The aug-cc-pVDZ basis was used for both regions, and orbitals were selected on the basis of their Mulliken populations, as in Bennie *et al.* For the Bzp-MeOH complex, the additional 6 atoms increased the cost significantly so I chose to run a preliminary CIS/aug-cc-pVDZ calculation embedded in density fitted DFT (B3LYP/aug-cc-pVDZ), iteratively increasing the active space from 8 to 58 MOs. This was to determine if a cheaper PBE calculation can guide us in the choice of the active region. I then executed CC2-in-DFT PBE calculations for the Bzp-MeOH complex selecting the active region based on the previous CIS calculation for the first 10 singlet, and first 10 triplet states.

All PBE calculations were performed in Molpro 2019.[286] Molecular orbitals are visualised using Avogadro V1.2.0.

6.4.3 Results and Discussion

Results of PBE calculations for gas-phase Bzp are given in Fig. 6.4. Initially we see the ordering of states shift drastically, but when 16 MOs are included in the active region the ordering stabilises, and the error against the full CC2 result falls to below 0.1 eV when 30 MOs are included in the active region. This highlights the power of the PBE approach, since the total CPU time required for the full CC2 calculation was 2.5× that at 30 MOs, and that most MOs do not have a significant unilateral impact on excitation energy.

The next step is to include a hydrogen bonded MeOH molecule in the system. Preliminary CIS results shown in Fig. 6.5 tell us that the excitation energies converge to within 0.1 eV of the full system CIS result when 44 of the total 58 MOs are included in the active region. Since the B3LYP/aug-cc-pVDZ orbitals that are used in the CIS PBE calculations are the same as those used in the CC2 calculations, we can use Fig. 6.5 to guide our choice of active region. Looking at the orbitals that lead to significant jumps in excitation energies shows us that that MOs localised on the solvent molecule play a crucial role. We see this at points C and E highlighted in Fig. 6.5. The MO at E is also the HOMO.

The CC2 embedded excitation energies for the Bzp-MeOH complex are shown in Fig. 6.6. Due to the expense of the method, a full CC2 calculation was not possible – with the largest active region size being 50 MOs out of 58. However, as with CIS, we see that at 44 MOs the excitation

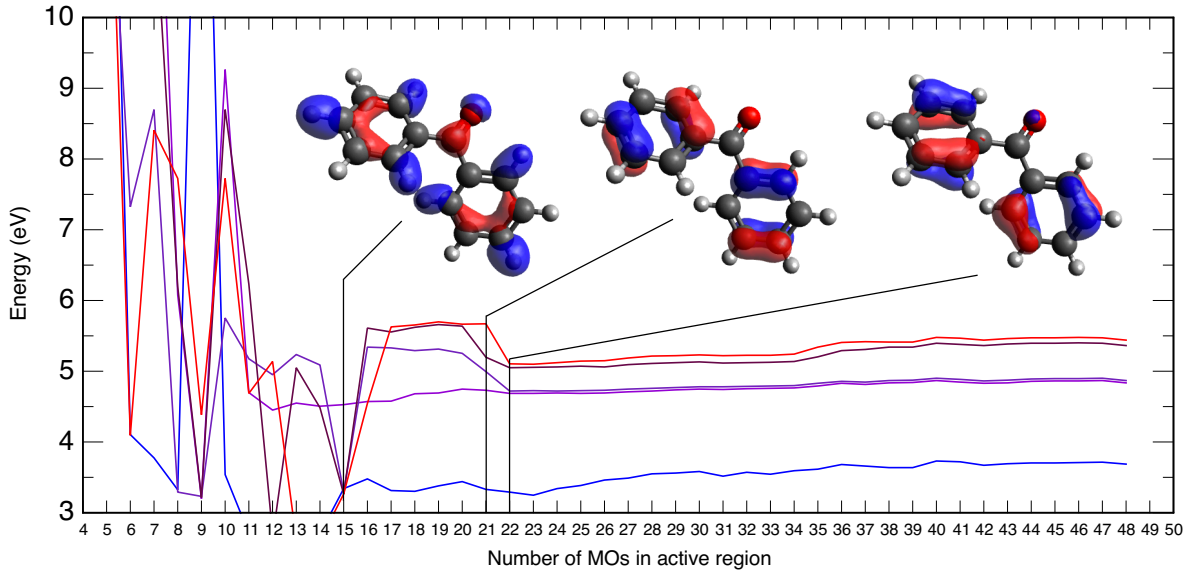

Figure 6.4: Convergence of the CC2/aug-cc-pVDZ//df-B3LYP/aug-cc-pVDZ excited state energies for the first 5 singlet states with increasing embedded region for gas phase Bzp. Molecular orbital diagrams highlight the orbitals that caused notable jumps in energy when they were added in to the active region.

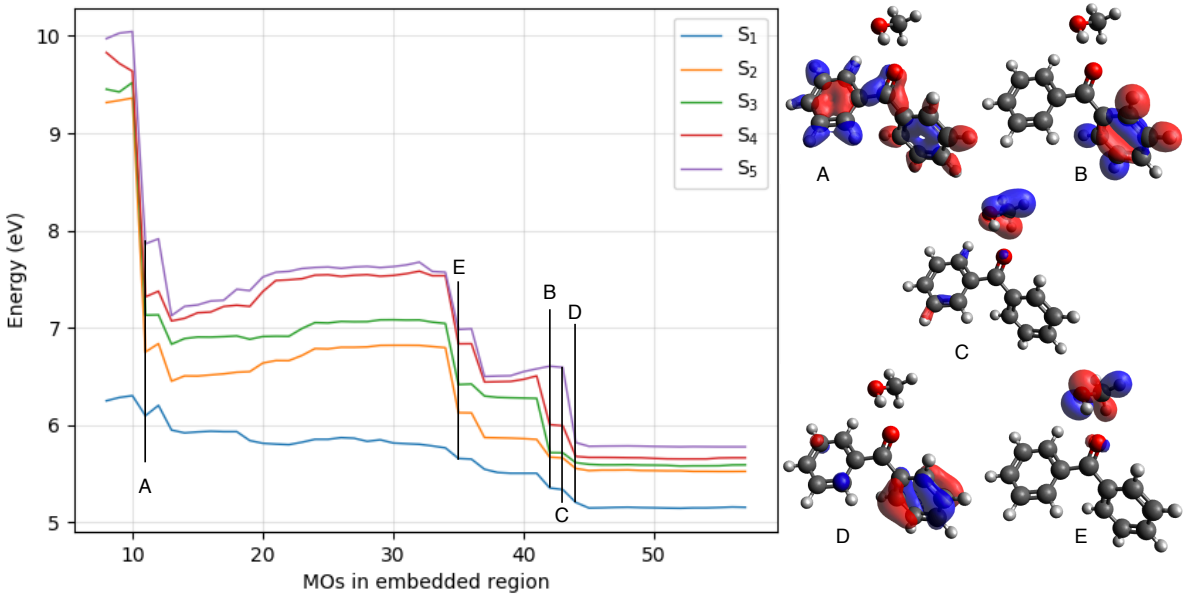

Figure 6.5: Convergence of the CIS/aug-cc-pVDZ//df-B3LYP/aug-cc-pVDZ excited state energies for the first 5 singlet states with increasing active region for the hydrogen bonded Bzp-MeOH complex. Molecular orbital diagrams highlight the orbitals that caused notable jumps in energy when they were added in to the active region.

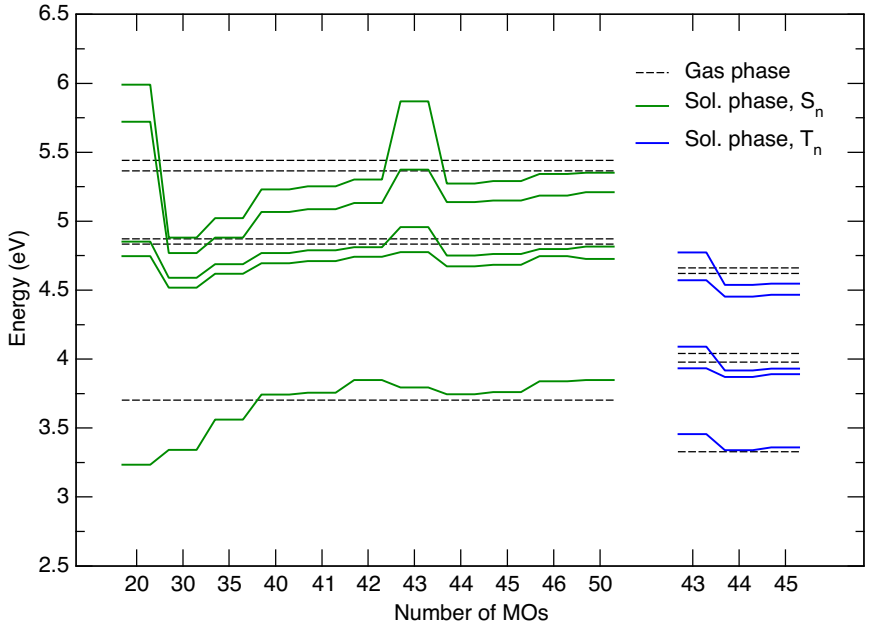

Figure 6.6: Left: First 5 singlet excited state energies, convergence with size of active region. Right: First 5 triplet energies for active regions of 43-45 MOs. The singlet and triplet energies from a full CC2 gas phase calculation are shown for comparison.

energies are converged to a stable value, and observe a similar jump in energy when the 44th MO, D, is added. Triplet calculations at the same geometry with active regions of 43-45 MOs also show that they are converged. The similarities between CIS and CC2 results in their convergence behaviour imply something quite useful. Lower cost methods can be used to test the convergence with active region size, as a way to guide the choice of active region for a more expensive method. These CC2 results also confirm that the T_2 state is indeed stabilised by hydrogen bonding, whilst the S_1 state is destabilised by it relative to gas phase Bzp causing the slowing of the ISC rate.

Determining accurate excitation energies at the Franck-Condon geometry is of course only the first step to fully understanding this mechanism. Other critical points on the PES, including the S_1/T_2 MECP and the T_2/T_1 CI can be optimised using PBE since analytical gradients are now available.[287] A single MeOH isn't necessarily representative of solvation, so more explicit solvent molecules can be included – in fact, a continuum solvent may be necessary to account for the polarizing nature of the environment. In terms of method development, the algorithm for molecular orbital selection that uses the Mulliken population criterion works for ground states but isn't optimal for excited state properties. The CIS vector could potentially be used to select the important orbitals for a particular excitation.

6.5 Conclusion

In the first part of this chapter I discussed continuum solvation approaches, in relation to the calculation of excitation energies. This approach can be useful for demonstrating that a state is either stabilised or destabilised by the polarization response of a particular solvent. However, these models are primarily optimised to return accurate solvation energies which is especially true of empirical models like SMD. Further work is needed to benchmark existing implicit solvent methods specifically for different types of excited states, so as to develop a set of guidelines for researchers seeking to model solution-phase experiments.

In the second part of this chapter projector-based embedding was applied to explore the excitation energies of a benzophenone molecule in a methanol solution. The role of hydrogen bonding in stabilising or destabilising electronic states was highlighted by the inclusion of solvent-localised orbitals as part of the active space in the PBE calculation. Calculating accurate CC2 energies, at a reduced cost, supports the hypothesis that hydrogen bonding is influential in determining the choice of the photodynamic ISC mechanism in this system.

Although both of the systems discussed in this chapter are not directly relevant to atmospheric chemistry, the development of reliable methods to treat aqueous solvation – especially at gas-water interfaces – is important for studying the chemistry of aerosols.[288] For example, the photochemistry of ozone at the gas-water interface has been shown to be significantly different from the gas phase.[289] Continuum models cannot capture the hydrogen bonding and solvent ordering effects which are especially important in water, therefore QM/MM models and projector-based embedding type approaches will be crucial to describing aqueous photochemistry.

CHAPTER 7

CONCLUSION

This thesis reviews a number of computational methods that are frequently used to address questions of practical interest in photochemical investigations. Presently, the field of nonadiabatic dynamics is developing very quickly, and its application is becoming more widespread as a way of interpreting the results of ultrafast experiments. Many electronic structure programs now include at least a rudimentary implementation of the surface hopping algorithm (Molpro, MOLCAS, Turbomole, Q-Chem, GAMESS, etc.) and more packages that can be interfaced with common electronic structure programs to perform on-the-fly nonadiabatic dynamics are being developed (Newton-X, SHARC, JADE, etc.). The availability of such software for emerging methods that are able to treat decoherence more accurately than FSSH will play a significant role in their popularity. Alongside QTSH, there are many competing algorithms that can be based on ideas of exact factorisation, coupled Gaussians, or even improved efficiency implementations of grid-based methods derived from MCTDH. However these approaches are still to costly to study long time photochemical dynamics especially in larger systems. Applying machine learning approaches to this end is being discussed within the community, however at the moment a significant barrier for nonadiabatic dynamics on neural network predicted PES is the accuracy of nonadiabatic coupling vectors that present strong discontinuities in regions of strong coupling since they are difficult to capture within an ML model. Using a nonadiabatic master equation approach, as discussed in chapter 3, may yield more accurate results for such systems.

Here I will overview the primary conclusions of each chapter in order and in greater detail. Methods of generating absorption cross sections with broadened absorption bands were discussed in chapter 2. Two main types of protocol were described: the Franck-Condon type methods which generate a vibrational progression, and nuclear ensemble approaches which collate a spectrum from single point calculations. I conclude that the former are somewhat limited in their scope,

since they rely on the excited state having a potential minimum near the Franck-Condon region of the PES and rely on the harmonic approximation. The ensemble type approaches are shown to be qualitatively successful in reproducing band shape, with one exception. Sampling from a classical trajectory is likely to underestimate the broadness of the peak because zero-point energy is neglected, so is not recommended for simulating $\sigma(\lambda)$. The Wigner ensemble method is practical for most cases because the computational cost is often less than that of running a trajectory, and an understanding of quantum thermostats isn't required to set up a calculation.

The nonadiabatic energy grained master equation (NA-EGME) was explored as an alternative approach to modelling slow nonadiabatic phenomena in chapter 3. The photodissociation of a model bi-chromophoric molecule, C_6-HPALD, was used as a test case. Comparing the results of nonadiabatic dynamics to that of the NA-EGME model showed that both methods captured important aspects of the dynamics, including kinetic timescales, and diabatic trapping. By showing that a NA-EGME model can work in the excited state, if a number of criteria are satisfied, these results open up the possibility of modelling long-time dynamics of photoexcited molecules with higher-level wavefunction based electronic structure approaches.

As the companion chapter to the previous one, chapter 4 discusses the role of HPALD photochemistry in the troposphere. An overview of the literature highlights that the quantity of HPALD produced in the isoprene oxidation cycle is still uncertain. However, we are able to describe the mechanism of OH loss following photoexcitation based on the nonadiabatic dynamics simulations described in the previous chapters. Rates of HPALD photolysis are also calculated from $\sigma(\lambda)$ which were simulated using the Wigner ensemble method. This calculated rate of 1×10^{-4} s^{-1} is within error of that used in the Master Chemical Mechanism.

In chapter 5 I discuss the challenges of implementing a novel nonadiabatic dynamics method, Quantum Trajectory Surface Hopping, in Newton-X. I show how it can be derived from the quantum Liouville equation, and explain the approximations necessary to take it to its independent trajectory limit. My implementation of QTSH is shown to agree with Tully's surface hopping in two key model systems.

Two case studies on the influence of solvation effects in excited states were presented in chapter 6. While continuum solvent models are shown to be useful for making comparative statements about the stabilisation or destabilisation of electronic states due to solvent polarization, as in the case of N-phenyl phenoxazine, they can fail when there are directional non-electrostatic interactions between solvent and solute. In such cases, projector-based embedding can be used to calculate accurate excitation energies of a molecule in a solvent cage at a significantly reduced cost.

In light of this, the following seem to me to be the most pertinent avenues for future work in computational atmospheric photochemistry. The first priority is developing electronic structure methods that can be used to calculate high quality PES and nonadiabatic couplings cheaply – this is necessary both for accurate dynamics, and for improved kinetic models. Correctly selecting

a density functional/method is always reliant on thoroughly benchmarking the system against a higher level method. Advancements in nonadiabatic dynamics algorithms enable us to make ever more accurate predictions about photochemical mechanisms. However, an open and interesting question remains about how to initiate dynamics in the limiting case of photoexcitation by sunlight, or for an arbitrary laser pulse. Lastly it is also necessary to develop protocols for including the environment in a realistic, possibly atomistic but still low-cost way, in order to model reactions in aerosols especially at their interfaces.

APPENDIX A

A.1 Benchmarking excited state methods

In order to determine the best approach for the calculation of nonadiabatic dynamics in C_6-HPALD I tested a number of electronic structure methods which included DFT, LR-TDDFT, CIS, CIS(D), ADC(2), EOM-CCSD, SA-CASSCF, and MS-CASPT2. All DFT, LR-TDDFT, CIS, and CIS(D) calculations were performed in Gaussian 16[64]. CC2 and ADC(2) calculations were performed in Turbomole v7.1[215]. The EOM-CCSD calculation is executed in Molpro 2018[286]. CASSCF and MS-CASPT2 calculations were performed in OpenMolcas v18.09.[181] In the CASSCF calculations the active space contained 10 electrons in 8 orbitals which includes σ/σ^* orbitals at the peroxide bond, π/π^* orbitals at the enone chromophore, and lone pairs on all the oxygen atoms.

All benchmarks were calculated for n=5 except CASSCF and CASPT2 which were calculated for n=3.

A.2 Fitting the survival probability

All fits of the decaying HPALD survival probability are performed using the non-linear curve fitting utility in qtgrace.[290] Trajectories where HO_2 is lost are excluded from the analysis. All fitted parameters reported to 3 s.f.

Fit 1: Survival probability of HPALD with respect to OH loss for conformer C, FSSH, figure 3.10.

$$[\text{HPALD}]_{FSSH} = 0.742\,e^{-0.536\,t} + 0.306\,e^{-8.67\,t}$$

Method	Basis Set	S_1	S_2	S_3	S_4	S_5
CIS	6-31G	4.4425	6.7454	6.7915	8.3597	8.3927
	6-311+G*	4.6675	6.4277	6.9813	7.9840	8.2861
	6-311++G**	4.6457	6.4155	6.9665	7.7852	8.2444
CIS(D)	6-31G	3.9083	6.6660	6.8104	7.7418	7.9101
	6-311+G*	3.7471	6.1951	6.4346	6.9162	7.6128
	6-311++G**	3.7468	6.1739	6.4064	6.9186	7.3769
ωB97XD	6-31G	3.6468	5.7016	6.0060	6.1120	6.9943
	6-311+G*	3.6694	5.6377	5.8160	6.1112	6.9448
	6-311++G**	3.6461	5.6161	5.8004	6.0781	6.9032
PBE0	6-31G	3.5260	4.8622	5.8700	5.9635	6.2205
	6-311+G*	3.5291	4.8701	5.6063	5.9754	6.1971
	6-311++G**	3.5046	4.8478	5.5920	5.9338	6.1755
lc-ωPBE	6-31G	3.6944	6.0125	6.2462	6.6052	7.4603
	6-311+G*	3.7482	5.9197	6.1152	6.5375	7.4241
	6-311++G**	3.7245	5.9069	6.0937	6.5056	7.2600
CAM-B3LYP	6-31G	3.6584	5.7352	5.9908	6.1034	7.0161
	6-311+G*	3.6840	5.6435	5.8159	6.0484	6.9394
	6-311++G**	3.6599	5.6240	5.7978	6.0136	6.8136
CC2	cc-pVDZ	3.8107	5.9433	6.4220	6.4997	7.4003
ADC(2)	cc-pVDZ	3.6180	5.9074	6.3592	6.4981	7.3464
	cc-pVTZ	3.5412	5.7588	6.1160	6.3720	7.1849
	cc-pVQZ	3.5151	5.7238	6.0326	6.2971	7.1033
	aug-cc-pVDZ	3.4504	5.5908	5.8035	5.9428	6.0525
EOM-CCSD	aug-cc-pVDZ	3.756	6.114	6.156	6.479	6.852
SA(4)-CASSCF(8/10)	6-31G*	2.63	6.22	6.62	-	-
MS(4)-CASPT2(8/10)	6-31G*	3.70	7.15	8.17	-	-

Table A.1: Benchmarks for excitation energies at the S_0 optimised geometry of conformer B.

Quality of fit: Chi-square: 0.0863563 ; Correlation coefficient: 0.996529 ; RMS per cent error: 6.00237

Fit 2: Survival probability of HPALD with respect to OH loss for conformer C, A-MD, figure 3.10.

$$[\text{HPALD}]_{A-MD} = 0.480\,e^{-0.777\,t} + 0.567\,e^{-19.6\,t}$$

Quality of fit: Chi-square: 0.133163 ; Correlation coefficient: 0.982910 ; RMS per cent error: 18.1362

Fit 3: Survival probability of HPALD with respect to OH loss for all conformers, NA-MD, figure 3.14.

$$[\text{HPALD}]_{NA-MD} = e^{-0.218t}$$

Quality of fit: Chi-square: 0.0517129 ; Correlation coefficient: 0.986696 ; RMS per cent error: 4.41419

Fit 4: Survival probability of HPALD with respect to OH loss for all conformers, A-MD, figure 3.14.

$$[\text{HPALD}]_{A-MD} = 0.759\,e^{-0.421t} + 0.248\,e^{-17.2t}$$

Quality of fit: Chi-square: 0.0479623 ; Correlation coefficient: 0.995265 ; RMS per cent error: 5.50479

A.3 Sensitivity testing the EGME model

Some parameters included in the EGME calculation might have a significant impact on the result. We test the robustness of the EGME model by comparing the result when those parameters are varied.

An assumption we make is that it is valid to use the average initial energy from FSSH initial conditions (IC), rather than a distribution. Figure A.1 shows results of an EGME model built to replicate the original 10 trajectories starting from the S_1 minimum of conformer C. An NA-EGME calculation is performed for each trajectory IC illustrating that the model is robust to modest variation in initial energy.

EGME results can also be sensitive to frequencies, especially low frequencies that have a significant impact on the density of states. Figure A.1 also compares EGME results calculated using critical points optimised with tight convergence conditions and a fine integration grid against results calculated with a standard grid and convergence criteria. Even with a slight difference in frequencies the decay rates calculated using a coarse (default) grid are visibly higher. This highlights the importance of using frequencies calculated in a consistent way for each isomer when constructing an EGME model.

A.4 Influence of hindered rotor corrections on the EGME results

Repeating the EGME calculations with the hindered rotor vibrations projected out of the Hessian produce results shown in Fig. A.2. These calculations use the S_1-B and S_1-TS geometries, both optimised with tight convergence criteria and ultra-fine integration grid.

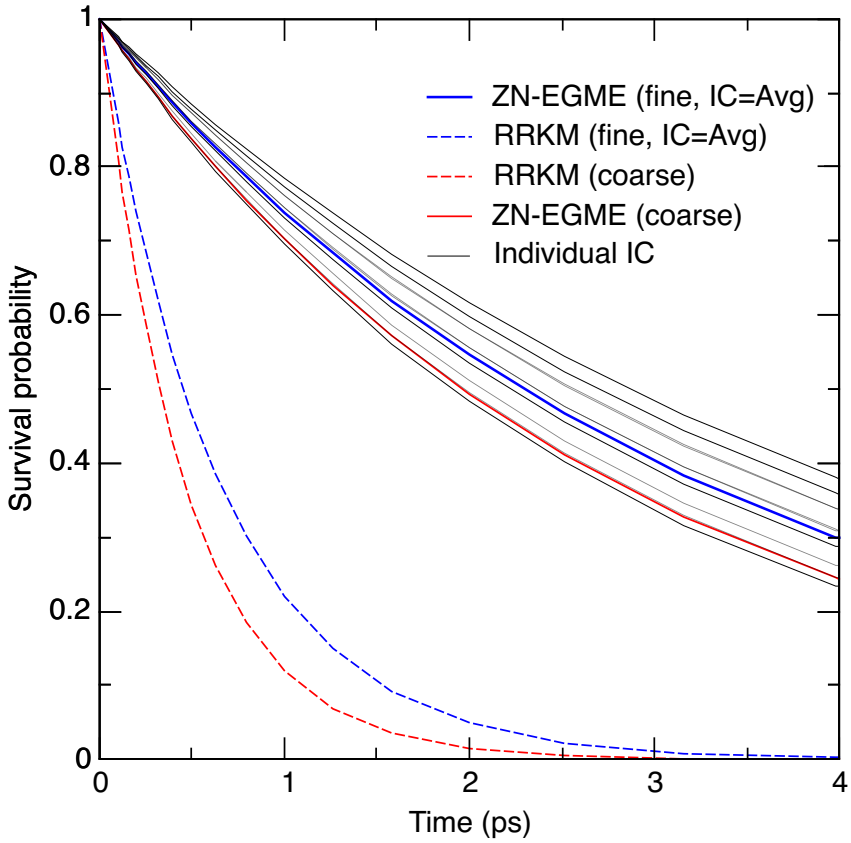

Figure A.1: Testing EGME robustness to initial energy and sensitivity to frequencies.

A.5 TS diabat fitting parameters

Fitted parameters for ZN transition probabilities calculated with LR-TDDFT potentials are given in table A.2.

Fitted parameters for ZN transition probabilities calculated with CASPT2 potentials are given in table A.3.

Analytical forms of the diabatic potentials are given in equations 3.28.

Parameter fitting was performed in Gnuplot v5.2 with resulting parameters are listed in the following table:

A.6 Critical Points

Table A.4 lists the complete energies, rotational constants, and frequencies used in the EGME calculations.

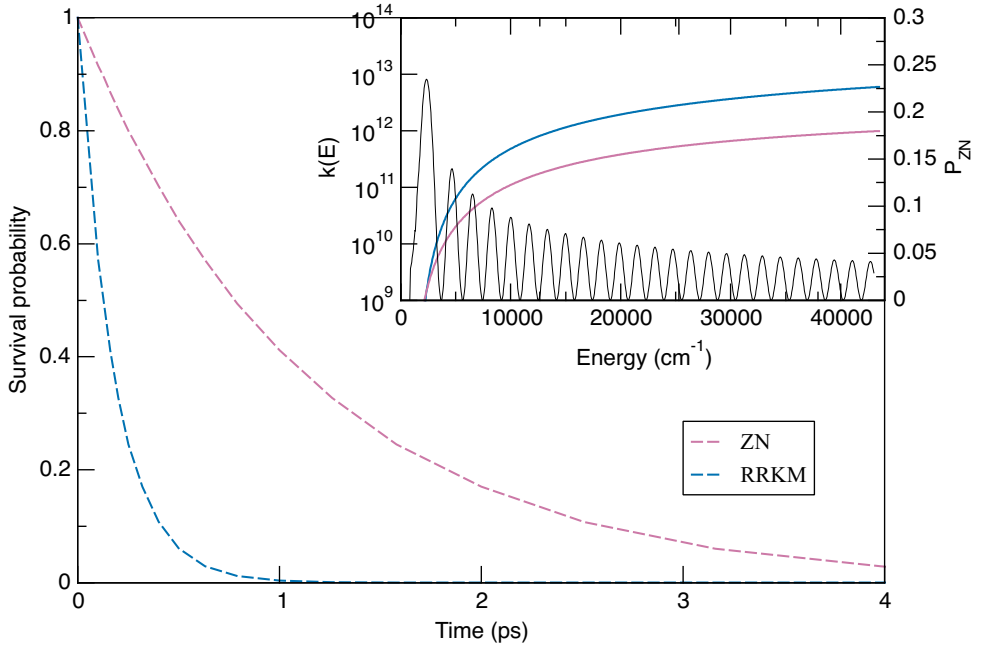

Figure A.2: EGME results with hindered rotor correction, that were obtained by projecting the anharmonic rotational modes out of the Hessian.

Parameter	Value	Standard Error
A_{σ^*}	495.051	± 15.01
β_{σ^*}	-0.119809	± 0.00349
ε_{σ^*}	11.0345	± 0.1939
A_{π^*}	66.9186	± 2.388
β_{π^*}	3.76346	± 1.307
ε_{π^*}	-46.4714	± 2.382
H_{12}	3.00481	± 0.01141

Table A.2: Parameters for LR-TDDFT/PBE0/6-31G diabats

Parameter	Value	Standard Error
A_{σ^*}	835.318	± 73.88
β_{σ^*}	-0.113482	± 0.009752
ε_{σ^*}	9.51291	± 0.8865
A_{π^*}	50.3379	± 4.159
β_{π^*}	5.85351	± 0.4645
ε_{π^*}	-29.9859	± 4.144
H_{12}	0.823152	± 0.04453

Table A.3: Parameters for MS(4)-CASPT2(10,8)/6-31G* diabats

	S_1 minimum (B)	S_1 minimum (C)	TS-S_1	CI - S_1/S_2
Energy (a.u.)	-459.429938897	-459.429169893	-459.42369136	-459.418027248
ZPE correction (a.u)	0.153697	0.153386	0.150686	0.1619025445
Rotational constants	0.06178	0.07586	0.07539	0.0222
	0.03267	0.02710	0.02689	0.0251
	0.02342	0.02170	0.02155	0.0938
Frequencies	53.7093	42.3725	-3534.0736	68.62
	69.0555	68.6738	63.7551	78.221
	91.7755	93.1878	67.9529	84.668
	134.5593	112.3241	95.3035	128.213
	145.3678	147.5971	110.0446	181.793
	171.9759	164.3655	148.6376	223.116
	221.3219	210.9118	207.6926	253.395
	225.2273	233.587	228.0155	254.783
	299.9763	278.9438	253.1427	301.067
	352.2649	300.8378	275.4055	329.293
	387.0304	388.1045	308.6733	362.679
	390.6556	447.713	364.2645	410.98
	478.609	461.5256	434.6985	485.264
	517.1127	512.0716	456.206	583.909
	649.0519	660.1531	497.9537	698.771
	709.1161	719.9368	680.2171	771.322
	801.9211	789.8532	791.6283	793.207
	827.045	829.3933	826.7497	872.964
	892.4528	834.7936	865.5645	915.326
	906.2169	905.0289	905.0682	960.249
	943.5918	944.631	956.5599	1036.699
	955.5396	966.1619	959.6579	1058.41
	1026.4537	1031.0846	1025.5298	1087.157
	1058.011	1061.9474	1071.0154	1093.907
	1107.599	1106.8674	1085.7322	1137.154
	1180.0393	1172.6581	1110.114	1163.242
	1184.4502	1185.0541	1132.9102	1185.308
	1214.5041	1216.4378	1162.4788	1262.67
	1291.3523	1272.7574	1213.9031	1287.216
	1311.938	1296.4804	1274.7914	1310.993
	1324.6155	1327.2453	1292.0703	1338.057
	1342.4468	1343.5821	1315.029	1352.212
	1343.5943	1346.6629	1337.7966	1376.988
	1393.5145	1393.9353	1345.5383	1398.868
	1428.1916	1425.6609	1379.918	1455.576
	1461.3167	1461.0041	1414.6639	1521.33
	1499.3381	1502.7229	1461.0081	1539.105
	1539.3167	1540.7134	1539.1839	1549.307
	1543.0902	1543.8922	1542.1446	1603.235
	1550.8704	1550.9794	1549.4011	3018.911
	1598.7604	1609.256	1604.491	3067.174
	3066.7762	3062.8107	3049.8769	3067.697
	3075.598	3064.5537	3050.92	3070.362
	3079.3257	3072.6858	3063.5567	3134.348
	3091.1291	3075.6386	3078.6837	3153.494
	3129.6292	3129.3525	3134.677	3177.919
	3156.2406	3152.4157	3154.9103	3209.011
	3162.2071	3158.2418	3159.2982	3235.128
	3211.1928	3222.2468	3218.3714	3644.865
	3237.3168	3238.926	3232.116	
	3623.5612	3650.8246	3646.0593	

Table A.4: Energies, rotational constants, and frequencies at the critical points used in the EGME calculations.

APPENDIX B

APPENDIX B

Here, I will outline the derivation for the time evolution of the off-diagonal terms $\rho_{mn} = \alpha_{mn} + i\beta_{mn}$ in the density matrix ρ for an arbitrary number of states. We start the derivation from the quantum-classical Liouville equation:

$$i\hbar\frac{\partial\rho_{mn}}{\partial t} = \sum_{k=1}^{N} H_{mk}\rho_{kn} - \rho_{mk}H_{kn} + \frac{i\hbar}{2}\sum_{k=1}^{N}\{H_{mk},\rho_{kn}\} - \{\rho_{mk},H_{kn}\}$$

In order to derive $\frac{\partial\alpha_{mn}}{\partial t}$ and $\frac{\partial\beta_{mn}}{\partial t}$ we need to separate the $k = m,n$ terms from the sum.

$$\begin{aligned} i\hbar\frac{\partial\rho_{mn}}{\partial t} = &\sum_{k\neq m,n}^{N} H_{mk}\rho_{kn} - \rho_{mk}H_{kn} + \frac{i\hbar}{2}\sum_{k\neq m,n}^{N}\{H_{mk},\rho_{kn}\} - \{\rho_{mk},H_{kn}\} \\ &+ H_{mm}\rho_{mn} - \rho_{mm}H_{mn} + \frac{i\hbar}{2}\{H_{mm},\rho_{mn}\} - \frac{i\hbar}{2}\{\rho_{mm},H_{mn}\} \\ &+ H_{mn}\rho_{nn} - \rho_{mn}H_{nn} + \frac{i\hbar}{2}\{H_{mn},\rho_{nn}\} - \frac{i\hbar}{2}\{\rho_{mn},H_{nn}\} \end{aligned}$$

Then it should be recalled that H_{mn} when $m \neq n$ is $-i\hbar\mathbf{d}_{mn}\cdot\frac{\mathbf{p}}{\mu}$ (where mass is μ), and that the off-diagonal density matrix terms can be separated into their real and imaginary parts $\rho_{mn} = \alpha_{mn} + i\beta_{mn}$. Dividing through by $i\hbar$:

$$\begin{aligned} \frac{\partial\rho_{mn}}{\partial t} = &\sum_{k\neq m,n}^{N}\left(-\mathbf{d}_{mk}\cdot\frac{\mathbf{p}}{\mu}(\alpha_{kn} + i\beta_{kn}) + (\alpha_{mk} + i\beta_{mk})\mathbf{d}_{kn}\cdot\frac{\mathbf{p}}{\mu}\right) \\ &+ \frac{i\hbar}{2}\sum_{k\neq m,n}^{N}\left(\left\{-\mathbf{d}_{mk}\cdot\frac{\mathbf{p}}{\mu},(\alpha_{kn} + i\beta_{kn})\right\} - \left\{(\alpha_{mk} + i\beta_{mk}),-\mathbf{d}_{kn}\cdot\frac{\mathbf{p}}{\mu}\right\}\right) \\ &+ \frac{1}{i\hbar}\left(H_{mm}\rho_{mn} - \rho_{mm}H_{mn}\right) + \frac{1}{2}\left(\{H_{mm},\rho_{mn}\} - \{\rho_{mm},H_{mn}\}\right) \\ &+ \frac{1}{i\hbar}\left(H_{mn}\rho_{nn} - \rho_{mn}H_{nn}\right) + \frac{1}{2}\left(\{H_{mn},\rho_{nn}\} - \{\rho_{mn},H_{nn}\}\right) \end{aligned}$$

Expanding the Poisson brackets in the last two lines allows us to rearrange them in terms of $H_0 = H_{mm} + H_{nn}$.

$$\begin{aligned}
\frac{\partial \rho_{mn}}{\partial t} &= \ldots + \frac{1}{i\hbar}\left(H_{mm}\rho_{mn} - \rho_{mm}H_{mn} + H_{mn}\rho_{nn} - \rho_{mn}H_{nn}\right) \\
&+ \frac{1}{2}\left(\{H_{mm},\rho_{mn}\} - \{\rho_{mm},H_{mn}\} + \{H_{mn},\rho_{nn}\} - \{\rho_{mn},H_{nn}\}\right) \\
&= \ldots + \frac{1}{i\hbar}\left(H_{mm}\rho_{mn} - \rho_{mm}H_{mn} + H_{mn}\rho_{nn} - \rho_{mn}H_{nn}\right) \\
&+ \frac{1}{2}\left(\left(\frac{\partial H_{mm}}{\partial r} + \frac{\partial H_{nn}}{\partial r}\right)\frac{\partial \rho_{mn}}{\partial p} - \frac{\partial \rho_{mn}}{\partial r}\left(\frac{\partial H_{mm}}{\partial p} + \frac{\partial H_{nn}}{\partial p}\right)\right) \\
&+ \frac{1}{2}\left(\frac{\partial H_{mn}}{\partial r}\left(\frac{\partial \rho_{nn}}{\partial p} + \frac{\partial \rho_{mm}}{\partial p}\right) - \left(\frac{\partial \rho_{nn}}{\partial r} + \frac{\partial \rho_{mm}}{\partial r}\right)\frac{\partial H_{mn}}{\partial p}\right) \\
&= \ldots + \frac{1}{i\hbar}\left(H_{mm} - H_{nn}\right)\rho_{mn} + \frac{1}{i\hbar}H_{mn}\left(\rho_{nn} - \rho_{mm}\right) \\
&+ \frac{1}{2}\{H_0,\rho_{mn}\} \\
&+ \frac{1}{2}\{H_{mn},\rho_{nn} + \rho_{mm}\}
\end{aligned}$$

By separating the real and imaginary parts of this expression, it is now possible to get the time evolution of the quantum coherences

$$\begin{aligned}
\frac{\partial \alpha_{mn}}{\partial t} &= \sum_{k\neq m,n}^{N}\left[\alpha_{mk}\mathbf{d}_{kn}\cdot\frac{\mathbf{p}}{m} - \alpha_{kn}\mathbf{d}_{mk}\cdot\frac{\mathbf{p}}{m}\right] + \{H_0,\alpha_{mn}\} + \omega\beta_{mn} \\
&+ \sum_{k\neq m,n}^{N}\left\{\alpha_{mk},\mathbf{d}_{kn}\cdot\frac{\mathbf{p}}{m}\right\} - \left\{\mathbf{d}_{mk}\cdot\frac{\mathbf{p}}{m},\alpha_{kn}\right\} + \mathbf{d}_{mn}\cdot\frac{\mathbf{p}}{m}\left(\rho_{nn} - \rho_{mm}\right) \\
\frac{\partial \beta_{mn}}{\partial t} &= \sum_{k\neq m,n}^{N}\left[\beta_{mk}\mathbf{d}_{kn}\cdot\frac{\mathbf{p}}{m} - \beta_{kn}\mathbf{d}_{mk}\cdot\frac{\mathbf{p}}{m}\right] + \{H_0,\beta_{mn}\} - \omega\alpha_{mn} \\
&+ \sum_{k\neq m,n}^{N}\left\{\beta_{mk},\mathbf{d}_{kn}\cdot\frac{\mathbf{p}}{m}\right\} - \left\{\mathbf{d}_{mk}\cdot\frac{\mathbf{p}}{m},\beta_{kn}\right\} - \frac{\hbar}{2}\left\{\mathbf{d}_{mn}\cdot\frac{\mathbf{p}}{m},\rho_{nn} + \rho_{mm}\right\}
\end{aligned}$$

where ω is the energy gap $\dfrac{E_m - E_n}{\hbar}$.

APPENDIX C

APPENDIX C

Here I present the results of calculations pertaining to the photochemical mechanism of N-phenyl phenoxazine. Results of normal mode frequency calculations performed at S_0, S_1, and T_1 geometries optimised with CAM-B3LYP/6-31+G* in implicit solvent are given in Table C.1. These frequencies have been adjusted with an anharmonicity correction of 0.953, as recommended in Kashinski *et al.*.[269]

Table C.1: Calculated frequencies at the optimised geometries in cm^{-1} with applied anharmonicity correction of 0.953; IR intensities (km $mole^{-1}$). Peaks observed in the TVAS spectra are highlighted in **bold**. Only the frequency range observable in TVAS spectra is given in the table (1300 - 1700 cm^{-1}).

S_0				S_1				T_1			
DMF		Toluene		DMF		Toluene		DMF		Toluene	
Freq	IR	Freq	IR	Freq	IR	Freq	IR	Freq	IR	Freq	IR
1298.87	1.6487	257.78	0.54	1313.63	55.0118	256.46	3.27	1298.94	1.2648	252.47	6.04
1301.45	1.5683	384.67	0.28	1324.15	174.5577	308.1	1.26	1309.41	92.6911	328.7	0.02
1312.27	128.7336	431.25	0.27	1338.98	277.6159	399.76	0.24	1338.05	22.887	393.85	0.28
1318.13	661.9832	494.02	8.06	1364.49	25.187	423.61	70.03	1355.4	63.1953	418.84	0.53
1438.19	4.3755	574.47	15.04	1428.18	53.869	560.5	9.11	1373.12	45.426	490.26	0.1
1438.85	0.4752	609.25	0.16	1437.69	46.4032	600.06	0.22	1378.7	30.5993	579.97	13.09
1450.96	25.9752	689.15	64.36	1440.7	430.2678	627.24	100.43	1424.54	1.3333	609.83	0.02
1476.64	**1122.36**	733.41	208.02	1463.15	21.7029	688.37	1.88	1433.68	6.7082	662.37	0.26
1485.46	49.7383	781.22	9.29	1471.31	63.849	768.96	0.99	1439.07	5.8156	734.04	0
1504.68	58.6597	839.96	0	1483.41	245.9607	825.73	0.07	1458.01	0.919	769.88	2.02
1577.91	0.5026	910.78	2.35	1486.47	43.436	896.24	0.9	1459.44	12.6056	882.25	0.03
1594.17	4.1055	935.67	5.78	1499.29	4.4928	919.27	4.23	**1486.01**	**46.1927**	890.61	1.44
1596.32	66.6992	965.79	0.02	1554.36	1.2256	956.03	0.48	1495.61	30.2436	932.24	65.79
1605.61	59.1303	1014.83	9.23	**1575.89**	**111.8486**	983.23	0.9	1513.46	19.9791	985.21	0.05
1611.41	0.6815	1061.08	11.34	1593.78	11.5577	1061.42	12.84	1597.75	3.925	1040.48	1.95
1632.52	34.7571	1133.92	1.17	1601.26	0.3814	1125.13	11.83	1606.81	13.34	1085.59	0.43
3065.01	1.2464	1146.83	0.13	3070.05	0.0429	1147.6	6.26	3069.02	0.1167	1136.91	0.31
3070.03	1.6461	1195.03	21.82	3070.38	2.799	1221.97	4.95	3071.13	0.2725	1203.94	12.18
3070.18	1.3339	1269.69	4.42	3070.87	0.2123	1280.64	47.94	3071.19	2.7862	1276.27	3.64
3070.65	1.768	1302.83	2.2	3076.75	2.3777	1319.59	0.84	3075.33	2.0034	1311.07	69.94
3077.18	19.5702	1438.85	4.16	3077	17.002	1435.73	400	3076.19	2.1576	1375.04	41.01
3079.1	28.2861	**1482.51**	**911.01**	3077.89	3.0458	1464.85	14.44	3076.54	11.9954	1435.11	5.24
3079.18	7.6498	1579.52	0.1	3083.41	20.9951	1487.96	34.33	3081.14	17.6899	1459.8	4.98
3083.32	27.6332	1607.73	48.26	3089.04	10.8836	**1580.17**	**100.68**	3087.45	19.9004	1509.07	1.99

To calculate excitations corresponding to the peaks in the TEAS spectrum, LR-TDDFT/CAM-B3LYP/6-31+G* calculations at the optimised geometries were performed using Orca v4.2.0. The SMD (continuum) solvent model is used for these calculations. The excitation energies and the corresponding oscillator strength f_{osc} are given in tables C.2, C.3, and C.4.

Table C.2: First 5 excitation energies and oscillator strengths at the S_0 geometry, singlets.

DMF			Toluene		
E (eV)	λ	f_{osc}	E (eV)	λ	f_{osc}
4.044	306.6	0.0216	4.036	307.2	0.0167
4.323	286.8	0.1278	4.099	302.5	0.0564
4.214	294.2	0.0290	4.282	289.5	0.0877
4.506	275.2	0.0009	4.51	274.9	0.0013
4.883	253.9	0.0023	4.644	267	0.0302

Table C.3: First 15 excitation energies and oscillator strengths at the S_1 geometry, singlets.

DMF			Toluene		
E (eV)	λ	f_{osc}	E (eV)	λ	f_{osc}
3.258	380.5	0.0189	3.279	378.2	0.0150
4.055	305.8	0.1592	3.626	341.9	0.0075
3.847	322.3	0.0078	3.989	310.8	0.1374
4.314	287.4	0.0004	4.32	287	0.0000
4.481	276.7	0.0058	4.464	277.7	0.0101
4.353	284.8	0.0295	4.352	284.9	0.0484
5.093	243.5	0.0017	4.981	248.9	0.0016
5.178	239.4	0.0009	5.054	245.3	0.0001
5.279	234.9	0.0049	5.108	242.7	0.0104
5.225	237.3	0.0111	5.221	237.5	0.0018
5.471	226.6	0.1885	5.473	226.6	0.1930
5.515	224.8	0.0107	5.512	224.9	0.0082
5.632	220.1	0.9089	5.642	219.8	0.9252
5.661	219	0.0001	5.532	224.1	0.0002
5.653	219.3	0.0092	5.491	225.8	0.0056

Single point LR-TDDFT calculations can only show the strengths of transitions from the SCF ground state – however, using tool implemented in “multiwfn”, a program for electronic wavefunction analysis it’s possible to calculate the transition dipole moment (and therefore the oscillator strength) between excited states.[270] This means that we can assign some of the peaks in the TEAS spectrum, although we are limited to qualitative statements since higher S_n states can be unreliable with TDDFT.

Highlighted in bold are the excitations that may correspond to the peaks observed in the TEAS spectra. The peak near 530 nm that appears in the DMF TEAS, but is much less prominent in Toluene, seems to correspond to the $S_1 \rightarrow S_{11}$ transition with high oscillator strength, 4 times higher in DMF - although I’m wary that this might well be confirmation bias.

Table C.4: First 15 excitation energies at the T_1 geometry, triplets. No oscillators since $S_0 \rightarrow T_1$ transitions are forbidden.

DMF			Toluene		
E (eV)	λ	f_{osc}	E (eV)	λ	f_{osc}
2.236	554.4	-	2.235	554.7	-
3.244	382.2	-	3.232	383.6	-
3.409	363.7	-	3.405	364.1	-
3.434	361	-	3.439	360.5	-
3.598	344.6	-	3.588	345.5	-
3.732	332.2	-	3.58	346.3	-
4.437	279.4	-	4.202	295.1	-
4.439	279.3	-	4.45	278.6	-
4.27	290.3	-	4.438	279.3	-
4.655	266.4	-	4.652	266.5	-
4.745	261.3	-	4.734	261.9	-
4.803	258.2	-	4.8	258.3	-
4.805	258	-	4.805	258	-
5.143	241.1	-	4.953	250.3	-
5.164	240.1	-	5.135	241.4	-

Table C.5: The transitions from the S_1 state, with corresponding oscillator strengths at the S_1 geometry.

DMF				Toluene			
	E (eV)	λ (nm)	f_{osc}		E (eV)	λ (nm)	f_{osc}
S1 $\rightarrow$ S1	0	Inf	0.0000	S1 $\rightarrow$ S1	0	Inf	0.0000
S1 $\rightarrow$ S2	0.797	1556	0.0321	S1 $\rightarrow$ S2	0.347	3573	0.0007
S1 $\rightarrow$ S3	0.589	2105	0.0020	S1 $\rightarrow$ S3	0.71	1746	0.0513
S1 $\rightarrow$ S4	1.056	1174	0.0002	S1 $\rightarrow$ S4	1.041	1191	0.0010
S1 $\rightarrow$ S5	1.223	1014	0.0013	S1 $\rightarrow$ S5	1.185	1046	0.0093
S1 $\rightarrow$ S6	1.095	1132	0.0000	S1 $\rightarrow$ S6	1.073	1156	0.0456
S1 $\rightarrow$ S7	1.835	676	0.0046	S1 $\rightarrow$ S7	1.702	729	0.0014
S1 $\rightarrow$ S8	1.92	646	0.0049	S1 $\rightarrow$ S8	1.775	699	0.0004
S1 $\rightarrow$ S9	2.021	614	0.0061	S1 $\rightarrow$ S9	1.829	678	0.0032
S1 $\rightarrow$ S10	1.967	630	0.0000	S1 $\rightarrow$ S10	1.942	639	0.0534
S1 $\rightarrow$ S11	**2.213**	**560**	**0.4391**	S1 $\rightarrow$ S11	**2.194**	**565**	**0.1371**
S1 $\rightarrow$ S12	2.257	549	0.0031	S1 $\rightarrow$ S12	2.233	555	0.0036
S1 $\rightarrow$ S13	2.374	522	0.0309	S1 $\rightarrow$ S13	2.363	525	0.0063
S1 $\rightarrow$ S14	2.403	516	0.0090	S1 $\rightarrow$ S14	2.253	550	0.0089
S1 $\rightarrow$ S15	2.395	518	0.0003	S1 $\rightarrow$ S15	2.212	561	0.0007

Table C.6: The transitions from the T_1 state, with corresponding oscillator strengths at the T_1 geometry.

DMF				Toluene			
	E (eV)	λ (nm)	f_{osc}		E (eV)	λ (nm)	f_{osc}
T1 $\rightarrow$ T1	0	Inf	0.0000	T1 $\rightarrow$ T1	0	Inf	0.000
T1 $\rightarrow$ T2	1.008	1230	0.1229	T1 $\rightarrow$ T2	0.997	1244	0.015
T1 $\rightarrow$ T3	1.173	1057	0.0311	T1 $\rightarrow$ T3	1.17	1060	0.004
T1 $\rightarrow$ T4	1.198	1035	0.0080	T1 $\rightarrow$ T4	1.204	1030	0.005
T1 $\rightarrow$ T5	1.362	910	0.0051	T1 $\rightarrow$ T5	1.353	916	0.018
T1 $\rightarrow$ T6	1.496	829	0.0001	T1 $\rightarrow$ T6	1.345	922	0.000
T1 $\rightarrow$ T7	2.201	563	0.0044	T1 $\rightarrow$ T7	1.967	630	0.004
T1 $\rightarrow$ T8	2.203	563	0.0000	T1 $\rightarrow$ T8	2.215	560	0.000
T1 $\rightarrow$ T9	2.034	610	0.0259	T1 $\rightarrow$ T9	2.203	563	0.003
T1 $\rightarrow$ T10	**2.419**	**513**	**0.1342**	T1 $\rightarrow$ T10	2.417	513	0.029
T1 $\rightarrow$ T11	2.509	494	0.0012	T1 $\rightarrow$ T11	**2.499**	**496**	**0.077**
T1 $\rightarrow$ T12	2.567	483	0.0131	T1 $\rightarrow$ T12	2.565	483	0.043
T1 $\rightarrow$ T13	2.569	483	0.0000	T1 $\rightarrow$ T13	2.57	482	0.000
T1 $\rightarrow$ T14	2.907	427	0.0869	T1 $\rightarrow$ T14	2.718	456	0.000
T1 $\rightarrow$ T15	2.928	423	0.0000	T1 $\rightarrow$ T15	2.9	428	0.019

BIBLIOGRAPHY

[1] W.-M. Wan, A. W. Baggett, F. Cheng, H. Lin, S.-Y. Liu, and F. Jäkle, "Synthesis by free radical polymerization and properties of BN-polystyrene and BN-poly(vinylbiphenyl)," *Chem. Commun.*, vol. 52, no. 93, pp. 13616–13619, 2016.

[2] P. K. Nayak, S. Mahesh, H. J. Snaith, and D. Cahen, "Photovoltaic solar cell technologies: analysing the state of the art," *Nat. Rev. Mater.*, vol. 4, no. 4, pp. 269–285, 2019.

[3] L. A. Baker, M. D. Horbury, S. E. Greenough, P. M. Coulter, T. N. V. Karsili, G. M. Roberts, A. J. Orr-Ewing, M. N. R. Ashfold, and V. G. Stavros, "Probing the ultrafast energy dissipation mechanism of the sunscreen oxybenzone after UV-A irradiation," *J. Phys. Chem. Lett.*, vol. 6, no. 8, pp. 1363–1368, 2015.

[4] M. Rigby, S. Park, T. Saito, L. M. Western, A. L. Redington, X. Fang, S. Henne, A. J. Manning, R. G. Prinn, G. S. Dutton, P. J. Fraser, A. L. Ganesan, B. D. Hall, C. M. Harth, J. Kim, K.-R. Kim, P. B. Krummel, T. Lee, S. Li, Q. Liang, M. F. Lunt, S. A. Montzka, J. Mühle, S. O'Doherty, M.-K. Park, S. Reimann, P. K. Salameh, P. Simmonds, R. L. Tunnicliffe, R. F. Weiss, Y. Yokouchi, and D. Young, "Increase in CFC-11 emissions from eastern China based on atmospheric observations," *Nature*, vol. 569, no. 7757, pp. 546–550, 2019.

[5] A. Rickard and J. Young, "Master Chemical Mechanism, MCM v3.2." `http://mcm.york.ac.uk/home.htt`, 2021.
Accessed: 2021-03-25.

[6] The International GEOS-Chem Community, "GEOS-Chem." `https://zenodo.org/record/4681204`, 2021.

[7] S. Chapman, "On ozone and atomic oxygen in the upper atmosphere," *London, Edinburgh Dublin Philos. Mag. J. Sci.*, vol. 10, pp. 369–383, 1930.

[8] D. J. Jacob, *Introduction to Atmospheric Chemistry*.
Princeton University Press, 1999.

[9] P. J. Crutzen, M. G. Lawrence, and U. Pöschl, "On the background photochemistry of tropospheric ozone," *Tellus A*, vol. 51, no. 1, pp. 123–146, 1999.

[10] M. A. H. Khan, C. J. Percival, R. L. Caravan, C. A. Taatjes, and D. E. Shallcross, "Criegee intermediates and their impacts on the troposphere," *Environ. Sci.: Process. Impacts*, vol. 20, no. 3, pp. 437–453, 2018.

[11] J. Jiang, L. Cao, D. G. MacMartin, I. R. Simpson, B. Kravitz, W. Cheng, D. Visioni, S. Tilmes, J. H. Richter, and M. J. Mills, "Stratospheric sulfate aerosol geoengineering could alter the high-latitude seasonal cycle," *Geophys. Res. Lett.*, vol. 46, no. 23, pp. 14153–14163, 2019.

[12] K. Tonokura, T. Ogura, and M. Koshi, "Near-UV absorption spectrum of the phenoxyl radical and kinetics of its reaction with $CH_3^{\dagger}$," *J. Phys. Chem. A*, vol. 108, no. 39, pp. 7801–7805, 2004.

[13] M. Jaoui and R. Kamens, "Gas phase photolysis of pinonaldehyde in the presence of sunlight," *Atmos. Environ.*, vol. 37, no. 13, pp. 1835–1851, 2003.

[14] L. Zhang and W. A. Anderson, "Kinetic analysis of the photochemical decomposition of gas-phase chlorobenzene in a UV reactor: Quantum yield and photonic efficiency," *Chem. Eng. J.*, vol. 218, pp. 247–252, 2013.

[15] A. E. R. Harris, M. Cazaunau, A. Gratien, E. Pangui, J.-F. Doussin, and V. Vaida, "Atmospheric simulation chamber studies of the gas-phase photolysis of pyruvic acid," *J. Phys. Chem. A*, vol. 121, no. 44, pp. 8348–8358, 2017.

[16] F. D. Pope, C. A. Smith, P. R. Davis, D. E. Shallcross, M. N. R. Ashfold, and A. J. Orr-Ewing, "Photochemistry of formaldehyde under tropospheric conditions," *Faraday Discuss.*, vol. 130, p. 59, 2005.

[17] T. J. Bixby, J. C. Bolinger, J. D. Patterson, and P. J. Reid, "Femtosecond pump-probe studies of actinic-wavelength dependence in aqueous chlorine dioxide photochemistry," *J. Chem. Phys.*, vol. 130, no. 15, p. 154503, 2009.

[18] D. W. Trainor and C. W. von Rosenberg, "Flash photolysis study of the gas phase recombination of hydroxyl radicals," *J. Chem. Phys.*, vol. 61, no. 3, pp. 1010–1015, 1974.

[19] M. Sangwan and L. Zhu, "Role of methyl-2-nitrophenol photolysis as a potential source of OH radicals in the polluted atmosphere: Implications from laboratory investigation," *J. Phys. Chem. A*, vol. 122, no. 7, pp. 1861–1872, 2018.

[20] L. Vereecken, D. R. Glowacki, and M. J. Pilling, "Theoretical chemical kinetics in tropospheric chemistry: Methodologies and applications," *Chem. Rev.*, vol. 115, no. 10, pp. 4063–4114, 2015.

[21] L. Vereecken and J. S. Francisco, "Theoretical studies of atmospheric reaction mechanisms in the troposphere," *Chem. Soc. Rev.*, vol. 41, no. 19, p. 6259, 2012.

[22] R. L. Caravan, M. F. Vansco, K. Au, M. A. H. Khan, Y.-L. Li, F. A. F. Winiberg, K. Zuraski, Y.-H. Lin, W. Chao, N. Trongsiriwat, P. J. Walsh, D. L. Osborn, C. J. Percival, J. J.-M. Lin, D. E. Shallcross, L. Sheps, S. J. Klippenstein, C. A. Taatjes, and M. I. Lester, "Direct kinetic measurements and theoretical predictions of an isoprene-derived criegee intermediate," *Proc. Natl. Acad. Sci. U. S. A.*, vol. 117, no. 18, pp. 9733–9740, 2020.

[23] J. F. Möller, T. Stavrakou, and J. Peeters, "Chemistry and deposition in the model of atmospheric composition at global and regional scales using inversion techniques for trace gas emissions (magritte v1.1)-part 1: Chemical mechanism," *Geosci. Model Dev.*, vol. 12, no. 6, pp. 2307–2356, 2019.

[24] J. Peeters, T. L. Nguyen, and L. Vereecken, "HO_x radical regeneration in the oxidation of isoprene," *Phys. Chem. Chem. Phys.*, vol. 11, pp. 5935–5939, 2009.

[25] A. Galano and J. R. Alvarez-Idaboy, "Branching ratios of aliphatic amines + OH gas-phase reactions: A variational transition-state theory study," *J. Chem. Theory Comput.*, vol. 4, no. 2, pp. 322–327, 2008.

[26] F. Agostini and B. F. E. Curchod, "Different flavors of nonadiabatic molecular dynamics," *Wiley Interdiscip. Rev. Comput. Mol. Sci.*, p. e1417, 2019.

[27] B. Lasorne, M.-C. Bacchus-Montabonel, N. Vaeck, and M. Desouter-Lecomte, "Nonadiabatic interactions in wave packet dynamics of the bromoacetyl chloride photodissociation," *J. Chem. Phys.*, vol. 120, p. 1271–1278, 2004.

[28] F. Plasser, G. Granucci, J. Pittner, M. Barbatti, M. Persico, and H. Lischka, "Surface hopping dynamics using a locally diabatic formalism: Charge transfer in the ethylene dimer cation and excited state dynamics in the 2-pyridone dimer," *J. Chem. Phys.*, vol. 137, p. 22A514, 2012.

[29] H. Park, N. Kumar, M. Melander, T. Vegge, J. M. G. Lastra, and D. J. Siegel, "Adiabatic and nonadiabatic charge transport in Li–S batteries," *Chem. Mater.*, vol. 30, no. 3, pp. 915–928, 2018.

[30] T. Northey and T. Penfold, "The intersystem crossing mechanism of an ultrapure blue organoboron emitter," *Org. Electron.*, vol. 59, pp. 45–48, 2018.

[31] Y. Li, Q. Gong, L. Yue, W. Wang, and F. Liu, "Photochemistry of the simplest criegee intermediate, CH_2OO: Photoisomerization channel toward dioxirane revealed by CASPT2 calculations and trajectory surface-hopping dynamics," *J. Phys. Chem. Lett.*, vol. 9, p. 978–981, 2018.

[32] A. Francés-Monerris, J. Carmona-García, A. U. Acuña, J. Z. Dávalos, C. A. Cuevas, D. E. Kinnison, J. S. Francisco, A. Saiz-Lopez, and D. Roca-Sanjuàn, "Photodissociation mechanisms of major mercury(II) species in the atmospheric chemical cycle of mercury," *Angew. Chem. Int. Ed.*, vol. 59, pp. 7605–7610, 2020.

[33] C. Lévêque, A. Komainda, R. Taïeb, and H. Köppel, "Ab initio quantum study of the photodynamics and absorption spectrum for the coupled $^1A_2$ and $^1B_1$ states of SO_2," *J. Chem. Phys.*, vol. 138, no. 4, p. 044320, 2013.

[34] P. Ehrenfest, "Bemerkung über die angenäherte gültigkeit der klassischen mechanik innerhalb der quantenmechanik," *Z. Phys.*, vol. 45, no. 7-8, pp. 455–457, 1927.

[35] B. F. E. Curchod and T. J. Martínez, "Ab initio nonadiabatic quantum molecular dynamics," *Chem. Rev.*, vol. 118, no. 7, pp. 3305–3336, 2018.

[36] T. Dresselhaus, C. B. A. Bungey, P. J. Knowles, and F. R. Manby, "Coupling electrons and vibrations in molecular quantum chemistry," *J. Chem. Phys.*, vol. 153, p. 214114, 2020.

[37] A. Dreuw and M. Head-Gordon, "Single-reference ab initio methods for the calculation of excited states of large molecules," *Chem. Rev.*, vol. 105, p. 4009–4037, 2005.

[38] H. Lischka, D. Nachtigallová, A. J. A. Aquino, P. G. Szalay, F. Plasser, F. B. C. Machado, and M. Barbatti, "Multireference approaches for excited states of molecules," *Chem. Rev.*, vol. 118, p. 7293–7361, 2018.

[39] E. Runge and E. K. U. Gross, "Density-functional theory for time-dependent systems," *Phys. Rev. Lett.*, vol. 52, pp. 997–1000, 1984.

[40] M. E. Casida, "Time-dependent density-functional response theory for molecules," in *Recent advances in density functional methods* (D. P. Chong, ed.), vol. 1, pp. 155–192, Singapore: World Scientific, 1995.

[41] C. A. Ullrich, *Time-Dependent Density-Functional Theory: Concepts and Applications*. Oxford University Press, 2012.

[42] F. Cordova, L. J. Doriol, A. Ipatov, and M. E. Casida, "Troubleshooting time-dependent density-functional theory for photochemical applications: Oxirane," *J. Chem. Phys.*, vol. 127, p. 164111, 2007.

[43] A. D. Laurent and D. Jacquemin, "TD-DFT benchmarks: A review," *Int. J. Quantum Chem.*, vol. 113, pp. 2019–2039, 2013.

[44] D. Mester and M. Kállay, "Reduced-scaling approach for configuration interaction singles and time-dependent density functional theory calculations using hybrid functionals," *J. Chem. Theory Comput.*, vol. 15, p. 1690–1704, 2019.

[45] M. Manathunga, Y. Miao, D. Mu, A. W. Götz, and K. M. M. Jr., "Parallel implementation of density functional theory methods in the quantum interaction computational kernel program," *J. Chem. Theory Comput.*, vol. 16, p. 4315–4326, 2020.

[46] S. B. Worster, O. Feighan, and F. R. Manby, "Reliable transition properties from excited-state mean-field calculations," *J. Chem. Phys.*, vol. 154, p. 124106, 2021.

[47] A. Tajti, L. Tulipán, and P. G. Szalay, "Accuracy of spin-component scaled ADC(2) excitation energies and potential energy surfaces," *J. Chem. Theory Comput.*, vol. 16, p. 468–474, 2020.

[48] H. Keller-Rudek, G. K. Moortgat, R. Sander, and R. Sörensen, "The MPI-Mainz UV/VIS spectral atlas of gaseous molecules of atmospheric interest," *Earth System Science Data*, vol. 5, no. 2, pp. 365–373, 2013.

[49] K. Sneskov and O. Christiansen, "Excited state coupled cluster methods," *Wiley Interdiscip. Rev. Comput. Mol. Sci.*, vol. 2, no. 4, pp. 566–584, 2012.

[50] D. Jacquemin, I. Duchemin, and X. Blase, "0-0 energies using hybrid schemes: Benchmarks of TD-DFT, CIS(D), ADC(2), CC2, and BSE/GW formalisms for 80 real-life compounds," *J. Chem. Theory Comput.*, vol. 11, no. 11, pp. 5340–5359, 2015.

[51] J. Segarra-Martí, F. Segatta, T. A. Mackenzie, A. Nenov, I. Rivalta, M. J. Bearpark, and M. Garavelli, "Modeling multidimensional spectral lineshapes from first principles: application to water-solvated adenine," *Faraday Discuss.*, vol. 221, pp. 219–244, 2019.

[52] R. Schinke, *Photodissociation Dynamics*.
University Press, Cambridge, 1993.

[53] R. Crespo-Otero and M. Barbatti, "Spectrum simulation and decomposition with nuclear ensemble: formal derivation and application to benzene, furan and 2-phenylfuran," *Theo. Chem. Acc.*, vol. 131, no. 6, pp. 1–14, 2012.

[54] S. L. Li, X. Xu, and D. G. Truhlar, "Computational simulation and interpretation of the low-lying excited electronic states and electronic spectrum of thioanisole," *Phys. Chem. Chem. Phys.*, vol. 17, pp. 20093–20099, 2015.

[55] E. J. Heller, "The semiclassical way to molecular spectroscopy," *Acc. Chem. Res.*, vol. 14, pp. 368–375, 1981.

[56] V. Barone, J. Bloino, M. Biczysko, and F. Santoro, "Fully integrated approach to compute vibrationally resolved optical spectra: from small molecules to macrosystems," *J. Chem. Theory Comput.*, vol. 5, no. 3, pp. 540–554, 2009.

[57] E. U. Condon, "A theory of intensity distribution in band systems," *Phys. Rev.*, vol. 28, pp. 1182–1201, 1926.

[58] E. U. Condon, "Nuclear motions associated with electron transitions in diatomic molecules," *Phys. Rev.*, vol. 32, pp. 858–872, 1928.

[59] J. Franck, "Elementary processes of photochemical reactions," *Trans. Faraday Soc.*, vol. 21, pp. 536–542, 1926.

[60] A. Baiardi, J. Bloino, and V. Barone, "General formulation of vibronic spectroscopy in internal coordinates," *J. Chem. Phys.*, vol. 144, no. 8, p. 84114, 2016.

[61] F. Duschinsky, "The importance of the electron spectrum in multi atomic molecules. concerning the Franck-Condon principle," *Acta Physicochim.*, vol. 7, pp. 551–556, 1937.

[62] F. Neese, "The ORCA program system," *Wiley Interdiscip. Rev. Comput. Mol. Sci.*, vol. 2, pp. 73–78, 2012.

[63] S. L. Li and D. G. Truhlar, "Franck–Condon models for simulating the band shape of electronic absorption spectra," *J. Chem. Theo. Comp.*, vol. 13, pp. 2823–2830, 2017.

[64] M. J. Frisch, G. W. Trucks, H. B. Schlegel, G. E. Scuseria, M. A. Robb, J. R. Cheeseman, G. Scalmani, V. Barone, G. A. Petersson, H. Nakatsuji, X. Li, M. Caricato, A. V. Marenich, J. Bloino, B. G. Janesko, R. Gomperts, B. Mennucci, H. P. Hratchian, J. V. Ortiz, A. F. Izmaylov, J. L. Sonnenberg, D. Williams-Young, F. Ding, F. Lipparini, F. Egidi, J. Goings, B. Peng, A. Petrone, T. Henderson, D. Ranasinghe, V. G. Zakrzewski, J. Gao, N. Rega, G. Zheng, W. Liang, M. Hada, M. Ehara, K. Toyota, R. Fukuda, J. Hasegawa, M. Ishida, T. Nakajima, Y. Honda, O. Kitao, H. Nakai, T. Vreven, K. Throssell, J. Montgomery, J. A., J. E. Peralta, F. Ogliaro, M. J. Bearpark, J. J. Heyd, E. N. Brothers, K. N. Kudin, V. N. Staroverov, T. A. Keith, R. Kobayashi, J. Normand, K. Raghavachari, A. P. Rendell, J. C. Burant, S. S. Iyengar, J. Tomasi, M. Cossi, J. M. Millam, M. Klene, C. Adamo, R. Cammi, J. W. Ochterski, R. L. Martin, K. Morokuma, O. Farkas, J. B. Foresman, and D. J. Fox, "Gaussian 16, Revision C.01," 2016.
Gaussian Inc. Wallingford CT.

[65] E. Wigner, "On the quantum correction for thermodynamic equilibrium," *Phys. Rev.*, vol. 40, pp. 749–759, 1932.

[66] W. B. Case, "Wigner functions and Weyl transforms for pedestrians," *Am. J. Phys.*, vol. 76, p. 937, 2008.

[67] L. Sun and W. L. Hase, "Comparisons of classical and Wigner sampling of transition state energy levels for quasiclassical trajectory chemical dynamics simulations," *J. Chem. Phys.*, vol. 133, p. 044313, 2010.

[68] M. Barbatti and K. Sen, "Effects of different initial condition samplings on photodynamics and spectrum of pyrrole," *Int. J. Quantum Chem.*, vol. 116, no. 10, pp. 762–771, 2016.

[69] N. O'Boyle, M. Banck, C. James, C. Morley, T. Vandermeersch, and G. R. Hutchison, "Open Babel:an open chemical toolbox.," *J. Cheminform.*, vol. 3, 2011.

[70] G. E. Sims, I.-G. Choi, and S.-H. Kim, "Protein conformational space in higher order ψ-ϕ maps," *Proc. Natl. Acad. Sci. U.S.A.*, vol. 102, no. 3, pp. 618–621, 2005.

[71] M. Barbatti, M. Ruckenbauer, F. Plasser, J. Pittner, G. Granucci, M. Persico, and H. Lischka, "Newton-X: A surface-hopping program for nonadiabatic molecular dynamics," *Wiley Interdiscip. Rev. Comput. Mol. Sci.*, vol. 4, no. 1, pp. 26–33, 2014.

[72] B. K. Carpenter, J. N. Harvey, and D. R. Glowacki, "Prediction of enhanced solvent-induced enantioselectivity for a ring opening with a bifurcating reaction path," *Phys. Chem. Chem. Phys*, vol. 17, pp. 8372–8381, 2014.

[73] C. Heidelbach, I. I. Fedchenia, D. Schwarzer, and J. Schroeder, "Molecular-dynamics simulation of collisional energy transfer from vibrationally highly excited azulene in compressed CO_2," *J. Chem. Phys.*, vol. 108, pp. 10152–10161, 1998.

[74] D. H. Lu and W. L. Hase, "Classical trajectory calculation of the benzene overtone spectra," *J. Phys. Chem.*, vol. 92, p. 3217–3225, 1988.

[75] D. H. Lu and W. L. Hase, "Classical mechanics of intramolecular vibrational energy flow in benzene. v. effect of zero-point energy motion," *J. Chem. Phys.*, vol. 91, pp. 7490 – 7497, 1989.

[76] V. Garbuio, M. Cascella, L. Reining, R. D. Sole, and O. Pulci, "Ab initio calculation of optical spectra of liquids: Many-body effects in the electronic excitations of water," *Phys. Rev. Lett.*, vol. 97, p. 137402, 2006.

[77] A. Hermann, W. G. Schmidt, and P. Schwerdtfeger, "Resolving the optical spectrum of water: Coordination and electrostatic effects," *Phys. Rev. Lett.*, vol. 100, p. 207403, 2008.

[78] L. Bernasconia, "Statistical average of model orbital potentials for extended systems: Calculation of the optical absorption spectrum of liquid water," *J. Chem. Phys.*, vol. 132, p. 184513, 2010.

[79] C. W. Dierking, F. Zurheide, T. Zeuch, J. Med, S. Parez, and P. Slavíček, "Revealing isomerism in sodium-water clusters: Photoionization spectra of $Na(H_2O)_n$ (n = 2–90)," *J. Chem. Phys.*, vol. 146, p. 244303, 2017.

[80] M. Tuckerman, D. Marx, and M. Parrinello, "The nature and transport mechanism of hydrated hydroxide ions in aqueous solution," *Nature*, vol. 417, pp. 925–929, 2002.

[81] N.-T. Van-Oanh, C. Falvo, F. Calvo, D. Lauvergnat, M. Basire, M.-P. Gaigeot, and P. Parneix, "Improving anharmonic infrared spectra using semiclassically prepared molecular dynamics simulations," *Phys. Chem. Chem. Phys.*, vol. 14, pp. 2381–2390, 2012.

[82] D. G. Truhlar and J. T. Muckerman, "Reactive scattering cross sections iii: Quasiclassical and semiclassical methods," in *Atom-Molecule Collision Theory: A Guide for the Experimentalist* (R. B. Bernstein, ed.), p. 505–566, New York: Plenum Press, 1979.

[83] K. Drużbicki, M. Krzystyniak, D. Hollas, V. Kapil, P. Slavíček, G. Romanelli, and F. Fernandez-Alonso, "Hydrogen dynamics in solid formic acid: insights from simulations with quantum colored-noise thermostats," *J. Phys. Conf. Ser.*, vol. 1055, p. 012003, 2018.

[84] M. Ceriotti, G. Bussi, and M. Parrinello, "Colored-noise thermostats à la carte," *J. Chem. Theo. Comp.*, vol. 6, pp. 1170–1180, 2010.

[85] M. Ceriotti, *A novel framework for enhanced molecular dynamics based on the generalized Langevin equation*.
PhD thesis, ETH Zurich, 2010.

[86] M. Ceriotti, D. E. Manolopoulos, and M. Parrinello, "Accelerating the convergence of path integral dynamics with a generalized Langevin equation," *J. Chem. Phys.*, vol. 134, p. 084104, 2011.

[87] F. D. Sala, R. Rousseau, A. Görling, and D. Marx, "Quantum and thermal fluctuation effects on the photoabsorption spectra of clusters," *Phys. Rev. Lett.*, vol. 92, p. 183401, 2004.

[88] M. Ceriotti, M. Parrinello, T. E. Markland, and D. E. Manolopoulos, "Efficient stochastic thermostatting of path integral molecular dynamics," *J. Chem. Phys.*, vol. 133, p. 124104, 2010.

[89] D. Hollas, J. Suchan, and S. Sršeň, "ABIN." `https://github.com/PHOTOX/ABIN`.
Accessed: 2020-10-13.

[90] M. J. Frisch, G. W. Trucks, H. B. Schlegel, G. E. Scuseria, M. A. Robb, J. R. Cheeseman, G. Scalmani, V. Barone, B. Mennucci, G. A. Petersson, H. Nakatsuji, M. Caricato, X. Li, H. P. Hratchian, A. F. Izmaylov, J. Bloino, G. Zheng, J. L. Sonnenberg, M. Hada, M. Ehara, K. Toyota, R. Fukuda, J. Hasegawa, M. Ishida, T. Nakajima, Y. Honda, O. Kitao, H. Nakai, T. Vreven, J. A. Montgomery, Jr., J. E. Peralta, F. Ogliaro, M. Bearpark, J. J. Heyd, E. Brothers, K. N. Kudin, V. N. Staroverov, R. Kobayashi, J. Normand, K. Raghavachari, A. Rendell, J. C. Burant, S. S. Iyengar, J. Tomasi, M. Cossi, N. Rega, J. M. Millam, M. Klene, J. E. Knox, J. B. Cross, V. Bakken, C. Adamo, J. Jaramillo, R. Gomperts, R. E. Stratmann, O. Yazyev, A. J. Austin, R. Cammi, C. Pomelli, J. W.

Ochterski, R. L. Martin, K. Morokuma, V. G. Zakrzewski, G. A. Voth, P. Salvador, J. J. Dannenberg, S. Dapprich, A. D. Daniels, O. Farkas, J. B. Foresman, J. V. Ortiz, J. Cioslowski, and D. J. Fox, "Gaussian 09 Revision E.01," 2009.
Gaussian Inc. Wallingford CT 2009.

[91] M. Ceriotti, "GLE4MD project: Automatic input generation." `http://gle4md.org/`, 2020. Accessed: 2020-10-15.

[92] F. Neese, "Software update: the ORCA program system, version 4.0," *Wiley Interdiscip. Rev.: Comput. Mol. Sci.*, vol. 8, p. e1327, 2017.

[93] F. Neese, "The ORCA program system," *Wiley Interdiscip. Rev.: Comput. Mol. Sci.*, vol. 2, pp. 73–78, 2012.

[94] D. Hollas, E. Muchová, and P. Slavíček, "Modeling liquid photoemission spectra: Path-integral molecular dynamics combined with tuned range-separated hybrid functionals," *J. Chem. Theory Comput.*, vol. 12, no. 10, pp. 5009–5017, 2016.

[95] F. Santoro and A. Lami, "Effective method to compute vibrationally resolved optical spectra of large molecules at finite temperature in the gas phase and in solution," *J. Chem. Phys.*, vol. 126, p. 184102, 2007.

[96] S. Nosé, "A unified formulation of the constant temperature molecular-dynamics methods," *J. Chem. Phys.*, vol. 81, pp. 511–519, 1984.

[97] W. G. Hoover, "Canonical dynamics: Equilibrium phase-space distributions," *Phys. Rev. A.*, vol. 31, pp. 1695–1697, 1985.

[98] H. C. Andersen, "Molecular dynamics simulations at constant pressure and/or temperature," *J. Chem. Phys.*, vol. 72, pp. 2384–2393, 1980.

[99] M. P. Allen and D. J. Tidlesley, *Computer Simulation of Liquids*.
Clarendon Press, 1987.

[100] P. H. Hünenberger, "Thermostat algorithms for molecular dynamics simulations," *Adv. Polym. Sci.*, vol. 173, pp. 105–149, 2005.

[101] Š. Sršeň, J. Sita, P. Slavíček, V. Ladányi, and D. Heger, "Limits of the nuclear ensemble method for electronic spectra simulations: Temperature dependence of the (E)-azobenzene spectrum," *J. Chem. Theory Comput.*, vol. 16, no. 10, pp. 6428–6438, 2020.

[102] J. B. Zobel, J. J. Nogueira, and L. Gonzaáles, "Finite-temperature Wigner phase-space sampling and temperature effects on the excited-state dynamics of 2-nitronaphthalene," *Phys. Chem. Chem. Phys.*, vol. 21, pp. 13906–13915, 2019.

[103] M. Hillery, R. F. O'Connell, M. O. Scully, and E. P. Wigner, "Distribution functions in physics: fundamentals," *Phys. Rep.*, vol. 106, pp. 121–167, 1984.

[104] L. Messaadia, G. E. Dib, A. Ferhati, E. Roth, and A. Chakir, "Gas phase UV absorption cross-sections for a series of hydroxycarbonyls," *Chem. Phys. Lett.*, vol. 529, pp. 16–22, 2012.

[105] F. Kossoski and M. Barbatti, "Nuclear ensemble approach with importance sampling," *J. Chem. Theo. Comp.*, vol. 14, pp. 3173–3183, 2018.

[106] H. Keller-Rudek, G. K. Moortgat, R. Sander, and R. Sörensen, "The MPI-Mainz UV/Vis spectral atlas of gaseous molecules of atmospheric interest," *Earth Sys. Sci. Data*, vol. 5, no. 2, pp. 365–373, 2013.

[107] J. D. Rogers, "Ultraviolet absorption cross sections and atmospheric photodissociation rate constants of formaldehyde," *J. Phys. Chem.*, vol. 94, no. 10, pp. 4011–4015, 1990.

[108] I. Magneron, "unpublished data, measured at the Max-Planck-Institut für Chemie, Mainz, Germany," 1998.

[109] D. Shchepanovska, R. J. Shannon, B. F. E. Curchod, and D. R. Glowacki, "Nonadiabatic kinetics in the intermediate coupling regime: Comparing molecular dynamics to an energy-grained master equation," *J. Phys. Chem. A*, vol. 125, no. 16, pp. 3473–3488, 2021.

[110] A. Sisto, D. Glowacki, and T. Martínez, "Ab initio nonadiabatic dynamics of multichromophore complexes: A scalable graphical-processing-unit-accelerated exciton framework," *Acc. Chem. Res*, vol. 47, no. 9, pp. 2857–2866, 2014.

[111] A. Sisto, C. Stross, M. W. Van Der Kamp, M. O'Connor, S. McIntosh-Smith, G. T. Johnson, E. G. Hohenstein, F. R. Manby, D. R. Glowacki, and T. J. Martínez, "Atomistic nonadiabatic dynamics of the LH2 complex with a GPU-accelerated: Ab initio exciton model," *Phys. Chem. Chem. Phys.*, vol. 19, no. 23, pp. 14924–14936, 2017.

[112] D. Hayes, G. B. Griffin, and G. S. Engel, "Engineering coherence among excited states in synthetic heterodimer systems," *Science*, vol. 360, pp. 1431–1434, 2013.

[113] M. K. Lee and D. F. Coker, "Modeling electronic-nuclear interactions for excitation energy transfer processes in light-harvesting complexes," *J. Phys. Chem. Lett.*, vol. 7, pp. 3171–3178, 2016.

[114] S. Shim, P. Rebentrost, S. Valleau, and A. Aspuru-Guzik, "Atomistic study of the long-lived quantum coherences in the Fenna-Matthews-Olson complex," *Biophys. J.*, vol. 102, pp. 649–660, 2012.

[115] L. Landau, "A theory of energy transfer," *Phys. Z. Sowjet.*, vol. 2, no. 46, 1932.

[116] C. Zener, "Non-adiabatic crossing of energy levels," *Proc. R. Soc. A*, vol. 137, no. 833, pp. 696–702, 1932.

[117] E. Stueckelberg, "Theory of inelastic collisions between atoms," *Helv. Phys. Acta*, vol. 5, no. 369, 1932.

[118] H. Nakamura, "Semiclassical treatment of nonadiabatic transitions: Multilevel curve crossing and nonadiabatic tunneling problems," *J. Chem. Phys.*, vol. 87, no. 7, pp. 4031–4041, 1987.

[119] C. Zhu, H. Nakamura, N. Re, and V. Aquilanti, "The two-state linear curve crossing problems revisited. I. Analysis of Stokes phenomenon and expressions for scattering matrices," *J. Chem. Phys.*, vol. 97, no. 3, pp. 1892–1904, 1992.

[120] C. Zhu and H. Nakamura, "The two-state linear curve crossing problems revisited. II. Analytical approximations for the Stokes constant and scattering matrix: The Landau-Zener case," *J. Chem. Phys.*, vol. 97, no. 11, pp. 8497–8514, 1992.

[121] C. Zhu and H. Nakamura, "The two-state linear curve crossing problems revisited. III. Analytical approximations for Stokes constant and scattering matrix: Nonadiabatic tunneling case," *J. Chem. Phys.*, vol. 98, no. 8, pp. 6208–6222, 1993.

[122] C. Zhu and H. Nakamura, "Two-state linear curve crossing problems revisited. IV. The best analytical formulas for scattering matrices," *J. Chem. Phys.*, vol. 101, no. 6, pp. 4855–4866, 1994.

[123] C. Zhu and H. Nakamura, "Theory of nonadiabatic transition for general two-state curve crossing problems. I. Nonadiabatic tunneling case," *J. Chem. Phys.*, vol. 101, no. 12, pp. 10630–10647, 1994.

[124] C. Zhu and H. Nakamura, "Theory of nonadiabatic transition for general two-state curve crossing problems. II. Landau-Zener case," *J. Chem. Phys.*, vol. 102, no. 19, pp. 7448–7461, 1995.

[125] J. C. Tully, "Molecular dynamics with electronic transitions," *J. Chem. Phys.*, vol. 93, no. 2, pp. 1061–22, 1990.

[126] I. Horenko, C. Salzmann, B. Schmidt, and C. Schutte, "Quantum-classical Liouville approach to molecular dynamics: Surface hopping gaussian phase-space packets," *J. Chem. Phys.*, vol. 117, p. 11075, 2002.

[127] E. Rodrigues, G. P.and Ventura, S. Andrade Do Monte, and M. Barbatti, "Photochemical deactivation process of HCFC-133a ($C_2H_2F_3Cl$): A nonadiabatic dynamics study," *J. Phys. Chem. A*, vol. 118, pp. 12041 – 12049, 2014.

[128] A. Prlj, L. M. Ibele, E. Marsili, and B. F. E. Curchod, "On the theoretical determination of photolysis properties for atmospheric volatile organic compounds," *J. Phys. Chem. Lett.*, vol. 11, pp. 5418–5425, 2020.

[129] R. B. Shemesh, D.; Gerber, "Femtosecond timescale deactivation of electronically excited peroxides at ice surfaces," *Mol. Phys.*, vol. 110, pp. 605–617, 2012.

[130] J. Westermayr, M. Gastegger, F. S. J. M. Menger, S. Mai, L. Gonzalez, and P. Marquetand, "Machine learning enables long time scale molecular photodynamics simulations," *Chem. Sci.*, vol. 10, pp. 8100–8107, 2019.

[131] M. A. Blitz, R. J. Salter, D. E. Heard, and P. W. Seakins, "An experimental and master equation study of the kinetics of OH/OD + SO_2: The limiting high-pressure rate coefficients," *J. Phys. Chem. A.*, vol. 121, no. 17, pp. 3184–3191, 2017.

[132] D. Glowacki, C. Liang, S. Marsden, J. Harvey, and M. Pilling, "Alkene hydroboration: Hot intermediates that react while they are cooling," *J. Am. Chem. Soc.*, vol. 132, no. 39, pp. 13621–13623, 2010.

[133] L. M. Goldman, D. R. Glowacki, and B. K. Carpenter, "Nonstatistical dynamics in unlikely places: [1,5]-hydrogen migration in chemically activated cyclopentadiene," *J. Am. Chem. Soc.*, vol. 133, pp. 5312–5318, 2011.

[134] D. R. Glowacki, W. J. Rodgers, R. Shannon, S. H. Robertson, and J. N. Harvey, "Reaction and relaxation at surface hotspots: using molecular dynamics and the energy-grained master equation to describe diamond etching," *Philos. Trans. R. Soc. A*, vol. 375, no. 2092, 2017.

[135] D. Bonhommeau and D. G. Truhlar, "Mixed quantum/classical investigation of the photodissociation of NH_3 and a practical method for maintaining zero-point energy in classical trajectories," *J. Chem. Phys.*, vol. 129, p. 014302, 2008.

[136] W. H. Miller, "Tunneling corrections to unimolecular rate constants, with application to formaldehyde.," *J. Am. Chem. Soc.*, vol. 101, pp. 6810–6814, 1979.

[137] B. C. Garrett and D. G. Truhlar, "Semi-classical tunneling calculations," *J. Phys. Chem.*, vol. 83, pp. 2921–2926, 1979.

[138] J. C. Lorquet and B. Leyh-Nihant, "Nonadiabatic unimolecular reactions. 1. a statistical formulation for the rate constants," *J. Phys. Chem.*, vol. 92, pp. 4778–4783, 1988.

[139] S. Hammes-Schiffer and J. C. Tully, "Nonadiabatic transition state theory and multiple potential energy surface molecular dynamics of infrequent events.," *J. Chem. Phys.*, vol. 103, no. 19, pp. 8528–8537, 1995.

[140] A. O. Lykhin, D. S. Kaliakin, G. E. dePolo, A. A. Kuzubov, and S. A. Varganov, "Nonadiabatic transition state theory: Application to intersystem crossings in the active sites of metal-sulfur proteins," *Int. J. Quantum Chem.*, vol. 116, pp. 750–761, 2016.

[141] J. N. Harvey, "Understanding the kinetics of spin-forbidden chemical reactions," *Phys. Chem. Chem. Phys.*, vol. 9, pp. 331–343, 2006.

[142] J. N. Harvey and M. Aschi, "Modelling spin-forbidden reactions: recombination of carbon monoxide with iron tetracarbonyl," *Faraday Discuss.*, vol. 124, pp. 129–143, 2003.

[143] R. R. Zaari and S. A. Varganov, "Nonadiabatic transition state theory and trajectory surface hopping dynamics: Intersystem crossing between $^3B_1$ and $^1A_1$ states of SiH_2," *J. Phys. Chem. A*, vol. 119, pp. 1332–1338, 2015.

[144] A. O. Lykhin and S. A. Varganov, "Intersystem crossing in tunneling regime: $T_1 \rightarrow S_0$ relaxation in thiophosgene," *Phys. Chem. Chem. Phys.*, vol. 22, pp. 5500–5508, 2020.

[145] B. Maiti, G. C. Schatz, and G. Lendvay, "Importance of intersystem crossing in the S(^{3}P, ^{1}D) + $H_2 \rightarrow$ SH + H reaction," *J. Phys. Chem. A*, vol. 108, pp. 8772–8781, 2004.

[146] G. Granucci, M. Persico, and G. Spighi, "Surface hopping trajectory simulations with spin-orbit and dynamical couplings," *J. Chem. Phys.*, vol. 137, no. 22, 2012.

[147] M. Richter, P. Marquetand, J. González-Vázquez, I. Sola, and L. González, "SHARC: *ab initio* molecular dynamics with surface hopping in the adiabatic representation including arbitrary couplings," *J. Chem. Theory Comput.*, vol. 7, pp. 1253–1258, 2011.

[148] S. Mai, P. Marquetand, and L. González, "A general method to describe intersystem crossing dynamics in trajectory surface hopping," *Int. J. Quantum Chem.*, vol. 115, pp. 1215–1231, 2015.

[149] J. Peeters and J. F. Müller, "HO_x radical regeneration in isoprene oxidation via peroxy radical isomerisations. II: Experimental evidence and global impact," *Phys. Chem. Chem. Phys.*, vol. 12, no. 42, pp. 14227–14235, 2010.

[150] J. Lelieveld, T. M. Butler, J. N. Crowley, T. J. Dillon, H. Fischer, L. Ganzeveld, H. Harder, M. G. Lawrence, M. Martinez, D. Taraborrelli, and J. Williams, "Atmospheric oxidation capacity sustained by a tropical forest," *Nature*, vol. 452, no. 7188, pp. 737–740, 2008.

[151] D. Taraborrelli, M. G. Lawrence, J. N. Crowley, T. J. Dillon, S. Gromov, C. B. Groß, L. Vereecken, and J. Lelieveld, "Hydroxyl radical buffered by isoprene oxidation over tropical forests," *Nat. Geosci.*, vol. 5, no. 3, pp. 190–193, 2012.

[152] R. Hansen, T. Lewis, L. Graham, L. Whalley, P. Seakins, D. Heard, and M. Blitz, "OH production from the photolysis of isoprene-derived peroxy radicals: cross-sections, quantum yields and atmospheric implications," *Phys. Chem. Chem. Phys.*, vol. 19, pp. 2332–2345, 2017.

[153] J. Peeters, J.-F. Müller, T. Stavrakou, and V. S. Nguyen, "Hydroxyl radical recycling in isoprene oxidation driven by hydrogen bonding and hydrogen tunneling: The upgraded LIM1 mechanism," *J. Phys. Chem. A*, vol. 118, pp. 8625–8643, 2004.

[154] G. M. Wolfe, J. D. Crounse, J. D. Parrish, J. M. St. Clair, M. R. Beaver, F. Paulot, T. P. Yoon, P. O. Wennberg, and F. N. Keutsch, "Photolysis, OH reactivity and ozone reactivity of a proxy for isoprene-derived hydroperoxyenals (HPALDs)," *Phys. Chem. Chem. Phys.*, vol. 14, no. 20, p. 7276, 2012.

[155] P. Dirac, "Note on exchange phenomena in the thomas atom," *Math. Proc. Camb. Philos. Soc.*, vol. 26, no. 3, pp. 376–385, 1930.

[156] M. H. Beck, A. Jäckle, G. A. Worth, and H. D. Meyer, "The multiconfiguration time-dependent Hartree (MCTDH) method: A highly efficient algorithm for propagating wavepackets," *Phys. Rep.*, vol. 324, no. 1, pp. 1–105, 2000.

[157] H. D. Meyer, U. Manthe, and L. S. Cederbaum, "The multi-configurational time-dependent Hartree approach," *Chem. Phys. Lett.*, vol. 165, no. 1, pp. 73–78, 1990.

[158] G. Worth, H. D. Meyer, and L. S. Cederbaum, "Relaxation of a system with a conical intersection coupled to a bath: A benchmark 24-dimensional wave packet study treating the environment explicitly.," *J. Chem. Phys.*, vol. 109, no. 3518, 1998.

[159] G. Worth, M. Robb, and I. Burghardt, "A novel algorithm for non-adiabatic direct dynamics using variational Gaussian wavepackets," *Faraday Discuss.*, vol. 127, pp. 307–323, 2004.

[160] B. Lasorne, M. J. Bearpark, M. A. Robb, and G. A. Worth, "Direct quantum dynamics using variational multi-configuration Gaussian wavepackets," *Chem. Phys. Lett.*, vol. 432, no. 4-6, pp. 604–609, 2006.

[161] G. Richings, I. Polyak, K. Spinlove, G. Worth, I. Burghardt, and B. Lasorne, "Quantum dynamics simulations using Gaussian wavepackets: the vMCG method," *Int. Rev. Phys. Chem.*, vol. 34, no. 2, pp. 269–308, 2015.

[162] T. J. Martínez, M. Ben-Nun, and R. D. Levine, "Multi-electronic-state molecular dynamics: A wave function approach with applications," *J. Phys. Chem.*, vol. 100, no. 19, pp. 7884–7895, 1996.

[163] B. Mignolet and B. F. Curchod, "A walk through the approximations of ab initio multiple spawning," *J. Chem. Phys.*, vol. 148, no. 13, 2018.

[164] J. C. Tully and R. K. Preston, "Trajectory surface hopping approach to nonadiabatic molecular collisions: The reaction of H^+ with D_2.," *J. Chem. Phys.*, vol. 55, no. 2, pp. 562–572, 1971.

[165] A. A. M. H. M. Darghouth, M. E. Casida, X. Zhu, B. Natarajan, H. Su, A. Humeniuk, E. Titov, X. Miao, and R. Mitrić, "Effect of varying the TD-lc-DFTB range-separation parameter on charge and energy transfer in a model pentacene/buckminsterfullerene heterojunction," *J. Chem. Phys.*, vol. 154, no. 5, p. 054102, 2021.

[166] W. K. Chen, X. Y. Liu, W. H. Fang, P. O. Dral, and G. Cui, "Deep learning for nonadiabatic excited-state dynamics," *J. Phys. Chem. Lett*, vol. 9, no. 23, pp. 6702–6708, 2018.

[167] P. O. Dral, M. Barbatti, and W. Thiel, "Nonadiabatic excited-state dynamics with machine learning," *J. Phys. Chem. Lett*, vol. 9, no. 19, pp. 5660–5663, 2018.

[168] D. Glowacki, J. Lockhart, M. Blitz, S. Klippenstein, M. Pilling, S. Robertson, and P. Seakins, "Interception of excited vibrational quantum states by O_2 in atmospheric association reactions," *Science*, vol. 337, no. 6098, pp. 1066–1069, 2012.

[169] J. M. C. Plane, C. L. Whalley, L. Frances-Soriano, A. Goddard, J. N. Harvey, D. R. Glowacki, and A. A. Viggiano, "$O_2(A_{1g})$ + Mg, Fe, and Ca: Experimental kinetics and formulation of a weak collision, multi-well master equation with spin-hopping," *J. Chem. Phys.*, vol. 137, p. 014310, 2012.

[170] H. Nakamura, "Dynamics of nonadiabatic chemical reactions," *J. Phys. Chem. A.*, vol. 110, pp. 10929–10946, 2006.

[171] T. Baer and W. L. Hase, *Unimolecular Reaction Dynamics*.
Oxford University Press, 1996.

[172] D. R. Glowacki, R. Lightfoot, and J. N. Harvey, "Non-equilibrium phenomena and molecular reaction dynamics: Mode space, energy space and conformer space," *Mol. Phys.*, vol. 111, no. 5, pp. 631–640, 2013.

[173] L. T. A. Ho and L. F. Chibotaru, "A simple derivation of the Landau-Zener formula," *Phys. Chem. Chem. Phys.*, vol. 16, no. 15, pp. 6942–6945, 2014.

[174] C. Zhu and H. Nakamura, " Erratum: Two-state linear curve crossing problems revisited. IV. The best analytical formulas for scattering matrices? ," *J. Chem. Phys.*, vol. 108, no. 17, pp. 7501–7501, 1998.

[175] H. Nakamura, *Nonadiabatic Transition: Concepts, Basic Theories And Applications*. World Scientific Publishing Company, 2002.

[176] D. Tozer, "Relationship between long-range charge-transfer excitation energy error and integer discontinuity in Kohn-Sham theory.," *J. Chem. Phys.*, vol. 119, no. 12697, 2003.

[177] B. Levine, C. Ko, J. Quenneville, and T. J. Martínez, "Conical intersections and double excitations in time-dependent density functional theory.," *Mol. Phys.*, vol. 104, pp. 5–7, 2006.

[178] F. Agostini, B. F. E. Curchod, R. Vuilleumier, I. Tavernelli, and E. K. U. Gross, "TDDFT and quantum-classical dynamics: A universal tool describing the dynamics of matter," in *Handbook of Materials Modeling* (W. Andreoni and S. Yip, eds.), pp. 1–47, Cham: Springer International Publishing, 2018.

[179] B. F. E. Curchod, U. Rothlisberger, and I. Tavernelli, "Trajectory-based nonadiabatic dynamics with time-dependent density functional theory," *Chem. Phys. Chem. Rev.*, vol. 14, pp. 1314–1340, 2013.

[180] H.-J. Werner, P. J. Knowles, G. Knizia, F. R. Manby, M. Schütz, *et al.*, "Molpro, version 2019.2, a package of ab initio programs," 2019.

[181] I. F. Galvãn, "OpenMolcas: From Source Code to Insight," *J. Chem. Theory Comput.*, vol. 15, no. 11, pp. 5925–5964, 2019.

[182] J. N. Harvey, M. Aschi, H. Schwarz, and W. Koch, "The singlet and triplet states of phenyl cation. a hybrid approach for locating minimum energy crossing points between non-interacting potential energy surfaces.," *Theo. Chem. Acc.*, vol. 99, pp. 95–99, 1997.

[183] R. Crespo-Otero and M. Barbatti, "Spectrum simulation and decomposition with nuclear ensemble: Formal derivation and application to benzene, furan and 2-phenylfuran," *Theo. Chem. Acc.*, vol. 131, no. 6, pp. 1–14, 2012.

[184] M. Barbatti, G. Granucci, M. Persico, M. Ruckenbauer, M. Vazdar, M. Eckert-Maksić, and H. Lischka, "The on-the-fly surface-hopping program system Newton-X: Application to ab initio simulation of the nonadiabatic photodynamics of benchmark systems," *J. Photochem. Photobiol. A*, vol. 190, no. 2-3, pp. 228–240, 2007.

[185] G. Granucci and M. Persico, "Critical appraisal of the fewest switches algorithm for surface hopping," *J. Chem. Phys.*, vol. 126, p. 134114, 2007.

[186] J. Pittner, H. Lischka, and M. Barbatti, "Optimization of mixed quantum-classical dynamics: Time-derivative coupling terms and selected couplings.," *Chem. Phys.*, vol. 356, pp. 147–152, 2009.

[187] K. Holbrook, M. Pilling, and S. Robertson, *Unimolecular Reactions*. Chichester: Wiley, 1996.

[188] S. Robertson, D. Glowacki, C.-H. Liang, C. Morley, R. Shannon, M. Blitz, and M. Pilling, "MESMER (master equation solver for multi energy well reactions)." `http://sourceforge.net/projects/mesmer`, 2020.

[189] T. Martínez, "Ab initio molecular dynamics around a conical intersection: Li(2p) + H_2," *Chem. Phys. Lett.*, vol. 272, pp. 139–147, 1997.

[190] L. Blancafort, P. Hunt, and M. A. Robb, "Intramolecular electron transfer in bis(methylene) adamantyl radical cation: A case study of diabatic trapping," *J. Am. Chem. Soc.*, vol. 127, pp. 3391–3399, 2005.

[191] M. Baasandorj, D. K. Papanastasiou, R. K. Talukdar, A. S. Hasson, and J. B. Burkholder, "$(CH_3)_3COOH$ (tert-butyl hydroperoxide): OH reaction rate coefficients between 206 and 375 K and the OH photolysis quantum yield at 248 nm," *Phys. Chem. Chem. Phys*, vol. 12, pp. 12101–12111, 2010.

[192] L. M. Ibele and B. F. E. Curchod, "A molecular perspective on Tully models for nonadiabatic dynamics," *Phys. Chem. Chem. Phys.*, vol. 22, pp. 15183–15196, 2020.

[193] D. R. Glowacki, S. K. Reed, M. J. Pilling, D. V. Shalashilin, and E. Martínez-Núñez, "Classical, quantum and statistical simulations of vibrationally excited $hoso_2$: Ivr, dissociation, and implications for oh + so_2 kinetics at high pressures," *Phys. Chem. Chem. Phys.*, vol. 11, p. 963—974, 2009.

[194] S. M. Parker and C. J. Schiltz, "Surface hopping with cumulative probabilities: Even sampling and improved reproducibility," *J. Chem. Phys.*, vol. 153, no. 17, p. 174109, 2020.

[195] G. A. Meek and B. G. Levine, "Accurate and efficient evaluation of transition probabilities at unavoided crossings in ab initio multiple spawning," *Chem. Phys.*, vol. 460, pp. 117–124, 2015.

[196] J. Zheng and D. G. Truhlar, "Multi-path variational transition state theory for chemical reaction rates of complex polyatomic species: Ethanol + OH reactions," *Faraday Discuss.*, vol. 157, pp. 59–88, 2012.

[197] S. Sharma, S. Raman, and W. H. Green, "Intramolecular hydrogen migration in alkylperoxy and hydroperoxyalkylperoxy radicals: Accurate treatment of hindered rotors," *J. Phys. Chem. A*, vol. 114, no. 18, pp. 5689–5701, 2010.

[198] J. B. Delos, "On the reactions of N_2 with O," *J. Chem. Phys.*, vol. 59, pp. 2365–2369, 1973.

[199] E. E. Nikitin, "Nonadiabatic transitions: What we learned from old masters and how much we owe them," *Annu. Rev. Phys. Chem.*, vol. 50, pp. 1–21, 1999.

[200] J. Suchan, D. Hollas, B. F. E. Curchod, and P. Slavíček, "On the importance of initial conditions for excited-state dynamics," *Faraday Discuss.*, vol. 212, pp. 307–330, 2018.

[201] M. Barbatti, "Simulation of excitation by sunlight in mixed quantum-classical dynamics," *J. Chem. Theo. Comput.*, vol. 16, pp. 4849–4856, 2020.

[202] Y. Wang, D. J. Jacob, and J. A. Logan, "Global simulation of tropospheric O_3-NO_x-hydrocarbon chemistry: 3. Origin of tropospheric ozone and effects of nonmethane hydrocarbons," *J. Geophys. Res. Atmos.*, vol. 103, no. D9, pp. 10757–10767, 1998.

[203] J. Lelieveld, W. Peters, F. J. Dentener, and M. C. Krol, "Stability of tropospheric hydroxyl chemistry," *J. Geophys. Res. Atmos.*, vol. 107, no. D23, 2002.

[204] M. G. Lawrence, P. J. Crutzen, P. J. Rasch, B. E. Eaton, and N. M. Mahowald, "A model for studies of tropospheric photochemistry: Description, global distributions, and evaluation," *J. Geophys. Res. Atmos.*, vol. 104, no. D21, pp. 26245–26277, 1999.

[205] U. Pöschl, R. Von Kuhlmann, N. Poisson, and P. J. Crutzen, "Development and intercomparison of condensed isoprene oxidation mechanisms for global atmospheric modeling," *J. Atmos. Chem.*, vol. 37, no. 1, pp. 29–52, 2000.

[206] P. O. Wennberg, K. H. Bates, J. D. Crounse, L. G. Dodson, R. C. McVay, L. A. Mertens, T. B. Nguyen, E. Praske, R. H. Schwantes, M. D. Smarte, J. M. St Clair, A. P. Teng, X. Zhang, and J. H. Seinfeld, "Gas-phase reactions of isoprene and its major oxidation products," *Chem. Rev.*, vol. 118, no. 7, pp. 3337–3390, 2018.

[207] A. P. Teng, J. D. Crounse, and P. O. Wennberg, "Isoprene peroxy radical dynamics," *J. Am. Chem. Soc.*, vol. 139, no. 15, pp. 5367–5377, 2017.

[208] J. D. Crounse, F. Paulot, H. G. Kjaergaard, and P. O. Wennberg, "Peroxy radical isomerization in the oxidation of isoprene," *Phys. Chem. Chem. Phys.*, vol. 13, no. 30, pp. 13607–13613, 2011.

[209] A. Novelli, L. Vereecken, B. Bohn, H. P. Dorn, G. I. Gkatzelis, A. Hofzumahaus, F. Holland, D. Reimer, F. Rohrer, S. Rosanka, D. Taraborrelli, R. Tillmann, R. Wegener, Z. Yu,

A. Kiendler-Scharr, A. Wahner, and H. Fuchs, "Importance of isomerization reactions for OH radical regeneration from the photo-oxidation of isoprene investigated in the atmospheric simulation chamber SAPHIR," *Atmos. Chem. and Phys.*, vol. 20, no. 6, pp. 3333–3355, 2020.

[210] T. Berndt, "Formation of carbonyls and hydroperoxyenals (HPALDs) from the OH radical reaction of isoprene for low-NO_x conditions: Influence of temperature and water vapour content," *J. Atmos. Chem.*, vol. 69, no. 4, pp. 253–272, 2012.

[211] T. Berndt, N. Hyttinen, H. Herrmann, and A. Hansel, "First oxidation products from the reaction of hydroxyl radicals with isoprene for pristine environmental conditions," *Commun. Chem.*, vol. 2, no. 1, p. 21, 2019.

[212] K. H. Møller, K. H. Bates, and H. G. Kjaergaard, "The importance of peroxy radical hydrogen-shift reactions in atmospheric isoprene oxidation," *J. Phys. Chem. A*, vol. 123, no. 4, pp. 920–932, 2019.

[213] M. Gerenkamp and S. Grimme, "Spin-component scaled second-order Møller-Plesset perturbation theory for the calculation of molecular geometries and harmonic vibrational frequencies," *Chem. Phys. Lett.*, vol. 392, no. 1-3, pp. 229–235, 2004.

[214] M. K. Kesharwani, B. Brauer, and J. M. Martin, "Frequency and zero-point vibrational energy scale factors for double-hybrid density functionals (and other selected methods): Can anharmonic force fields be avoided?," *J. Phys. Chem. A*, vol. 119, no. 9, pp. 1701–1714, 2015.

[215] S. G. Balasubramani, G. P. Chen, S. Coriani, M. Diedenhofen, M. S. Frank, Y. J. Franzke, F. Furche, R. Grotjahn, M. E. Harding, C. Hättig, A. Hellweg, B. Helmich-Paris, C. Holzer, U. Huniar, M. Kaupp, A. Marefat Khah, S. Karbalaei Khani, T. Müller, F. Mack, B. D. Nguyen, S. M. Parker, E. Perlt, D. Rappoport, K. Reiter, S. Roy, M. Rückert, G. Schmitz, M. Sierka, E. Tapavicza, D. P. Tew, C. van Wüllen, V. K. Voora, F. Weigend, A. Wodyński, and J. M. Yu, "TURBOMOLE: Modular program suite for ab initio quantum-chemical and condensed-matter simulations," *J. Chem. Phys.*, vol. 152, no. 18, p. 184107, 2020.

[216] T. Gaumnitz, A. Jain, Y. Pertot, M. Huppert, I. Jordan, F. Ardana-Lamas, and W. H. J., "Streaking of 43-attosecond soft-x-ray pulses generated by a passively cep-stable mid-infrared driver," *Optics Express*, vol. 25, pp. 27506–27518, 2017.

[217] E. Pradhan, K. Sato, and A. V. Akimov, "Non-adiabatic molecular dynamics with ΔSCF excited states," *J. Phys.: Condens. Matter*, vol. 30, no. 48, p. 484002, 2018.

[218] M. Huix-Rotllant, N. Ferré, and M. Barbatti, "Time-dependent density functional theory: from the fundamentals to nonadiabatic dynamics," in *Quantum Chemistry and Dynamics of Excited States: Methods and Applications* (L. González and R. Lindh, eds.), p. 15, Wiley, 2020.

[219] G. Granucci, M. Persico, and A. Zoccante, "Including quantum decoherence in surface hopping," *J. Chem. Phys.*, vol. 133, no. 13, p. 134111, 2010.

[220] J. E. Subotnik, A. Jain, B. Landry, A. Petit, W. Ouyang, and N. Bellonzi, "Understanding the surface hopping view of electronic transitions and decoherence," *Annu. Rev. Phys. Chem.*, vol. 67, no. 1, pp. 387–417, 2016.

[221] J. E. Subotnik, W. Ouyang, and B. R. Landry, "Can we derive Tully's surface-hopping algorithm from the semiclassical quantum Liouville equation? Almost, but only with decoherence," *J. Chem. Phys.*, vol. 139, p. 214107, 2013.

[222] C. C. Martens, "Surface Hopping without Momentum Jumps: A Quantum-Trajectory-Based Approach to Nonadiabatic Dynamics," *J. Phys. Chem. A*, vol. 123, no. 5, pp. 1110–1128, 2019.

[223] M. J. Falk, B. R. Landry, and J. E. Subotnik, "Can surface hopping sans decoherence recover Marcus theory? Understanding the role of friction in a surface hopping view of electron transfer," *J. Phys. Chem. B*, vol. 118, no. 28, pp. 8108–8117, 2014.

[224] J. Y. Fang and S. Hammes-Schiffer, "Improvement of the internal consistency in trajectory surface hopping," *J. Phys. Chem. A*, vol. 103, no. 47, pp. 9399–9407, 1999.

[225] B. J. Schwartz, E. R. Bittner, O. V. Prezhdo, and P. J. Rossky, "Quantum decoherence and the isotope effect in condensed phase nonadiabatic molecular dynamics simulations," *J. Chem. Phys.*, vol. 104, pp. 5942–5955, 1996.

[226] C. C. Martens, "Classical and nonclassical effects in surface hopping methodology for simulating coupled electronic-nuclear dynamics," *Faraday Discuss.*, vol. 221, pp. 449–477, 2020.

[227] C. C. Martens and J. Y. Fang, "Semiclassical-limit molecular dynamics on multiple electronic surfaces," *J. Chem. Phys.*, vol. 106, no. 12, pp. 4918–4930, 1997.

[228] S. J. Cotton, R. Liang, and W. H. Miller, "On the adiabatic representation of Meyer-Miller electronic-nuclear dynamics," *J. Chem. Phys.*, vol. 147, no. 6, p. 064112, 2017.

[229] D. Donnelly and E. Rogers, "Symplectic integrators: An introduction," *Am. J. Phys.*, vol. 73, no. 938, 2005.

[230] M. Tao, "Explicit symplectic approximation of nonseparable Hamiltonians: Algorithm and long time performance," *Phys. Rev. E*, vol. 94, no. 4, p. 043303, 2016.

[231] R. Kosloff, "Propagation methods for quantum molecular dynamics," *Annu. Rev. Phys. Chem.*, vol. 45, pp. 145–178, 1994.

[232] A. J. Leggett, S. Chakravarty, A. T. Dorsey, M. P. Fisher, A. Garg, and W. Zwerger, "Dynamics of the dissipative two-state system," *Rev. Mod. Phys.*, vol. 59, no. 1, pp. 1–85, 1987.

[233] S. Hammes-Schiffer and J. C. Tully, "Proton-transfer in solution - molecular-dynamics with quantum transitions," *J. Chem. Phys.*, vol. 101, pp. 4657–4667, 1994.

[234] F. Plasser, M. Ruckenbauer, S. Mai, M. Oppel, P. Marquetand, and L. González, "Efficient and flexible computation of many-electron wave function overlaps," *J. Chem. Theory Comput.*, vol. 12, pp. 1207–1219, 2016.

[235] M. Sneha, L. Lewis-Borrell, D. Shchepanovska, A. Bhattacherjee, J. Tyler, and A. J. Orr-Ewing, "Solvent-dependent photochemical dynamics of a phenoxazine-based photoredox catalyst," *Z. Phys. Chem.*, vol. 234, no. 7-9, pp. 1475–1494, 2020.

[236] P. Jaramillo, K. Coutinho, B. J. Cabral, and S. Canuto, "Explicit solvent effects on the visible absorption spectrum of a photosynthetic pigment: Chlorophyll-c2 in methanol," *Chem. Phys. Lett.*, vol. 516, no. 4-6, pp. 250–253, 2011.

[237] R. Naumann and M. Goez, "How the sustainable solvent water unleashes the photoredox catalytic potential of ruthenium polypyridyl complexes for pinacol couplings," *Green Chem.*, vol. 21, no. 16, pp. 4470–4474, 2019.

[238] M. M. Alam, M. Chattopadhyaya, S. Chakrabarti, and K. Ruud, "High-polarity solvents decreasing the two-photon transition probability of through-space charge-transfer systems — a surprising in silico observation," *J. Phys. Chem. Lett.*, vol. 3, no. 8, pp. 961–966, 2012.

[239] C. Randino, M. Moreno, R. Gelabert, and J. M. Lluch, "Peek at the potential energy surfaces of the LSSmKate1 and LSSmKate2 proteins," *J. Phys. Chem. B*, vol. 116, no. 49, pp. 14302–14310, 2012.

[240] D. Koyama, M. J. Milner, and A. J. Orr-Ewing, "Evidence for a double well in the first triplet excited state of 2-thiouracil," *J. Phys. Chem. B*, vol. 121, no. 39, pp. 9274–9280, 2017.

[241] X. F. Yu, S. Yamazaki, and T. Taketsugu, "Solvent effects on the excited-state double proton transfer mechanism in the 7-azaindole dimer: A TDDFT study with the polarizable continuum model," *Phys. Chem. Chem. Phys.*, vol. 19, no. 34, pp. 23289–23301, 2017.

[242] F. Lu, N. Kitamura, T. Takaya, K. Iwata, T. Nakanishi, and Y. Kurashige, "Experimental and theoretical investigation of fluorescence solvatochromism of dialkoxyphenyl-pyrene molecules," *Phys. Chem. Chem. Phys.*, vol. 20, no. 5, pp. 3258–3264, 2018.

[243] M. De Vetta, M. F. Menger, J. J. Nogueira, and L. González, "Solvent effects on electronically excited states: QM/continuum versus QM/explicit models," *J. Phys. Chem. B*, vol. 122, no. 11, pp. 2975–2984, 2018.

[244] T. J. Zuehlsdorff, P. D. Haynes, M. C. Payne, and N. D. Hine, "Predicting solvatochromic shifts and colours of a solvated organic dye: The example of Nile Red," *J. Chem. Phys.*, vol. 146, no. 12, p. 124504, 2017.

[245] S. Miertuš, E. Scrocco, and J. Tomasi, "Electrostatic interaction of a solute with a continuum. A direct utilizaion of AB initio molecular potentials for the prevision of solvent effects," *Chem. Phys.*, vol. 55, no. 1, pp. 117–129, 1981.

[246] A. Klamt and G. Schüürmann, "COSMO: A new approach to dielectric screening in solvents with explicit expressions for the screening energy and its gradient," *J. Chem. Soc., Perkin Trans. 2*, pp. 799–805, 1993.

[247] J. M. Herbert, "Dielectric continuum methods for quantum chemistry," *WIREs Comput. Mol. Sci.*, vol. 11, no. 4, 2021.

[248] F. R. Manby, M. Stella, J. D. Goodpaster, and T. F. Miller, "A simple, exact density-functional-theory embedding scheme," *J. Chem. Theo. Comput.*, vol. 8, no. 8, pp. 2564–2568, 2012.

[249] S. J. Bennie, B. F. Curchod, F. R. Manby, and D. R. Glowacki, "Pushing the limits of EOM-CCSD with projector-based embedding for excitation energies," *J. Phys. Chem. Lett.*, vol. 8, no. 22, pp. 5559–5565, 2017.

[250] X. Wen, D. S. Graham, D. V. Chulhai, and J. D. Goodpaster, "Absolutely localized projection-based embedding for excited states," *J. Chem. Theo. Comput.*, vol. 16, no. 1, pp. 385–398, 2019.

[251] J. M. Olsen, K. Aidas, and J. Kongsted, "Excited states in solution through polarizable embedding," *J. Chem. Theo. Comput.*, vol. 6, no. 12, pp. 3721–3734, 2010.

[252] M. Scheurer, M. F. Herbst, P. Reinholdt, J. M. H. Olsen, A. Dreuw, and J. Kongsted, "Polarizable embedding combined with the algebraic diagrammatic construction: Tackling excited states in biomolecular systems," *J. Chem. Theo. Comput.*, vol. 14, no. 9, pp. 4870–4883, 2018.

[253] N. H. List, J. M. H. Olsen, and J. Kongsted, "Excited states in large molecular systems through polarizable embedding," *Phys. Chem. Chem. Phys.*, vol. 18, no. 30, pp. 20234–20250, 2016.

[254] K. Sneskov, T. Schwabe, J. Kongsted, and O. Christiansen, "The polarizable embedding coupled cluster method," *J. Chem. Phys.*, vol. 134, no. 10, p. 104108, 2011.

[255] "Solvent physical properties." `https://people.chem.umass.edu/xray/solvent.html`. Accessed: 2021-05-30.

[256] J. Pascual-Ahuir, E. Silla, and I. Tunon, "GEPOL: An improved description of molecular surfaces. iii. a new algorithm for the computation of a solvent-excluding surface.," *J. Comput. Chem.*, vol. 15, no. 10, pp. 1127–1138, 1994.

[257] J. Tomasi, B. Mennucci, and R. Cammi, "Quantum mechanical continuum solvation models," *Chem. Rev.*, vol. 105, no. 8, pp. 2999–3094, 2005.

[258] J. G. Kirkwood, "Theory of solutions of molecules containing widely separated charges with special application to zwitterions," *J. Chem. Phys.*, vol. 2, no. 7, pp. 351–361, 1934.

[259] S. Jurinovich, G. Pescitelli, L. Di Bari, and B. Mennucci, "A TDDFT/MMPol/PCM model for the simulation of exciton-coupled circular dichroism spectra," *Phys. Chem. Chem. Phys.*, vol. 16, no. 31, pp. 16407–16418, 2014.

[260] A. Klamt, "The COSMO and COSMO-RS solvation models," *WIREs Comput. Mol. Sci.*, vol. 1, no. 5, pp. 699–709, 2011.

[261] A. V. Marenich, C. J. Cramer, and D. G. Truhlar, "Universal solvation model based on solute electron density and on a continuum model of the solvent defined by the bulk dielectric constant and atomic surface tensions," *J. Phys. Chem. B*, vol. 113, no. 18, pp. 6378–6396, 2009.

[262] S. Jockusch and Y. Yagci, "The active role of excited states of phenothiazines in photoinduced metal free atom transfer radical polymerization: singlet or triplet excited states?," *Polym. Chemi.*, vol. 7, pp. 6039–6043, 2016.

[263] N. J. Treat, H. Sprafke, J. W. Kramer, P. G. Clark, B. E. Barton, J. R. de Alaniz, B. P. Fors, and C. J. Hawker, "Metal-free atom transfer radical polymerization.," *J. Am. Chem. Soc.*, vol. 136, pp. 16096–16101, 2014.

[264] J. C. Theriot, C. H. Lim, H. Yang, M. D. Ryan, C. B. Musgrave, and G. M. Miyake, "Organocatalyzed atom transfer radical polymerization driven by visible light.," *Science*, vol. 352, pp. 1082–1086, 2016.

[265] Y. Du, R. M. Pearson, C. H. Lim, S. M. Sartor, M. D. Ryan, H. S. Yang, N. H. Damrauer, and G. M. Miyake, "Strongly reducing, visible-light organic photoredox catalysts as sustainable alternatives to precious metals.," *Chem. Eur. J.*, vol. 23, pp. 10962–10968, 2017.

[266] R. M. Pearson, C. H. Lim, B. G. McCarthy, C. B. Musgrave, and G. M. Miyake, "Organocatalyzed atom transfer radical polymerization using n-aryl phenoxazines as photoredox catalysts.," *J. Am. Chem. Soc.*, vol. 138, pp. 11399–11407, 2016.

[267] X. C. Pan, C. Fang, M. Fantin, W. Y. S. N. Malhotra, L. A. Peteanu, A. A. Isse, A. Gennaro, P. Liu, and K. Matyjaszewskit, "Mechanism of photoinduced metal-free atom transfer radical polymerization: Experimental and computational studies.," *J. Am. Chem. Soc.*, vol. 138, pp. 2411–2425, 2016.

[268] B. G. McCarthy, R. M. Pearson, C.-H. Lim, S. M. Sartor, N. H. Damrauer, and G. M. Miyake, "Structure-property relationships for tailoring phenoxazines as reducing photoredox catalysts.," *J. Am. Chem. Soc.*, vol. 140, no. 15, pp. 5088–5101, 2018.

[269] D. O. Kashinski, G. M. Chase, R. G. Nelson, O. E. D. Nallo, A. N. Scales, D. L. VanderLey, and E. F. C. Byrd, "Harmonic vibrational frequencies: Approximate global scaling factors for TPSS, M06, and M11 functional families using several common basis sets.," *J. Phys. Chem. A*, vol. 121, pp. 2265–2273, 2017.

[270] T. Lu and F. Chen, "Multiwfn: A multifunctional wavefunction analyzer.," *J. Comput. Chem.*, vol. 33, no. 49, pp. 580–592, 2012.

[271] S. M. Sartor, B. G. McCarthy, R. M. Pearson, G. M. Miyake, and N. H. Damrauer, "Exploiting charge-transfer states for maximizing intersystem crossing yields in organic photoredox catalysts," *J. Am. Chem. Soc.*, vol. 140, no. 14, pp. 4778–4781, 2018.

[272] M. P. Grubb, A. J. Orr-Ewing, and M. N. R. Ashfold, "KOALA: A program for the processing and decomposition of transient spectra," *Rev. Sci. Instru.*, vol. 85, no. 6, p. 064104, 2014.

[273] T. J. Zuehlsdorff, P. D. Haynes, F. Hanke, M. C. Payne, and N. D. M. Hine, "Solvent effects on electronic excitations of an organic chromophore," *J. Chem. Theo. Comput.*, vol. 12, no. 4, pp. 1853–1861, 2016.

[274] A. P. de Lima Batista, A. G. S. de Oliveira-Filho, and S. E. Galembeck, "Photophysical properties and the NO photorelease mechanism of a ruthenium nitrosyl model complex investigated using the CASSCF-in-DFT embedding approach," *Phys. Chem. Chem. Phys.*, vol. 19, no. 21, pp. 13860–13867, 2017.

[275] M. C. Cuquerella, V. Lhiaubet-Vallet, J. Cadet, and M. A. Miranda, "Benzophenone photosensitized DNA damage," *Acc. Chem. Res.*, vol. 45, no. 9, pp. 1558–1570, 2012.

[276] N. A. Romero and D. A. Nicewicz, "Organic photoredox catalysis," *Chem. Rev.*, vol. 116, no. 17, pp. 10075–10166, 2016.

[277] R. K. Venkatraman, C. Verma, and S. Umapathy, "Molecular dynamics and simulations study on the vibrational and electronic solvatochromism of benzophenone," *J. Chem. Phys.*, vol. 144, no. 6, p. 064302, 2016.

[278] R. K. Venkatraman, S. Kayal, A. Barak, A. J. Orr-Ewing, and S. Umapathy, "Intermolecular hydrogen bonding controlled intersystem crossing rates of benzophenone," *J. Phys. Chem. Lett.*, vol. 9, no. 7, pp. 1642–1648, 2018.

[279] D.-C. Sergentu, R. Maurice, R. W. A. Havenith, R. Broer, and D. Roca-Sanjuán, "Computational determination of the dominant triplet population mechanism in photoexcited benzophenone," *Phys. Chem. Chem. Phys.*, vol. 16, no. 46, pp. 25393–25403, 2014.

[280] L. Favero, G. Granucci, and M. Persico, "Surface hopping investigation of benzophenone excited state dynamics," *Phys. Chem. Chem. Phys.*, vol. 18, no. 15, pp. 10499–10506, 2016.

[281] R. Anderson, R. Hochstrasser, H. Lutz, and G. Scott, "Measurements of intersystem crossing kinetics using 3545-Å picosecond pulses: nitronaphthalenes and benzophenone," *Chem. Phys. Lett.*, vol. 28, no. 2, pp. 153–157, 1974.

[282] M. Marazzi, S. Mai, D. Roca-Sanjuán, M. G. Delcey, R. Lindh, L. González, and A. Monari, "Benzophenone ultrafast triplet population: Revisiting the kinetic model by surface-hopping dynamics," *J. Phys. Chem. Lett.*, vol. 7, no. 4, pp. 622–626, 2016.

[283] K. Freundorfer, D. Kats, T. Korona, and M. Schütz, "Local CC2 response method for triplet states based on laplace transform: Excitation energies and first-order properties," *J. Chem. Phys.*, vol. 133, no. 24, p. 244110, 2010.

[284] C. Hättig and F. Weigend, "CC2 excitation energy calculations on large molecules using the resolution of the identity approximation," *J. Chem. Phys.*, vol. 113, no. 13, p. 5154, 2000.

[285] M. Schreiber, M. R. Silva-Junior, S. P. A. Sauer, and W. Thiel, "Benchmarks for electronically excited states: CASPT2, CC2, CCSD, and CC3," *J. Chem. Phys.*, vol. 128, no. 13, p. 134110, 2008.

[286] H.-J. Werner, P. J. Knowles, G. Knizia, F. R. Manby, and M. Schütz, "Molpro: a general-purpose quantum chemistry program package," *WIREs Comput. Mol. Sci.*, vol. 2, pp. 242–253, 2012.

[287] S. J. R. Lee, F. Ding, F. R. Manby, and T. F. Miller, "Analytical gradients for projection-based wavefunction-in-DFT embedding," *J. Chem. Phys.*, vol. 151, no. 6, p. 064112, 2019.

[288] D. Shemesh, M. Luo, V. H. Grassian, and R. B. Gerber, "Absorption spectra of pyruvic acid in water: insights from calculations for small hydrates and comparison to experiment," *Phys. Chem. Chem. Phys.*, vol. 22, no. 22, pp. 12658–12670, 2020.

[289] J. Zhong, M. Kumar, J. Anglada, M. Martins-Costa, M. Ruiz-Lopez, X. Zeng, and J. S. Francisco, "Atmospheric spectroscopy and photochemistry at environmental water interfaces," *Annual Review of Physical Chemistry*, vol. 70, no. 1, pp. 45–69, 2019.

[290] A. Winter, "QtGrace v0.2.6." `https://sourceforge.net/projects/qtgrace/`, 2017. Accessed: 2019-04-09.